

# **Synchrotron X-ray Studies on Structural and Chemical Ordering in Group IV-Based Magnetic Epitaxial Films**

**Brian Akira Collins**

A dissertation submitted to the faculty of the University of North Carolina at Chapel Hill  
in partial fulfillment of the requirements for the degree of Doctor of Philosophy  
in the Department of Physics and Astronomy.

Chapel Hill  
2009

Approved by:

Dr. Frank Tsui

Dr. Yong S. Chu

Dr. Rene Lopez

Dr. Jianping Lu

Dr. Sean Washburn

© 2009

Brian Akira Collins

ALL RIGHTS RESERVED

## **Abstract**

Brian Akira Collins: Synchrotron X-ray Studies on Structural and Chemical Ordering  
in Group IV-Based Magnetic Epitaxial Films

(Under the direction of Dr. Frank Tsui and Dr. Yong S. Chu)

In this thesis, complementary synchrotron x-ray techniques have been used to study compositional and epitaxial effects on structural and chemical ordering of Ge-based magnetic semiconductor films and Heusler alloys  $\text{Co}_2\text{MnGe}$  and  $\text{Co}_2\text{MnSi}$  on the atomic scale. Combinatorial x-ray methods have been developed in this work to enhance the study of these materials. The study of transition metal doping in Ge reveals that the stability of magnetic dopants can be enhanced when two magnetic dopants (Mn and Co or Fe and Co) are used to reduce epitaxial strains and alter energetics and kinetics of epitaxial growth, resulting in suppression of metallic precipitates and significantly higher doping levels. Codoping is also shown to be responsible for an increase in populations of substitutional states over those in films with a single dopant. The study also reveals the strong interplay between dopant states and structural, magnetic, and electronic properties. In  $\text{Co}_x\text{Mn}_y\text{Ge}_z$  films, epitaxial constraints are shown to play an important role in stabilizing the Heusler structure over a large region of chemical composition. Additionally, it is found that structural and chemical ordering of these alloys are sensitive to the atomic ratio between Co and Mn and are strongly affected by epitaxial strains. Experiments and analysis of an anomalous diffraction technique have been developed in order to quantitatively probe structural and chemical disorders that can contribute to the suppression of the half metallic state. These studies reveal that the primary defects occurring in these films are Mn-Ge site swapping, as Co vacancies and Ge antisites

constitute secondary defects that depend strongly on composition and epitaxial constraints. However, defects previously predicted to suppress the half metallic state, specifically Co-Mn swapping and antisites, are not present. These findings demonstrate that compositional and epitaxial effects can be used as viable means to control structure and magnetism on the atomic scale.

## **Acknowledgements**

I would like to thank Dr. Frank Tsui for his excellent mentorship in a complex and competitive field. He has shown outstanding abilities as a research scientist and an impressive prowess at understanding the direction and importance of a project and its results. His candor and friendly discussions have increased my respect for and understanding of academia.

I would also like to thank Dr. Yong Chu for his one-on-one mentorship in developing the experimental skills necessary to complete successful complex experiments. His expertise in numerous aspects of x-ray scattering has helped me to understand the experimental opportunities in synchrotron radiation. His upbeat personality and extreme patience throughout weeks-long continuous runs has made the studies in this thesis successful.

The contributions of the members of the Tsui group have also provided me with support. Particularly, this study would not have been possible without the devoted expertise of Dr. Liang He, who produced all of the samples used in this work and contributed many of the complementary studies and much of the analysis, including RHEED and magnetotransport measurements. He also contributed to many useful intellectual discussions on my own analysis and results. Others in the group provided intellectual and moral support. They are Dr. Pranaba Muduli; graduate students William Rice, Matthew Wolboldt, and Charles Malmberg; and undergraduates Alexander Mellnik and Jeffrey Haller.

At the Advanced Photon Source, Dr. Stefan Vogt at the beamline 2-ID-E provided customized fitting software and expertise on quantitative fitting analysis of x-ray fluorescence spectroscopy.

Dr. Yuncheng Zhong is acknowledged for providing assistance in beamline setup and data taking at the

2-BM beamline. The former X-ray Microscopy and Imaging Group leader Dr. Qun Shen (who is now the director of Experimental Facilities Division of the NSLS II) is also gratefully acknowledged for his support of the close collaboration between his group and the Tsui group at UNC. Dr. Daniel Haskel and Dr. Evgeny Krastov in the Magnetic Materials Group at the APS provided much expertise and guidance for all aspects of extended x-ray absorption fine structure (EXAFS), including experimental methods, data processing and analysis, and interpretation of results. Dr. Krastov provided initial EXAFS fitting and training for mastery in this analysis. Dr. Haskel also provided critical *ab initio* calculations and discussions for the development and analysis of the anomalous diffraction studies in this work.

The National School for Neutron and X-ray Scattering at Argonne National Laboratory provided background understanding and hands-on experience in synchrotron and neutron radiation properties and techniques, which led to the expansion of x-ray studies into the local probe techniques for this thesis.

This thesis would not have been possible without the enthusiastic encouragement and moral support of my wife Deborah and daughter Sophie.

The thesis research has been supported by Department of Energy, Office of Sciences, Office of Basic Energy Sciences, Grant No. DE-FG02-05ER46216, including support for RA, travel, and tuition and supplies. MBE synthesis was supported by U.S. National Science Foundation, Grant No. DMR-0441218. The work on developing an in-situ SPM instrument was supported by NSF DMR-0526893. Combinatorial synthesis instrumentation was supported by U.S. Department of Defense, Grant No. W911NF-05-1-0173. Support by Dr. John Zavada at Army Research Office is also

acknowledged. Support for one half research assistantship from Sector 2 of the Advanced Photon Source under subcontract No. 5F-00428 is gratefully acknowledged. Use of the Advanced Photon Source is supported by the U. S. Department of Energy, Office of Sciences, Office of Basic Energy Sciences, under Contract No. DE-AC02-06CH11357. Research assistantship for the 2008-2009 academic year was supported under the University of North Carolina Graduate School Dissertation Completion Research Fellowship.

## Table of Contents

<b>Chapter 1 Introduction .....</b>	<b>1</b>
1.1 Background .....	1
1.2 Magnetic Semiconductors .....	4
1.3 Halfmetallic Materials.....	8
1.4 MBE Synthesis .....	10
1.5 Synchrotron X-Ray Techniques.....	12
1.6 Investigation of Atomic Scale Structural and Chemical Ordering .....	14
Bibliography .....	16
 <b>Chapter 2 Samples .....</b>	 <b>21</b>
1.1 Materials Synthesis.....	21
1.2 Reflection High Energy Electron Diffraction.....	26
1.3 Sample Preparation .....	30
Bibliography .....	33
 <b>Chapter 3 X-ray Techniques and Theory .....</b>	 <b>35</b>
3.1 Experimental Setup .....	35
3.1a: Source Parameters.....	35
3.1b: Beamline Components.....	36
3.1c: Diffractometer Alignment .....	41
3.1d: X-ray Focusing .....	43
3.1e: Energy Calibration.....	44
3.2 X-ray Diffraction Techniques .....	45



3.2a: X-ray Diffraction Theory .....	45
3.2b: Single Crystal X-ray Diffraction .....	47
3.2c: Crystal Truncation Rod Analysis.....	50
3.2d: Wide-Angle Diffraction .....	57
3.3 Spectroscopic Techniques .....	59
3.3a: X-ray Fluorescence Spectroscopy .....	59
3.3b: Extended X-ray Absorption Fine Structure.....	63
3.4 Anomalous Diffraction .....	67
3.4a: Data Collection and Processing .....	67
3.4b: Modeling .....	70
3.5 Combinatorial X-ray Methods .....	74
3.5a: Beam Footprint.....	74
3.5b: Beam Position Reproducibility and Combinatorial Scans .....	76
3.6 Data Processing and Exploration .....	80
3.6a: Import Spec Data v2.1.....	81
3.6b: Peak Analysis v1.2.....	83
Bibliography .....	87
<b>Chapter 4 Dopant Stability and Ordering in a Germanium Matrix .....</b>	<b>89</b>
4.1 Growth Studies <i>In Situ</i> .....	90
4.1a: RHEED analysis on $\text{Co}_x\text{Mn}_y\text{Ge}_{1-x-y}$ .....	90
4.1b: Other codoping systems .....	95
4.2 Dopant Segregation and Stacking Faults .....	97
4.2a: Ternary Phase Diagram of Disorders .....	97
4.2b: Depth Dependence and Diffusion .....	102
4.3 Strain States and Epitaxial Coherence .....	104
4.3a: Fitting Methods and Elastic Correction.....	105
4.3b: Ternary Phase Diagram for Strain.....	107

4.4 Local Atomic Ordering and Dopant States .....	113
4.4a: Qualitative Elemental Environments .....	114
4.4b: Dopant Populations .....	120
4.4c: Electronic and Magnetic Properties .....	124
4.5 The $(\text{FeCo})_x\text{Ge}_{1-x}$ System.....	126
4.5a: Disorders .....	127
4.5b: Strain States .....	129
4.5c: Dopant and Magnetic States .....	132
4.5d: Bulk Electronic and Magnetic Properties .....	134
4.6 Summary .....	136
Bibliography .....	138
<b>Chapter 5 Crystallographic and Chemical Ordering in Heusler Alloys .....</b>	<b>141</b>
5.1 Epitaxial Phase Diagram of $\text{Co}_x\text{Mn}_y\text{Ge}_z$ .....	142
5.1a: Crystallographic Phases.....	143
5.1b: Ordering and Phase Transitions .....	147
5.2 Ordering of the Ge Heusler .....	151
5.2a: Structure Factor Considerations, Atomic Site Ordering and Strain States .....	151
5.2b: Structural and Chemical Stacking Sequences.....	157
5.3 Quantitative Study of Site-Specific Elemental Disorders in the Ge Heusler .....	162
5.3a: Individual Elemental Resonances and Reflections .....	162
5.3b: Fitting Procedures for the Complete Model .....	165
5.3c: Full Spectrum Fit Results .....	169
5.4 Structural and Chemical Ordering of the Si Heusler.....	174
5.4a: Thickness and Temperature Dependence.....	175
5.4b: Ternary Phase Diagram .....	178
5.5 Summary .....	182
Bibliography .....	184

<b>Chapter 6 Conclusions .....</b>	<b>186</b>
<b>Curriculum Vitae.....</b>	<b>190</b>

## List of Tables

Table 4-1: Vegard's law coefficients for the coherent regions of $\text{Co}_x\text{Mn}_y\text{Ge}_{1-x-y}$ .....	108
Table 5-1: Three unique Bragg reflections of the Heusler structure .....	152
Table 5-2: Parameters used in anomalous diffraction fitting and their relation to occupancy.....	166
Table 5-3: Fit results for the full spectrum anomalous diffraction .....	170

## List of Figures

Figure 1-1: Spin-resolved density of electron states in various material phases. ....	8
Figure 2-1: Combinatorial molecular beam epitaxy growth system.....	23
Figure 2-2: Schematic for depositing combinatorial samples .....	24
Figure 2-3: Diagram of how RHEED patterns are created .....	26
Figure 2-4: RHEED patterns of the four growth modes .....	28
Figure 2-5: Visibility of scribed crosses on a ternary sample using various probes.....	31
Figure 3-1: Experimental setup at the 2-BM beamline experiment station.....	38
Figure 3-2: Pictures of detector setup, geometry, and sample mounting .....	40
Figure 3-3: Diffractometer Alignment.....	43
Figure 3-4: Diagrams of single crystal x-ray diffraction.....	48
Figure 3-5: Schematic of crystal truncation rods (CTR). ....	52
Figure 3-6: Fits of various models to a CTR intensity profile at (00L). ....	55
Figure 3-7: HRTEM image showing contrasting layers of the film and the CTR Analysis program.....	56
Figure 3-8: Data and processing powder diffraction using wide-angle XRD .....	58
Figure 3-9: X-ray florescence spectroscopy (XRF) spectra and analysis.....	61
Figure 3-10: EXAFS EXAFS data and processing in Athena. ....	64
Figure 3-11: Example EXAFS data reproducibility and processing.....	66
Figure 3-12: Anomalous diffraction and EXAFS data .....	69
Figure 3-13: Data assembly of full spectrum anomalous diffraction .....	70
Figure 3-14: Modeling and fitting the instrumental resolution function .....	73

Figure 3-15: Beam footprint comparison for various reflections .....	75
Figure 3-16: XRF maps of scribed crosses for position reproducibility .....	77
Figure 3-17: Beam positioning and combinatorial scan setup .....	79
Figure 3-18: Simplified Import SPEC Data panel .....	81
Figure 3-19: Advanced panels of Import SPEC Data .....	82
Figure 3-20: Peak Analysis main panel .....	84
Figure 3-21: Peak Analysis secondary panels and windows .....	85
Figure 4-1: RHEED analysis and HRTEM images for a typical $\text{Co}_x\text{Mn}_y\text{Ge}_{1-x-y}$ binary sample .....	91
Figure 4-2: Real-time RHEED analysis .....	93
Figure 4-3: Full ternary phase diagram of the roughening transition for $\text{Mn}_x\text{Co}_y\text{Ge}_{1-x-y}$ .....	94
Figure 4-4: RHEED analysis on the $(\text{Fe}_{0.46}\text{Co}_{0.54})_x\text{Ge}_{1-x}$ system grown on GaAs (001) .....	95
Figure 4-5: RHEED patterns of various codoping systems.....	96
Figure 4-6: Wide angle diffraction results from $\text{Co}_x\text{Mn}_y\text{Ge}_{1-x-y}$ films.....	98
Figure 4-7: Reciprocal space mapping and analysis of stacking fault peaks .....	99
Figure 4-8: Ternary epitaxial phase diagram of disorders in the $\text{Co}_x\text{Mn}_y\text{Ge}_{1-x-y}$ system.....	101
Figure 4-9: Depth dependent Mn and Co concentrations for $\text{Co}_x\text{Mn}_y\text{Ge}_{1-x-y}$ .....	103
Figure 4-10: Example fits of a specular and an in-plane CTR at one composition .....	106
Figure 4-11: Ternary epitaxial phase diagram of film strain for $\text{Co}_x\text{Mn}_y\text{Ge}_{1-x-y}$ (001).....	109
Figure 4-12: Strain, Debye-Waller disorder and fringe coherence from CTR analysis.....	111
Figure 4-13: EXAFS data and analysis at the Co edge on $(\text{Co}_x\text{Mn}_{1-x})_{0.05}\text{Ge}_{0.95}$ films .....	116
Figure 4-14: Atomic models used in the EXAFS fitting process .....	117

Figure 4-15: EXAFS data and analysis at the Mn edge on $(\text{Co}_x\text{Mn}_{1-x})_{0.05}\text{Ge}_{0.95}$ films .....	118
Figure 4-16: EXAFS data and analysis at the Ge edge on $(\text{Co}_x\text{Mn}_{1-x})_{0.05}\text{Ge}_{0.95}$ films and a bare substrate .....	119
Figure 4-17: Physical characteristics of substitutional dopant states calculated from EXAFS fit parameters .....	121
Figure 4-18: Strain comparison between XRD measurements and EXAFS fit results .....	122
Figure 4-19: Physical characteristics of the secondary dopant states calculated from EXAFS fit parameters .....	123
Figure 4-20: Magnetic and magnetotransport properties of $\text{Co}_x\text{Mn}_{0.04-x}\text{Ge}_{0.96}$ (001) epitaxial films.....	125
Figure 4-21: Evolution of stacking faults for $(\text{FeCo})_x\text{Ge}_{1-x}/\text{GaAs}$ .....	128
Figure 4-22: [00L] CTR intensities for $(\text{FeCo})_x\text{Ge}_{1-x}$ on Ge and GaAs .....	130
Figure 4-23: Strain versus doping concentration for films grown on Ge and GaAs.....	131
Figure 4-24: EXAFS on $(\text{FeCo})_x\text{Ge}_{1-x}/\text{Ge}$ (001) films.....	133
Figure 4-25: Transport properties of $(\text{FeCo})_x\text{Ge}_{1-x}$ .....	135
Figure 5-1: Schematic diffraction patterns of crystallographic phases in $\text{Co}_x\text{Mn}_y\text{Ge}_z/\text{Ge}(111)$ .....	144
Figure 5-2: Ternary epitaxial phase diagram of the $\text{Co}_x\text{Mn}_y\text{Ge}_z/\text{Ge}(111)$ system .....	146
Figure 5-3: Nature of phase transitions and structural ordering in $(\text{Co}_x\text{Mn}_{1-x})_{0.75}\text{Ge}_{0.25}$ .....	148
Figure 5-4: Evolution of structural ordering in the $\text{Co}_x\text{Mn}_y\text{Ge}_z/\text{Ge}(111)$ system .....	149
Figure 5-5: Ferromagnetic regions in the $\text{Co}_x\text{Mn}_y\text{Ge}_z/\text{Ge}(111)$ system .....	150
Figure 5-6: Schematic of the Heusler structure .....	151
Figure 5-7: Composition evolution Bragg reflection intensities in the Heusler structure.....	153
Figure 5-8: Compositional evolution of strain and lattice parameter of Heusler films.....	155

Figure 5-9: Structural and chemical stacking sequence of the Heusler alloy in the (111) orientation .....	157
Figure 5-10: Models for different stacking sequences of the unit cell.....	158
Figure 5-11: Models for different chemical sequences of the unit cell .....	160
Figure 5-12: Ratio Diffracted intensity ratios taken at the Co edge to those taken below the edge .....	161
Figure 5-13: Models of Co-antisites and a fit to intensities of the S2 reflection around the Co absorption edge .....	163
Figure 5-14: Anomalous diffraction intensities and fit results from the S1 reflection around the Ge-edge as a function of Ge composition .....	164
Figure 5-15: Evolution of key anomalous diffraction fit parameters with the Debye-Waller factor .....	167
Figure 5-16: Models of disorders discussed in the literature compared with data .....	168
Figure 5-17: Full spectrum anomalous diffraction fits .....	169
Figure 5-18: Data and fits of the S1 reflection at the Ge edge with different solid state effects.....	172
Figure 5-19: Compositional trends of disorder populations found from the full spectrum anomalous diffraction analysis .....	173
Figure 5-20: Thickness dependent RHEED intensities of a (CoxMn1-x)0.77Si0.23 binary sample .....	176
Figure 5-21: XRD analysis of (CoxMn1-x)0.77Si0.23 samples.....	177
Figure 5-22: Ternary epitaxial phase diagram of CoxMnySiz/Ge(111).....	179
Figure 5-23: Crystallographic ordering in CoxMnySiz/Ge(111).....	180
Figure 5-24: Compositional evolution of strain and lattice parameter in CoxMnySiz/Ge(111) .....	181



# Chapter 1 Introduction

---

## 1.1 Background

One of the most interesting aspects of materials science is exploring the relationships and interactions between structure, magnetism and electronic properties. Today much of our information technology exploits ferromagnetic materials for information storage and uses electronic charge in semiconductors for logic processing. It is well known that electronic states carry both electron charge and spin degrees of freedom, and the potential of utilizing the full spin dependent states for information technology has long been sought after.<sup>1-4</sup> The study of magnetoelectronics has been a subject where both degrees of freedom are used with one of the first breakthroughs being the discovery of giant magnetoresistance (GMR).<sup>5,6</sup> In GMR, an electron traveling from one ferromagnetic layer to an oppositely polarized layer is scattered at the interface, causing significantly more resistance than would be present in two layers with parallel magnetization. With this initial success making its way into mainstream technology used today, possibilities involving the manipulation of spin have resulted in a vast array of proposed novel devices like nonvolatile memories such as magnetic RAM and logic devices like the spin valve or even reprogrammable logic gates. Discovery of ferromagnetism in (GaMn)As and long electron spin coherence length in GaAs have given rise to the modern field of spintronics, which requires the control of spin coherence, transport, and interactions.<sup>3,7-9</sup> The aim of furthering information technology has long been to create nonvolatile devices that enhance data storage, processing speeds and energy efficiency, and

the use of the electron spin degree of freedom could significantly enhance progress toward these goals.

So far, the current technology includes only devices based on ‘traditional’ materials such as the Fe and Cr superlattices used in GMR hard drive read heads. Further advances in this field will require similar breakthroughs in spintronics materials candidates. For example, with the limited spin polarization of the conduction electrons ( $P_{\text{Fe}} < 45\%$ ) defined by  $P = \frac{n_{\uparrow} - n_{\downarrow}}{n_{\uparrow} + n_{\downarrow}}$ , where  $n_{\uparrow}$  is the density of spin up electron states, traditional materials produce relatively small magnetoresistance signals at room temperature ( $\sim 10\%$ ). Materials containing 100% spin polarizations, known as half metals, could act as a spin filter, making spin injection, extraction, manipulation and processing possible.<sup>10-12</sup> Numerous materials systems have shown promise in exhibiting these novel properties, but only a few, such as Heusler alloys, are systems suitable for integration into devices due to issues of poor ordering at interfaces and low Curie temperatures affecting viability of other materials.<sup>13-16</sup> The half metallic state, however, has not been realized in Heusler alloys due to outstanding issues of structural and chemical ordering at the atomic level, such as site-specific chemical defects brought on by deviations from stoichiometry and low defect formation energies. Unfortunately, there exists a lack of experimental techniques able to probe these defects, making progress on this front slow. In this work, the influences of epitaxial constraints and composition on these defects in Heusler alloys are studied in detail through development of complementary x-ray scattering techniques.

To realize information technologies that employ the electron spin degree of freedom, spin coherence and manipulation must be achievable in semiconducting materials. Only semiconductors have a band structure allowing for large signal amplification seen in current transistor technology, and many logic devices are based on these properties. With a ferromagnetic state in a semiconductor, conduction electrons can spontaneously polarize resulting in high spin injection

efficiencies into regular semiconductors.<sup>17</sup> Even more revolutionary, spin field effect transistors could lead to reprogrammable logic gates if directly made from these magnetic semiconductor materials.<sup>3</sup> These device concepts, however, cannot become a reality without these materials, which themselves have many unresolved issues. Since they rely on incorporation of magnetic elements well beyond solubility limits of the semiconducting host, phase separations and precipitates become prevalent, causing breakdowns in both their magnetic and semiconducting properties. Non-equilibrium growth techniques such as molecular beam epitaxy (MBE), therefore, have been used extensively in an attempt to resolve these issues, and recently, it was shown that the presence of multiple magnetic dopant species can help stabilize the semiconducting matrix.<sup>18,19</sup>

In this thesis, high quality single crystalline samples that contain two transition metal elements and a group IV element (Ge or Si) were synthesized using molecular beam epitaxy (MBE) techniques. The interplay of growth kinetics and energetics exploited in MBE allow for the synthesis of materials containing specifically tailored properties that are not exhibited in nature. Recent development of combinatorial synthesis approaches show that synthesis of a single sample containing a linearly changing growth parameter can greatly enhance a study's sensitivity, speed and reproducibility over a study based on synthesis of numerous individual samples.<sup>20</sup> In this work, parameters of epitaxial constraints and composition are varied systematically using the combinatorial method.

Synchrotron x-ray scattering is well suited to satisfy the need of an atomic level probe to study the structural ordering of these materials and position sensitivity to successfully probe combinatorial samples. Numerous diffraction and spectroscopic techniques have been developed with the high brightness of a synchrotron x-ray source, going well beyond the capabilities of table-top sources. In addition to x-ray crystallography and powder diffraction for probing structural

ordering and defects, surface diffraction can probe strain states, interfaces, and disorders in an epitaxial thin film. The unique flexibility of x-ray energy tuneability in synchrotron radiation adds local probe capabilities and chemical sensitivity, while the high brightness allows for high-precision composition measurements through spectroscopic techniques. Using focusing optics, micron sized x-ray beams are easily attainable, well within the requirements of studying a combinatorial sample. Therefore, development of combinatorial x-ray techniques designed to study and solve specific structural issues of these spintronics materials via growth in non-equilibrium environments of MBE are the focus of this thesis.

In the sections that follow, the background of each topic outlined above are discussed in detail. In Section 1.2 and 1.3, the history of study and specific issues pertaining to magnetic semiconducting and halfmetallic materials, respectively, are described. Characteristics of combinatorial molecular beam epitaxy are discussed in Section 1.4, while those of synchrotron x-ray probes are laid out in Section 1.5. The chapter is concluded in Section 1.6 with how the study of spintronics materials and development of these techniques were combined in this thesis to advance the physical understanding of structural and chemical ordering in materials and their effect on materials properties.

## **1.2 Magnetic Semiconductors**

In the late 1980s and early 1990s, Ohno and coworkers began reporting successes in realizing new properties in a class of materials known as doped magnetic semiconductors (DMS)<sup>7,17,21</sup>, which exhibited a ferromagnetic state while retaining semiconducting electrical properties. Using growth techniques based on molecular beam epitaxy (MBE), a III-V semiconductor host lattice of InAs or GaAs was doped with the magnetic ion Mn substituting cation sites, causing dramatic changes to the materials' transport, optical and magnetic properties. At 3-4 atomic

percent Mn doping, the ions are too far apart to interact with each other directly, yet in the case of GaAs, ferromagnetic ordering was initially achieved with a magnetic ordering (Curie) temperature ( $T_c$ ) of 75K.<sup>7</sup> This and the nature of the experiments showed that the magnetic ordering of the dopants is mediated by the carriers<sup>22</sup>. By 2000, Dietl *et. al.* had developed a successful model for these materials, which described the magnetic properties arising from the electron exchange interaction between itinerant carriers of the host and the localized spins from the Mn dopants<sup>23</sup>. This “Zener model” predicted that ferromagnetic ordering could occur in (Ga,Mn)As above room temperature with higher doping and carrier concentration, following the formula  $T_c = Cxp^{1/3}$ , where  $C$  is a proportionality constant,  $x$  is the magnetic doping concentration, and  $p$  is the carrier concentration. Later that year, the group led by Ohno showed that ferromagnetic ordering in (In,Mn)As could be controlled by changing the carrier concentration by an electric field using a gated field effect structure.<sup>24</sup> The ability to reversibly alter magnetic properties in a semiconductor opened enormous possibilities for new spintronics applications that included spin manipulation and transport.

Although III-V semiconductors have become the paradigm of a successful DMS system, there remain many challenges to actual use in spin-based devices which are perhaps insurmountable. To start, electric-field control of magnetism in (In,Mn)As has only been shown to occur at large fields (with 125V biases) and at low temperatures (22K).<sup>24</sup> In agreement with the Zener model, higher doping levels ( $x$ ) of Mn causes higher  $T_c$ , but Mn has a low solubility limit in semiconductors making it difficult to increase  $T_c$  above room temperature. In (Ga,Mn)As, some success has been shown with Mn’s higher solubility; however, at ~5 at.% doping, the Fermi level goes below the valence band edge and the material becomes metallic,<sup>22</sup> ruining the effect of electric field control of magnetism.

More recently, study of III-V materials has been revived after focusing on the atomic ordering of the Mn dopants. Mn ions substituting in the lattice do more than contributing a magnetic moment by also contributing an electron acceptor or hole, increasing the carrier concentration ( $p$ ), yet measurements of these materials showed that  $p \ll x$ .<sup>22</sup> Collaborations between experiment and theory revealed that the Mn acceptors were heavily compensated by interstitial Mn double donors.<sup>25-27</sup> Even worse, interstitial Mn was shown to diffuse rapidly in the host during growth until it found an energetically meta-stable position near a substitutional Mn dopant. There, it interacted antiferromagnetically reducing both  $x$  and  $p$ , and more importantly, ferromagnetic interactions.<sup>25</sup> Low temperature MBE followed by low temperature annealing and delta-doping are some of the non-equilibrium techniques demonstrated to be effective in increasing the population of substitutional Mn and drastically increasing both the carrier concentration and the Currie temperature to  $T_c=172\text{K}$ .<sup>28-31</sup> While ongoing work has not been successful in achieving  $T_c>300\text{K}$ , it is clear that understanding structure, magnetism and electronic states in these materials through atomic scale synthesis and characterization are of critical importance.

In the 2000s, research began turning to group IV-based DMS with incorporation of Mn into Ge and Si films.<sup>32,33</sup> Although III-V systems have advantageous optical properties for sensors or light-emitting diodes, group IV materials have long been the choice of the semiconductor industry, making their incorporation into current technology relatively easy. Park et. al. demonstrated electric field control of  $\text{Mn}_{0.035}\text{Ge}_{0.965}$  at higher temperatures than  $(\text{In,Mn})\text{As}$  and much more reasonable 0.5V applied bias.<sup>34</sup> They even showed a linearly increasing  $T_c$  with Mn concentration. Ge-based DMS were also shown to have a higher metal-insulator transition,<sup>35</sup> preserving the possibility of increasing  $T_c$  above room temperature while retaining the semiconducting properties.

Even with these initial successes,  $\text{Mn}_x\text{Ge}_{1-x}$  has subsequently proven difficult to study. Both transport and magnetization studies have uncovered significant deviations from theory, calling into question the applicability of the Zener model in these systems.<sup>34-38</sup> A new model involving magnetic polarons and transport percolation of the spins has been developed as a competing theory that better describes insulating materials.<sup>39,40</sup> However, structural studies of these materials have shown that Mn incorporates into the lattice inhomogeneously and even forms  $\text{Mn}_x\text{Ge}_y$  precipitates,<sup>41-46</sup> making it difficult to test these theories. Standard powder diffraction methods used exclusively in early studies cannot detect the nanometer sized precipitates because they have limited sensitivity, but due to their ferromagnetic nature, the presence of precipitates interferes with the study of ferromagnetic origins in the DMS and potentially its use in spintronics applications. Moreover, these disorders act as sinks for the dopants, reducing the amount of those active in the matrix<sup>46</sup> and lowering the possibility of true ferromagnetic ordering and spin transport in these materials. This is not surprising considering the doping concentrations used here that are far above dopant solubility levels as well as the large lattice strains such doping causes.

Low temperature growth and low temperature annealing have been shown to limit formation of the precipitates.<sup>33,34,46</sup> Recent studies of Ge have shown that the use of codopants can also relieve lattice strains if chosen based on their covalent bond lengths as well as promote dopant stability by altering growth kinetics.<sup>18,19,47</sup> Furthermore, studies in magnetic oxides suggest two dopants could alter dopant energetics to allow for homogeneous dispersal into the matrix.<sup>48</sup> Utilizing non-equilibrium growth conditions, MBE is well suited to study these effects in detail. Therefore, the kinetic and energetic effects of codoping is studied thoroughly in this thesis.

### 1.3 Halfmetallic Materials

The second class of materials studied in this work is a promising candidate for realizing a halfmetal, with fully spin polarized states at the Fermi level. In 1983, de Groot *et. al.* calculated the spin-resolved band structure of the Heusler alloy NiMnSb and found that while the majority spin density of states looked like a normal metal, the minority spin density of states was insulating.<sup>49</sup> These ferromagnetic materials are very different than that of normal ferromagnets like Fe or Ni, who simply have an imbalance of states at the Fermi level in their two metallic spin bands as shown in Figure 1-1.

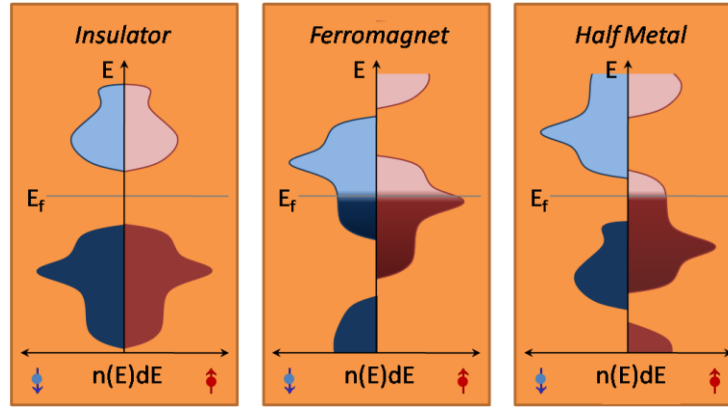


**Figure 1-1: Spin-resolved density of electron states in various material phases. Light colored states are empty and dark ones are filled.**

Although theorists predicted the existence of the half metallic state in numerous Heusler alloys,<sup>50</sup> this phenomenon has not been demonstrated experimentally in these systems. In the mean time, two other compounds showed evidence of being half metals:  $\text{CrO}_2$  and double perovskites such as  $\text{La}_{0.3}\text{Sr}_{0.7}\text{MnO}_3$  (LSMO). Using various techniques such as spin-resolved photoemission<sup>13,51</sup> and point contact Andreev reflection (PCARS),<sup>52,53</sup> these materials exhibited many of the novel halfmetallic characteristics at low temperatures. Particularly,  $\text{CrO}_2$  has indeed been confirmed to have a pure spin population at the Fermi level at liquid helium temperatures,<sup>54,55</sup> however, all subsequent attempts to make spin-based devices like MTJs failed, showing little to no magnetoresistance.<sup>14,15</sup> It is thought that the unstable surface of the material completely scatters



the spin polarization, making it difficult for device applications<sup>15,56</sup>. Conversely, a small minority spin band exists in LSMO at the Fermi level, destroying its half metallic state, but nevertheless the low carrier mobility of its minority states causes it to be a “transport” halfmetal<sup>16,57</sup>. Indeed, MTJs constructed using this material have shown magnetoresistances of an astounding 1800% at liquid helium temperatures, but the effect is lost at room temperature<sup>58</sup>. Unfortunately, both of these materials may never make useful devices. Theories base on independent spin bands are accurate only at  $T \approx \frac{1}{3}T_c$  when magnetic interactions to align spins are significantly stronger than thermal fluctuations<sup>10</sup>. Both of these materials systems have  $T_c$ 's only nominally above room temperature (386K for CrO<sub>2</sub> and 350K for LSMO) and therefore have their novel properties severely degraded in these conditions.

By contrast, the Heusler alloys have  $T_c$ 's well above room temperature<sup>59</sup> and, therefore, have much more potential for uses in spin-based devices. They are also more stable than other materials such as CrO<sub>2</sub>, which slowly breaks down in both air and UHV conditions.<sup>15</sup> This allows for the easy growth of epitaxial heterostructures, which are typically required for devices. Moreover, the large variety of Heusler alloys afford real possibilities of finding an ideal material that can easily be probed for the new physical properties they promise as well as be utilized in new technologies in a straightforward manner. Heusler alloys have been shown to form robust L2<sub>1</sub> structures, following an intermetallic chemical formula of A<sub>2</sub>BC where A and B are magnetic elements and C is a group III or IV element.<sup>59</sup> Particularly Co<sub>2</sub>MnGe and Co<sub>2</sub>MnSi have enjoyed the most interest<sup>60,61</sup> due to their extremely high Curie temperatures of 905K and 985K respectively.<sup>59</sup> Their relatively large gap of ~0.5eV and 0.8eV, respectively also suggests a more robust half-metallic state.<sup>62</sup> In fact, recent work has shown that these materials are excellent for use in MTJs. In late 2008, Tsunegi *et. al.* demonstrated tunneling through a fully epitaxial MgO barrier, which produced 217% MR at room

temperature using  $\text{Co}_2\text{MnSi}$  as an electrode.<sup>63</sup> Furthermore, a group from Hitachi has recently published the first successful incorporation of these alloys in hard drive read heads.<sup>64</sup>

In terms of their half-metallic nature, Heusler alloys still have yet to show direct evidence of 100% spin-polarized transport. In fact, the most direct measurement of spin-polarization, PCARS, has only reported a spin polarization of ~58%.<sup>65</sup> Numerous x-ray and neutron based studies have revealed the presence of structural and chemical disorders in these materials.<sup>66-68</sup> Theoretical calculations have suggested that a small amount of specific disorders in these materials can create minority states to appear at the Fermi level, specifically elemental site swapping or antisites that disrupt local bonding arrangements.<sup>69</sup> However, samples studied for their structure have been grown via methods with little to no control over the thermodynamics of the process, such as magnetron sputtering or the Czochralski technique (used in growing Si single crystals from the melt). Creating a stoichiometrically accurate sample has also proven difficult with standard deposition techniques. Therefore, composition is thought to potentially be a large influence on these disorders. These difficulties open the question of whether combinatorial MBE with its nonequilibrium growth capabilities and linear composition profiles can be used to systematically study stoichiometric effects and alter the kinetics and energetics of growth to control these defects in Heusler alloys and fulfill the original prediction of half-metallicity.

#### **1.4 MBE Synthesis**

Ever since its initial development in the 1970s,<sup>70</sup> molecular beam epitaxy (MBE) has been at the forefront of the quest to control materials properties, understand the physics of nonequilibrium materials synthesis and create nanoscale heterostructures with ordering on the atomic level. Using highly controlled and purified atomic or molecular sources in clean, ultra-high vacuum environments, MBE has demonstrated its ability to control synthesis of a wide range of materials

from amorphous to single crystalline. Surface energetics and kinetics as well as forces such as epitaxial strain are controlled through deposition conditions, chemical environments and substrates of various crystallographic structure, size and orientation. These nonequilibrium conditions make tailoring a material's chemical, structural, electrical, and magnetic properties possible, opening up the potential for new technologies and allowing for the development of a more accurate physical description of solid state physics.

There has been a great deal of MBE research undertaken to explore quantum interactions and materials properties arising from new structural and chemical environments unseen in nature, including the spintronics materials of interest in this thesis. Materials systems of this nature are at a state where physics theory and experiment have yet to fully merge, but these novel states of matter can be fragile, relying on the nonequilibrium growth capabilities possessed by MBE. On this front, there are definite uncertainties as to the full capabilities of epitaxial techniques. Creating local environments to counter thermodynamic behavior during crystal growth can only do so much, and because these effects occur on the atomic scale, it becomes necessary to use probes that are sensitive to both local atomic structure and have statistical capabilities to sense global fluctuations in structure on a macroscopic level. To ascertain the physical origin of novel materials properties such as the examples above, thorough structural investigations of these materials are required.

Recently, combinatorial techniques have been developed for this materials synthesis method.<sup>20</sup> Since MBE involves careful control of numerous growth parameters it is also a complex and time-consuming process. To carry out a systematic study on effects of a particular growth parameter requires numerous samples to be grown and characterized if standard practices involving individual samples are utilized, making such a study tedious. Furthermore, non-linear effects of varying growth conditions in MBE can cause small, potentially undesired variations in these

conditions to drastically alter the resulting material's properties, reducing repeatability of an experimental result. In combinatorial MBE, continuous variation of a particular growth parameter such as thickness, composition, or strain can be established across one sample and can dramatically enhance the speed to probe a larger parameter space and the ability to resolve abrupt transitions. The varied growth parameter can also be well isolated as other growth conditions are guaranteed to be identical at each point on the sample. Therefore, combinatorial techniques developed for this synthesis method were utilized to explore spintronic materials candidates and potentially control their properties via non-equilibrium growth to address issues related to their structural and chemical ordering.

### **1.5 Synchrotron X-Ray Techniques**

While epitaxial techniques are capable of producing materials and heterostructures with atomic precision, studying these materials on the atomic scale is still challenging. Many studies past and present have used the powerful methods of reflection high electron diffraction (RHEED) or scanning probe microscopy (SPM). These are excellent methods to probe the surface directly, whereas by and large much of the bulk-like information beneath the surface can only be inferred from the measurements. X-rays, with their relatively weaker interactions and deeper penetration, offer a variety of powerful tools to probe the bulk, surface, and interfacial properties of films.

Cross-sectional transmission electron microscopy (TEM) is another commonly used method, but the difficulty of sample preparation and its destructive nature often make it undesirable and are intrinsically incompatible with large numbers of samples. Like RHEED or any electron-based probes, TEM has the added complication of large dynamic effects such as multiple or inelastic scattering, making results more difficult to interpret. In contrast, x-ray scattering techniques are non-destructive and require relatively little sample preparation. Dynamic effects are negligible,

especially for thin samples, thus allowing the use of simple kinematical models for quantitative analysis.

Standard x-ray diffraction techniques have been around for decades and are excellent at probing the basic crystal structure of an epitaxial material. This technique probes reciprocal space, which through a Fourier transform, involves a vast average of the structure over the entire illuminated portion of the sample. Thus, one point in reciprocal space needs to be monitored to be sensitive to global changes of structure in the crystal, a characteristic extremely amenable to development of combinatorial probe techniques. With higher intensity of the beam, synchrotron radiation has made studies of crystal surfaces and interfaces possible. The analysis of crystal truncation rods (CTR) in reciprocal space allows for probing the quality of epitaxially grown materials and heterostructures and is used in this work along with the technique's ability to measure lattice strain down to 0.003%.<sup>71</sup> Spectroscopic techniques such as x-ray fluorescence spectroscopy (XRF), in particular when used together with a microbeam, also rely on the high brilliance in probing a sample's composition with high precision, making studies of composition-dependent material properties achievable. Furthermore, the energy-tuning ability of synchrotron radiation makes possible the study of extended x-ray absorption fine structure (EXAFS). This technique utilizes photo-electrons from absorbing atoms in a material to interact with neighbors and provide information on the local atomic structure and has been used to explore dopant states and structures in DMS materials in this thesis. Using combined information of diffraction and absorption, anomalous diffraction has high sensitivity to site-specific chemical ordering in a crystal. Typically, there is very low contrast in x-ray scattering between various elements due to its dependence on the slowly varying atomic number  $Z$ . Near a resonance, however, scattering becomes dominated by element-specific absorption effects. Therefore, methods based on this technique are developed

and shown to successfully quantify specific elemental disorders in Heusler alloys studied in this work.

### **1.6 Investigation of Atomic Scale Structural and Chemical Ordering**

This thesis work investigates compositional and epitaxial effects on the structural and chemical ordering in novel group IV-based magnetic materials grown by combinatorial molecular beam epitaxy. To accomplish this, a number of synchrotron x-ray techniques are utilized and expanded to encompass the combinatorial method. Numerous procedures are developed and techniques altered in this thesis to successfully probe these complex samples in a systematic fashion. With DMS materials, a systematic study of codoping effects of two magnetic elements – Co and Mn or Co and Fe – in Ge has been completed to examine dopant states and interaction at the atomic level. Altered kinetics of epitaxial growth is demonstrated with the incorporation of a codopant to impede diffusion channels. It is further shown that the energetics of their growth has been changed in the new chemical environment, suppressing the formation of metallic precipitates and stabilizing dopant dilution into the matrix at much higher doping levels. Complementary x-ray techniques of both bulk and local atomic probes have been used to explore the effect of codoping on dopant states in an effort to understand and control their formation.

Effects of non-equilibrium growth and stoichiometry have also been studied on the epitaxial ordering of  $\text{Co}_x\text{Mn}_y\text{Ge}_z$  and  $\text{Co}_x\text{Mn}_y\text{Si}_z$  systems, resulting in ternary epitaxial phase libraries of these materials systems. Focusing on epitaxial films at and around the Heusler composition, it is shown that nonequilibrium conditions of MBE can stabilize the growth of the Heusler structure in a large region of compositional phase space even in the presence of epitaxial strains. The general ordering of these materials has also been found to depend highly on strain states, composition, and growth temperature. Additionally, the objective of measuring elemental and site-specific defects in an

epitaxial film is achieved by fully exploring the synchrotron-based technique of anomalous diffraction for its ability to avoid elemental z-contrast limitations of traditional x-ray techniques. The development of a full-spectrum analysis method of anomalous diffraction is shown to quantitatively probe a large array of atomic disorders such as antisites, elemental site swapping and vacancies occurring in an epitaxial thin film. This technique reveals that the main atomic disorder in epitaxial  $\text{Co}_2\text{MnGe}$  is Mn-Ge swapping, with little to no Mn-Co swapping present as has recently been suspected. This thesis work thus develops a new synergy between the advancement of MBE capabilities and synchrotron x-ray based techniques to study new materials and atomic phenomena within them.

The thesis is organized as follows. Combinatorial synthesis techniques, *in situ* characterization methods, and sample preparation are discussed in Chapter 2. Chapter 3 covers primary synchrotron x-ray techniques and analysis methods used in this thesis, including the development of anomalous diffraction theory and combinatorial x-ray methods. The study of codoping in Ge-based DMS materials and the study of Si and Ge Heusler are respectively presented in Chapters 4 and 5. The thesis is summarized in Chapter 6.

## Bibliography

1. Prinz, G.A. Magnetoelectronics. *Science* **282**, 1660-1663 (1998).
2. Prinz, G.A. Spin-Polarized Transport. *Physics Today* **48**, 58-63 (1995).
3. Wolf, S.A. et al. Spintronics: A Spin-Based Electronics Vision for the Future. *Science* **294**, 1488-1495 (2001).
4. Bandyopadhyay, S. Single-spin measurement in the solid state: A reader for a spin qubit. *Phys. Rev. B* **67**, 193304 (2003).
5. Baibich, M.N. et al. Giant Magnetoresistance of (001)Fe/(001)Cr Magnetic Superlattices. *Phys. Rev. Lett.* **61**, 2472 (1988).
6. Binasch, G., Grunberg, P., Saurenbach, F. & Zinn, W. Enhanced magnetoresistance in layered magnetic structures with antiferromagnetic interlayer exchange. *Phys. Rev. B* **39**, 4828 (1989).
7. Ohno, H. et al. (Ga,Mn)As: A new diluted magnetic semiconductor based on GaAs. *Appl. Phys. Lett.* **69**, 363-365 (1996).
8. Kikkawa, J.M. & Awschalom, D.D. Resonant Spin Amplification in n-Type GaAs. *Phys. Rev. Lett.* **80**, 4313 (1998).
9. Awschalom, D.D. & Kikkawa, J.M. Electron Spin and Optical Coherence in Semiconductors. *Physics Today* **52**, 33 (1999).
10. Pickett, W.E. & Moodera, J.S. Half Metallic Magnets. *Physics Today* **54**, 39-44 (2001).
11. Hammar, P.R., Bennett, B.R., Yang, M.J. & Johnson, M. Observation of Spin Injection at a Ferromagnet-Semiconductor Interface. *Phys. Rev. Lett.* **83**, 203 (1999).
12. Monzon, F.G. & Roukes, M.L. Spin injection and the local Hall effect in InAs quantum wells. *Journal of Magnetism and Magnetic Materials* **198-199**, 632-635 (1999).
13. Park, J. et al. Direct evidence for a half-metallic ferromagnet. *Nature* **392**, 794-796 (1998).
14. Gupta, A., Li, X.W. & Xiao, G. Inverse magnetoresistance in chromium-dioxide-based magnetic tunnel junctions. *Appl. Phys. Lett.* **78**, 1894-1896 (2001).
15. Anguelouch, A. et al. Properties of epitaxial chromium dioxide films grown by chemical vapor deposition using a liquid precursor. *J. Appl. Phys.* **91**, 7140-7142 (2002).
16. Nadgorny, B. The case against half-metallicity in La<sub>0.7</sub>Sr<sub>0.3</sub>MnO<sub>3</sub>. *Journal of Physics: Condensed Matter* **19**, 315209 (2007).
17. Munekata, H. et al. Diluted magnetic III-V semiconductors. *Phys. Rev. Lett.* **63**, 1849 (1989).
18. Tsui, F., He, L., Tkachuk, A., Vogt, S. & Chu, Y.S. Evidence for strain compensation in stabilizing epitaxial growth of highly doped germanium. *Phys. Rev. B* **69**, 081304 (2004).
19. Tsui, F. et al. Novel Germanium-Based Magnetic Semiconductors. *Phys. Rev. Lett.* **91**, 177203 (2003).



20. Tsui, F. & He, L. Techniques for combinatorial molecular beam epitaxy. *Rev. Sci. Instrum.* **76**, 062206-5 (2005).
21. Ohno, H. Making Nonmagnetic Semiconductors Ferromagnetic. *Science* **281**, 951-956 (1998).
22. Matsukura, F., Ohno, H., Shen, A. & Sugawara, Y. Transport properties and origin of ferromagnetism in (Ga,Mn)As. *Phys. Rev. B* **57**, R2037 (1998).
23. Dietl, T., Ohno, H., Matsukura, F., Cibert, J. & Ferrand, D. Zener Model Description of Ferromagnetism in Zinc-Blende Magnetic Semiconductors. *Science* **287**, 1019-1022 (2000).
24. Ohno, H. et al. Electric-field control of ferromagnetism. *Nature* **408**, 944-946 (2000).
25. Blinowski, J. & Kacman, P. Spin interactions of interstitial Mn ions in ferromagnetic GaMnAs. *Phys. Rev. B* **67**, 121204 (2003).
26. Yu, K.M. et al. Effect of the location of Mn sites in ferromagnetic Ga<sub>1-x</sub>Mn<sub>x</sub>As on its Curie temperature. *Phys. Rev. B* **65**, 201303 (2002).
27. Edmonds, K.W. et al. Mn Interstitial Diffusion in (Ga,Mn)As. *Phys. Rev. Lett.* **92**, 037201 (2004).
28. Ishiwata, Y. et al. Manganese concentration and low-temperature annealing dependence of Ga<sub>1-x</sub>Mn<sub>x</sub>As by x-ray absorption spectroscopy. *Phys. Rev. B* **65**, 233201 (2002).
29. Ku, K.C. et al. Highly enhanced Curie temperature in low-temperature annealed [Ga,Mn]As epilayers. *Appl. Phys. Lett.* **82**, 2302-2304 (2003).
30. Chiba, D., Takamura, K., Matsukura, F. & Ohno, H. Effect of low-temperature annealing on (Ga,Mn)As trilayer structures. *Appl. Phys. Lett.* **82**, 3020-3022 (2003).
31. Nazmul, A.M., Sugahara, S. & Tanaka, M. Ferromagnetism and high Curie temperature in semiconductor heterostructures with Mn delta -doped GaAs and p-type selective doping. *Phys. Rev. B* **67**, 241308 (2003).
32. Stroppa, A., Picozzi, S., Continenza, A. & Freeman, A.J. Electronic structure and ferromagnetism of Mn-doped group-IV semiconductors. *Phys. Rev. B* **68**, 155203 (2003).
33. Park, Y.D. et al. Magnetoresistance of Mn:Ge ferromagnetic nanoclusters in a diluted magnetic semiconductor matrix. *Appl. Phys. Lett.* **78**, 2739-2741 (2001).
34. Park, Y.D. et al. A Group-IV Ferromagnetic Semiconductor: Mn<sub>x</sub>Ge<sub>1-x</sub>. *Science* **295**, 651-654 (2002).
35. Li, A.P. et al. Magnetism in Mn<sub>x</sub> Ge<sub>1-x</sub> semiconductors mediated by impurity band carriers. *Phys. Rev. B* **72**, 195205 (2005).
36. Cho, S. et al. Ferromagnetism in Mn-doped Ge. *Phys. Rev. B* **66**, 033303 (2002).
37. Li, A.P., Shen, J., Thompson, J.R. & Weitering, H.H. Ferromagnetic percolation in Mn<sub>x</sub>Ge<sub>1-x</sub> dilute magnetic semiconductor. *Appl. Phys. Lett.* **86**, 152507-3 (2005).

38. Pinto, N. et al. Magnetic and electronic transport percolation in epitaxial Ge<sub>1-x</sub>Mn<sub>x</sub> films. *Phys. Rev. B* **72**, 165203 (2005).
39. Kaminski, A. & Das Sarma, S. Polaron Percolation in Diluted Magnetic Semiconductors. *Phys. Rev. Lett.* **88**, 247202 (2002).
40. Kaminski, A. & Das Sarma, S. Magnetic and transport percolation in diluted magnetic semiconductors. *Phys. Rev. B* **68**, 235210 (2003).
41. Kang, J. et al. Spatial Chemical Inhomogeneity and Local Electronic Structure of Mn-Doped Ge Ferromagnetic Semiconductors. *Phys. Rev. Lett.* **94**, 147202 (2005).
42. Ottaviano, L. et al. Phase separation and dilution in implanted Mn<sub>x</sub>Ge<sub>1-x</sub> alloys. *Appl. Phys. Lett.* **88**, 061907-3 (2006).
43. Bihler, C. et al. Structural and magnetic properties of Mn<sub>5</sub>Ge<sub>3</sub> clusters in a dilute magnetic germanium matrix. *Appl. Phys. Lett.* **88**, 112506-3 (2006).
44. Jamet, M. et al. High-Curie-temperature ferromagnetism in self-organized Ge<sub>1-x</sub>Mn<sub>x</sub> nanocolumns. *Nat Mater* **5**, 653-659 (2006).
45. Bougeard, D., Ahlers, S., Trampert, A., Sircar, N. & Abstreiter, G. Clustering in a Precipitate-Free GeMn Magnetic Semiconductor. *Phys. Rev. Lett.* **97**, 237202-4 (2006).
46. Li, A.P. et al. Dopant segregation and giant magnetoresistance in manganese-doped germanium. *Phys. Rev. B* **75**, 201201-4 (2007).
47. Matsumoto, Y. et al. Combinatorial investigation of spintronic materials. *MRS BULLETIN* **28**, 734-739 (2003).
48. Kuroda, S. et al. Origin and control of high-temperature ferromagnetism in semiconductors. *Nat Mater* **6**, 440-446 (2007).
49. de Groot, R.A., Mueller, F.M., Engen, P.G.V. & Buschow, K.H.J. New Class of Materials: Half-Metallic Ferromagnets. *Phys. Rev. Lett.* **50**, 2024 (1983).
50. Fujii, S., Sugimura, S., Ishida & Asano, S. Hyperfine fields and electronic structures of the Heusler alloys Co<sub>2</sub>MnX (X=Al, Ga, Si, Ge, Sn). *Journal of Physics: Condensed Matter* **2**, 8583-8589 (1990).
51. Kämper, K.P., Schmitt, W., Güntherodt, G., Gambino, R.J. & Ruf, R. CrO<sub>2</sub>—A New Half-Metallic Ferromagnet? *Phys. Rev. Lett.* **59**, 2788 (1987).
52. Soulen, R.J. et al. Measuring the Spin Polarization of a Metal with a Superconducting Point Contact. *Science* **282**, 85-88 (1998).
53. Strijkers, G.J., Ji, Y., Yang, F.Y., Chien, C.L. & Byers, J.M. Andreev reflections at metal/superconductor point contacts: Measurement and analysis. *Phys. Rev. B* **63**, 104510 (2001).
54. Ji, Y. et al. Determination of the Spin Polarization of Half-Metallic CrO<sub>2</sub> by Point Contact Andreev Reflection. *Phys. Rev. Lett.* **86**, 5585 (2001).

55. Anguelouch, A. et al. Near-complete spin polarization in atomically-smooth chromium-dioxide epitaxial films prepared using a CVD liquid precursor. *Phys. Rev. B* **64**, 180408 (2001).
56. Jr, C.A.V. et al. Are the surfaces of CrO<sub>2</sub> metallic? *Journal of Physics: Condensed Matter* **19**, 315207 (2007).
57. Nadgorny, B. et al. Origin of high transport spin polarization in La<sub>0.7</sub>Sr<sub>0.3</sub>MnO<sub>3</sub>: Direct evidence for minority spin states. *Phys. Rev. B* **63**, 184433 (2001).
58. Bowen, M. et al. Nearly total spin polarization in La<sub>2/3</sub>Sr<sub>1/3</sub>MnO<sub>3</sub> from tunneling experiments. *Appl. Phys. Lett.* **82**, 233-235 (2003).
59. Webster, P. Magnetic and chemical order in Heusler alloys containing cobalt and manganese. *Journal of Physics and Chemistry of Solids* **32**, 1221-1231 (1971).
60. Ishida, S., Masaki, T., Fujii, S. & Asano, S. Theoretical search for half-metallic films of Co<sub>2</sub>MnZ (Z = Si, Ge). *Physical Review B: Condensed Matter* **245**, 1-8 (1998).
61. Ishida, S., Fujii, S., Nagayoshi, H. & Asano, S. Novel half-metallic films of Co<sub>2</sub>MnZ (Z=Si, Ge) coated with Mn layers. *Physica B: Condensed Matter* **254**, 157-165 (1998).
62. Picozzi, S., Continenza, A. & Freeman, A.J. Co<sub>2</sub>MnX (X=Si, Ge, Sn) Heusler compounds: An ab initio study of their structural, electronic, and magnetic properties at zero and elevated pressure. *Phys. Rev. B* **66**, 094421 (2002).
63. Tsunegi, S., Sakuraba, Y., Oogane, M., Takanashi, K. & Ando, Y. Large tunnel magnetoresistance in magnetic tunnel junctions using a Co<sub>2</sub>MnSi Heusler alloy electrode and a MgO barrier. *Appl. Phys. Lett.* **93**, 112506-3 (2008).
64. Childress, J. et al. All-Metal Current-Perpendicular-to-Plane Giant Magnetoresistance Sensors for Narrow-Track Magnetic Recording. *Magnetics, IEEE Transactions on* **44**, 90-94 (2008).
65. Rajanikanth, A., Takahashi, Y.K. & Hono, K. Spin polarization of Co<sub>2</sub>MnGe and Co<sub>2</sub>MnSi thin films with A2 and L2<sub>1</sub> structures. *J. Appl. Phys.* **101**, 023901-5 (2007).
66. Brown, P.J., Neumann, K.U., Webster, P.J. & Ziebeck, K.R.A. The magnetization distributions in some Heusler alloys proposed as half-metallic ferromagnets. *Journal of Physics: Condensed Matter* **12**, 1827-1835 (2000).
67. Ravel, B., Raphael, M.P., Harris, V.G. & Huang, Q. EXAFS and neutron diffraction study of the Heusler alloy Co<sub>2</sub>MnSi. *Phys. Rev. B* **65**, 184431 (2002).
68. Raphael, M.P. et al. Presence of antisite disorder and its characterization in the predicted half-metal Co<sub>2</sub>MnSi. *Phys. Rev. B* **66**, 104429 (2002).
69. Picozzi, S., Continenza, A. & Freeman, A.J. Role of structural defects on the half-metallic character of Co<sub>2</sub>MnGe and Co<sub>2</sub>MnSi Heusler alloys. *Phys. Rev. B* **69**, 094423 (2004).
70. Cho, A.Y. Recent developments in molecular beam epitaxy (MBE). *J. Vac. Sci. Technol.* **16**, 275-284 (1979).

71. Zhong, Y., Chu, Y.S., Collins, B.A. & Tsui, F. High-resolution X-ray diffraction studies of combinatorial epitaxial Ge (0 0 1) thin-films on Ge (0 0 1) substrates. *Applied Surface Science* **254**, 714-719 (2007).

# Chapter 2 Samples

---

In this work, the samples were grown using advanced combinatorial molecular beam epitaxy (MBE) techniques. Due to its atomic scale deposition and its highly developed nonequilibrium environments, this method is ideal for synthesis of the materials studied where crystallographic ordering is critical for the physical properties of interest. Through the use of combinatorial methods, a composition gradient is produced on a single sample, allowing for the study of compositional effects on these physical properties while holding all other crystal growth conditions constant. Furthermore, MBE is well suited to allow for monitoring of material quality and crystal ordering via electron diffraction techniques, providing *in situ* structural analysis for most samples. In the following sections, a detailed description of the materials synthesis and initial characterization process is described as well as sample processing techniques required to conduct the numerous complementary *ex situ* experiments for a detailed exploration of the materials' properties.

## 1.1 Materials Synthesis

The samples studied in this work were grown using advanced combinatorial MBE techniques in the Tsui laboratory by Dr. Liang He, who also performed *in situ* measurements including real time electron diffraction discussed later. Sample synthesis involved a meticulous set of processing parameters to ensure the highest quality of materials synthesis and repeatable results. Ge and GaAs (001) and (111) oriented substrates used were 400-800 microns thick with  $< 1^\circ$  miscut. Each wafer was cleaved along the [110] direction into  $\sim 10 \times 10$  mm pieces, using a scribe and subsequently sonicated for 10-15 minutes in each trichloroethylene (TCE), acetone, and 100% ethyl alcohol

solvents to remove any particulate or organic matter on the surface. Under a hepafilter clean hood, the substrates were immediately attached to a molybdenum sample holder with leaf spring clamps and placed in the UHV MBE chamber. The substrate was then annealed at 700°C for 30 minutes to further clean the surface and remove surface oxides before deposition. To provide an atomically smooth surface for crystal growth, a Ge buffer layer was grown, burying any surface defects or remaining impurities. These layers were grown in cycles where approximately 30Å were deposited at 300°C and then annealed at 700°C for 15 minutes. Typical substrates required three of these cycles until electron diffraction confirmed an atomically flat surface and a layer-by-layer growth mode.

Figure 2-1 shows the components of the MBE growth chamber used to create the epitaxial thin film. Elemental sources are situated on the chamber bottom with the sample and monitoring devices on the top. Low melting point materials are heated via effusion cells, which utilize tungsten filaments to radiatively heat boron nitride crucibles containing the material to be evaporated. High current electron beam hearths (5-8keV) are used to directly strike high melting point materials inside water-cooled Cu crucibles. For each of these methods, the power applied controls the atomic flux. Each of the four effusion cells or four electron beam hearths has a computer-controlled pneumatic shutter to block the port of a liquid N<sub>2</sub> shroud. Facing down, the substrate is fixed to a 6-axis manipulator and temperature controller. The manipulator and stepper motor masks are used to create the composition gradient across the sample for combinatorial samples. Structural evolution of the films is characterized by real-time scanning reflection high-energy electron diffraction (RHEED) imaging system, which includes a 30keV electron gun reflecting off the sample surface into a phosphor screen and recorded via a CCD camera. A residual gas analyzer, Quartz crystal monitors, and atomic absorption spectroscopy (AAS) are used to monitor and control deposition of each element.<sup>1-4</sup> Lab-View-based software developed for this system is used to

automate deposition control, while simultaneously controlling sample and mask manipulation and RHEED imaging.

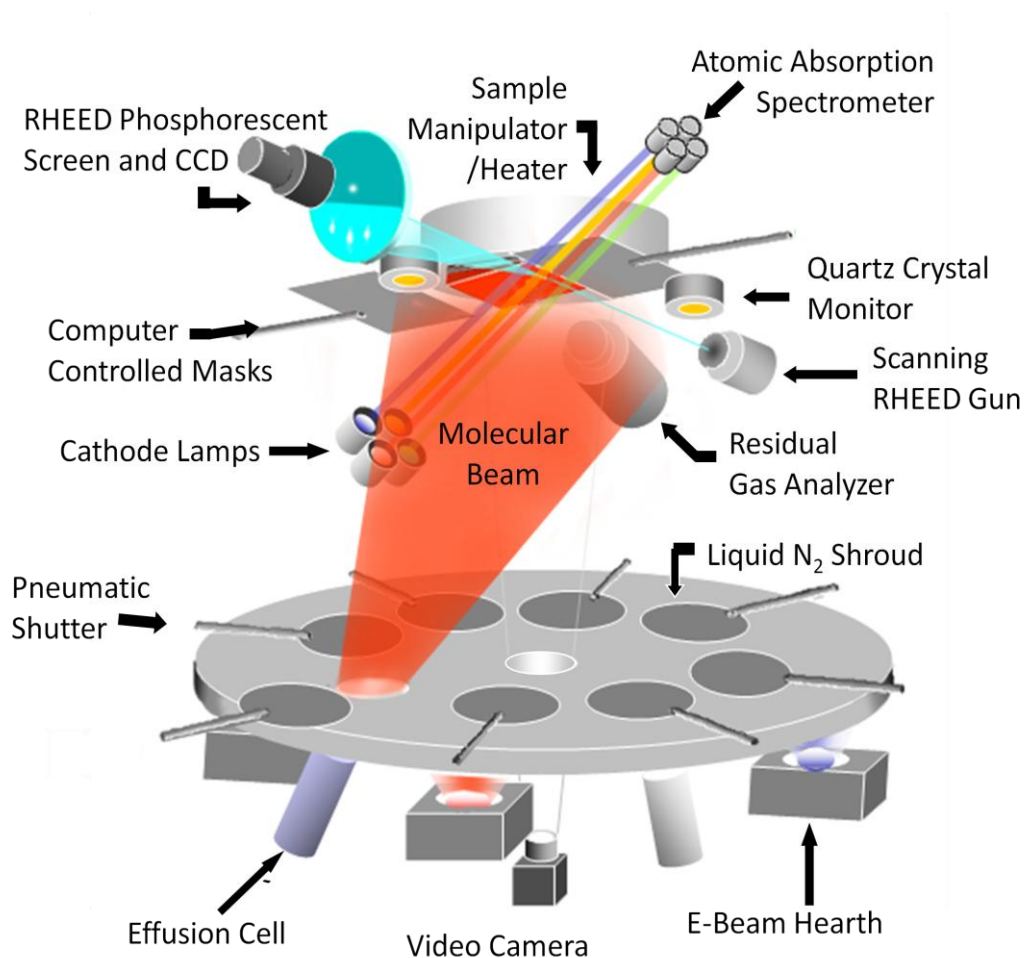


**Figure 2-1: Schematic diagram of the combinatorial molecular beam epitaxy growth system. (Excerpt from Ref. 13)**

With all of the careful preparation, controlled deposition conditions and in situ characterization, the production of each sample requires a long, painstaking process. Therefore, it can be extremely difficult and time-consuming to produce identical growth conditions for numerous samples. Still, most material studies involving compositional evolution are completed through studying a series of individual samples. In this case, four or five samples are typically the maximum utilized in a given study, and because phase discontinuities are expected, studying the atomic

mechanisms involved in the evolution of important materials properties becomes challenging. Since this work is based on the study of compositional effects on atomic level ordering, the recently developed combinatorial approach<sup>5,6</sup> is critical for its success. This approach involves deposition under a constant atomic flux while computer controlled shadow masks move across the substrate to deposit submonolayer wedges of material in a multilayer fashion. This results in linear composition profiles across the sample. Through this method, identical growth conditions are guaranteed for each composition studied, and structural phase transitions can be probed under small compositional variations. All that is then required is a position sensitive probe to investigate the resulting sample, something for which a synchrotron x-ray microprobe is well suited.

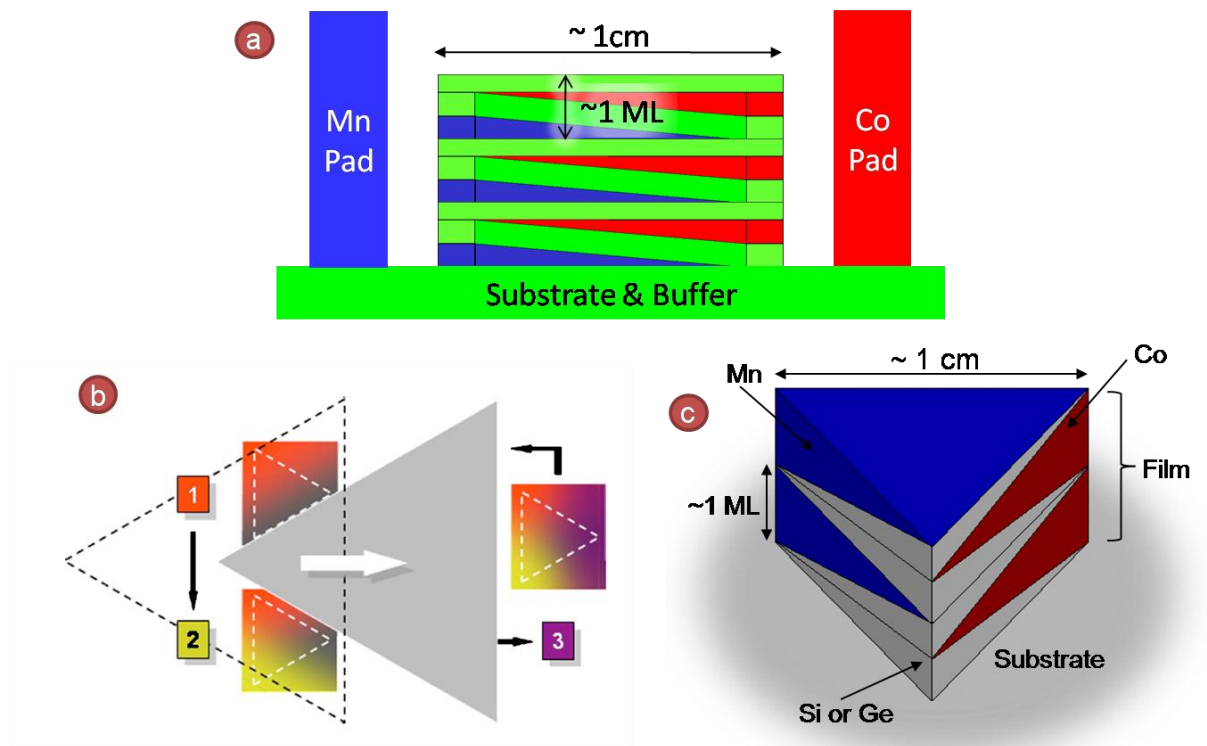


**Figure 2-2: Schematic for depositing combinatorial samples. (a) Binary sample with a composition gradient. Pads are deposited to correlate complementary measurements. (b) Triangular mask movements for creating a ternary combinatorial sample (excerpt from Reference 5). Actual movement is along the axis of the white arrow, each edge creating a composition gradient along appropriate directions. (c) Schematic of a ternary sample showing the multilayer deposition profile.**

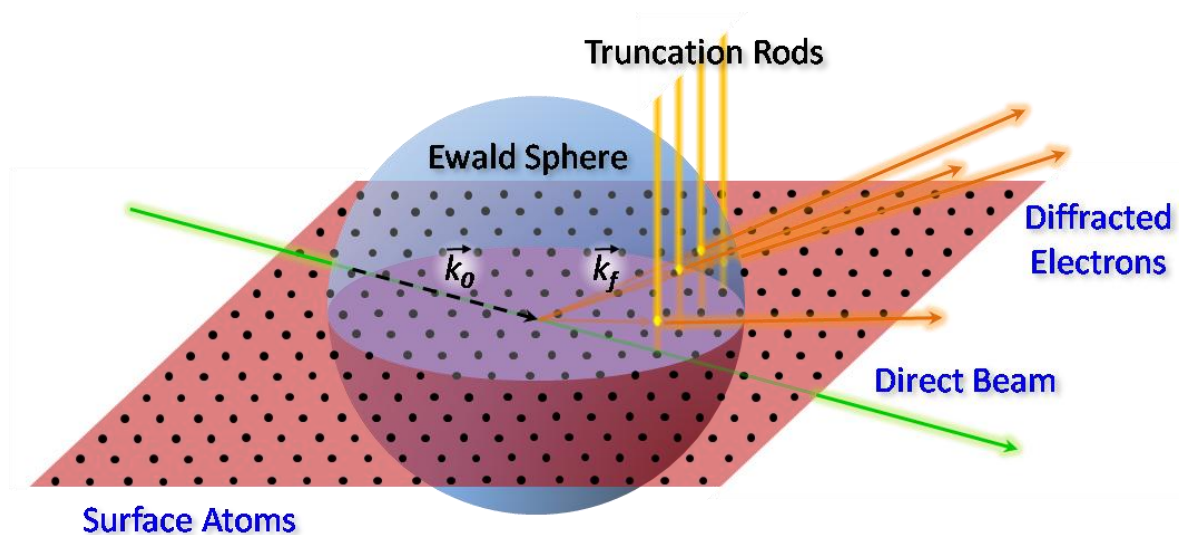


Figure 2-2 shows examples of combinatorial samples synthesized for this work. Once the buffer has been deposited, the mask creates a linear composition profile approximately 1 cm across the length of the substrate. The mask is typically 3 mm from and parallel to the surface, minimizing shadow edge broadening. Figure 2-2(a) is a typical deposition profile of a binary sample resulting in a constant concentration of metal dopants relative to the semiconductor material with the relative concentration of the dopant species linearly varied from Mn to Co. This monolayer wedge approach is similar in nature to digital alloying<sup>7,8</sup> or delta doping<sup>9,10</sup> techniques and are deposited in individual stages for each element. In the example provided, the metallic dopant species are kept separated by the semiconductor host via a four-stage ABAC multilayer scheme. It is important to note, however, that due to thermal diffusion and the submonolayer thickness of the layers, complete elemental mixing occurs in the growth direction. In-plane, the composition gradient is too small at approximately 1 at.%/100 $\mu$ m to be affected by diffusion. After film deposition, thick pads of a high contrast species are deposited at each end of the sample profile to ensure precise correlation of position for the large number of complementary studies to be performed. A 10-20Å cap layer of the most stable species (typically Ge) is deposited at the surface to protect the sample from environmental effects of the atmosphere.

Figure 2-2 (b) and (c) depict the deposition method and resulting profile of a ternary sample, which was used in this work for the study of the full compositional phase diagram of ternary alloys. Here, three composition profiles each 60° apart are deposited by the edges of a triangular sample mask. Figure 2-2 (b) shows this three-step process by which the mask travels along one axis during deposition of all three profiles. High-precision video equipment (shown at the bottom of Figure 2-1) and software are used to program the automated sample manipulator and mask movements, reducing the potential for operator error in this 30+ hour process.

## 1.2 Reflection High Energy Electron Diffraction

RHEED was used to probe structural qualities and morphology at the surface during growth.<sup>11</sup> In the MBE chamber, a Staib 30keV coherent electron gun and electromagnetic scanning coil assembly produce a collimated 50 $\mu$ m diameter electron beam directed at the sample. The grazing angle of incidence of 1-2 degrees results in a penetration of and a diffraction pattern sensitive to only the outermost atomic layers of the sample. A phosphor screen and CCD imaging system developed by kSA Associates record the diffraction pattern at the other side of the chamber. These patterns are monitored during growth and after completion of final deposition or annealing at each composition on the sample via the scanning coil assembly.



**Figure 2-3: Diagram of how RHEED patterns are created.** Diffraction from a plane of atoms creates rods in reciprocal space. Where rods intercept the Ewald sphere (radius determined by the elastic wavevector  $k$ ), diffracted electrons are produced. For clarity, only the rods creating the measured pattern are shown, producing an arc of points on the screen. Black labels are objects in reciprocal space, while blue represents those in real (lab) space.

In grazing incidence, the forward scattered electrons are mainly elastic and the Laue diffraction condition holds. This condition is met when an incident wavevector  $k_i$  is diffracted where the Ewald sphere of radius  $k_i$  intersects a Bragg reflection in reciprocal space. As noted in Chapter 1, diffraction involves structural averages over the entire illuminated portion of the sample. For

RHEED, therefore, reciprocal space is populated by a 2D grid of Bragg reflections in the form of rods as seen in Figure 2-3 resulting from a Fourier transform of the 2D surface atoms illuminated by the electron beam. These rods intersect the Ewald sphere in many places. However, due to the long working distance of the phosphor screen and the large Ewald sphere relative to the rod spacing ( $k_i \sim 35 \times$  the rod spacing), only one or two rows of rods typically diffract into the detector, creating a streaky circle of points including the direct electron beam spot as can be seen in Figure 2-3. The diffraction mechanism is discussed in more detail by He<sup>1</sup> for RHEED as well as in Chapter 3 for x-ray scattering.

Basic characteristics of the crystal can be obtained from the RHEED patterns assuming such a perfect plane of atoms. The intensity of the spots is proportional to the number of atoms contributing to the reflection. Scattering from stray atoms or surface defects will interfere destructively and reduce this intensity. The spacing of the reciprocal lattice of rods are related to the direct lattice spacing of a cubic crystal by  $r = 2\pi/d$ , where  $r$  is the rod spacing and  $d$  is the in-plane direct lattice spacing.<sup>12-14</sup> The in-plane width of these spots is inversely proportional to the coherence length of the atomically flat area on the crystal surface,<sup>15</sup> minimized when surface coherence is larger than the coherence of the beam which, in the case of the beam produced here, is on the order of several hundred angstroms.

With a miscut of less than 1° on the substrates used in this work, the resulting atomic terraces are larger than that of the electron beam coherence, so the surface seems like a perfect 2D monolayer of atoms. Deposition of a material with extremely high crystal quality can exhibit the patterns described above and is known as '2D growth', seen in Figure 2-4 (a). Also prominent in these patterns is the existence of the 2x1 surface reconstruction, which is exhibited as a halving of the period between the rods. In fact, with such a high quality surface, this pattern can experience

intensity oscillations with deposition as each monolayer is formed, decreasing intensity by disruptions from the increasing number of adatoms followed by restoration of intensity with the completion of the layer. The in-plane width also exhibits these oscillations but with a  $180^\circ$  phase relative to the intensity due to a reduction of coherent diffraction during monolayer assembly. These 'RHEED oscillations' are signs of layer-by-layer growth and are considered to be the hallmark of the highest quality of epitaxial growth achievable.<sup>16-18</sup>

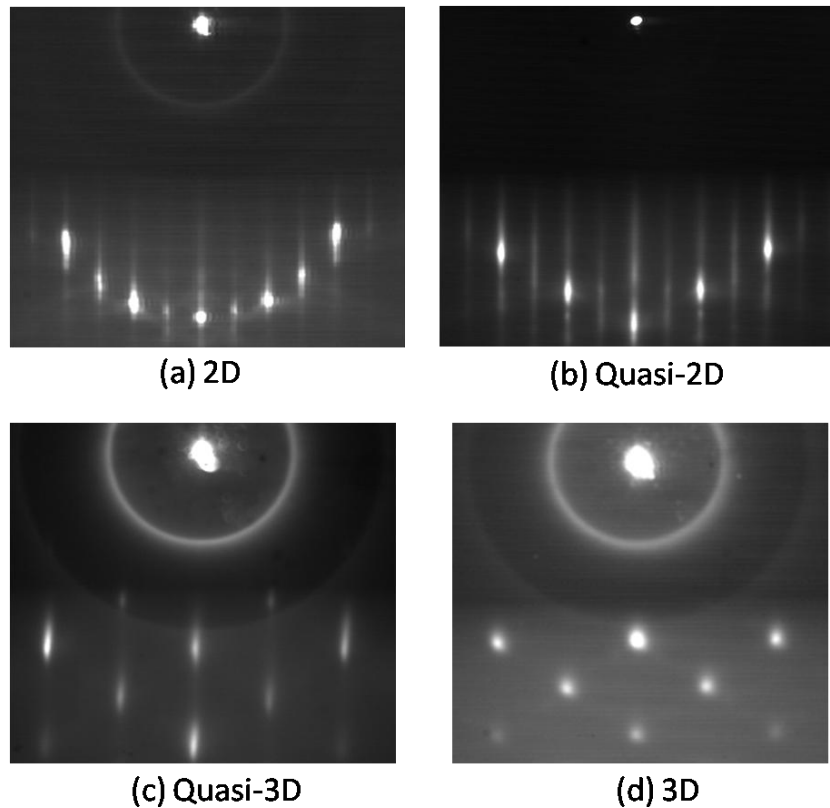


**Figure 2-4: RHEED patterns of the four classes of surface considered to be epitaxial with the direct beam on top (sample surface points down). (a) 2D reflection pattern with a ring of spots concentric with the direct beam at the top. (b) Quasi-2D pattern where spots are still roughly on an arc, but are elongated along increasingly intense streaks. (c) Quasi-3D pattern where the streaks begin to fade in favor of the 3D lattice but are still elongated. (d) 3D transmission pattern with a lattice of Bragg diffraction spots as in a bulk crystal.**

If defects cause the surface crystal coherence to be reduced to length scales similar to those of the electron beam coherence, the RHEED pattern will become somewhat disrupted. The rods will thicken due to shorter coherence and the pattern will become streakier, while spots will elongate

along the streaks. Figure 2-4 (b) shows an example of this 'Quasi-2D' pattern, with the spots still largely along the arc. The resulting film is still very highly ordered but will clearly have a higher RMS surface roughness. In less ideal growth modes, patches of the surface may grow preferentially causing islands to form. The interplay between surface energy and bulk strain is a very delicate balance, which can often tip either way depending on locality and plays a large role in the formation of these islands. This shows up in RHEED patterns as a modulating of the rod intensity into a more familiar bulk diffraction pattern as seen in Figure 2-4 (c). This 'Quasi-3D' pattern is caused by electrons transmitted through the first atomic layer and interacting with buried layers and is associated with the loss of the surface reconstruction pattern. A qualitative boundary can be determined between smooth and rough growth by location of intensity peaks along the streaks with a careful choice of incident angle that places the 2D specular reflected beam at the anti-Bragg position (between to Bragg reflections in the 3D pattern).

In the final stage, shown in Figure 2-4 (d), the islands become more mountainous, exposing multiple facets of the crystal. This 3D growth mode has a high roughness due to high epitaxial strains or chemical instabilities. The electrons are able to fully penetrate these nanocrystal surface structures, causing a bulk diffraction pattern consisting of a lattice of circular spots. When the strains and instabilities are too great, the epitaxial film breaks down either into a polycrystalline or amorphous material. At this point the RHEED patterns will become numerous concentric circles (powder pattern) or no pattern, respectively (not shown). The film is thus considered disordered and the novel properties under investigation are often lost or impossible to study in a systematic fashion.

Using these qualitative classifications and quantitative parameters of relative peak intensities, spacings and widths, the structural qualities of a uniform or binary sample are

investigated during the growth process. However, some limitations of this technique result in the need for further investigations using complementary techniques such as x-ray scattering studies at the root of this thesis. For example, by being at a grazing angle, the electron beam footprint covers a large portion of the sample, and therefore RHEED lacks the compositional resolution to analyze the structural qualities of a ternary sample. Additionally, the electron beam is highly influenced by electromagnetic fields present along the scattering path. With these fields emanating from electron-beam hearths of the sources below and the resistive heating elements present just behind the substrate, the diffraction patterns are susceptible to distortions, making impossible high-precision quantitative analysis of various features. Finally, the surface sensitivity of RHEED is advantageous for monitoring the growth front during deposition, but cannot be used to probe bulk structural changes in the crystal occurring afterward (e.g. annealing). By contrast, the micron-sized spot of the x-ray beam used as well as its high-angle diffraction geometry produce relatively small sample footprints. Furthermore, x-rays are not affected by electromagnetic fields and have much larger penetration depths allowing for bulk measurements of the film. With their lower scattering cross-section, single scattering events are more probable, allowing for kinematical models to represent data in a more quantitative way.

### **1.3 Sample Preparation**

Although pads were very effective in locating compositions on the one-dimensional binary samples, locating compositions on a ternary sample presented a much deeper challenge. Therefore once these samples were removed from the growth chamber system, a series of crosses were drawn near the sample edges (Figure 2-5) for 2-dimensional position correlation of *ex situ* measurements. The sample was mounted on an xyz micrometer stage using low-tack double-sided tape. A diamond scribe was positioned just above the sample surface and gradually lowered (~0.5 micron steps) between perturbations of the in-plane x-micrometer ( $\Delta x \sim 100$  microns). A microscope was used to

observe a visible scratch on the sample surface indicating a proper height of the diamond scribe. An approximately 600x600micron cross with arms 20-50 microns wide was then drawn onto the sample at this height. Between 6 and 10 crosses were scribed onto each ternary sample as seen in Figure 2-5, allowing ample points for triangulation of compositional positions of interest. These crosses were easily imaged by the complementary *ex situ* techniques available to the laboratory including scanning probe microscopy, laser-based studies, and the x-ray studies discussed in this work. The imaging techniques and triangulation analysis is discussed in the next chapter.

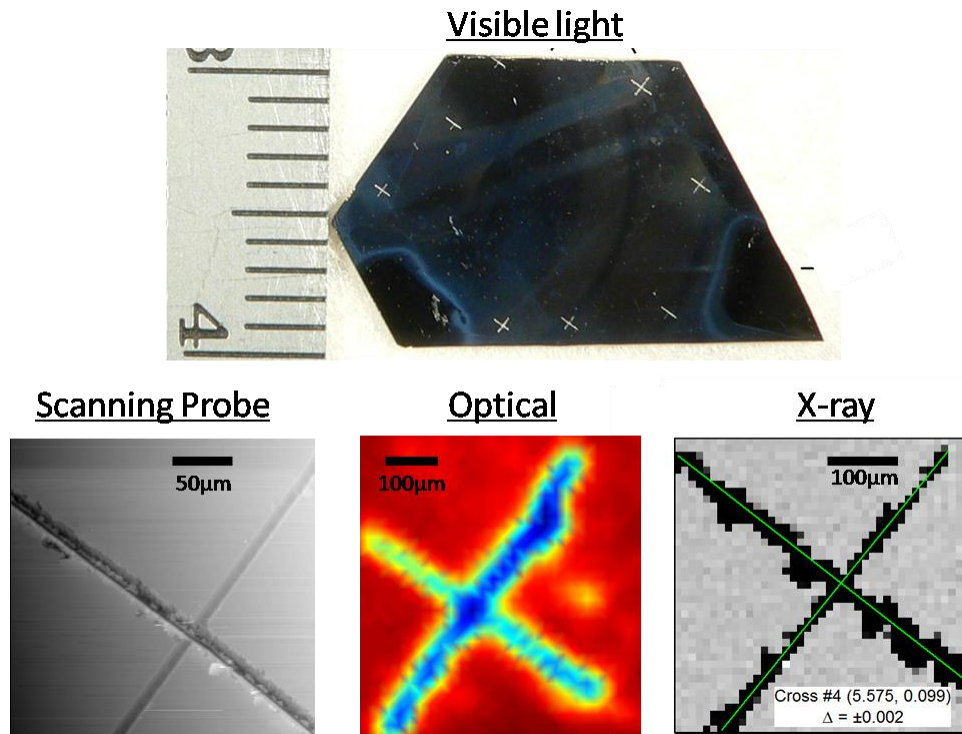


**Figure 2-5: Visibility of crosses scribed onto the surface of a ternary sample to precisely triangulate sample position and therefore composition between a large variety of measurement techniques. The visible light photograph is taken next to a straight edge with millimeter markings and centimeter labels. X-ray data depicts the process of locating the precise center of the cross within a few microns – equal to the typical footprint of the x-ray beam.**

Other sample processing applied prior to x-ray studies involved cutting binary samples for multiple experiments. For this, the sample was fixed to a cutting stage coated with resin liquefied at 80°C. Once hardened from cooling, the binary samples were cut by a diamond rotary saw into 1.5-

2mm strips along the composition gradient resulting in 2-3 pieces. The samples were then removed by sonication in acetone and then further cleaned using multiple solvents. The pieces could then be simultaneously probed using complementary techniques. A wider sample was particularly important for x-ray studies since epitaxial strain from the film was measured to twist the substrate in pieces thinner than 1mm. Before and after use in x-ray studies, each sample was again cleaned by sonication cycles in acetone to remove any contaminants built up during the transit process to the synchrotron.



## Bibliography

1. He, L. *Novel properties of magnetic epitaxial films of Co, Mn and Ge ternary system*. (2005).
2. Lu, C. & Guan, Y. Improved method of nonintrusive deposition rate monitoring by atomic absorption spectroscopy for physical vapor deposition processes. *J. Vac. Sci. Technol. A* **13**, 1797-1801 (1995).
3. Klausmeier-Brown, M., Eckstein, J., Bozovic, I. & Virshup, G. Accurate measurement of atomic beam flux by pseudo-double-beam atomic absor... *Appl. Phys. Lett.* **60**, 657-659 (1992).
4. Kometani, T.Y. & Wiegmann, W. Measurement of Ga and Al in a molecular-beam epitaxy chamber by atomic absorption spectrometry (AAS). *J. Vac. Sci. Technol.* **12**, 933-936 (1975).
5. Tsui, F. & He, L. Techniques for combinatorial molecular beam epitaxy. *Rev. Sci. Instrum.* **76**, 062206-5 (2005).
6. Tsui, F. & Chu, Y.S. The Combinatorial Approach: A Useful Tool for Studying Epitaxial Processes in Doped Magnetic Semiconductors. *Macromolecular Rapid Communications* **25**, 189-195 (2004).
7. Kaspi, R. & Donati, G.P. Digital alloy growth in mixed As/Sb heterostructures. *Journal of Crystal Growth* **251**, 515-520 (2003).
8. Ivanov, S.V. et al. MBE growth and properties of bulk BeCdSe alloys and digital (BeSe : CdSe)/ZnSe quantum wells. *Journal of Crystal Growth* **214-215**, 109-114 (2000).
9. Ploog, K. Delta- ( $\delta$ -) doping in MBE-grown GaAs: Concept and device application. *Journal of Crystal Growth* **81**, 304-313 (1987).
10. Ploog, K., Hauser, M. & Fischer, A. Fundamental studies and device application of  $\delta$ -doping in GaAs Layers and in  $\text{Al}_x\text{Ga}_{1-x}\text{As}/\text{GaAs}$  heterostructures. *Applied Physics A: Materials Science & Processing* **45**, 233-244 (1988).
11. Mahan, J.E., Geib, K.M., Robinson, G.Y. & Long, R.G. A review of the geometrical fundamentals of reflection high-energy electron diffraction with application to silicon surfaces. *J. Vac. Sci. Technol. A* **8**, 3692-3700 (1990).
12. de Siervo, A. et al. Growth study of Cu/Pd(1 1 1) by RHEED and XPS. *Surface Science* **575**, 217-222 (2005).
13. Paniago, R., de Siervo, A., Soares, E.A., Pfannes, H.-. & Landers, R. Pd growth on Cu(1 1 1): stress relaxation through surface alloying? *Surface Science* **560**, 27-34 (2004).
14. Koida, T., Lippmaa, M., Komiyama, D., Kawasaki, M. & Koinuma, H. Oscillation of surface in-plane lattice spacing during epitaxial growth of BaTiO<sub>3</sub> and SrTiO<sub>3</sub> on SrTiO<sub>3</sub>(1 0 0). *Applied Surface Science* **185**, 226-230 (2002).
15. Fukutani, K. Promotion of epitaxial growth of Ge by Ag and Pb deposited on a clean Ge(111) surface. *Surface Science* **281**, 285-295 (1993).

16. Aït-Mansour, K. et al. A structural parallel between Ge- and Si-induced  $4 \times 4$  and  $3 \times 3$  reconstructions on SiC(0 0 0 1) drawn from comparative RHEED oscillations. *Surface Science* **565**, 57-69 (2004).
17. Dentel, D., Bischoff, J.L., Kubler, L., Werckmann, J. & Romeo, M. Surface smoothing induced by epitaxial Si capping of rough and strained Ge or Si<sub>1-x</sub>Gex morphologies: a RHEED and TEM study. *Journal of Crystal Growth* **191**, 697-710 (1998).
18. Zaima, S. et al. Surfactant effect of H atoms on the suppression of Ge segregation in Si overgrowth on Ge(n ML)/Si(100) substrates by gas source molecular beam epitaxy. *Journal of Crystal Growth* **150**, 944-949 (1995).

# Chapter 3 X-ray Techniques and Theory

---

All of the primary experimental studies completed in this work were conducted at the Advanced Photon Source (APS) in Argonne National Laboratory, using scattering x-ray diffraction and spectroscopic techniques. Because of its high brightness and continuous energy tuneability, synchrotron radiation is ideal for studying the combinatorial epitaxial films produced by MBE. The small volume of material to be studied is made smaller with position sensitivity requirements of a composition gradient across the sample. The high brightness of the Advanced Photon Source made it possible to produce a small focused beam with sufficiently high flux density, providing the position sensitivity required to probe individual compositions. In addition, x-ray absorption characteristics of constituent elements are windows into the local atomic interactions within these materials, that can help uncover structural, electronic and magnetic properties and their underlying atomic mechanisms. The energy tuneability of the synchrotron source allows for a variety of element-specific probes through spectroscopic methods. In the sections below, the synchrotron-based experimental methods used and developed in this work on epitaxial materials are discussed in detail.

## **3.1 Experimental Setup**

### 3.1a: Source Parameters

At the APS, electrons are boosted to 7GeV with a current of 100mA along a circular trajectory in its 1104m circumference storage ring. Due to this centripetal acceleration at relativistic speeds, the electrons emit synchrotron radiation which is collimated in the forward direction

tangent to the trajectory with a divergence of  $\delta\theta_{lab} \approx 1/\gamma = 73\mu rad$ . Most of the techniques used in this work were carried out at the 2-BM bending magnet beamline of the APS. In a bending magnet, radiation is produced by a single dipole magnet to deflect electrons into the horizontal circular trajectory, producing photons linearly polarized parallel to the orbital plane. With the 0.6 Tesla magnet, maximum photon flux occurs at the critical photon energy of 19.5keV, but for this work, photons in the energy range of 6-12keV were used due to the constituent elements of the materials studied. A few studies were conducted at the 2-ID-D and 2-ID-E undulator beamlines, in which x-rays are produced by forcing the electrons into a sinusoidal path via periodic permanent magnets. Both beamlines utilize APS undulator A with a period of 3.3cm and length of 2.4m, consisting of 72 sinusoidal periods. The x-rays produced by each of the undulations are coherently added to produce a smaller x-ray source size and divergence compared with a bending magnet, resulting in up to 3 orders of magnitude higher maximum beam brightness [photons/(s·mm<sup>2</sup>·mrad<sup>2</sup>·0.1% energy bandwidth)]. A more in-depth discussion of the synchrotron and the source parameters can be found in Reference 1.

### 3.1b: Beamline Components

Although the undulator beamlines were used intermittently for fast data acquisition of some of the more standardized techniques such as x-ray fluorescence spectroscopy for composition characterization (see section 3.3a), 2-BM was used for the entire array of x-ray experiments completed in this work. Due to the complex nature of the samples studied, numerous constraints on the methodology of even relatively simple techniques required the buildup of specialized capabilities, so this work required a primary beamline where the equipment could remain relatively permanent. Also, the measurements were typically not limited by the x-ray flux but rather a large overhead of multiple motor motions and detector hand-shakes. A combinatorial sample requires multiple scans to be taken at up to thousands of positions on the sample to map out compositional

dependence of materials properties, causing these overheads and reducing the advantage of a high flux beamline. Furthermore, the need for development of x-ray combinatorial techniques benefitted from a close collaboration with scientists at the APS, which allowed for a typical 12-day continuous run at this beamline. Therefore, development of experimental techniques specific to the needs of this thesis work and optimized instrumentation resulted in a higher efficiency of data collection compared with the other available beamlines.

At the 2-BM beamline, the x-ray beam was first conditioned via a series of x-ray optics for use in this work. From the source, the white x-ray beam is reflected from a Cr-coated harmonic rejection x-ray mirror, which serves as a low energy filter. With a fixed incident angle of 0.15 deg, this mirror provides a cut-off energy of 20 keV. The beam is further conditioned by a Si(111) double-bounced crystal monochromator (DCM), resulting in a monochromatic x-rays with a typical energy bandwidth of  $dE/E \sim 1e-4$ . Water-cooling is sufficient for the APS bending magnet crystal monochromators. However, liquid nitrogen cryo-cooling is needed for the monochromator at an undulator beamline.

Figure 3-1 shows the apparatus in the experiment hutch, 48m from the source. Precision hutch slits with encoder resolution of  $2\mu\text{m}$  are used to constrain the beam profile for eventual focusing by grazing incidence total-reflection mirrors in Kirkpatrick-Baez (KB) geometry.<sup>2</sup> Using elliptical bending, these mirrors focus the beam horizontally and vertically to micron-size spots without chromatic aberration. The bending curve applied here uses the method developed by B. Yang et al in 1994,<sup>3</sup> which employs two bending points to a Rh coated Si crystal mirror whose trapezoidal shape allows for an approximate elliptical bending moment. The microfocusing KB mirrors at 2-BM were designed to provide a long working distance up to  $\sim 0.5\text{m}$  and, therefore, reduce incident beam divergence on the sample and allow for high resolution diffraction

capabilities. The horizontal and vertical mirrors are 20cm and 10cm long, respectively, accepting approximately 0.8 x 0.4 mm beam size at a nominal incident angle of 4mrad. With these parameters, the x-ray beam was focused to a typical spot size of about 5x5 $\mu$ m and an x-ray flux of about 10<sup>9</sup> photons/sec at 10.5keV. For the combinatorial samples studied, 5 $\mu$ m represents ~0.05% of the composition spread, smaller than the compositional gradient present in the samples. The KB mirrors' focusing property is independent on wavelength, which is critical for completing x-ray energy dependent studies over several keV conducted here. A set of computer-controlled pneumatic Al filters with up to 16 possible combinations of x-ray attenuation are used to extend intensity variation of diffraction profiles by three orders of magnitude. The slits after the KB mirrors are used to block out the unreflected x-rays and eliminate intensity tails from the KB-mirrors, due to surface roughness or figure errors. Two ion chamber detectors before and after the KB mirrors are used to monitor the incoming flux.

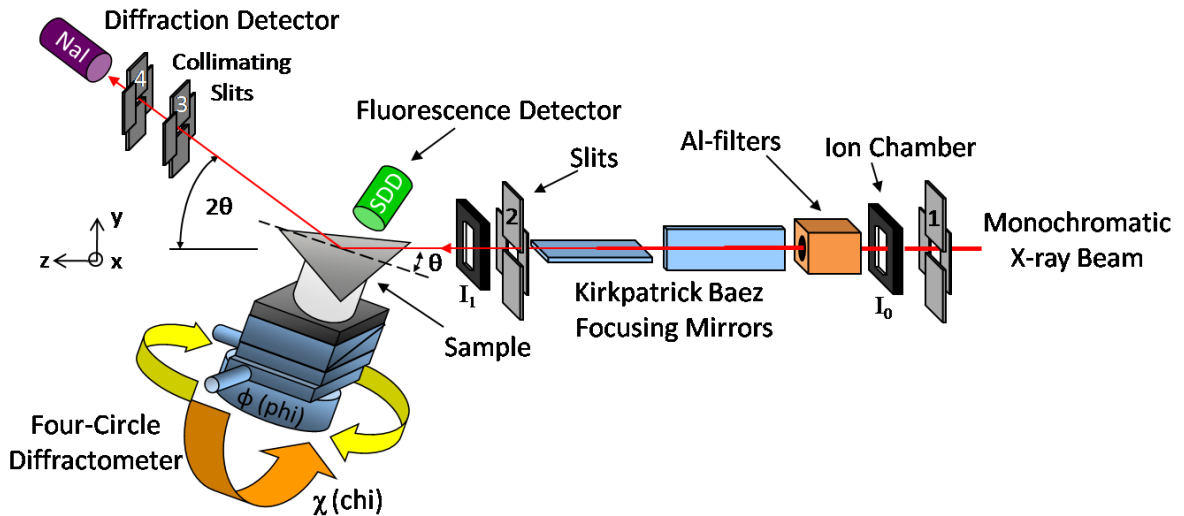


**Figure 3-1: Typical experimental setup constructed at the 2-BM beamline experiment station. Slits are labeled in the text as S1='Hutch Slits', S2='Mirror Slits', S3='Guard Slits', S4='Detector Slits'.**

After the focusing optics, the beam is incident on the sample mounted in a four-circle Huber diffractometer, which contains three sample rotation axes  $\theta$ , polar angle  $\chi$ , and azimuth  $\phi$  and the vertical diffraction angle  $2\theta$  for the detector. Driven by stepper motors and gear reducers resulting

in an angular resolution up to  $0.00025^\circ$ , the Huber diffractometer provided both flexible diffraction capabilities with sufficiently high angular resolution. A high resolution ( $0.25\mu\text{m}$ ) long travel ( $20\times 20\times 3\text{mm}$ ) xyz-stage is mounted on top of the  $\phi$ -stage to provide accurate scanning capability on combinatorial samples. The sample is secured by nail polish solution to a Teflon sample holder mounted on a kinematic base with positional reproducibility better than  $50\mu\text{m}$  (see Figure 3-2 for the various configurations). Some hysteresis occurs in placement below this length scale, but careful attachment can often reproduce the kinematic sample positioning within motor resolution.

Three primary detectors are used in this work to gather experimental data. A Vortex silicon drift diode (SDD) energy-dispersive detector is placed very near the sample to collect x-ray fluorescence (see section 3.4a). This is a solid state detector based on a reverse-biased PIN junction (the intrinsic region collecting the x-rays) and is capable of moderate energy resolution of about 180 eV with a shaping time of  $3\mu\text{s}$ . Consequently, it can linearly handle count rates up to  $\sim 30,000\text{cts/sec}$ , after which double photon events become probable. It is placed within 2cm of the sample to be sensitive to trace doping levels or low-energy fluorescing elements such as Si at a constant angle of approximately  $40^\circ$  from the surface normal and perpendicular to the incident x-rays, in order to minimize the detection of the scattered x-rays from the sample. Figure 3-2(a) shows this device in normal operation attached to the chi-circle, whereas Figure 3-2(b) shows it with a aluminum collimator to remove fluorescence from spurious sources such as the air (Ar) or nearby glass (if used in sample mounting as shown in the figure).

For high angular resolution diffraction a “point detector” is typically used. This involves a Bicron NaI scintillator with standard amplification electronics behind two sets of collimating slits as seen in Figure 3-1 and Figure 3-2(a). The detector slit is 610cm from the sample, and the guard slit accepts a larger solid angle. High resolution scans are often conducted with the vertical detector

slits at 0.1mm, giving the point detector a 160 $\mu$ rad opening angle. The final detector used in this setup is custom built and includes a CsI scintillator fiber optically coupled to a charged coupled device (CCD) based on the Quantix model by Photometrix. With the opposite intention of the point detector, this detector is 2.7x1.8cm wide with 3k x 2k pixels 9 $\mu$ m in size and placed <4cm from the sample (see Figure 3-2b) to yield a large acceptance solid angle for diffraction. It is used to record reciprocal space maps and using integration techniques in this work is sensitive to trace powder diffraction signals (see section 3.3d).

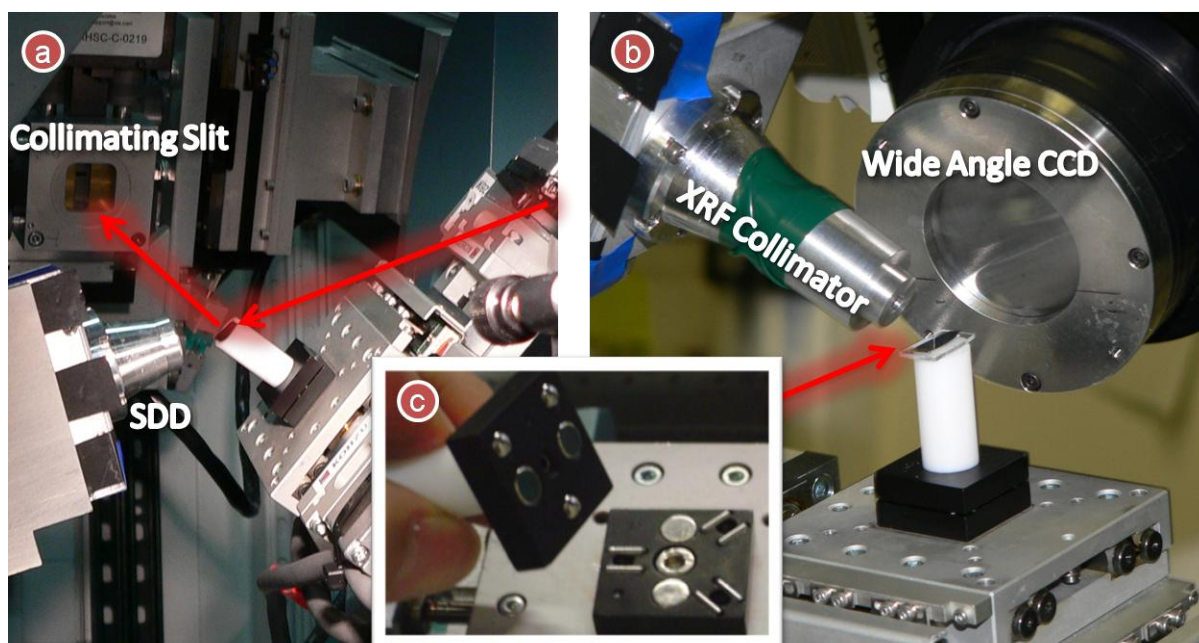


**Figure 3-2: Pictures of detector setup, geometry, and sample mounting. Red arrows are the x-ray beam. (a)** point-detector setup positions. The SSD is mounted on the  $\chi$ -circle to have a constant relative angle to the sample surface. **(b)** Setup for wide-angle powder diffraction. Because this setup can detect even the faint crystallinity of the Teflon holder, a glass slide is placed beneath the sample. This, in turn, requires a collimator placed on the SSD detector to remove fluorescence from the large variety of elements in the glass. **(c)** Kinematic sample mounts use a magnetic tripod to precisely reproduce sample positioning.

The beamline 2-ID-D was used for diffraction experiments. For a minimum beam divergence resulting in high-diffraction resolution, focusing optics were not used. Instead, slits narrowed the beam to sizes of 10x30microns, allowing compositional studies of binary combinatorial samples. Here, the Newport six-circle kappa diffractometer allowed for unique diffraction conditions



unachievable by the Huber diffractometer at 2-BM. The 2-ID-E beamline, in contrast, is setup only for high-throughput x-ray fluorescence spectroscopy, and so was used often for full characterization of each sample's composition. Here, zone plate optics focused the beam to sub-micron (down to 0.25 $\mu$ m) spots on the sample in a He-flow box. The angle of incidence was fixed at 15° from the sample surface normal and an SSD detector placed approximately 10cm and 90° from the incident beam (to minimize detection of scattered x-rays) was used to collect x-ray fluorescence from the sample. To minimize detector dead time, the signal was amplified with a lower shaping time (0.5 $\mu$ s), resulting in a lower energy resolution of ~280 eV.

### 3.1c: Diffractometer Alignment

In order to carry out accurate diffraction measurements, three important alignment conditions must be achieved. First, all the circles must have the common center. This condition is extremely difficult to achieve because the rotation motions are never perfect. A typical rotary stage exhibits axial displacement of its center during the rotation (known as axial run-out error) and the wobbling of the rotary plate (known as wobble error). The run-out error for a diffractometer circle depends on the size, weight, and the actual mechanical guidance method to achieve a circular motion. A typical run-out error is about 1-5 microns for phi, 5-20 microns for theta and two theta, and ~100 microns for the chi circle. The large run-out error for the chi circle is due to the imperfection of the mechanical guidance. When all the circles are used together, the combined error, known as "sphere of confusion" is much larger than the error for each circle. A typical value of the sphere of confusion for a well-maintained diffractometer is ~50 microns. For a conventional x-ray diffraction measurement using a large beam size (~mm), the sphere of confusion does not pose a significant problem. For a microdiffraction measurement on a combinatorial sample, such a large error is detrimental and needs to be corrected. Figure 3-3a shows a large axial run-out error (~100 microns) for the chi circle of the diffractometer. After painstaking mechanical adjustment,

we achieved a concentricity value of about 35 microns between the chi and phi circle. The estimated sphere of confusion for the diffractometer used for this thesis work is ~50 microns. Since this is still much larger than the beam size used for the experiment, an elaborate correction method has been developed in order to perform accurate microdiffraction measurements. The details on this method will be discussed later.

The second condition is that the x-ray beam must go through the center of the diffractometer. This is the condition that most diffraction experimenters loosely refer to as “diffractometer alignment”. Alignment of the x-ray beam through the center of the diffractometer is carried out by first placing an alignment pin (its shape is shown in Figure 3-3a,b) at the center of the diffractometer using a telescope. To accomplish this, the diffractometer xyz stage is adjusted and zeroed when 180° motions of the sample phi and chi circles maintain the pin at a constant position. Next, the diffractometer is translated until the pin resides at the center of the focused beam. The beam position is then monitored by a detector as it is translated along the  $2\theta$  arm of the diffractometer, and the diffractometer is rotated along the vertical axis until the beam position is parallel with the  $2\theta$  arm. In principle, this alignment is only accurate to the sphere of the confusion of the diffractometer.

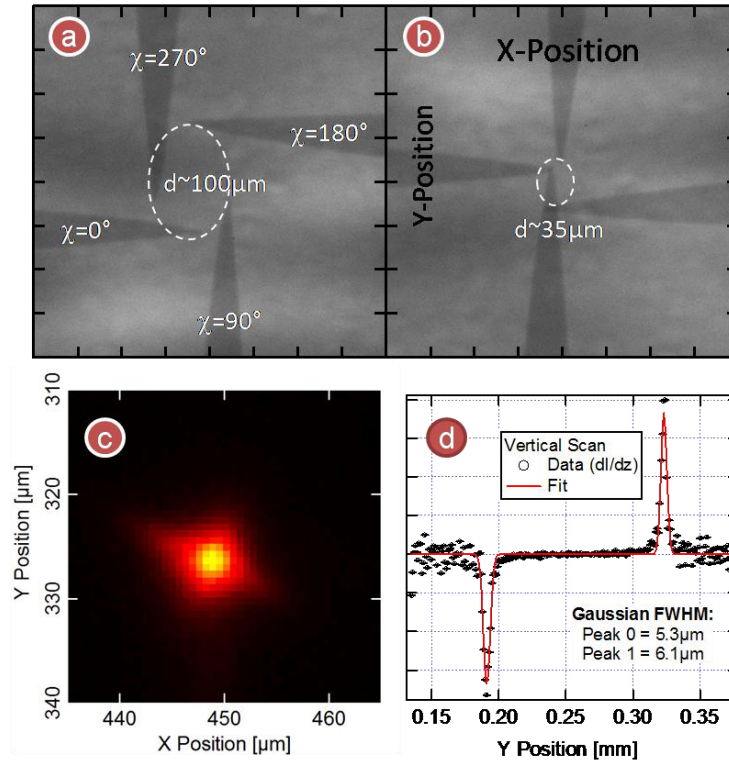


**Figure 3-3: Circle of confusion (a) before and (b) after increasing concentricity of diffractometer circles. (c) Maximally focused beam profile measured by a real-time CCD camera. (d) Measurement of beam size using the derivative of the transmission intensity profile of Au wires and analyzed using peak fitting techniques discussed in Section 3.6.**

The third condition is met by correctly zeroing the all the diffractometer angles. The zero of the two theta circle is set by aligning the detector slits parallel to the incident beam through the center of the diffractometer. The zero of theta and chi are achieved using the symmetry of the x-ray diffraction from a perfect single crystal. The substrate of the combinatorial thin-films works well for this purpose. The zero of phi does not affect the accuracy of reciprocal mapping and is set arbitrarily.

### 3.1d: X-ray Focusing

The microfocusing KB mirrors at 2-BM uses the four-point KB bender designed by University of Chicago.<sup>3</sup> The trapezoidal shape of the mirrors is determined separately by the ellipticity (i.e. distance from the x-ray source to KB and KB to the focus) in both horizontal and vertical directions.

The mirror is focused by monitoring the two dimensional intensity at the focal point using a high-resolution CCD camera system, which consists of a scintillation screen and optical microscope to magnify the x-ray intensity at the scintillation screen. This method provides sub-micron sampling resolution. Figure 3-3c shows a typical focused intensity with a beam size of  $\sim 5 \times 5$  microns. Another way of testing the beam position and the size is to scan a Au wire ( $\sim 100$  microns in thickness) across the beam and monitor the transmitted intensity using the point detector. The derivative of the intensity with respect to the position of the wire yields two sharp intensity peaks as shown in Figure 3-3d. Although this method is too cumbersome to use in KB-mirror alignment, it can be set up more quickly and provides a higher precision measurement of horizontal and vertical beam size.

Though the focusing takes only about 1 hr, the beam is subsequently monitored for several hours to assure its size and the position is stable before beginning the measurements. Due to the lack of temperature control in the experimental station, the focused beam tends to drift and change its focal size. Therefore, these are periodically checked using the quick Au-wire scans. The high-resolution CCD camera system is mounted on xyz linear stages on the diffractometer table so that it can be easily positioned at the diffractometer center in the event that refocusing is needed.

### 3.1e: Energy Calibration

Because spectroscopic techniques requiring high energy resolution were employed in this work, the Si(111) double-bounce crystal monochromator was calibrated using NIST standards. These standards comprised of elemental foils with absorption edges known to better than 1eV, which is the energy resolution of the monochromator in the energy range used for this work. The x-ray beam energy was scanned through the absorption edge of the foil located between the two ion chamber detectors, and the absorption edge was defined as the highest derivative of the resulting

absorption step-function. Typically, the NIST foils were chosen to coincide with the elements of the materials under study.

## 3.2 X-ray Diffraction Techniques

### 3.2a: X-ray Diffraction Theory

To be precise regarding the concepts of diffraction emphasized in this work as well as to create a coherent terminology, a short description of 3D x-ray diffraction is provided. A more complete discussion can be found in Warren.<sup>90</sup> Diffracted intensity is the typical quantity calculated from diffraction theory. However, in a real measurement of a real crystal, factors such as instrument resolution function, detector dwell time, and the finite spread of a Bragg reflection in reciprocal space make an absolute measurement of this quantity impossible. Therefore, diffraction experiments rely on measurements of relative intensities, and even in this case, careful measurement and control of these factors must be included for quantitative comparison. These factors are discussed in the following sections whereas the important basic principles of diffraction are covered here.

The diffracted intensity from a crystal can be described by the following formula.

$$I(\mathbf{q}, E) \propto |F(\mathbf{q}, E) \cdot S(\mathbf{q}, E)|^2 \quad (3-1)$$

where  $E$  is the photon energy and  $\mathbf{q}$  is known as the momentum transfer wavevector and is defined by the change in photon momentum  $\mathbf{q} \equiv \mathbf{k}_f - \mathbf{k}_i$  upon scattering within the crystal. Here,  $F(\mathbf{q}, E)$  is the structure factor describing the symmetry of the unit cell, the constituent atoms and their coordinates as described below.  $S(\mathbf{q}, E)$  is the 3D slit function, representing the diffraction contribution from all the unit cell illuminated by the x-ray beam.. With numerous unit cells illuminated in a macroscopic crystal, this can be represented by a parallelepiped and the slit function has the following form:

$$S(\mathbf{q}) = \sum_{n_1=0}^{N_1-1} \sum_{n_2=0}^{N_2-1} \sum_{n_3=0}^{N_3-1} e^{i\mathbf{q} \cdot (n_1 \mathbf{a}_1 + n_2 \mathbf{a}_2 + n_3 \mathbf{a}_3)} = \prod_j^3 \frac{1 - e^{iN_j \mathbf{q} \cdot \mathbf{a}_j}}{1 - e^{i\mathbf{q} \cdot \mathbf{a}_j}} \quad (3-2)$$

where the sum is over the number of unit cells  $N_j$  in each of the three crystallographic directions and  $\mathbf{a}_j$  are the lattice vectors of the crystal. The exponential term results from modeling the photon wave function as a plane wave. Because of the large sum, this function results in diffracted intensity only when  $\mathbf{q}$  has integer components when dotted with the three lattice vectors. These components are known as the Miller indices  $h$ ,  $k$ , and  $l$ , and for a given crystal, are used exclusively in this work to describe the momentum transfer wavevector.

Each crystal is made up of one of 13 Bravais lattices (for example, hexagonal or face-centered-cubic), which represent the possible unique lattices of three-dimensional space. A real crystal structure can also have a basis, where atoms in the unit cell occupy more than just the pattern of points composing the Bravais lattice, allowing for the vast number of crystal structures seen in nature. In diffraction, the structure factor  $F(\mathbf{q}, E)$  is assembled by summing all the atoms in the unit cell, including both Bravais and basis atoms, and therefore identifies the specific crystal being studied.

$$F(\mathbf{q}, E) = \sum_{j=1}^N f_j(\mathbf{q}, E) e^{i\mathbf{q} \cdot \mathbf{r}_j} \quad (3-3)$$

where  $N$  is the number of atoms in the unit cell each located at position  $\mathbf{r}_j$ , and  $f_j(\mathbf{q}, E)$  is the atomic form factor representing the atoms from which the photon is scattered. Far away from atomic excitation energies, the atomic form factor is proportional to the number of electrons it contains ( $z$ ) within the atom. In general, this factor has a complex value due to the resonance behavior corresponding to the ground state energy levels of the electrons in the atom. Consequently, each atom has a unique signature, known as an “anomalous correction”:

$$f(\mathbf{q}, E) = f^0(\mathbf{q}) + f'(E) + if''(E) \quad (3-4)$$

Here,  $f^0(\mathbf{q})$  is the classical Thomson scattering factor, whereas the other energy-dependent terms result from the resonance cross section of an atom with respect to the incident energy. The method of calculating these corrected form factors was developed by Cromer and Liberman in 1970,<sup>5</sup> and was necessary for many aspects of this work.

### 3.2b: Single Crystal X-ray Diffraction

Similar to electron diffraction discussed in Chapter 2, in x-ray diffraction (XRD) real space and reciprocal space can be connected through the Ewald sphere as seen in Figure 3-4(a). Here, however, the diffractometer typically probes individual points in reciprocal space rather than large spherical surfaces as in RHEED. The position in reciprocal space is determined by the momentum transfer  $\mathbf{q}$ , which always lies on the Ewald sphere. With four rotation axes and one vector to place, only three are independent, and the diffractometer is run with one of several possible constraints, which removes a degree of freedom. The constraint used most often in this work is  $\omega = \theta - ('2\theta'/2) = 0$  and is known as symmetric mode. Figure 3-4(a) demonstrates this for examining a Bragg reflection. Positioning of the momentum transfer wavevector is accomplished through a command-line computer control program known as SPEC developed for the APS and other synchrotrons. Given the position of two Bragg reflections, this program can navigate through reciprocal space via  $h, k, l$  and  $E$  input values.

As with any real instrument, the point probed is not infinitesimal, and the resolution function is determined by the slit sizes (horizontal and vertical) as seen in Figure 3-4, the incident beam divergence, and the energy spread of the beam.<sup>6</sup> While the slit sizes have definitive cutoffs, the divergence and energy spread are Gaussian functions in space, causing a blurring of the Ewald sphere. As long as the resolution function is kept much smaller than the feature size, the volume probed can be considered to be a point, and various characteristics of the reciprocal lattice can be

precisely probed and measured to learn about the crystal lattice. To compare quantitative intensities, however, the effects of this resolution function must be taken into account and are discussed later.

With photons, the simple relations hold  $k=2\pi/\lambda$  and  $E=hc/\lambda$ , where  $h$  is Planck's constant, so the magnitude of the photon momentum  $k$  is proportional to the x-ray energy (set by the beamline monochromator). Therefore, the beamline energy determines the size of the Ewald sphere, and in turn the viewable region of reciprocal space. For diffraction studies, an energy of 10.5keV ( $\lambda=1.1808\text{\AA}$ ) was selected as it was nearest the critical energy of the beamline, maximizing brightness, but below the absorption edge of the Ge substrate (11.103keV), reducing diffuse background.

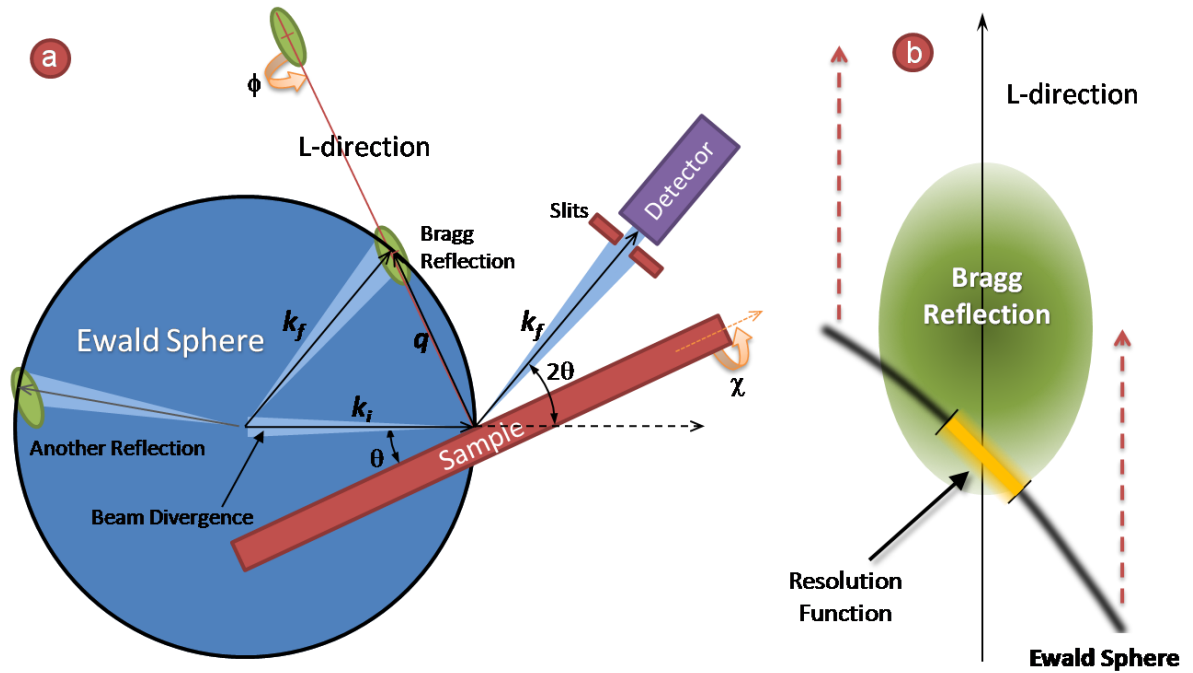


Figure 3-4: Diagrams of single crystal x-ray diffraction shown in the plane of incidence (always the vertical plane in the lab due to constraints on the detector motion). (a) Sample and detector positions and angles are connected to  $k$  and  $q$  through the Ewald sphere. This 2D rendering only shows diffraction features and beamline components in the plane of incidence. (b) Zoom of a Bragg reflection during an L-scan. Red dashes are the motion of the Ewald sphere during the scan. Thickness of the resolution function is from beam divergence and energy spread whereas detector horizontal and vertical slits determine the other dimensions.



XRD can be used with crystallography to better understand the crystalline phase of the sample studied. These techniques are ideal for the materials studied in this work because of the interest in composition effects on structure. With the possibility of the entire compositional phase space in one sample, a high throughput of crystallographic information can be obtained. In scanning particular sections of reciprocal space, the symmetry of the reciprocal lattice can be revealed at each position on the sample, and therefore the complete crystallographic phase diagram of a material system can be determined to large precision in one experiment. Because the samples studied are grown via MBE, the effect of non-equilibrium conditions on phase boundaries are also studied to better understand the physical mechanisms of crystal growth.

Possibly more interesting than crystallographic phase is how composition and epitaxy affects crystallographic ordering. For example, the position of a Bragg reflection is inversely proportional to the crystal lattice spacing, and a reflection from the film can be compared with that of the substrate, revealing the film's strain state. The integrated intensity of a reflection typically gives an overall level of ordering, which is directly proportional to the number of atoms participating in the reflection and therefore those that are well ordered in the crystal lattice. However, some reflections result from chemical ordering due to their structure factor and are used in this work to probe for specific chemical defects within the crystal. Structure factors specific to crystals studied are discussed later. The width of Bragg reflections is also important as they can be broadened significantly due to defects, crystal size, or coherent domains.<sup>90</sup> This is similar to surface coherence probed in RHEED; however, due to the full penetration of the x-ray beam, both in-plane and out-of-plane coherence of the bulk film can be measured through measurement of the peak width along various directions.

Figure 3-4(b) shows how an out-of-plane scan or L-scan is taken. Typically, detector slits are set at 1mm vertically and 5mm horizontally for such a scan, which provides good resolution of the peak width and position and allows an accurate representation of the integrated intensity, respectively. To obtain an accurate measurement of the position, successively refining scans in-plane and out-of-plane are routinely taken. If a reflection is highly skewed in reciprocal space, it may take many cycles to arrive at the correct position, so reciprocal space mapping is done instead by rasterizing a 2D scan in the out-of-plane and the radial in-plane directions. Reflections arising from defects often have a skewed shape due to disorder and strain associated with their formation, and this method was used to locate them. Finally, the mosaicity of a crystal grown epitaxially is measured by rotating the crystal along the phi-direction. A narrow peak results from a highly ordered crystal conforming well to the substrate. A wide peak suggests smaller relaxed domains with total rotational incoherence resulting from a powder-like or poly crystalline sample.

### 3.2c: Crystal Truncation Rod Analysis

In the late 1980s and early 90's the development of x-ray surface science grew into a large body of research,<sup>7-9</sup> and due to the full penetration of x-rays into epitaxial films, many of the techniques are applicable to the materials studied in this work. In particular, crystal truncation rod (CTR) analysis was used to study various qualities of epitaxial films such as strain states, ordering, and film thickness. For doped magnetic semiconductors, regular XRD techniques discussed above were not possible due to the identical crystal structures of the film and substrate. By contrast, this high-resolution technique, developed extensively by Robinson and Tweet,<sup>7</sup> is excellent at parsing the film from the substrate.

**Theory:** Crystal truncation rods arise from the existence of crystal surfaces. Here, only the incident surface is considered because of the sample size and the limited x-ray penetration in the

substrate. A schematic of these rods in reciprocal space emanating from the sample surface is shown in Figure 3-5(a). The slit function in the surface normal direction in Equation (3-2) becomes

$$S_{CTR}(q) = \sum_{n=0}^{\infty} e^{-(iqa + \epsilon)n} = \frac{1}{1 - e^{-iqa - \epsilon}} \quad (3-5)$$

where  $q$  and  $a$  are surface normal components of the respective vectors and  $\epsilon$  represents absorption from one layer to the next. This is an “ad hoc” treatment for dynamical effects from the substrate, which typically is a near-perfect crystal. In the case of the samples studied in this work, Equation (3-5) represents the substrate. Typically, an epitaxial film will have a lattice constant that differs from that of the substrate. This between the substrate and film will interfere coherently due to the added terms in to the sum of Equation (3-5) that contain a different value  $d$  for the lattice spacing along the direction perpendicular to the surface.

$$S_{N,d}(q) = \sum_{n=0}^{N-1} e^{-iqad} = \frac{1 - e^{iNqd}}{1 - e^{iqd}} \quad (3-6)$$

$N$  is the number of repeated layers (i.e. unit cells) in the film. Figure 3-5(b) shows a film with 100 layers strained by 5% showing a superposition of the bare rod and several fringes. The number of fringes between each reflection is the number of layers, and the phase shift of the fringes from the substrate reflection give the strain.

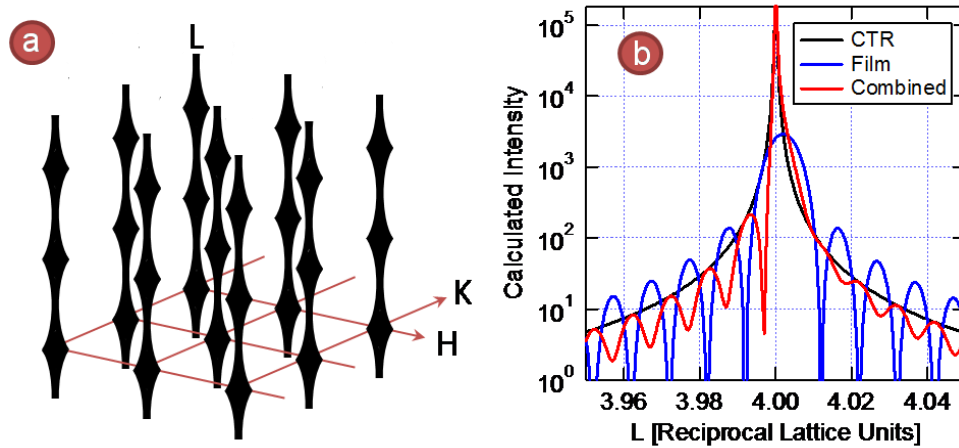


**Figure 3-5: (a) Schematic of CTRs for x-rays. They are similar to those for RHEED but due to crystal penetration, superimposed by Bragg reflections. (b) Modeling rod intensity as a function of L for the first two orders.**

To successfully fit these models to actual data, Debye-Waller disorder was also considered. This is a thermal effect of atoms vibrating about their equilibrium position in the lattice. In a film, this can also be a result of slight perturbations of atomic positions averaged over the lattice due to a non-thermodynamic formation process such as MBE. They can come about by being ‘frozen’ in by a low temperature growth, or slightly different bond lengths from multiple dopant species interacting in the crystal. Debye-Waller disorder is derived by taking a time-average of incoherent perturbations  $u$  of atomic positions and results in an added factor in the diffracted intensity.

$$I = I_e e^{-q^2 \langle u^2 \rangle} |F|^2 |S|^2 \quad (3-7)$$

This is simply an exponentially decreasing envelope function with  $|q|$ . A full derivation can be found in Warren.<sup>90</sup> With this factor in the model for both the substrate and film, trends of disorder from the growth process can be separated from thermal effects and studied as a function of composition.

A final factor used in the CTR model is that representing a rough surface. The entire illuminated surface may not be terminated at the same atomic layer, but contain monolayer islands or other atomic structures. A statistical model resulting from exponentially decreasing layer occupancy can be used as developed by Robinson.<sup>10</sup>

$$I_{Rough} = I_{CTR} \frac{(1 - \beta)^2}{1 + \beta^2 - 2\beta \cos(\mathbf{q} \cdot \mathbf{d})} \quad (3-8)$$

Here  $\beta^n$  is the fraction of sites filled in the  $n^{\text{th}}$  layer above the one last fully occupied. Different methods of accounting for roughness, for example, based on a Gaussian distribution, can be used. The  $\beta$ -roughness description shown above is commonly used because this method offers a closed-form analytical expression, while other methods require numerical summation. In all cases, the roughness results in a reduction of the intensities of the rod away from the Bragg Reflection.

**Model:** The approach taken in this study was slightly different from more conventional surface diffraction<sup>11</sup> due to a variety of differences in the sample studied. Because the films studied contained thicknesses from approximately 500Å to 1000Å, the oscillations period was very small and sampling rod intensity profiles over a small range (~0.1 in L) around a substrate reflection was sufficient to obtain a large number of interference fringes needed to determine the strain of the film accurately. Also, the pattern of fringes surrounding the substrate reflection was seen to have complexities arising from multiple Fourier components. Contrast at the substrate interface with the Ge buffer arose from higher densities of crystal dislocations and contaminants that initial substrate annealing was unable to remove. This was confirmed by HRTEM images of the film cross section (Figure 3-7a) and also resolved in the dynamic secondary ion mass spectrometry (SIMS) measurements where diffusing dopants tend to collect. A three-tiered model including a thin, disordered interface, an unstrained buffer, and the doped film was found to reproduce these complexities very well. Finally, the typical  $\theta$  or “rocking” scan for diffuse background subtraction was not necessary so near the Bragg reflection as intensities were found to be several orders of magnitude higher than the background.

Using these considerations, detailed structural properties of the films, including the strain normal to the surface were quantified by fitting the measured CTR intensity profiles to a kinematical

formula of the form  $I(q) = A R(q)|S(q)|^2 + B(q)$ . Here  $q$  is the normal component of the momentum transfer wavevector and is related to the reciprocal lattice unit  $L$  by  $q=2\pi L/a$  with the Ge substrate lattice parameter  $a=5.658\text{\AA}$ . The intensity  $I(q)$  consists of two contributions, one from the slit function from the atomic layers,  $S(q)$ , with an overall scale factor ( $A$ ) and surface roughness  $R(q)$  discussed in Equation (3-8). The other term  $B(q)$  was used depending on the conditions of data collection. With some datasets, wider detector slits caused a broadening of the narrow substrate reflection, which in turn, is much narrower than the interference fringes. In this case, a Voigt function with four parameters (DC background, amplitude, width and shape) was used to simulate the added broadening of the delta-function peak. The only effect of this portion was found to be a reduction of the chi squared values, as the other parameters are not affected by this region of the data. The slit function was expressed as

$$S(q) = e^{-\frac{1}{2}q^2\sigma_s^2} S_{CTR}(q) + e^{-\frac{1}{2}q^2\sigma_i^2} S_{N_i,d_i}(q) + e^{-\frac{1}{2}q^2\sigma_b^2} S_{N_b,d_b}(q) + e^{-\frac{1}{2}q^2\sigma_f^2} S_{N_f,d_f}(q) \quad (3-9)$$

The first term is the CTR of the substrate as shown in Equation (3-5). The other terms are the N-slit interference functions (Equation (3-6) of the interface, buffer and film, respectively. The fit parameters here are the number of atomic layers ( $N$ ) and the film lattice parameter perpendicular to the surface ( $d$ ), assumed to be constant throughout the tier. The prefactors on each term  $e^{-\frac{1}{2}q^2\sigma^2}$  represent the Debye-Waller factor, with fit parameters  $\sigma$  representing the RMS displacement amplitudes of the atoms from their equilibrium positions. Here the magnitude of  $\sigma$  should be interpreted as the variance in the unit cell position, or the magnitude of crystalline disorder as they are larger than the time-averaged thermal vibrations.

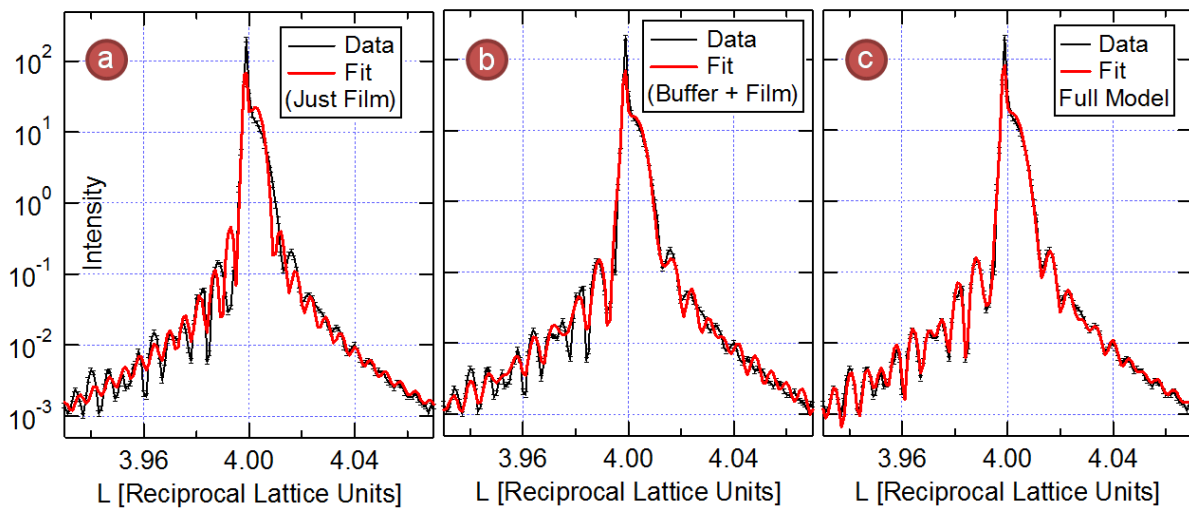


**Figure 3-6: Fits to a CTR intensity profile at (00L) from models containing (a) Just a film and substrate; (b) a film, buffer and substrate; and (c) a film, buffer, interface, and substrate.**

**Fitting Methods:** To emphasize the importance of a complete model, an example data set taken from a doped magnetic semiconductor sample is fit with three different models in Figure 3-6. The simplest of the three (Figure 3-6a) shows just a film on the substrate. Although many of the fringes in the fit look to be in phase with the data, the complex amplitude modulation is clearly not duplicated. Also, the film Bragg reflection near  $L=4.005$  is too narrow. The fit near the Bragg peak looks better in Figure 3-6b where the layers from (a) have been split into two tiers (buffer and film) based on known deposition thicknesses for the sample. While there is some modulation in the amplitude of the modeled fringes below  $L=4.0$ , they are clearly out of phase in several places and, in some cases, fringes are missing. The full model discussed above is used to fit the data in Figure 3-6c where all features are reproduced extremely well.

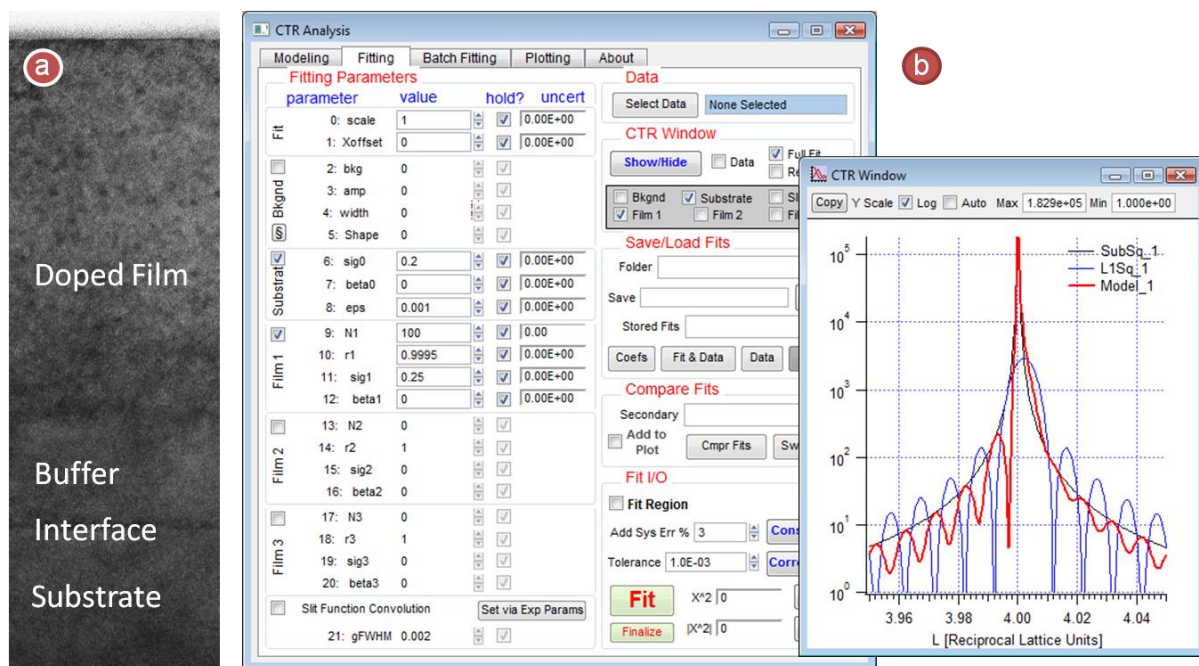


**Figure 3-7: (a)** Cross sectional HRTEM image of the film highlighting the contrasting deposited tiers. Typically annealing was not able to remove all defects and contaminants present on the substrate surface, producing a contrast picked up by the x-ray interference pattern and therefore necessitating a three layer model. **(b)** The *CTR Analysis* program written to systematically model and fit large datasets in an iterative fashion.

Although the ratio of fit parameters to data points is relatively small for a non-linear model, (10 without the Voigt function fit to hundreds of data points) finding the global minimum was challenging. The first step in the process was modeling just the substrate to reproduce the general form of the data by manipulating the scale,  $q$ -offset (accounting for a misalignment of the substrate, typically on the order of the data spacing),  $\sigma_s$ , and  $\epsilon$ . Next, rough estimates of  $N$  for each tier were set based on recorded deposition during growth, with the interface typically given 5 layers. The scale,  $q$ -offset and  $\epsilon$  were then held fixed with the  $d$ ,  $N$ , and  $\sigma$  parameters open to fitting for each tier, using the reduced chi squared routines provided in the IGOR analysis platform.  $N$  was specially restricted to integer values. The scale was held due to the high correlation with the Debye-Waller parameters, and therefore, only relative disorders between the tiers were measured. As each scan consisted of data taken from several consecutive positions on a binary or ternary sample, there were anywhere from 30 to over one thousand scans in one dataset. Therefore tailored fitting



software *CTR Analysis* was developed to handle all steps of the fitting process, including modeling, individual fits, batch fitting and parameter trend plotting. The individual fitting tab, along with the scan window plotting a simple model, is displayed in Figure 3-7b. A critical component in the process of finding the global minimum in the fit was the batch fitting routine. Here, each consecutive scan was iteratively fit from the fit results of the previous scan. The plotted trends from the batch fit helped to detect paradigm shifts in the model as the evolving sets of data perturbed it, eventually causing the model to fall from a local minimum in parameter space to the global minimum. Batch fitting, therefore, was repeatedly run on a dataset in each direction until each fit in the series stabilized. Typically, once the global minimum was found, the interface contained large values of disorder and strain relative to the other layers, and the buffer strain was nearly zero with buffer and film thicknesses in good agreement with the deposited values.

### 3.2d: Wide-Angle Diffraction

To detect powder XRD signals, a typical method is to scan  $2\theta$  with the point detector. Although this is adequate for a well prepared powder sample, trace powder detection is desired in this work and significant enhancement of the signal is required. As discussed in Chapter 1, doping a semiconductor well beyond the solubility level of the dopant can cause phase separation in the form of small nanocrystal precipitates randomly embedded in the matrix. Early on, powder diffraction was performed on these materials without detection of this phase separation<sup>30</sup> even though these samples were later confirmed to have these defects using more advanced techniques<sup>35</sup>. To enhance the sensitivity of powder XRD to these small precipitates, XRD with a wide field-of-view ( $60^\circ$ ) was carried out using a CCD placed very close to the sample (<4cm).

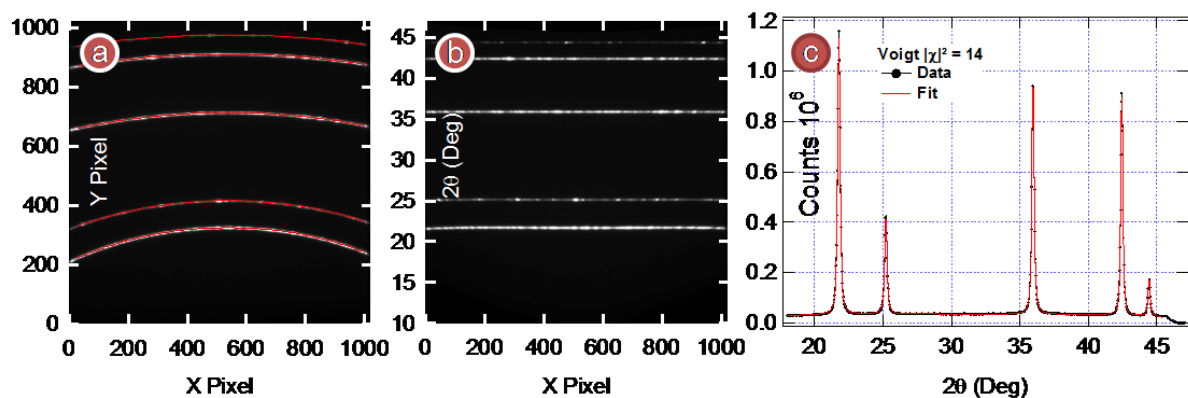


**Figure 3-8: Data and processing of CeO<sub>2</sub> powder diffraction using wide-angle XRD. (a) Powder rings of a standard are fit (red curves) to calibrate  $2\theta$  for the detector. (b) Subsequent images are transformed to allow indexing of features with  $2\theta$ . (c) A large increase in sensitivity is reached by integrating over the X Pixels, and the peaks are fit (in *Peak Analysis*) to integrate over  $2\theta$ .**

The detector setup is similar to RHEED, but due to the short working distance, a much larger portion of reciprocal space is detected. Figure 3-8a displays an example image of a regular powder signal from the CeO<sub>2</sub> calibration powder sample used along with the analysis methods developed to take advantage of the wide angle of capture. Using an image transform program developed in IGOR, the powder signal of the standard was fit to calibrate the angular space of the image and then used to transform data from the sample. This way a wide in-plane angle could be integrated, with final intensity measured by peak fits of the resulting data as seen in Figure 3-8c. While this resulted in an integrated signal many times larger than with standard practices, it also allowed for long integration times. Similar to with film recording,<sup>90</sup> the diffraction pattern is recorded at each angle simultaneously, and significantly longer dwell times can be used over those of a scintillation detector. Typical dwell times on epitaxial samples for this study were 300 seconds, while some were many times this value. While it is difficult to place a lower detection limit for XRD, a recent study<sup>14</sup> at the same beamline (2-BM) using standard point detector powder diffraction methods reports detection of <0.2-0.4% volume fraction of Zr(Fe<sub>1.5</sub>Cr<sub>0.5</sub>)<sub>2</sub> second-phase particles in a Zr matrix measured well above the detection limit. The methods used here are estimated to increase sensitivity for dispersed powders and match this sensitivity for those that are highly textured.

Another use of this technique was in making detailed, although qualitatively indexed, reciprocal space maps. Defects in the crystal resulting in new features in reciprocal space were easily detected with this 2D probe of reciprocal space that could be missed using the point detector.

### **3.3 Spectroscopic Techniques**

#### **3.3a: X-ray Fluorescence Spectroscopy**

The previous sections have dealt with x-ray scattering techniques used in this work, where the elastic scattering process was used. Absorption processes were also very important for the study of these materials. One such interaction used extensively was x-ray fluorescence (XRF). This is a two-step process where an incident x-ray photon is absorbed by an atom, ejecting a core-level electron. The core hole is then filled with an outer shell electron whose lost energy leaves the sample as a fluorescence x-ray photon. The energy of the photon is then a finger print for the elemental species of the absorbing atom. Since the number of emitted photons is proportional to the number of excited atoms, fluorescence can be used to quantify the number of atoms and their elemental species in a sample. Their relatively low cross section when compared with charged particles allows much larger penetration depth with a minimum detection level down to a few parts per million.<sup>15</sup> Therefore, this technique was used for precise quantification of each sample's composition.

Due to the experimental setup used, XRF spectroscopy could be completed simultaneous to other diffraction techniques as slight changes to sample orientation do not affect the signal. As discussed above, the energy-dispersive detector itself was anchored to be at a constant orientation and distance with respect to the sample surface at any diffraction condition. One drawback of the technique, however, is that the x-ray penetration is much larger than the film thickness, making it difficult to distinguish the Ge atoms in the film from those in the Ge substrate. Therefore, sample characterization of Ge composition was successfully accomplished via one of two methods. For all

DMS samples in Chapter 4, Ge composition was found by measuring the Ge profile on the molybdenum sample holder used when depositing the film. In anticipation of this necessity, sample holders were thoroughly polished beforehand to remove deposition from previous samples as well as to limit any matrix effects from a rough Mo surface. Characterization of the Ge content of the ternary sample studied in Chapter 5 was accomplished through measurement of film thickness of the Ge 100 at.% apex via CTR analysis. The Ge deposition profile was then calculated from this value and location of the Ge zero-deposition line on the sample, which defines the bottom of the ternary triangle. This line was located by measuring discontinuities in x-ray diffraction features correlated with a plateau in the Ge signal of the more surface sensitive energy dispersive x-ray (EDX) spectroscopy in a scanning electron microscope (SEM).

Si fluorescence, on the other hand, was distinguishable from the Ge substrate but difficult to measure due to its small x-ray cross section and low energy. In fact, it could not be detected in air due to the additional absorption effects of Ar. Therefore, a helium environment was created around the detector and sample. In the 2-ID-E beamline, a plastic box with an x-ray port covered with kapton tape was used. To be flexible for diffraction measurements, a thin plastic bag was used at 2-BM, whose absorption was measured to be less than that of kapton tape. Even with these precautions, fluorescence yield of Si were  $\sim 100$  times lower compared with other elements used in this study. This necessitated taking separate spectra for Si quantification with long dwell times at a few strategic positions on the sample. For a ternary sample, this included finding the Si zero-deposition line and obtaining the Si profile gradient to, relying on the well known linearity of the deposition profile produced by the combinatorial MBE process.

Figure 3-9(a) shows an example spectrum of a  $\text{Co}_x\text{Mn}_y\text{Si}_z/\text{Ge}$  sample in a helium environment. Most prominent at mid energies are the Co and Mn  $K_\alpha$  (L-K shell transition) and  $K_\beta$  (M-

K shell transition) lines. The small peak at 1.74keV corresponds to the combined Si  $K_{\alpha,\beta}$  lines. At high energies the elastic peak at 10.5keV is present in the spectra along with a Compton shoulder.

Creating a large background is the Stokes phonon interactions of the substrate. The presence of this background, along with the Ge L lines at 1.2keV (seen only in He environments), reveals the physical boundary of the sample.

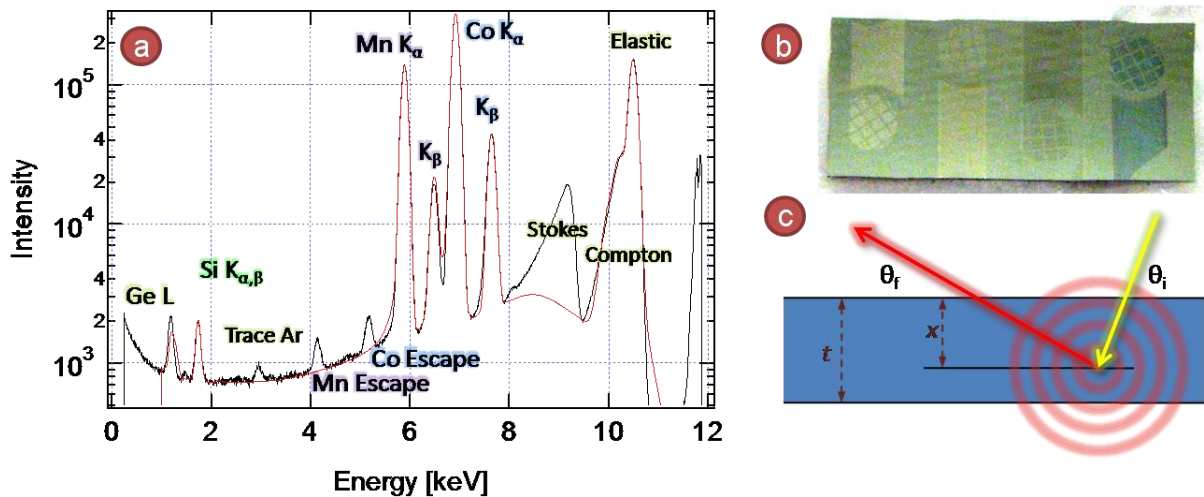


**Figure 3-9: (a)** Spectra from a  $\text{Co}_x\text{Mn}_y\text{Si}_z$  sample on a Ge substrate taken in a He environment to minimize Ar absorption from the air. Escape peaks are Si  $K_{\alpha}$  photons escaping from the Si detector element. Ge L and Stokes peaks are interactions with the substrate. **(b)** A typical calibration standard with four elements. The waffle pattern is from contact masks for profilometer thickness measurements. **(c)** Diagram of the incident and fluoresced photon path used to model matrix effects.

Although XRF has a very linear signal with composition, sub-percent level compositional precision and accuracy was necessary in some samples. Quantification of atom number for each element requires numerous correction factors<sup>15</sup> because each element has a different absorption cross section and x-ray fluorescence yield, for example. These values are well known, but others such as differing transmission coefficients through the air or various layers in the detector depend highly on environmental and detector conditions. Therefore, a set of calibration standards were carefully developed to eliminate these factors. Also grown via MBE, multiple samples were placed on one Si or Ge substrate in strips using the shadow masks. TEM grids acted as additional contact masks in order to have a sharp square wave deposition profile for accurate thickness

measurements. A typical calibration sample is shown in Figure 3-9(b). This profile was immediately measured by two profilometers – one stylus based, and the other based on interferometry, and a 20Å gold protective layer was then deposited over the entire substrate to limit oxidation. The XRF signals of these standards could then be compared with that of the epitaxial samples to quantify their composition without any vague correction factors as long as the data were taken with identical environments and geometry of the sample and detector. As described above, the SDD detector has count rate limitations. To avoid the use of beamline attenuators, the thickness of the standards were kept within an order of magnitude of the samples.

Once the raw XRF spectra are taken from each of the standards and the samples, several analysis steps are necessary to obtain a quantitative composition. First, each spectra is fit to a full quantum fluorescence model using an IDL-based program MAPS v1.6.3.0<sup>16,17</sup>. A typical fit is shown in Figure 3-9(a). Spectra from an entire sample were first summed and fit to refine the energy calibration and peak shape. Individual spectra were subsequently fit with intensities as the only open parameters, and the integrated intensity from the  $K_{\alpha}$  peaks is used in the calculation of compositions. Data from each element in the sample are transformed into nominal thicknesses  $t^0$  by the following equation.

$$t^0 = \frac{\tilde{I}_s n_c}{\tilde{I}_c n_s} t_c \quad \tilde{I} = \frac{I_{raw}}{I_1 \tau} \left[ \frac{\text{cts}}{\text{ph} \cdot \text{sec}} \right] \quad (3-10)$$

where  $n_{c,s}$  are number densities of the calibration standard and sample, respectively. In the case of the sample, this is known via structural measurements, while the bulk value for that element is used for the standard.  $I_1$  is the incoming flux seen in Figure 3-1 and  $\tau$  is the live dwell time (excluding detector dead time, which was kept below 15% of the total).

The concentration  $\eta$  in atomic percent is then calculated for each element  $i$  by

$$\eta_i = \frac{t_i}{t_{total}} = \frac{t_i^0 / \langle A_i \rangle}{\sum_j t_j^0 / \langle A_j \rangle} \quad (3-11)$$

where  $\langle A \rangle$  is the self absorption averaged over the film thickness, and  $j$  represents each constituent element in the matrix. Although using a standard removes many of the correction factors, matrix effects such as self absorption are present and must be removed from the signal for accurate results. Figure 3-9(c) shows how this effect is modeled. The incident x-ray comes in at  $\theta_i$  and Energy  $E_i$ , and leaves for the detector at  $\theta_f$  and Energy  $E_f$ , all of which are fixed and known. The absorption  $A$  then depends on the path length  $d$  in the following manner.

$$A = e^{-\mu \rho d} = e^{-x \left( \frac{\mu_l(E_i)}{\sin \theta_i} + \frac{\mu_l(E_f)}{\sin \theta_f} \right)} = e^{-Bx} \quad \mu_l(E) = \sum_j \mu_j(E) \rho_j \quad (3-12)$$

Where  $\mu$  and  $\mu_l$  are the mass and linear absorption coefficients, respectively, and are calculated using the Cromer Liberman theory.<sup>5</sup> The mass density  $\rho$  is calculated from the atomic structure and the uncorrected concentrations  $\eta^0$ . The expectation value is then

$$\langle A \rangle = \frac{\int_0^t e^{Bx} dx}{\int_0^t dx} = \frac{1 - e^{-Bt}}{Bt} \quad (3-13)$$

For the calibration standards, the correction is applied directly to the intensities as thicknesses are measured directly. Using this perturbative method to correct for matrix effects in the samples proved crucial to measure accurate compositions, especially in samples containing Si.

### 3.3b: Extended X-ray Absorption Fine Structure

The final purely spectroscopic technique in this work is used for examination of the element specific local structure within the crystal. It is a second order crystal effect that modifies elemental absorption and the resulting x-ray fluorescence. In this process, the photoelectron wavefunction interferes with itself as it scatters off neighboring atoms. This interference pattern can be seen superimposed on the absorption spectrum as a Fourier transformed set of harmonics as a function of increasing photoelectron energy. The absorption coefficient  $\mu(E)$  for a bare atom is a simple step

function at the characteristic absorption edge of an element, which is well modeled by Corner-Liberman theory.<sup>5</sup> In a crystal, however, these solid state effects cause oscillatory fine structure in  $\mu(E)$  above the step as seen in the data of Figure 3-10(a). By scanning the energy of the incident x-ray beam through the absorption edge of a constituent element in a material, these oscillations can be seen in the fluorescence yield, revealing the effect of extended x-ray absorption fine structure (EXAFS). The spectrum can be measured via monitoring the transmitted beam, taking advantage of the high count rate abilities of ion chamber detectors, but here, fluorescence is monitored instead due to beam extinction in the sample substrate.

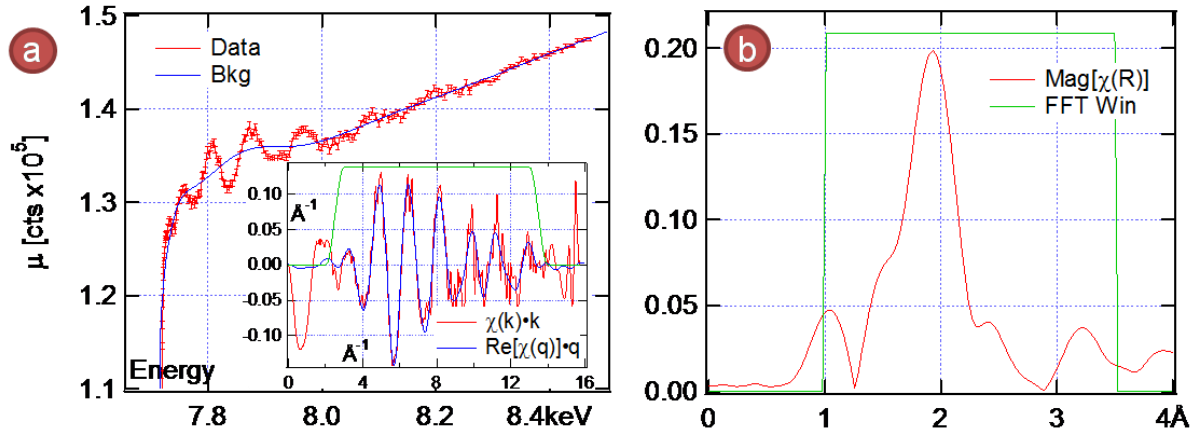


Figure 3-10: EXAFS data and processing in Athena (a) Data (Co XRF vs. energy) from a  $(\text{CoFe})_x\text{Ge}_{1-x}$  DMS sample and spline-fit background (bare atom absorption). Inset: Background subtracted data  $[\chi(k)]$  and reverse Fourier transformed data  $[\chi(q)]$ . Both are multiplied by  $k$  to emphasize high- $k$  features. (b) Fourier transformed  $\chi$  indicating positions and quantities of neighboring atoms. A Hanning window is used for both forward and reverse FFT.

To probe the local structure around the absorbing atom, only the fine structure  $\chi$  is necessary, so the bare atom absorption  $\mu_0$  is removed.

$$\chi(E) = \frac{\mu(E) - \mu_0(E)}{\Delta\mu_0(E)} \quad (3-14)$$

where the bare atom edge step height  $\Delta\mu_0$  is used to normalize the oscillations to one absorption event. The oscillations can then be plotted with respect to photoelectron wavenumber  $k$  as seen in the inset of Figure 3-10(a). The conversion from energy is



$$k = \sqrt{\frac{2m_e(E - E_0)}{\hbar^2}} \quad (3-15)$$

$E_0$  being the edge energy (when the photoelectron has no kinetic energy). This data can then be modeled using *ab-initio* calculations to the EXAFS equation.

$$\chi(k) = \sum_j \frac{N_j S_0^2 f_j(k) e^{-2k^2 \sigma_j^2 - 2R_j/\lambda_j(k)}}{k R_j^2} \sin[2k R_j + \delta_j(k)] \quad (3-16)$$

where  $N$  represents the coordination number of neighboring atoms with scattering factors  $f$  at distance  $R$ .  $S_0^2$  is the amplitude reduction factor from higher orbital electrons filling the core hole, which is element specific and is usually obtained from standards. The sum is over shells of atoms, or equivalently, scattering paths of the photoelectron, interfering with itself via a phase shift of  $\delta$ . Damping the fine structure oscillations are the Debye-Waller disorder determined by  $\sigma$  and the finite core-hole lifetime  $\lambda$ , limiting this technique to local structures of only a few atomic shells. More details of this theory can be found elsewhere.<sup>18</sup> Using this equation, a model structure can be fit to a data set to obtain local coordination number, elemental species, bond distance, and Debye-Waller disorder for potentially several atomic shells – each of these localities corresponding to a particular elemental constituent in the material under investigation.

Due to constraints involving the sample studied as well as the beamline used (2-BM) in this work, several extra steps were taken to ensure quality data. In doped magnetic semiconductor materials, the amount of dopant elements is very small, and therefore, count rates are lower than in bulk samples. Additionally, the bending magnet beamline has a lower flux than undulators typically used for this experiment. To improve measurement efficiency, each data set was taken with dwell times proportional to  $k$ , providing a more constant signal to noise ratio of the data. (This is not seen in the figure as separate segments are combined and count rate is normalized to the shortest dwell times for clarity.) Also, fewer separate compositions were examined than with other x-ray

techniques and all data was taken in an He environment to enhance the signal. Above the edge,  $k$ -spacing (or photoelectron momentum) rather than that of energy was used,<sup>19</sup> which reduced the number of data points needed in each set [Equation (3-15)]. This is because EXAFS features oscillate with respect to  $k$  as shown in Equation (3-16). Finally, multiple data sets were taken at each composition and monitored both for repeatability and sharp features caused by Bragg reflections from the crystalline sample as seen in Figure 3-11. As energy is varied through approximately  $\sim 1\text{keV}$ , so is the radius of the Ewald sphere. Eventually it will intersect a Bragg reflection, channeling much of the flux out of the crystal and resulting in a sharp dip in fluorescence or a sharp peak if the detector happens to be at the proper angle. For the most part, these features can be removed as their energy width is that of the monochromator  $\sim 1\text{-}2\text{eV}$  compared to tens of eV for the smallest EXAFS features. Although with lower signal to noise ratios, Bragg reflection identification and removal becomes increasingly difficult.

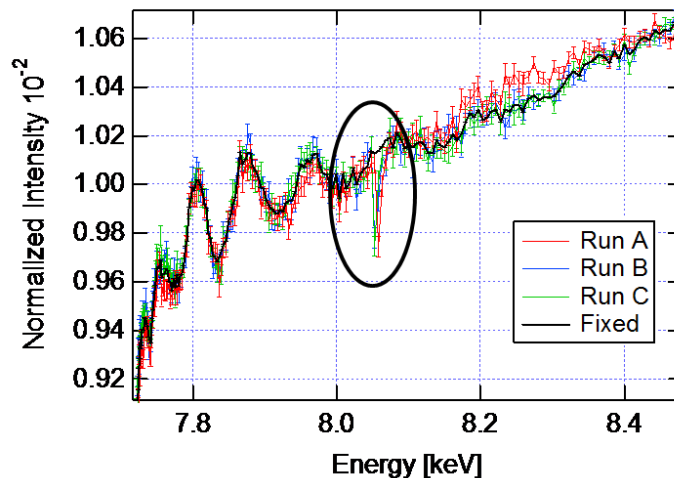


**Figure 3-11:** Example EXAFS data which is taken under multiple runs to increase statistics and judge data reproducibility. Shown in the black circle is raw data containing a non-EXAFS feature from a substrate Bragg reflection (red, blue, and green curves) that has been corrected and combined for EXAFS data analysis (black curve).

Data analysis was completed in two steps using software developed by Ravel and Newville.<sup>20-22</sup> Once raw data sets were combined and normalized, the data was processed by the software package ATHENA v0.8.054. This program removes the smooth background and completes

the Fourier transforms to arrive at  $\chi(R)$ , which is a complex function whose magnitude resembles several peaks as a function of distance from the central absorber. Apart from the  $\delta$  phase shift in Equation (3-16) this is the pair distribution function of that element's local structure [Figure 3-10(b)]. EXAFS theories were then modeled and fit based on the EXAFS equation and the *ab-initio* FEFF8 code in ARTEMIS v0.8.011. This technique is only element specific, and there exists the possibility of the same element occupying different sites in the lattice. In this case, EXAFS data from one element will be a superposition of several local environments, and therefore, multiple EXAFS theories were fit to each data set to obtain good reproduction of the data. By comparing the relative strengths of the peaks in each theory, the proportion of site occupancies were determined, allowing both features of the local atomic structure to be probed and statistical measures of these features prevalence in the crystal.

### 3.4 Anomalous Diffraction

The types of techniques discussed thus far involve either elastic scattering or absorption of an x-ray. A final technique used in this thesis combines both of these interactions, allowing for sensitivity to atomic structure and chemistry. In particular, the procedures used to implement this technique and the methods developed to analyze the data provide a quantitative measurement of element-specific site occupancy within the crystal studied. Here the data collection, processing and modeling are described in detail. In Chapter 5, full spectrum fitting analysis on this data using the model is discussed along with results and its implications.

#### 3.4a: Data Collection and Processing

The anomalous x-ray diffraction technique involves diffraction as a function of incident photon energy through a characteristic absorption edge of an element, in order to gain additional sensitivity to the crystalline structure with multiple constituent atoms. To obtain the diffraction intensity as a function of energy, the Bragg reflection was first located in reciprocal space via in-

plane and out-of-plane scans. Following this, the diffractometer was set to the observed peak position of the reflection, and the energy was scanned while the diffractometer was continuously adjusted to maintain a constant magnitude of the momentum transfer wavevector ( $q$ ). With the completion of each energy scan, the momentum transfer position in reciprocal space was confirmed by additional in-plane and out-of-plane scans to assure the diffractometer was at the peak of the Bragg reflection throughout the scan. Simultaneous to each energy scan, the x-ray fluorescence was also acquired using the SSD energy-dispersive detector. This allowed for EXAFS data to be taken along with the diffraction data as seen in Figure 3-12. The data were later used to calculate the anomalous correction factor  $f''(E)$  of Equation (3-4) as it is related through the optical theorem and finally  $f'(E)$  through Kramers-Krönig relations. These atomic form factors were used in the full spectrum analysis rather than those calculated by Cromer and Liberman<sup>5</sup> because the solid-state perturbations causing the fine structure in the atomic form factors affect the anomalous diffraction behavior above the absorption edge as can be seen in the diffraction data in Figure 3-12. Fluorescence background in the diffraction signal was also measured (with the point detector) by positioning the diffractometer away from the Bragg reflection and conducting a full scan. This background was then subtracted from the measured diffraction data at each edge leaving just the anomalous diffraction signal.

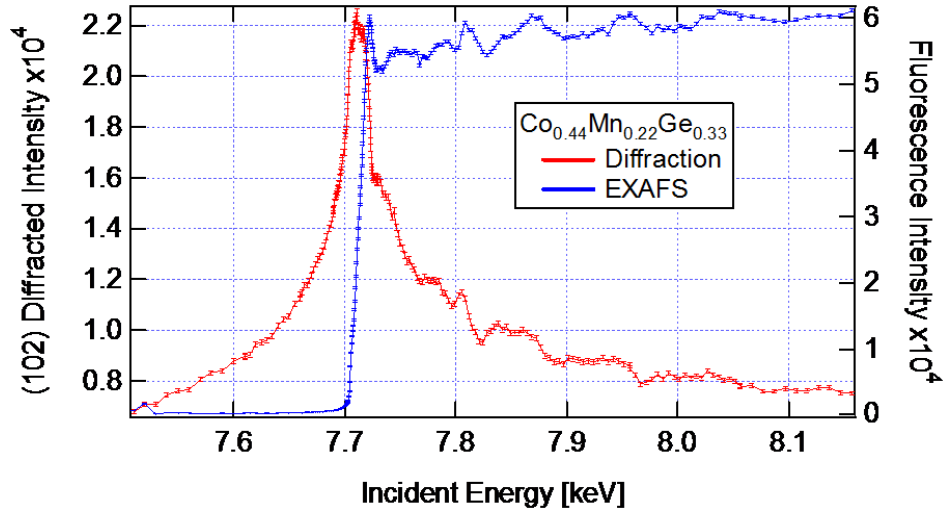


**Figure 3-12:** Anomalous diffraction (red curve) and EXAFS (blue) taken simultaneously via the NaI point detector and the SSD detector, respectively. The fine structure in the diffraction is due to the connection between the atomic scattering factors and absorption (the optical theorem of quantum mechanics).

For full spectrum analysis, this data was taken at each  $K_\alpha$  elemental absorption edge of the material and at each unique Bragg reflection of the material's crystal structure. As the width of the Bragg reflection in reciprocal space does not change significantly with energy, rocking scans for each data point were not necessary to obtain the integrated intensity. Instead, in-plane, out-of-plane and azimuthal ( $\phi$ ) scans were taken at each reflection and key energies, where their integrated intensities from Voigt peak fits (Figure 3-13a) were used to scale each anomalous dataset to one continuous spectrum for each reflection (Figure 3-13b).

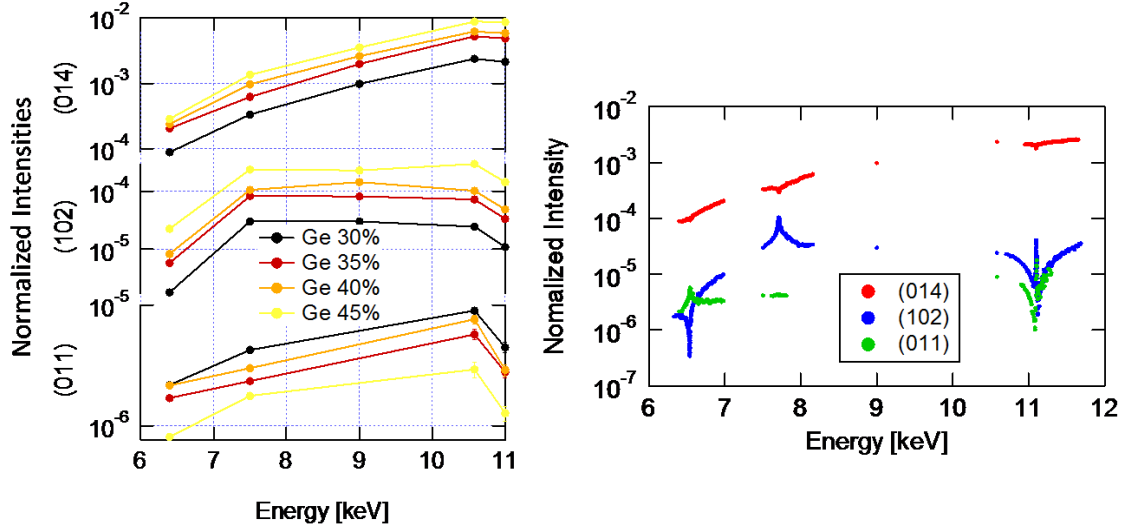


**Figure 3-13: Data assembly of full spectrum anomalous diffraction for three unique reflections in the Ge Heusler alloy. (a) Integrated intensities from out-of-plane scans at four compositions (values of  $x$ ) in  $(\text{Co}_{0.5}\text{Mn}_{0.25})_{1-x}\text{Ge}_x$  used to scale the anomalous diffraction. (b) Scaled and assembled dataset for three Bragg reflections at the composition  $(\text{Co}_{0.5}\text{Mn}_{0.25})_{0.7}\text{Ge}_{0.3}$ .**

### 3.4b: Modeling

As noted in Section 3-2a, measured photon counts from the detector can be directly linked to diffracted intensity for quantitative analysis. In this case, several experimental factors must be accounted for, expanding Equation (3-1).

$$I_m(\mathbf{q}, E) = I_0(E) \left| \sum_n [f_n^0(\mathbf{q}) + f_n'(E) + i f_n''(E)] e^{i\mathbf{q} \cdot \mathbf{r}_n} \right|^2 A(\mathbf{q}, E) \cdot R(\mathbf{q}, E) \cdot D(\mathbf{q}) \cdot T(\mathbf{q}) \quad (3-17)$$

Here,  $A(\mathbf{q}, E)$  is the self absorption as discussed in Equation (3-13) where  $B(\mathbf{q}, E) = \frac{2\mu(E)t}{\sin \alpha(\mathbf{q})}$  ( $\alpha$  is the angle between the incident beam and the sample surface).  $R(\mathbf{q}, E)$  is the resolution function discussed in Section 3.2b,  $D(\mathbf{q})$  is the Debye-Waller disorder factor, and  $T(\mathbf{q})$  is the film thickness correction. The apparent thickness involves the same correction for the thickness in  $B(\mathbf{q}, E)$ :  $T(\mathbf{q}) = 1/\sin \alpha(\mathbf{q})$ . Inside the modulus squared is the structure factor [Equation (3-3)] with anomalous correction factors discussed above. Finally,  $I_0(E)$  are other instrumental effects such as x-ray attenuation through the air and other beamline components in addition to energy dependence of the ion chamber detectors' sensitivity to the incoming x-ray flux. This factor varies only with

energy and can be modeled using a linear amplitude function over short energy ranges (<1keV). However, in the full spectrum analysis, this factor was eliminated altogether by using the intensity ratios of two anomalous diffraction data sets.

**Resolution Function:** As discussed above, the resolution function is a volume that comes from three primary sources. In two directions this function is well defined by the detector slits, opening a window on the Ewald sphere. The third direction is a combination of the other two sources, the incident beam divergence and the energy spread of the beam, which due to their Gaussian distributions, effectively “blur” the Ewald sphere (see Figure 3-4). All three were known for this experiment, but because the latter two are nearly an order of magnitude smaller than the former and their effect on measurement is nearly constant throughout the experiment, they were not included in the correction factor.

The measured intensity is actually a convolution of the diffracted intensity with the instrumental resolution function. However, in this experiment, there is a separation between a Bragg reflection’s integrated intensity and its size in reciprocal space. Here, the chemical ordering determines the energy dependence of the reflection’s intensity, which is the parameter to be measured. The size of the reflection is not affected and was measured to be constant for compositions containing different amounts of chemical disorders. The resolution function, on the other hand, is convoluted with the size of the reflection. Therefore, these two aspects of the diffracted intensity can be separated into the terms seen in Equation (3-20) with the chemical information residing within the magnitude squared term. The resolution function was modeled in the following form:

$$R(\mathbf{q}, E) = \int d^3\mathbf{q}' \mathcal{R}(\mathbf{q}', E) \frac{d^2\sigma(\mathbf{q} + \mathbf{q}')}{d\Omega dA} \quad (3-18)$$

where  $\mathbf{q}'$  is the deviation from  $\mathbf{q}$  due to the detector slit function  $\mathcal{R}$ . The term  $d^2\sigma/d\Omega dA$  is the intrinsic differential scattering cross section of the Bragg reflection whose integral has been normalized to one, leaving only the size information. By knowing the diffraction geometry, beam energy and slit spacings,  $\mathcal{R}(\mathbf{q}', E)$  is known. In a typical XRD experiment, the size information of the reflection is found through reciprocal space scans in three directions (e.g. in-plane, out-of-plane, and azimuth). However, these are the convoluted widths and cannot be used to accurately describe the widths of the differential scattering cross section. Instead, an intensity-normalized Bragg reflection was modeled for  $d^2\sigma/d\Omega dA$  to obtain  $R(\mathbf{q}, E)$  which was, in turn, fit by hand to actual scans normalized to their peak intensities.

The model used was a 3D Lorentzian with two FWHM parameters ( $\Delta h = \Delta k$  and  $\Delta l$ ) for the Bragg reflection. The detector slit function was modeled as a 2D grid of points in lab space and transformed into reciprocal space, the details of which are shown in Appendix A of Reference 6. Examples of the intersection of the detector slit function at the center of the Lorentzian are shown in Figure 3-14 (a-c) for different positions  $(h, k, l)$  of the Lorentzian. For the specular reflection (003) the intersection is symmetric, whereas the two in-plane reflections are intersected by the slit function in an asymmetric fashion. Due to wider horizontal slits used in the experiment, scans in some directions of reciprocal space show higher sensitivity to the detector slit function than others. Figure 3-14 (d-h) shows these very different behaviors for scans of two different reflections. The scans shown in each window are from four different compositions whose shape is constant. The model, using one set of width parameters, is able to reproduce the shape of each type of scan on each reflection. Others, not shown here, are reproduced equally well. The final window, Figure 3-14(i), shows three model results of varying vertical slit spacing scaled to three data sets with just one scale parameter. Here, changing the slit spacing by a factor of 2 and 4 changes the peak intensity by the same amount seen in the data. If the widths of the modeled Bragg reflection were



off from those of the true reflection, the intensities would not scale correctly with the data. The slightly incorrect shape of the model in Figure 3-14 (d) and (i) are due to the model not including CTR interference fringes. All of the models shown use the same parameters, yielding fit values of  $\Delta h = \Delta k = 0.005(1)$  rlu (reciprocal lattice units) and  $\Delta l = 0.055(3)$  rlu. As the integrated intensities of the out-of-plane ( $L$ ) scans were used to scale the anomalous diffraction data,  $L$ -scans produced from this model were integrated and used for the resolution factor in Eq. (3-17).

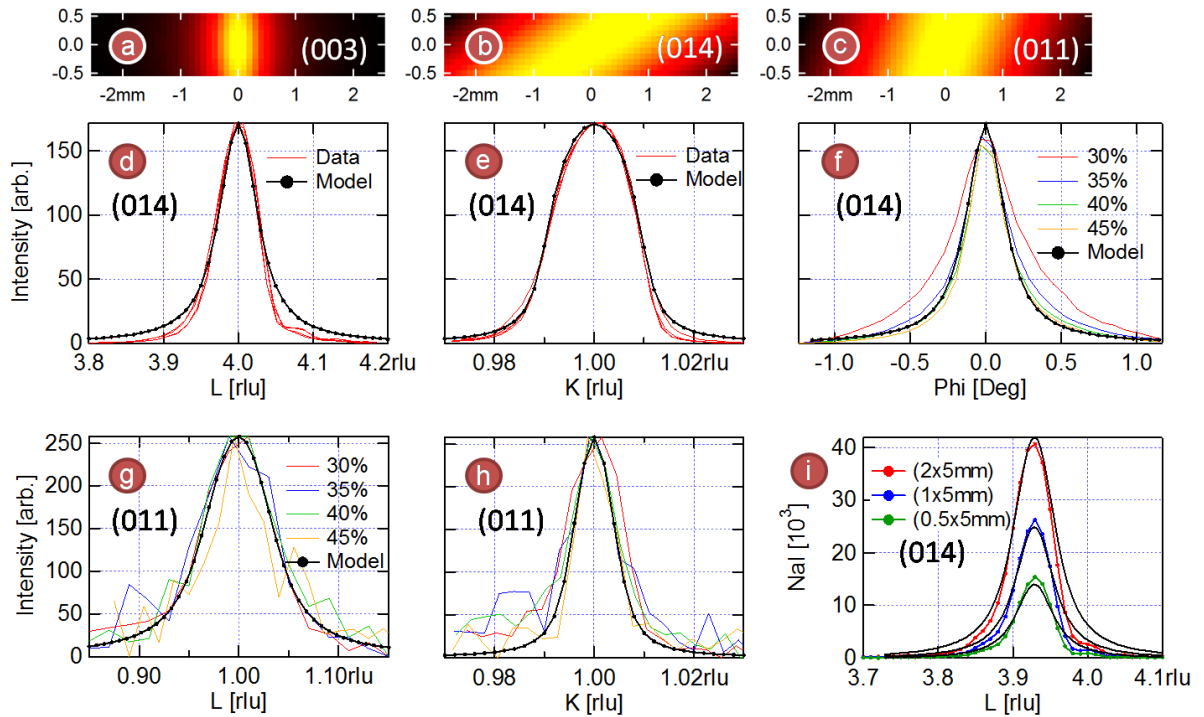


**Figure 3-14: Modeling and fitting the instrumental resolution function.** (a)-(c) Modeled intensity distribution within the detector slit function at specific points in reciprocal space. (d)-(f) Comparison of model to normalized data of out-of-plane, in-plane, and azimuthal scans, respectively, of the (014) reflection. Each contains four datasets taken at the same energy but different compositions. Percentages in the legend of (f) represent  $x$  in  $(\text{Co}_{0.5}\text{Mn}_{0.25})_{1-x}\text{Ge}_x$ . (g)-(h) are the same model and data for out-of-plane and in-plane scans, respectively, of the (011) reflection. (i) Model and data to scans of the (014) reflection with varying vertical slit spacing.

**Debye-Waller Factor:** Because the Debye-Waller factor is an exponentially decaying function of the magnitude squared of the momentum transfer [Equation (3-7)], it was measured by comparing the integrated intensities of scans from multiple orders of the same Bragg reflection.

The variance parameter in the Debye-Waller factor could then be extracted using the following equation:

$$\sigma = \frac{\ln(I_0 / I_1)}{(q_1^2 - q_0^2)} \quad (3-19)$$

where the integrated intensities  $I_n$  are corrected for the other factors in Equation (3-17). To calculate this factor, two pairs of reflections were measured for all compositions studied.

### 3.5 Combinatorial X-ray Methods

Although the several x-ray techniques used in this work comprised of a thorough probe into the state of a material, the combinatorial samples investigated made necessary a complex set of precautions and procedures for successfully probing the changing material's properties across these samples. These "combinatorial methods" involved careful considerations of beam size and position on the sample, as well as scanning techniques to systematically study the material's properties evolution in a meaningful way.

#### 3.5a: Beam Footprint

Particularly difficult was the task of keeping the illuminated portion of the sample confined to a quasi-uniform composition on the film. As a sample's compositional distribution is typically ~1cm across, a maximum beam spread of 50 $\mu$ m on the sample is required for the desired minimum of 0.5 at.% probe precision. With a beam typically focused to just 6 $\mu$ m across in either direction, this requirement would seem fulfilled except when one considers the nature of sample orientation with respect to the beam. Because diffraction geometry requires the beam to make an angle with the surface other than that of the normal, the beam footprint on the sample will naturally grow. With particular reflections of interest in this study, the angle of incidence  $\alpha$ , where  $\sin \alpha = \sin \theta \sin \chi$ , can be as small as 3.5° causing the beam to spread well beyond 50 $\mu$ m. Diffraction conditions for a reflection in a single crystal also often require a specific azimuthal angle which could

cause the beam to straddle key features such as phase changes in a crystal. This can be counteracted on a binary sample by carefully choosing the reflections to study.

Figure 3-15 shows the calculated FWHM intensity of the beam footprint on a binary sample for several reflections of interest. Because the composition gradient on such a sample exists only in one direction, the beam spread is free to be large in the direction perpendicular to this. Specifically, the  $(1\bar{1}1)$  reflection was of interest in crystallographic studies; however, as shown in the figure, such a reflection causes undesired spread along the composition gradient. By considering the different diffraction conditions required by a set of reflections in the same family, one containing a spread perpendicular to the gradient direction was chosen such as  $(\bar{1}11)$ . Another possibility is to choose a higher order reflection such as  $(113)$ , which contains a minimal footprint but often offers less intensity due to its higher order. If intensity is not an issue, this is an ideal candidate for a ternary sample, which has a gradient in both directions. This reflection, however, was found to lack diffraction intensity in some cases due to particular disorders in the atomic structure. The solution was to grow a sample whose composition spread contained only a portion of the entire phase diagram, thus relaxing to some degree the size requirements on the footprint for such ternary samples.

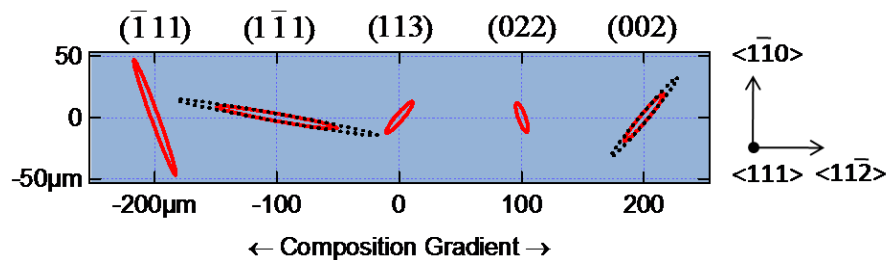


**Figure 3-15:** Beam footprint comparison on a binary sample on a  $\langle 111 \rangle$  substrate (blue rectangle shrunk  $\sim 20\times$ ) with a red ellipse demonstrating the extent of the beam-sample intersection (FWHM intensity) when focused to  $6\times 6\mu\text{m}$  size. The three reflections on the left are of the same family. The black dotted ellipses are models with horizontal defocusing to  $10\mu\text{m}$ . All are  $60^\circ$  twinned reflections used to avoid those of the substrate.

A final difficulty was in keeping a constant size and position of the incident beam. Because the KB focusing optics involved holding a precise mechanical force on two mirrors and because the focused size desired was near their maximum capability, there existed a real possibility of beam movement or focus relaxation. The black dotted ellipses in Figure 3-15 demonstrate this possibility with the horizontal mirror relaxing to a beam size of 10 $\mu$ m or a beam movement in either horizontal direction of just 2 $\mu$ m. Due to its larger size and the non-symmetric gravitational force from its orientation, the horizontal KB mirror had particular difficulties in creating a stable focused beam. Additionally, the diffractometer's sphere of confusion could cause the position of the sample surface be slightly different with differing diffraction geometries. Therefore, a critical component of any scan was to periodically measure and correct beam size and position as discussed in Section 3.1c.

#### 3.5b: Beam Position Reproducibility and Combinatorial Scans

Much of initial work involved development of methods to reproducibly position the x-ray beam at the same point on the sample for multiple measurements. Diffractometer sphere of confusion, slight sample mismount, and even sample surface miscut played a role in apparent sample movements at different diffraction conditions in addition to beam movement from KB mirror relaxation. A robust method for reproducibility in beam position was also desired to successfully complete multiple experiments on the same sample during different runs at the APS or at different beamlines.

Initially, sample boundaries or random fiducial marks were utilized to recognize and correct for differences in beam position on the sample. However, these features were found to either change morphologically with sample orientation (sample edges) or disappear altogether (random fiducial marks). In ternary samples, therefore, ~8 crosses were scribed into the film after deposition as discussed in Chapter 2. These crosses were then be imaged by either XRF from lack of material or

XRD owing to damage in the crystal. And because they represented a purely surface feature, their morphology remained constant with angle to the x-ray beam. An example of XRF maps of the crosses are shown in Figure 3-16. The precise location of the crosses were measured by determining the intersection of two perpendicular lines placed along the cross arms by hand. Because crosses on a particular sample all had the same orientation, lines with the same slopes could be used for all crosses, enhancing the precision. Additionally, with low signal or blurred cross arms due to grazing incident angle, the center could still be located due to this common orientation. Cr1 and Cr4 are taken with a 10 $\mu$ m resolution which at 0.2sec dwell time required ~30minutes per scan due to the large overhead from the xy positioners. Cr6 in Figure 3-16 was taken with 20 $\mu$ m resolution requiring only ~5 minutes. Under ideal conditions shown in Cr1 and Cr4, crosses could be located to within 2 $\mu$ m, expanding to ~5 $\mu$ m in poor conditions or low resolution (Cr6).

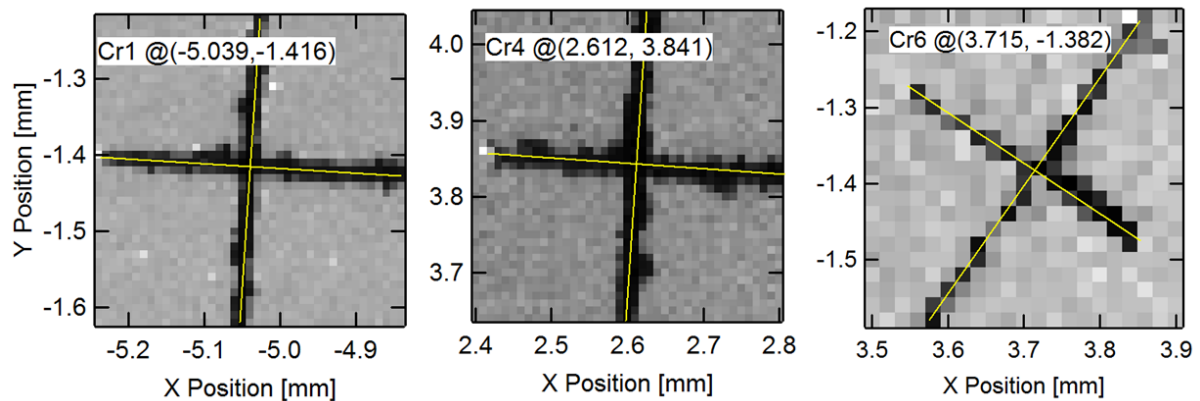


**Figure 3-16: XRF maps of three crosses scribed onto a ternary combinatorial sample using the Co fluorescence channel with dwell times of 0.2sec per pixel. Cr1 and Cr4 are from the same sample. Analysis of these crosses are shown, locating their position to a precision of a few microns.**

In the different sample orientations of crystal reflections, these crosses were observed to move to a degree larger than the desired composition resolution. Therefore, using these cross positions, linear transformations were made to allow for repeatable beam positioning down to a few microns on the sample. A transformation matrix could be constructed by solving the overdetermined linear system.

$$\begin{bmatrix} Cr1_x & Cr1_y & 1 \\ Cr2_x & Cr2_y & 1 \\ \vdots & \vdots & \vdots \\ CrN_x & CrN_y & 1 \end{bmatrix} = \begin{bmatrix} Cr1'_x & Cr1'_y & 1 \\ Cr2'_x & Cr2'_y & 1 \\ \vdots & \vdots & \vdots \\ CrN'_x & CrN'_y & 1 \end{bmatrix} \times \begin{bmatrix} A \cos \theta & B \sin \theta & 0 \\ -A \sin \theta & B \cos \theta & 0 \\ dx & dy & 1 \end{bmatrix} \quad (3-20)$$

where  $Cr1_x$  represents cross 1 x-position on the sample motors. Translations are represented by  $dx$  and  $dy$  whereas  $\theta$  allows for rotation.  $A$  and  $B$  allow for linear stretching or contraction of sample space correlating with a slight miss-orientation of the sample surface normal to that of the positioning stage. Once the transformation matrix was created using the crosses, all other features were then corrected using this matrix. Figure 3-17(a) shows several sets of these crosses with one set (crosses for the XRF compositional measurement) already transformed along with the transformed data it represented (compositional contours) into the position space of another [(022) diffraction orientation]. When transformed, the beam positions were reproduced to within 5 $\mu$ m even when data was taken at separate beamlines (as in the provided example). Therefore, these crosses were located for each diffraction geometry both before and after a combinatorial scan (defined below) along with the beam size measurements.

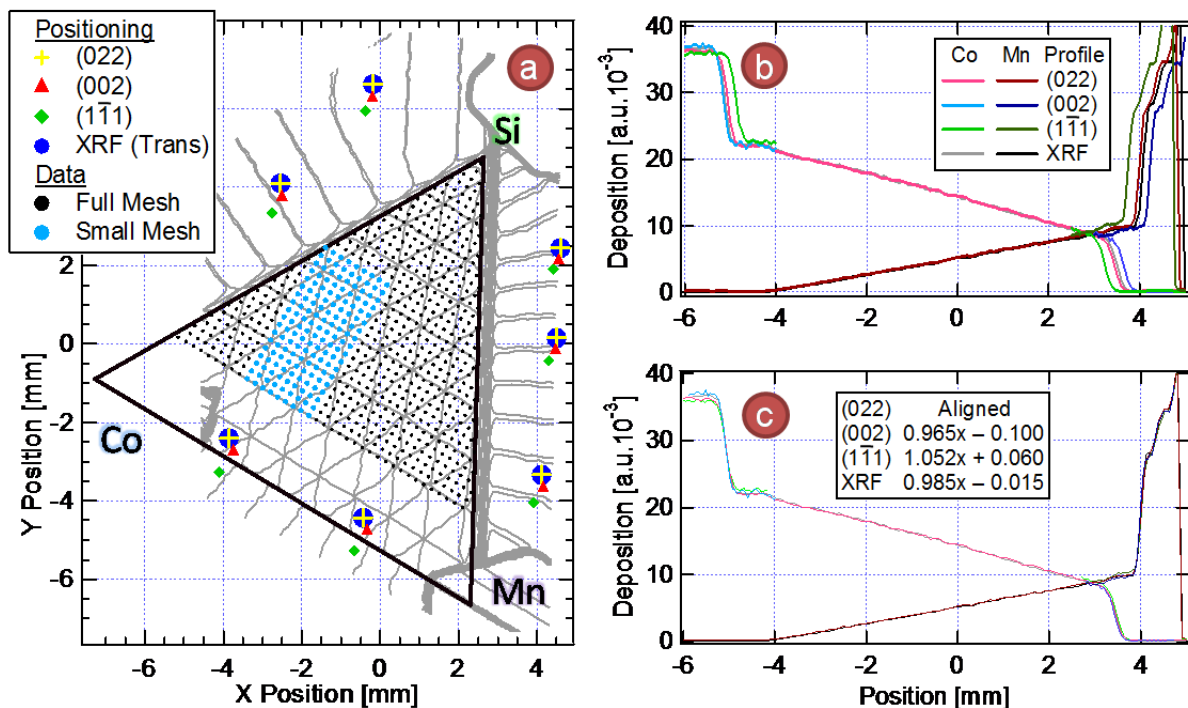


Figure 3-17: Beam positioning and combinatorial scan setup. (a) Cross positions on a ternary sample are shown for four different experiments (yellow, red, green and dark blue symbols) with a transformation applied to align one scan (XRF-dark blue circles) with one of the others (yellow pluses). Grey XRF (composition) contours are 5 at.% compositional increments. Several combinatorial mesh scan positions are also shown (black and light blue circles) aligned with the composition contours. (b) as taken and (c) aligned XRF profiles on a binary sample, which are used to align the various data sets.

Similar steps were taken and positional precision attained for binary samples with use of thickly deposited pads on either end of the sample as shown in Figure 3-17(b) and (c). Here, a much simpler process of aligning the measured pad positions from XRF data taken during various experiments involved applying linear transformation equations on the measured positions.

Combinatorial scans consisted of a set of repeated individual experiments at each unique location on the sample to systematically probe the parameter varied across that sample (created by combinatorial MBE techniques discussed in Chapter 2). On a binary sample, it is rather simple to create a set of scans that linearly travels across the composition gradient present on samples studied in this work. However, a ternary sample requires a mesh of positions to be scanned on a region of interest that is often not rectangular, yet a regular mesh is best for ease of analyzing the

data and creating compositional maps. Therefore, a grid of positions was created on the sample constrained to be both within the often triangular region of interest and along a meaningful axis of composition by complex macros written in the language of the beamline control program SPEC. An example is seen by the black dots in Figure 3-17(a) whose rows are aligned with constant Si compositions rather than the axes of the sample positioning stage and yet stay within the ternary region of interest. Because the control program had connections to any of the more than 80 beamline motors, attenuators, monochromator, detector control programs, etc., automated macros were written to both create a complex grid of sample positions and run sets of intelligent scans based on detector feedback. For example, with high resolution scans, any changes in the substrate crystallographic orientation (slight substrate bending from film strain for instance) could be corrected by a tailored set of alignment scans at each position across the sample. This would allow for the potentially several thousand scans to be taken under identical conditions, corrected for instrumental effects, and significantly shorten the time needed to run such a large scan by hand.

### **3.6 Data Processing and Exploration**

As programming complex SPEC macros provided a rapid way to systematically acquire combinatorial data, comprehensive software was needed to rapidly assemble and explore that data. The data acquisition program stores all information in a large ASCII file with header information for each scan containing most of the various beamline readouts, in addition to the scan data from all detectors and pertinent positioners. This complexity requires specialized decoding software for interpretation. Assembling a multidimensional data set from many single scans also can be a tedious process in a large series or mesh. In such a series, multiple types of scan are taken at each position potentially including alignment scans, multi-segment/multi-attenuator scans, or multi-dimensional XRD scans. Each of these must be selectively chosen and assembled. Furthermore, the compact 24/7 time constraints imposed at a synchrotron facility make an experiment with periodic



down time impossible, yet a moderate level of analysis must often be completed on a large survey-type mesh scan before decisions on the next experiment can be made. For example, phases and phase boundaries must be established in a new ternary system before new sample and reciprocal space regions-of-interest can be identified for the next experiment. Therefore, to complete a comprehensive study on a combinatorial sample, fully automated data processing and analysis software was developed in this work.

### 3.6a: Import Spec Data v2.1

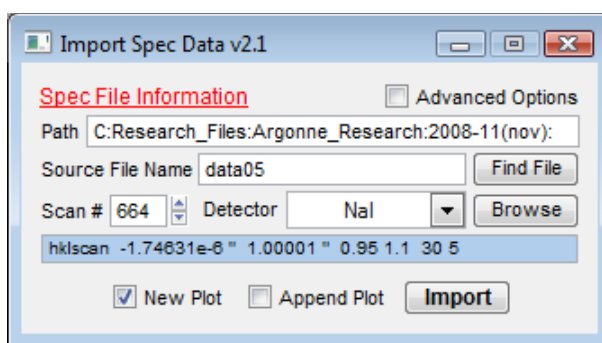


**Figure 3-18: Simplified Import SPEC Data panel used to browse and import single scans for review, which includes a “Browse” window to list and select scans of interest (not shown).**

At the start of work at the APS, SPEC decoding software in the form of simple file I/O macros existed for the IGOR analysis software platform. This platform includes an enhanced compiled language based on C, and contains multi-dimensional data handling and analysis capabilities, which was used to create a GUI-based program *Import SPEC Data* (ISD) to handle the data assembly and processing. Initially, it is desirable to check individual scans and/or browse a scan file to locate a particular scan. Figure 3-18 shows the simple ISD panel used to locate a file (using OS dialog boxes), browse the scans taken, and import and plot the desired scan. Used most often, the advanced options panel is shown in Figure 3-19(a). By selecting the appropriate boxes in the Data Structure section, multiple scans can be assembled. Options used most include a single multi-segment scan (with multiple scans to link in the Scan Pattern section), 1D trend scans (monitoring a beamline component as a function of scan number), 2D ‘line scans’ (usually comprising of a diffraction scan

and motor positioner as the independent variables), and 3D mesh scans. In addition to quickly assembling a complex data set once acquisition is completed, a critical use of this program was to monitor progress of such an experiment *during* data acquisition to ensure data quality and correct acquisition procedures.

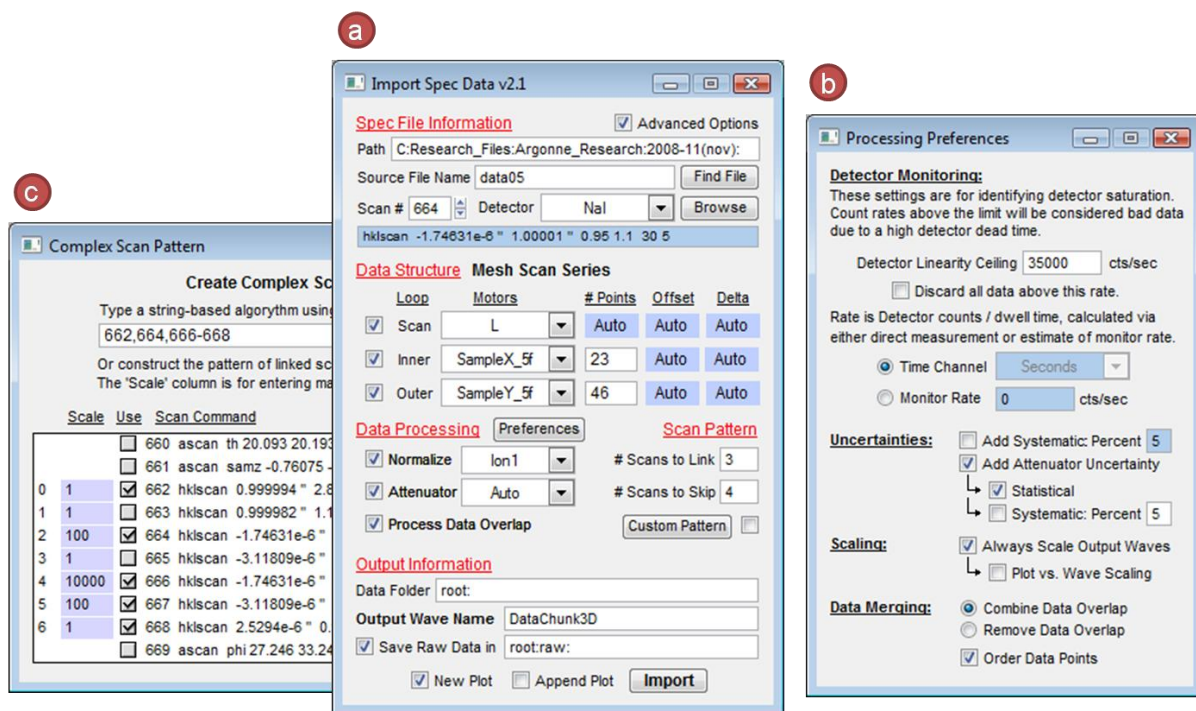


**Figure 3-19: Advanced panels of Import SPEC Data. (a) Main expanded panel is setup to assemble and process a mesh scan. (b) Processing preferences for ISD include monitoring the detector rate to judge data quality as well as preferences on how to assemble a separate uncertainty data set. (c) If a more complex scan pattern is required (often when needing to link a few scans taken by hand), this panel is used to create whatever scan pattern is necessary.**

Data processing was just as critical as a primary function of the program. The normalization to a second detector or “monitor” channel and calculation of uncertainties based on detector statistics were standard procedure. Also important was the process of correctly linking scans. An attenuator channel was included with each scan and could be used to scale a dataset; however, the constant value given for each filter was based on the measured filter foil thickness and did not include energy considerations. Therefore, intelligent attenuation calculation subroutines were written to correctly merge data, which involved recognizing data overlap and determining the best

data to use in calculating a scale factor. Since detector data is given in photon counts, good statistics are required to calculate an accurate factor. Each detector also has increasing dead times with count rate, and subroutines in ISD were written to monitor this as well. Figure 3-19(b) shows various preferences on how this rate is monitored and what actions are taken. If data overlap is unsuitable for automated merging, a manual mode is possible. These can be entered in the Complex Scan Pattern panel shown in Figure 3-19(c). In addition to manually entering scale factors, a customized scan pattern can be constructed through check box selection or text algorithm, bypassing the simple two-step pattern in the main panel. Figure 3-19(a) shows an example setup to assemble L-scans in a 23x46 x/y mesh. Three scans are to be combined and then four (alignment scans) skipped at each position in the mesh. Data will be normalized to  $I_1$ , each link scaled appropriately by intelligent attenuator calculation, and overlapping data combined. The data is set to output to a 3D data array named "DataChunk3D", with raw data from each scan also saved.

### 3.6b: Peak Analysis v1.2

Once the data was assembled and processed, exploration and peak fitting was completed in the *Peak Analysis* software package also written specifically for these studies. Figure 3-20(a) shows the main panel, where 1-3 dimensional data in the format created by the ISD program can be loaded, navigated, fitted, and plotted in a variety of interactive ways. Navigation fields act as readouts as well as inputs, but the DataMap panel (Figure 3-20b), is most often used for navigation for high dimensionality data. ISD creates an initial data map for each dataset, but subsequent maps of fit parameters can be easily substituted. The power of the DataMap panel is in the two interactive cursors which, connected by a dotted line, define where the program will slice the data to be displayed in a variety of panels, some of which are shown in Figure 3-21(c). These live updating panels were used to explore qualitative characteristics of the data. The example shown is a 3D dataset sliced where two competing crystallographic phases occur in the sample as evidenced

by two peaks near each other in reciprocal space along the L direction. One of the peaks being located near an integer value of L suggests a similar lattice spacing to that of the substrate. The fit image shows good reproduction of this data except where the two phases disappear and a third begins just outside of the data window. For a more quantitative comparison, fit parameter trends can also be live plotted with the cursors. As these windows contain actively updated data arrays, copy buttons are included to create a separate frozen copy of the data for lab book recording or later publication.

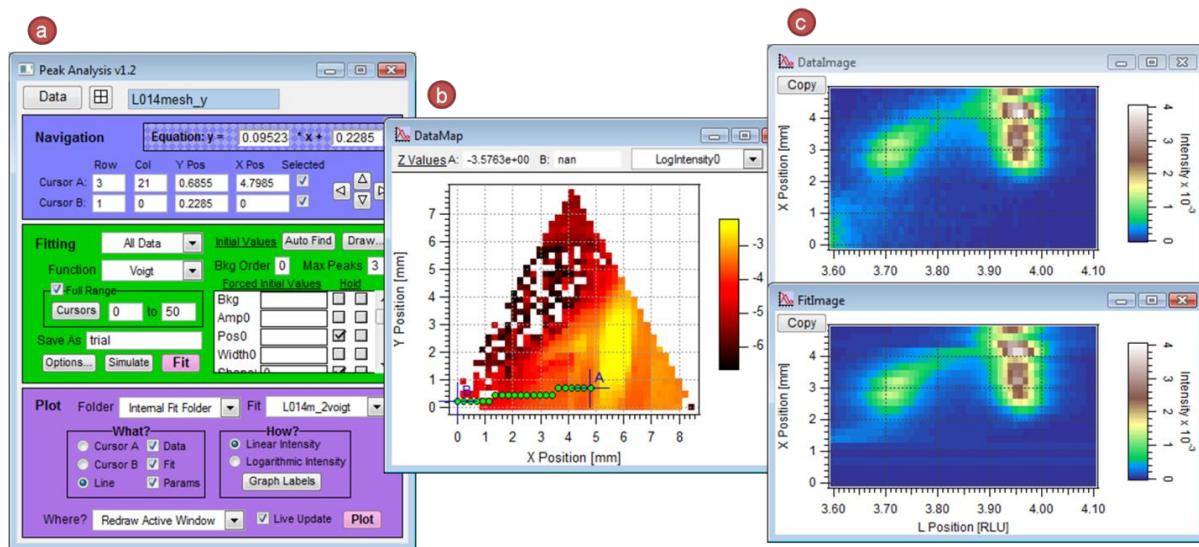


**Figure 3-20: (a) Peak Analysis main panel containing three main functions of data navigation, fitting and plotting on 1-3 dimensional data. (b) For 2D and 3D data sets, a data map panel is created with live tools to interactively slice through the data. (c) Live updating slices of the data and fit in image format. Fit parameter trend panels also can be displayed live (not shown).**

*Peak Analysis* multippeak fit routines were developed specifically for the XRD-type data taken in this work. To this end, Gaussian and Voigt (convolution between Gaussian and Lorentzian) peak functions with polynomial backgrounds were programmed to use the Levenberg-Marquardt iterative reduced chi-squared fitting routine provided by the IGOR analysis platform. To aid in the analysis of large datasets, fully automated subroutines were written to search for peaks, do error correcting fit routines, and intelligently determine a fit's success in reproducing the data with physically correct parameters. Much emphasis was devoted to peak finding routines, which used

smoothed differential algorithms to identify any number of peaks in one dataset up to the maximum specified by the user. Noise level estimates, relative estimated peak intensities and widths, and peak shoulder detection were employed to ensure detection of all real peaks to produce a stable fit result. Figure 3-21(a) shows an example of a dataset containing two peaks successfully found and fit by the automated routine whose distance is well below Raleigh's criteria, requiring little to no manual work necessary to complete initial analysis stages on large datasets and reducing the time required for such an analysis to a matter of minutes after the completion of data acquisition.

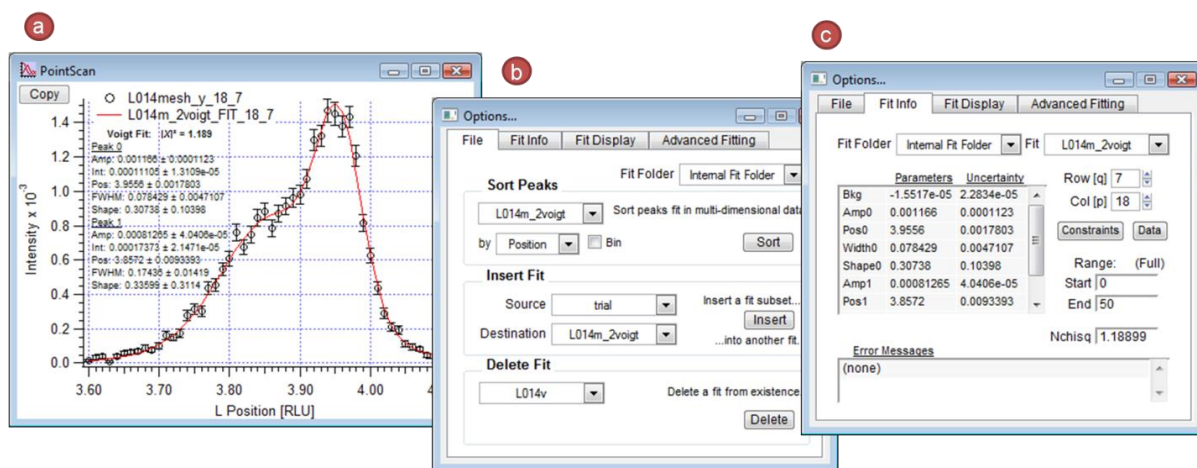


**Figure 3-21: (a) PointScan panel which interactively displays one scan for review or fitting. The case of high sensitivity to automated peak finding routines is demonstrated where a shoulder has been automatically detected and fit. (b) File Options panel allowing organization of fits such as sorting peaks using fit parameter values, inserting fit subsets (potentially correcting failed fits) into a large array of fits, or deleting fits. (c) Fit Info panel display a full individual fit record for review.**

Although, the fitting process could be fully automated, numerous manual controls, overrides and checks were used to ensure a high quality of fits to be used in the final analysis. The main panel (Figure 3-20a) allows a user to fit partial ranges, force initial parameters, and set custom patterns for parameters held during the cycles of fitting. Additionally, the find peaks' initial parameters or user set parameters can be graphed for inspection of a proper starting function, and custom data masks and fit constraints can be added prior to fitting. Several fit manipulation controls were also included in the program as seen in Figure 3-21(b). Peak order can be rather random with automated

detection, and routines were included to sort them into physical categories (based on intensity or peak position, for example). Functionality was also included for individual unsatisfactory fits to be over written by insertion of successful ones into the larger array. Finally, Figure 3-21(c) shows the FitInfo panel which displays the full record of each fit completed for detailed review.

These programs were developed and of primary use in conjunction with numerous others to successfully prepare for, acquire, and analyze data on the combinatorial epitaxial films discussed in Chapter 2 and to better understand how atomic structure and ordering can be influenced by the large array of non-equilibrium parameters possessed by the MBE growth process. In the chapters that follow, results from these synchrotron x-ray techniques are combined with RHEED and other complementary probes to uncover formation processes and final states of the novel magnetic materials of interest: dilute magnetic semiconductors and Heusler alloys.

## Bibliography

1. Thompson, A.C., Vaughan, D. & source, C.F.X.O.A.A.L. *X-ray data booklet*. (Lawrence Berkeley National Laboratory, University of California: 2001).
2. Suzuki, Y. & Uchida, F. Hard x-ray microprobe with total-reflection mirrors. *Review of Scientific Instruments* **63**, 578-581 (1992).
3. Yang, B., Rivers, M., Schildkamp, W. & Eng, P. GeoCARS microfocusing Kirkpatrick-Baez mirror bender development. *Review of Scientific Instruments* **66**, 2278-2280 (1995).
4. Warren, B. *X-ray diffraction*. (Dover: Mineola, NY, 1990).
5. Cromer, D.T. & Liberman, D. Relativistic Calculation of Anomalous Scattering Factors for X Rays. *J. Chem. Phys.* **53**, 1891-1898 (1970).
6. Toney, M.F. & Weisler, D.G. Instrumental effects on measurements of surface X-ray diffraction rods: resolution function and active sample area. *Acta Crystallographica Section A* **49**, 624-642 (1993).
7. Robinson, I.K. & Tweet, D.J. Surface X-ray diffraction. *Reports on Progress in Physics* **55**, 599-651 (1992).
8. Feidenhans'l, R. Surface structure determination by X-ray diffraction. *Surface Science Reports* **10**, 105-188 (1989).
9. Fuoss, P. & Brennan, S. Surface sensitive x-ray-scattering. *Annual Review of Materials Science* **20**, 365-390 (1990).
10. Robinson, I.K. Crystal truncation rods and surface roughness. *Phys. Rev. B* **33**, 3830 (1986).
11. Robinson, I. *Surface Crystallography, Handbook on Synchrotron Radiation*. III, (North-Holland: 1991).
12. Cho, S. et al. Ferromagnetism in Mn-doped Ge. *Phys. Rev. B* **66**, 033303 (2002).
13. Kang, J. et al. Spatial Chemical Inhomogeneity and Local Electronic Structure of Mn-Doped Ge Ferromagnetic Semiconductors. *Phys. Rev. Lett.* **94**, 147202 (2005).
14. Erwin, K.T. et al. Observation of second-phase particles in bulk zirconium alloys using synchrotron radiation. *Journal of Nuclear Materials* **294**, 299-304 (2001).
15. Vogt, S. et al. Composition characterization of combinatorial materials by scanning X-ray fluorescence microscopy using microfocused synchrotron X-ray beam. *Applied Surface Science* **223**, 214-219 (2004).
16. Vogt, S. MAPS : A set of software tools for analysis and visualization of 3D X-ray fluorescence data sets. *Journal de Physique IV (Proceedings)* **104**, 635 (2003).
17. Vogt, S. Stefan Vogt's Virtual Home. (2008).at <<http://www.stefan.vogt.net/index.html>>

18. Koningsberger, D.C. & Prins, R. *X-ray absorption : principles, applications, techniques of EXAFS, SEXAFS, and XANES* /. (Wiley: New York, 1987).
19. Lang, J. & Sole, V.A. *qxscan\_sri.mac*. (APS & ESRF,).
20. Ravel, B. & Newville, M. ATHENA and ARTEMIS: interactive graphical data analysis using IFEFFIT. *Physica Scripta* **T115**, 1007-1010 (2005).
21. Ravel, B. & Newville, M. ATHENA, ARTEMIS, HEPHAESTUS: data analysis for X-ray absorption spectroscopy using IFEFFIT. *Journal of Synchrotron Radiation* **12**, 537-541 (2005).
22. Newville, M. IFEFFIT: interactive XAFS analysis and FEFF fitting. *Journal of Synchrotron Radiation* **8**, 322-324 (2001).



# Chapter 4 Dopant Stability and Ordering in a Germanium Matrix

---

We begin with the study of compositional and epitaxial effects on both ordering and breakdown of a Ge crystal upon heavy doping. To achieve a ferromagnetic state at room temperature, the semiconductor must be doped to levels of several percent, well beyond the solubility of typical dopants. At these levels, it is well known that the dopant tends to incorporate inhomogeneously and eventually phase separate into crystallites randomly embedded in the matrix, reducing their effect on a carrier mediated ferromagnetic state. Furthermore, it has been shown that magnetic elements doping substitutionally both create a local moment and enhance carrier concentration,<sup>1</sup> while dopants in other states such as interstitial sites can compensate both the substitutional moments and carriers.<sup>20,19,108</sup> The goal is, therefore, to study the limit of how atomic-scale mechanisms resulting in the variety of dopant disorders and dopant states can be altered by nonequilibrium growth techniques and codoping to produce a dopant state promoting carrier mediated ferromagnetism in the crystal.

In the chapter that follows, *in situ* techniques are used to better understand the effects of film thickness and doping concentration on the growth mode in a variety of codopant systems. Due to the predicted high magnetic moment of Mn and the strain relieving affects of Co, the  $\text{Co}_x\text{Mn}_y\text{Ge}_{1-x-y}$  system is studied in detail using complementary x-ray techniques. Disorders and strain states in this system are probed as a function of composition to reveal ternary phase diagrams examining the limit to which dopants can be stabilized via nonequilibrium growth conditions. By combining x-ray

probes of strain states and local atomic ordering, a variety of dopant states and their effect on the lattice are revealed. A second promising system of  $(\text{FeCo})_x\text{Ge}_{1-x}$  is then studied in the final section, where disorders and dopant states reveal the importance of controlling the stability of the semiconducting matrix at high doping levels.

#### 4.1 Growth Studies *In Situ*

Numerous studies were initially undertaken using primarily *in situ* measurements of the sample surface during deposition using RHEED. This technique revealed the condition of the sample surface during crystal growth and was used to characterize the crystal growth mode as a function of film thickness and doping concentration. Monitoring this “growth front” during atomic deposition was a key first step in probing the quality and properties of the film in its final state. Due to the large foot print of the grazing electron beam along one direction of the sample surface, RHEED is only able to resolve individual compositions along the direction perpendicular to the beam. Therefore, only binary samples were studied in detail, and a large number of these samples were grown each with unique ratios of the dopants and a continuously varying doping concentration ( $x$ ) to assemble a full ternary phase diagram. As growth temperatures below 200°C and above 350°C were generally disordered, the substrate for all samples was kept between 250 and 300°C.

##### 4.1a: RHEED analysis on $\text{Co}_x\text{Mn}_y\text{Ge}_{1-x-y}$

Figure 4-1 shows an example of RHEED analysis on a 1000Å binary film grown on a Ge(100) substrate. To identify the growth mode of the film, two specular diffraction peaks are tracked as a function of doping concentration – one associated with the 2D growth mode and the other with 3D. The 2D specular reflection is shown by the arrow in Figure 4-1a, where as in pure Ge, the 2x1 surface reconstruction can also be seen. As described in Chapter 2, this growth mode is associated with a well ordered film and an atomically smooth surface. Figure 4-1e shows a typical HRTEM cross-sectional image of a 2D film, indicating a smooth surface and a precipitate-free film beneath,

as evidenced by the continuous diagonal mesh representing the (111) atomic planes. The 3D specular reflection is shown to the right of the arrow in Figure 4-1c with a typical cross sectional HRTEM image of a film in 3D growth mode in Figure 4-1f. Transition to this mode is defined to be when the 3D peak intensity surpasses that of the 2D peak and is accompanied by the suppression of the surface reconstruction. Here the rough surface can expose other crystal facets such as the (111), as shown by the dark bands in Figure 4-1f, where stacking faults and other disorders occur. The specular peak intensities and widths are plotted for a  $(\text{Co}_{0.7}\text{Mn}_{0.3})_x\text{Ge}_{1-x}$  sample in Figure 4-1d where the 2D growth mode persists up to the transition point at 8.5 at.%. Here the 2D peak intensity weakens below that of the 3D peak and the 2D peak width increases dramatically. An image of RHEED at the transition point is shown in Figure 4-1b. As  $x$  increases beyond this point, the surface roughens further and becomes fully 3D.

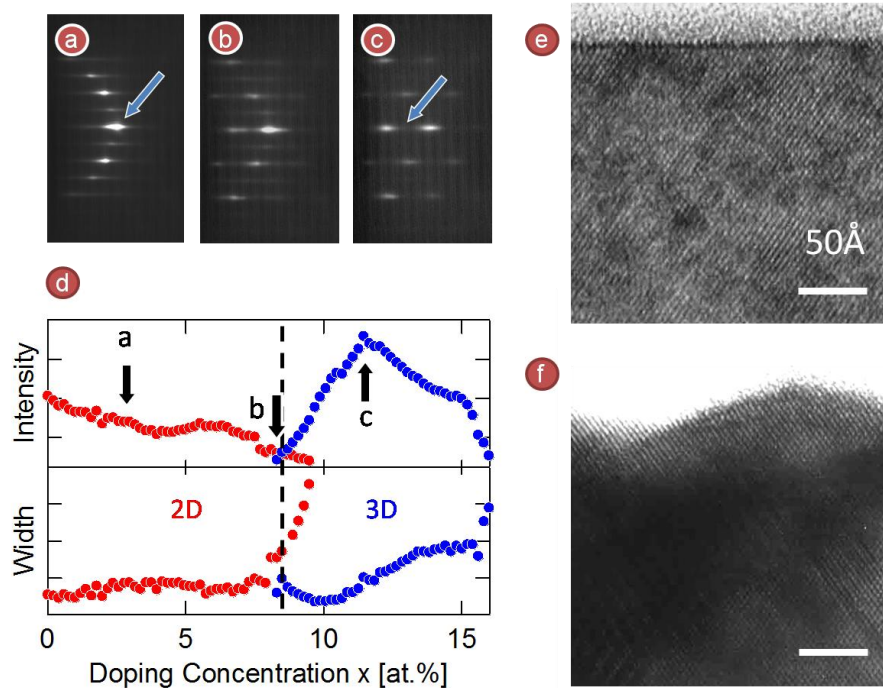


**Figure 4-1: RHEED analysis for a typical binary sample. (a)-(c) are typical RHEED patterns of  $(\text{Co}_{0.7}\text{Mn}_{0.3})_x\text{Ge}_{1-x}$  in the 2D growth mode, at the roughening transition, and in the 3D growth mode, respectively. To enhance the sensitivity to the transition, the 2D reflection [arrow in (a)] was positioned at the anti-Bragg position [arrow in (c)]. (d) Peak intensity and width as a function of doping concentration. (e) & (f) Typical HRTEM images of a film cross section in 2D and 3D growth mode, respectively. (Data courtesy of Liang He)**

Although the overall quality of the film could be summarized from the RHEED analysis on a completed film, a significant amount of information could be obtained by monitoring RHEED as a function of deposition. Figure 4-2a shows the 2D specular peak intensity and width during deposition of an iteration of a  $(\text{CoMn})_x\text{Ge}_{1-x}/\text{Ge}$  superlattice. After completing deposition and anneal cycles for the Ge Buffer, the specular intensity is very high and the width is narrow. Once deposition of the doped film commences, there is an initial reduction in intensity accompanied by a slight broadening in the width, as the dopants add a small amount of disorder to the surface. During deposition, however, oscillation in specular peak intensity and width show that the film continues to exhibit layer-by-layer growth. Discussed in Chapter 2, these oscillations result from a periodic variation in surface roughness and coherence during the formation of a monolayer, as evidenced by the  $180^\circ$  phase shift between the intensity and width oscillations. The amplitude of the oscillations gradually decreases with each layer as the global coherent organization of monolayer growth gradually becomes out of phase in localities. However, upon deposition of the pure Ge layer in the superlattice, both the layer-by-layer coherence and much of the original intensity seen at the beginning of deposition is recovered, showing that the 2D surface continues to be very high quality even after significant deposition of doped film. This trend was seen in all  $\text{Co}_x\text{Mn}_y\text{Ge}_{1-x-y}$  samples with 2D growth mode.

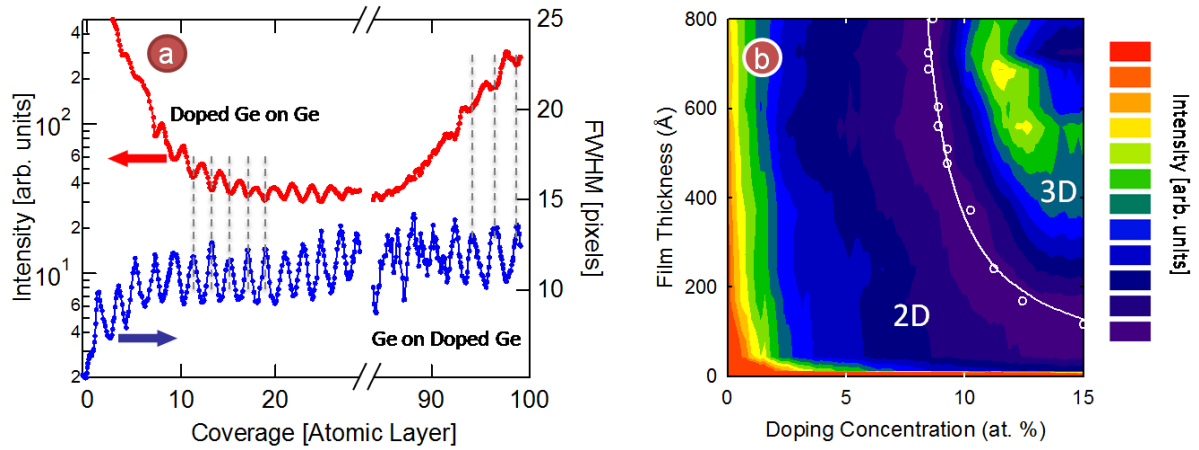


**Figure 4-2: (a) RHEED 2D specular peak intensity and width as a function of deposition of a  $(\text{CoMn})_x\text{Ge}_{1-x}/\text{Ge}$  superlattice unit cell. (b) RHEED 2D and 3D specular intensity as a function of doping concentration and film thickness in the  $(\text{Co}_{0.7}\text{Mn}_{0.3})_x\text{Ge}_{1-x}$  film. The circles show the 2D to 3D transition point, while the curve is a fit of the critical thickness,  $h_c = \alpha/(x_0 - x)$ . (Data courtesy of Liang He)**

Evolution of the roughening transition as a function of thickness and composition was also used to help study the underlying processes dictating the growth mode. It is well known that strain makes coherent epitaxial growth unstable, but doping the Ge matrix well beyond the dopant solubility can also promote surface roughness and phase separation, even in the absence of strain. A simple model describing such a “solubility gap” gives rise to a mixing energy proportional to thickness and to a quadratic polynomial in concentration.<sup>5</sup> This energy cost to remain in solid solution can be balanced through the formation of interfacial defects, which generally depends on concentration but not thickness.<sup>6,7</sup> Homogeneous epitaxial growth becomes unstable at a critical thickness  $h_c$  when these two energies become comparable, leading to the functional form of  $h_c = \alpha/(x - x_0)$ . Figure 4-2b shows RHEED intensities of the 2D and 3D specular reflections with the points designating the transitions between the two growth modes. This simple model fits very well to the transition points for a  $(\text{Co}_{0.7}\text{Mn}_{0.3})_x\text{Ge}_{1-x}$  binary sample where strain was shown to be largely compensated, yielding fit parameters of  $\alpha = 10 \pm 2 \text{ \AA}$  and  $x_0 = 7.3 \pm 0.5\%$ .<sup>8</sup> This indicates that the solubility gap plays a role in determining the stability of the film, but in other cases, strain, whose energy depends on  $\epsilon^2$  and  $h$ , could become the dominant process.

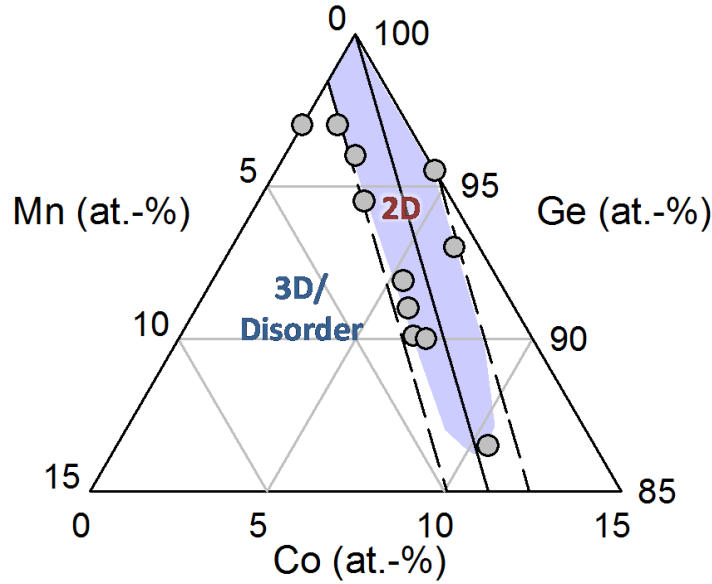


**Figure 4-3:** Full ternary phase diagram of the roughening transition for  $\text{Mn}_x\text{Co}_y\text{Ge}_{1-x-y}$  up to 15 at.% total doping. The dots represent the measured transition points from numerous binary samples all grown in a  $(\text{Co}_a\text{Mn}_b)_x\text{Ge}_{1-x}$  configuration, where  $x$  is the varied parameter in a single sample. The shaded area indicates the region of smooth 2D epitaxial growth, with the solid line along the  $a/b=3$  ratio where strain is fully compensated. Dotted lines are those where strain reaches 0.07% as measured by x-ray techniques. (Data courtesy of Liang He)

Indeed strain is an important consideration when the 2D to 3D transition is plotted as a function of composition in the full ternary phase diagram (Figure 4-3). Here the composition region associated with smooth 2D growth can be seen to closely follow the dopant ratio of  $\text{Co}/\text{Mn}=3$  with a spread symmetrical about this ratio. In Section 4.3, it is determined that lattice strain is fully compensated at this atomic ratio suggesting strain plays a role in stabilizing epitaxial growth. The coincidence of a measured lattice strain of  $\pm 0.07\%$  with the border of the 2D region supports this theory.<sup>8</sup> From these results, it can be concluded that the  $\text{Co}_x\text{Mn}_y\text{Ge}_{1-x-y}$  system is a good epitaxial materials candidate for further study of dopant states.

#### 4.1b: Other codoping systems

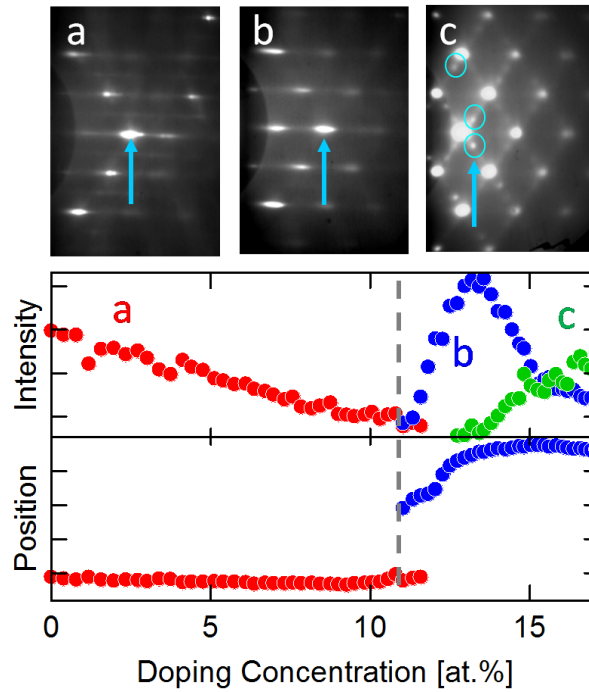


**Figure 4-4: RHEED analysis on the  $(\text{Fe}_{0.46}\text{Co}_{0.54})_x\text{Ge}_{1-x}$  system grown on GaAs (001). RHEED patterns along the [110] azimuth (vertical) at different doping concentrations: 5 at.% (a) 11 at.% (b), and 16 at.% (c). The satellite spots in (c) are from stacking faults in the  $\langle 111 \rangle$  direction. (Bottom panels) Intensity and position of the 2D, 3D, and Stacking Fault peaks as indicated by the arrows in (a)-(c), respectively. The dashed line indicates the 2D to 3D transition. (Data courtesy of Liang He)**

A second promising materials candidate for use as a doped magnetic semiconductor is the  $\text{Fe}_x\text{Co}_y\text{Ge}_{1-x-y}$  system. Figure 4-4 shows the RHEED analysis for a  $1000\text{\AA}$   $(\text{Fe}_{0.46}\text{Co}_{0.54})_x\text{Ge}_{1-x}$  binary sample. This time the width is replaced by the peak position, which also can be used to determine the transition point. At low doping concentrations, the film exhibits a 2D growth mode with RHEED oscillations and a  $2\times 1$  surface reconstruction as shown in Figure 4-4a. This mode persists up to the roughening transition at 11 at.% doping. Here the streaks modulate into a 3D pattern (Figure 4-4b) similar to the Co-Mn system. However, as doping concentration increases beyond the transition, the 3D peaks become fully spot-like and satellite peaks form along the  $\langle 111 \rangle$  directions. These peaks arise from stacking faults associated with film growth on exposed (111) facets. Since particular stacking sequences are required to preserve the diamond lattice, growth along this

crystallographic direction is prone to stacking faults. This pattern has been seen in a variety of other systems including low temperature growth of Si.<sup>9-11</sup> It is of note that these satellite peaks are a significant fraction of the primary peak's intensity. Because RHEED is only sensitive to the exposed atomic planes, this intensity suggests a large density of these defects at the surface.

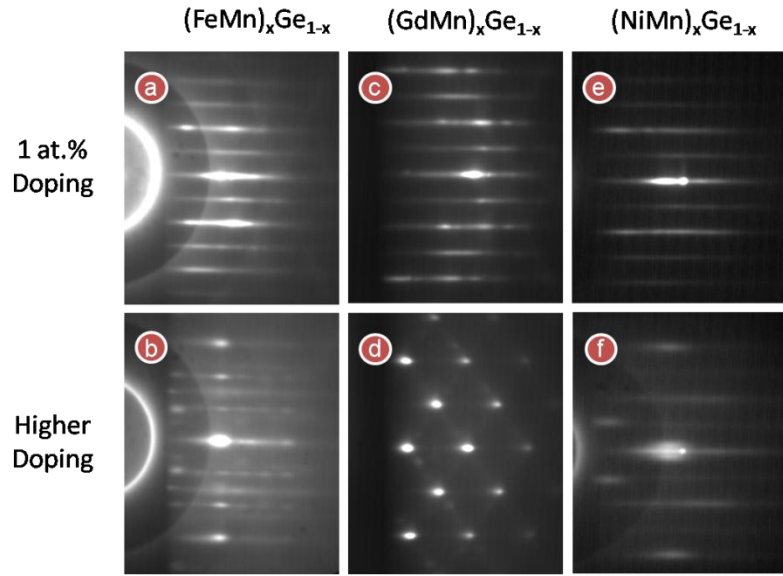


**Figure 4-5: RHEED patterns of other systems with degraded quality of growth compared with the Co-Mn and Fe-Co systems. (a) & (b) the Fe-Mn system at 1 and 4 at.% doping concentrations, respectively. (c) & (d) Gd-Mn system at 1 and 4 at.%. (e) & (f) the Ni-Mn system at 1 and 15 at.%. (Data courtesy of Liang He)**

Along with these two systems, a number of others were studied through these *in situ* measurements. The Fe-Mn system was studied with only quasi-2D growth at low concentrations (Figure 4-5a) and a roughening transition abruptly at approximately 2 at.% doping, containing multiple competing epitaxial phases (Figure 4-5b). A Gd-Mn sample was also attempted as the system could potentially possess a high magnetic moment from the Gd f-orbitals. However, this system was shown to be highly unstable with an initial quasi-2D growth (Figure 4-5c) also roughening to a 3D stacking faulted pattern at low concentrations (Figure 4-5d). By approximately 5 at.% doping, all patterns disappeared, indicating a fully amorphous film. Finally, the Ni-Mn system was investigated. It showed a gradual transition from quasi-2D to quasi-3D RHEED patterns (Figure 4-5e and f, respectively) making a transition point difficult to define. With the system never fully in



a 2D growth mode, further study was suspended, but as a full transition to 3D rough growth does not occur over the entire doping profile up to 15 at.%, future studies could be warranted. However, both the Mn-Co and Fe-Co systems were selected as the best candidates for further study based on the RHEED analysis.

## **4.2 Dopant Segregation and Stacking Faults**

To better identify dopant induced disorders in the semiconductor matrix, a set of complementary x-ray experiments were used, relying on wide angle diffraction and reciprocal space mapping techniques. Because the x-ray foot print could be kept much smaller than that in RHEED, a single ternary sample was studied to probe the full compositional phase space up to an approximately 25 at.% doping concentration. The 480Å film with a ternary region approximately 5 mm across was deposited on a Ge (001) substrate at 250°C after surface preparation, including growth of a 400Å Ge buffer. The sample was subsequently annealed at 450°C. Through the ternary phase diagram, the effects of dopant concentration and dopant type on crystal disorders were studied in detail. Secondary ion mass spectrometry was also used in concert with x-ray fluorescence spectroscopy to determine the concentration and depth profile of the dopants to study codoping effects on dopant diffusion.

### 4.2a: Ternary Phase Diagram of Disorders

Using the wide angle detector geometry, both disorders associated with rough growth and dopant segregation were detected with high sensitivity. The CCD image system discussed in Chapter 3 was placed approximately 3.9cm from the diffractometer center and tilted at a 28.5° angle to the incident beam, which provided a 30° field of view in  $2\theta$  and a 60° field of view in  $\chi$  at the center. The sample was oriented so the (111) direction lies in the vertical scattering plane bisecting the image. Figure 4-6a shows a typical image from the sample when no disorders are detectable with the only features being the thermal diffuse scattering running along  $\langle 111 \rangle$  directions from distant

substrate reflections. The crystal was oriented specifically to detect twinned reflections arising from rough growth as is shown in Figure 4-6b. Discussed in the previous section, (111) facets are exposed during 3D rough growth, and if large enough, crystal growth can commence on these atomic planes, which are prone to stacking faults. The reflections shown here were indexed as the  $(-1/3, 1/3, 5/3)$  and the  $(1/3, -1/3, 5/3)$  reflections, which are from the six-fold rotated {111} family of reflections. Finally, Figure 4-6c shows signs of powder diffraction from dopant precipitation in the matrix. Here three lines can easily be distinguished, and although this is due to trace amounts of phase separations distributed in the matrix, the example shown is one containing the largest signals from the sample studied. From the methodology discussed in Chapter 3, both types of disorders were tracked as a function of composition in the sample, and powder signals too faint to detect in the image by eye became apparent upon integration along the polar angle  $\chi$ .

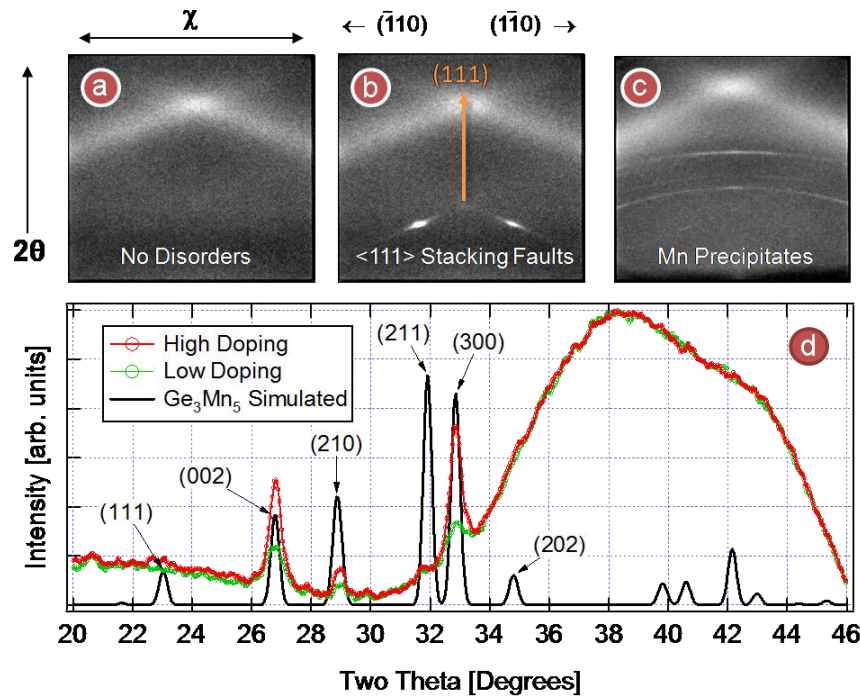


**Figure 4-6: Wide angle diffraction results from a  $\text{Co}_x\text{Mn}_y\text{Ge}_{1-x-y}$  ternary film (a) CCD image with no detectable disorders (b) Image with twinned reflections along the  $\langle 111 \rangle$  direction resulting from rough growth (c) Powder signal from precipitates (d) Indexing the precipitates as resulting from  $\text{Ge}_3\text{Mn}_5$  phase separation. Two calibrated image profiles are shown superimposed on a simulated powder diffraction signal. The large hump in the profile is due to the integrated diffuse scattering from the substrate.**

To determine the actual phase represented by the powder diffraction signal, the integrated profile was compared to numerous possibilities. In all, the simulated powder signals from four known ternary phases,  $\alpha$ -Mn,  $\beta$ -Mn, nine Mn germanicides, and the three most common Mn oxides were compared with the data. Other Co-related phases were ignored due to the prevalence of these signals in Mn-rich and Mn-only regions of compositional phase space. Figure 4-6d shows the Mn germanicide  $\text{Ge}_3\text{Mn}_5$  simulated powder spectrum superimposed on high-Mn doping and low-Mn doping image profiles. This phase has been noted in numerous studies of Mn doping into Ge with concentrations above 5 at.% or with heavy annealing.<sup>36, 37,40,115, 116</sup> The profiles shown have a good match with three of the four most prominent peaks in the germanicide. A small peak in the profile also is well aligned with the fourth (211) reflection in the alloy. All other phases studied contained numerous prominent reflections where none exist in the data. The relative peak intensity in the powder diffraction exhibit differences from that of  $\text{Ge}_3\text{Mn}_5$  due to film texture and strain.

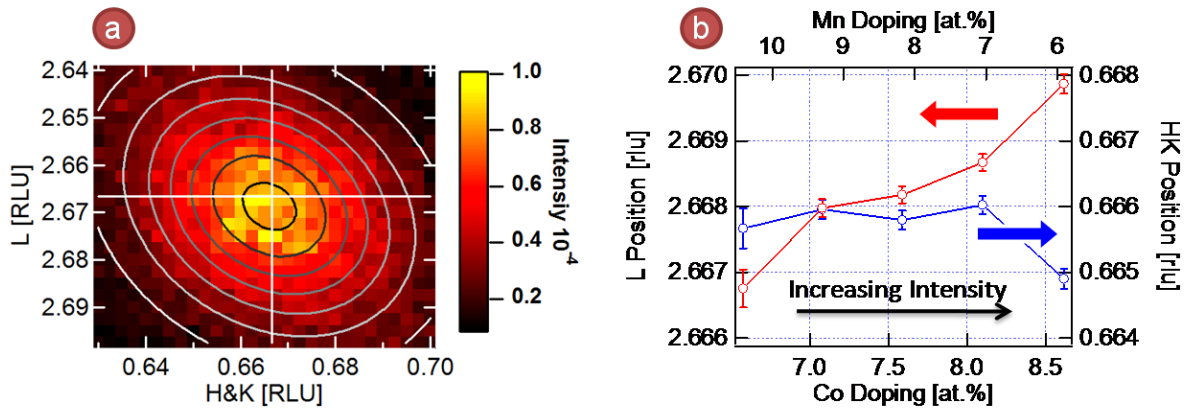


**Figure 4-7: (a)** Reciprocal space mapping of stacking fault peaks. Ellipses are 2D Gaussian fits whose positions are compared with the (2/3, 2/3, 8/3) positions indicated by the cross hairs. **(b)** In-plane and out-of-plane position of the peaks as a function of increasing Co dopant ratio, with increasing intensity indicated by the black arrow.

Being epitaxial, the positions of the twinned reflections were registered with respect to the reciprocal space of the substrate. A point detector with narrow slits was used to map reciprocal space along the out-of-plane (L) and in-plane radial (H=K) directions (Figure 4-7a) to locate the (2/3,

$2/3, 8/3$ ) reflection twinned from the  $\{022\}$  family. For high precision positional measurement, the data were fit to a 2D Gaussian surface and tracked as a function of composition at high doping concentrations (15-17 at.%). Figure 4-7b shows the trends of position both out-of-plane and in-plane. The integrated intensities increase with increasing Co concentration (left-to-right in the figure). Correspondingly, the out-of-plane lattice constant is lattice matched at the onset of the twinning reflection with increasing tetragonal distortion with Co concentration. The in-plane position, however, remains relatively constant and nearly lattice matched with the substrate, suggesting coherent epitaxy even as stacking faults increase.

As the wide angle diffraction measurements had superior sensitivity to both stacking faults and precipitates, their integrated intensities were tracked across the composition spread of the ternary sample and are plotted in the ternary phase diagram in Figure 4-8a. No detectable disorders occur within the ternary region up to a critical doping concentration. In Co-rich regions, rough growth, seen in RHEED, is accompanied by the onset of XRD intensities of the stacking faults or twinned reflections. With equal parts Co and Mn marked by the orange arrow in Figure 4-8a and extracted in Figure 4-8b, the onset of stacking faults occurs at approximately 11 at.% combined doping concentration with an exponential increase through 17 at.% doping where the signal saturates (Figure 4-8b). Prior to saturation, these stacking faults are spread throughout the depth of the film as they are not seen in RHEED; however, near saturation, satellite peaks associated with (111) stacking faults emerge in the RHEED images (not shown), suggesting an increased density near the surface.

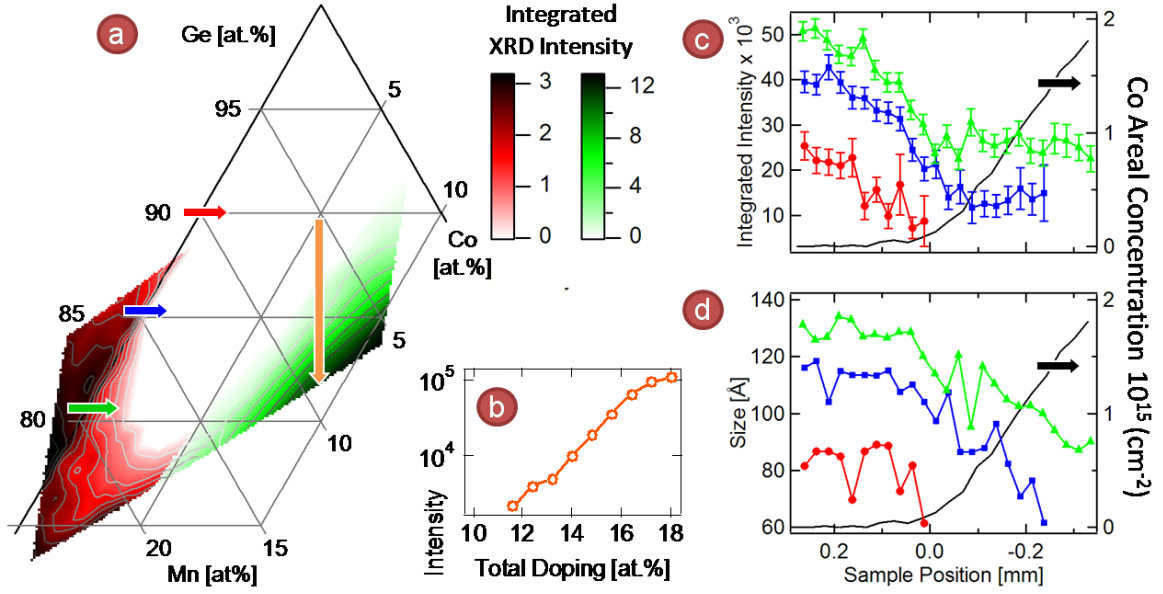


Figure 4-8: (a) Ternary phase diagram of disorders in the  $\text{Co}_x\text{Mn}_y\text{Ge}_{1-x-y}$  system. Integrated XRD intensity from the  $\text{Ge}_3\text{Mn}_5$  (300) secondary phase is shown in red and stacking faults in green. (b) Twinned reflection intensity profile as a function of doping concentration at the Co:Mn ratio of one. (c) XRD intensity and (d) particle size as a function of Co concentration at 90, 85, and 81 at.% Ge as shown in (a).

By contrast to the stacking faults, Mn precipitates are not detected in Co-rich regions. These disorders primarily occur in the  $\text{Mn}_x\text{Ge}_{1-x}$  binary region of the sample, increasing in diffracted intensity with  $x$  as seen in Figure 4-8a. With codoping, no dopant precipitation is detected up to 15 at.% after which powder signals begin to encroach on the ternary region. The precipitate integrated signal and grain size is shown with the onset of Co codoping at 10, 15, and 20 at.% total doping in Figure 4-8 (c) and (d), respectively. The grain size was estimated using the Scherrer method from peak widths in  $2\theta$  of the  $\text{Ge}_3\text{Mn}_5$  (300) reflection. Correcting for the 0.5 mrad instrumental broadening ( $B$ ) from the beam divergence caused by focusing with the vertical KB mirrors, the particle size was calculated as follows:

$$D = \frac{2\lambda\sqrt{\pi \cdot \ln 2}}{2 \cos \theta \sqrt{W^2 - B^2}} \quad (4-1)$$

where  $\lambda$  is the x-ray wavelength,  $\theta$  is half  $2\theta$ , and  $W$  is the peak FWHM. Strain broadening due to residual stress in the film is not included in this calculation. A sudden drop in integrated intensities

upon the onset of Co codoping and the continued decrease in grain size as Co concentration increases demonstrate the critical role Co plays in suppressing precipitates and stabilizing Mn in Ge. With the stabilizing effects of Co as a codopant, much higher doping concentrations free of dopant defects are achieved compared with individual doping.

#### 4.2b: Depth Dependence and Diffusion

Dopant concentrations and their depth dependence further support the critical role Co plays in stabilizing Mn in Ge. Figure 4-9(a-d) shows these results from dynamic secondary ion mass spectrometry (SIMS) measurements taken at selected positions (compositions) on the same ternary sample. Oxygen ions at 9.22 keV were used to obtain a sputtering rate of  $\sim 0.25$  nm/s. For each depth profile, the ion beam was rastered over an area  $100\text{ }\mu\text{m} \times 100\text{ }\mu\text{m}$ , while the measurements were taken within a gated area of  $30\text{ }\mu\text{m} \times 30\text{ }\mu\text{m}$  at the center of the raster. The near surface concentrations cannot be determined by dynamic SIMS, owing to initial ion beam damage within a depth that depends on the ion energy (in this case,  $\sim 10$  nm). Beneath the surface layer, each SIMS depth profile exhibits three distinct regions: the doped film, the Ge buffer, and the Ge substrate, which are separated by exponential decays. In the absence of Co doping (Figure 4-9a), the Mn depth profile within the film exhibits a rounded shape with an integrated amount of Mn that is significantly lower than what was deposited (Figure 4-9d). This indicates a depletion of Mn dopants to the surface, which is consistent with recent studies.<sup>21,117,118</sup> However, trace amounts of Co have led to a flattening of the Mn profile in the film with a well-defined interface (Figure 4-9b) and a corresponding sharp increase in the amount of Mn remaining in the film (Figure 4-9d). As Co concentration increases, the Mn concentration rapidly reaches what was deposited (the dotted line in Figure 4-9d), and its depth profile becomes constant within the film, which is accompanied by a sharp exponential drop at the film-buffer interface (Figure 4-9c).

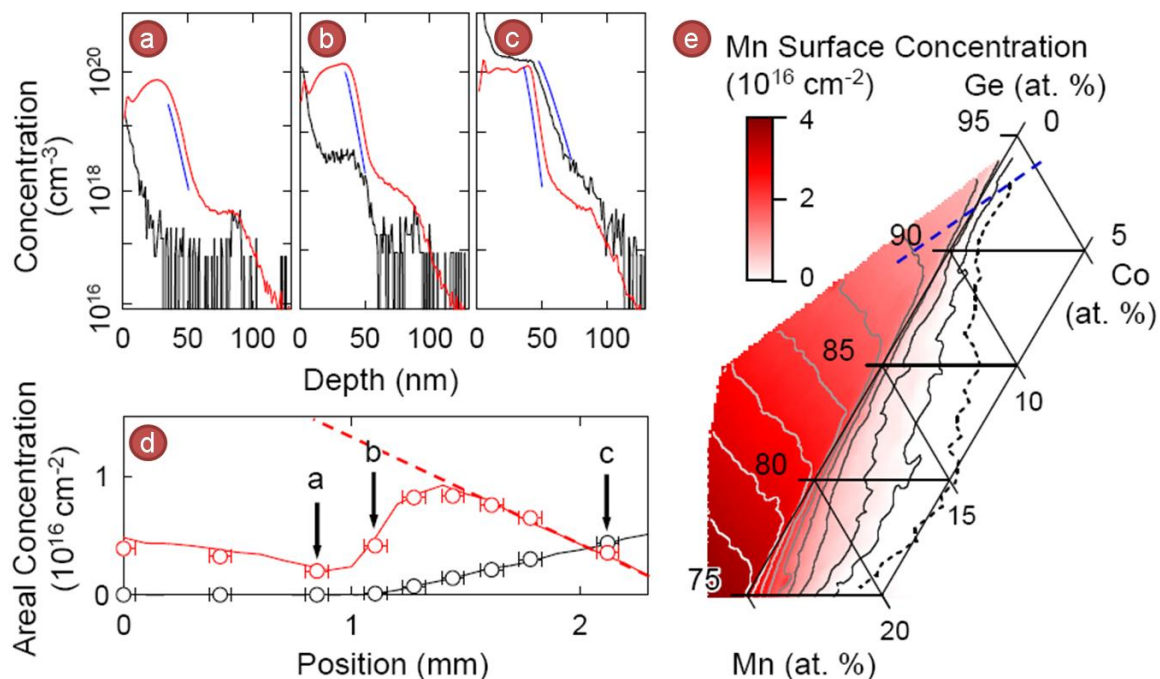


**Figure 4-9: Depth dependent Mn and Co concentrations for  $\text{Co}_x\text{Mn}_y\text{Ge}_{1-x-y}$ .** Dynamic SIMS profiles in Ge (a) without Co, (b) trace amount of Co ( $\sim 10^{14} \text{ cm}^{-2}$ ), and (c) few at.% Co. The blue lines correspond to  $\exp(-\alpha z^n)$  fits with respective  $n$  of 1.10, 1.16, 1.22, and 1.17, horizontally shifted for clarity. (d) Evolution of dopants within the film versus position of the sample, as determined by integrating the SIMS yields (circles) and by XRF measurements (lines). The dashed line corresponds to XRF measurements before removal of the surface Mn, whereas solid lines correspond to those after the treatment. (e) Areal concentration of surface Mn determined by XRF measurements before and after removal of the surface aggregates, i.e., the difference between the two measured concentrations. The contours are in steps of  $5 \times 10^{15} \text{ cm}^{-2}$  except for the last two, with the dotted curve equivalent of one atomic layer, and the second to last about three atomic layers ( $2 \times 10^{15} \text{ cm}^{-2}$ ). The blue dashed line indicates the location of the results shown in (d). (Excerpt from Ref. 20)

Since Mn is very brittle and slowly decomposes in water, excessive sonication in organic solvents was used to remove the surface aggregate without damaging the film underneath. The removal of the surface Mn precipitates was confirmed by XRD and XRF measurements with significantly increased dwell times, in addition to electron energy dispersive x-ray spectroscopy and optical reflectivity measurements.<sup>21</sup> In Figure 4-9d, XRF results for Mn before and after removing the surface Mn are compared to the integrated SIMS yields (circles), taken along the same line on the sample (the dashed line in Figure 4-9e). The excellent agreement between the latter two indicates that the XRF results after removing the surface Mn are the Mn concentration dispersed

into the film. In contrast, Co is fully dispersed in the film, and removing the surface precipitates does not appear to affect the film beneath. Most importantly, the concentration of surface Mn, as shown in Figure 4-9e, exhibits an exponential decrease as Co is introduced as a codopant, leading ultimately to the suppression of surface precipitation and stable Mn in the film.

The SIMS depth profiles also provide insight into the diffusion processes, since the decay rate below the film-buffer interface is a direct measure of diffusion rate. The increase in slope from Figure 4-9 (a) to (c) indicates that the presence of Co significantly limits the diffusion of Mn. Furthermore, studies<sup>22</sup> show that the functional form on depth ( $z$ ) depends on the diffusion mechanism, such that single channel interstitial diffusion via Fick's law gives rise to an asymptotic exponential dependence on  $z^2$ , whereas multichannel diffusion in the presence of traps yields a corresponding dependence on  $z$ . The best fits of the depth profiles yield exponents of  $z$  that are between 1 and 1.2 Figure 4-9 (a)-(c) rather than 2, indicating multichannel diffusion as the dominant mechanism. As discussed below, the likely diffusion traps are substitutional Co that tends to attract interstitial Mn to form a stable dimer.

### **4.3 Strain States and Epitaxial Coherence**

In section 4.1 it was suggested that strain plays a large role in the growth mode of a highly doped semiconductor. In the Ge (001) on Ge (001) epitaxial system that we investigate, however, determining the strain of the film is rather difficult, because the film reflections are all completely "buried" under those of the substrate, owing to the identical crystalline structures and the low level of strain (<0.1%) between the two. In other words, the film reflections are extremely close to those of the substrate, while their intensities are many orders of magnitude lower than the substrate's. Therefore, to investigate the effects of strain on film coherence as well as to help reveal information regarding the dopant states, crystal truncation rod analysis was undertaken. As detailed in Section



3.2c, a crystal lattice of the film that is coherent with the substrate atoms forms 2D atomic planes whose spacing differs from the substrate based on elastic strain, resulting from different preferred bond lengths of the dopants. These planes and the film interfaces can interfere coherently with those of the substrate, causing a fringe pattern to appear on the rod surrounding the substrate reflections. Where these patterns occurred in the ternary composition revealed key information on crystallographic ordering, and the kinematical model discussed in Section 3.2c were used to extract precise measurements of the strain state and disorder parameters of the film. A calculation of correcting for the elastic distortion to obtain the film lattice parameter is also provided.

#### 4.3a: Fitting Methods and Elastic Correction

Truncation rod intensity profiles were obtained and analyzed at each composition on the ternary sample discussed above as well as a number of binary samples grown under different conditions. While both RHEED and cross-sectional HRTEM measurements indicate that the deposited material is coherent at the interface in regions of 2D growth, that is they are lattice matched to the substrate parallel to the surface, further evidence is provided by comparisons of the (00L) and the (11L) rods and their fits as shown in Figure 4-10. Since the (00L) CTR is insensitive to the lateral atomic position of the film, this CTR intensity profile contains the contribution from all of the atomic layers in the film, regardless of the in-plan strain, so long as these layers can scatter coherently with the substrate and one another. In contrast, only the commensurate (i.e. in-plane lattice matched) atomic layers of the film contribute to the (11L) CTR profile. In the figure, both data sets have good fits whose corresponding output parameter values agree (as seen in the insets). If the film lattice were to be relaxed, a noticeable intensity drop and phase shift would occur in the (11L) CTR intensity profile with respect to that of the (00L) in addition to fits producing different output parameters. With larger relaxation, rods from the film and substrate will no longer overlap, and fringes near in-plane reflections will disappear. Therefore, the identical phase and intensity of

the fringes and the matching fit parameters between the two profiles provides strong evidence for all of the atomic layers in the film to be coherent with the substrate.

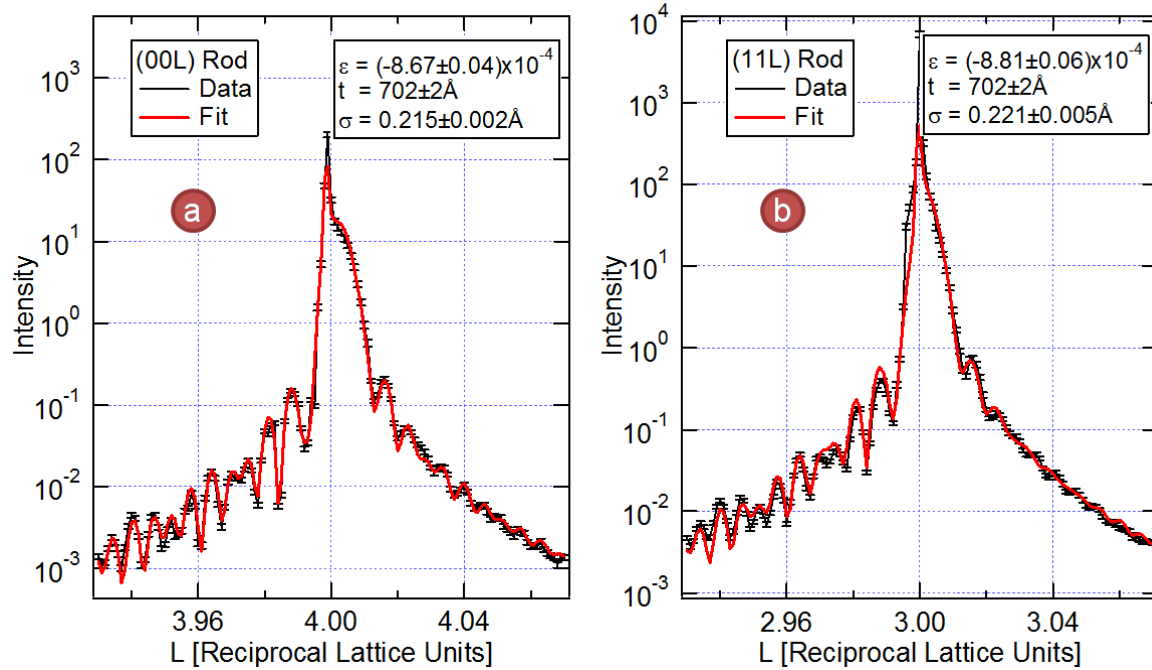


**Figure 4-10: Example fits of a scans of two rods at one composition on the sample. (a) the (00L) rod around  $L=4$  and (b) the (11L) rod around  $L=3$ . The output film parameters from each fit are displayed, showing general agreement of the state of the film and providing additional confidence in the measurements.**

The strain information displayed in Figure 4-10 has been corrected assuming elastic deformation of the lattice and is not the spacing ( $d_f$ ) of the lattice planes. This “bulk strain” is defined as  $\epsilon = \frac{a_f - a_{Ge}}{a_{Ge}}$  where  $a_f$  is the lattice constant of the film (when unconstrained by epitaxial coherence with the substrate) and can be calculated from the measured lattice spacing of the film by solving the generalized Hooks law in three dimensions. For a cubic lattice such as Ge, the stresses ( $\sigma$ ) and strains ( $\epsilon$ ) are related through three elastic moduli in the second order elastic tensor equation:

$$\begin{pmatrix} \sigma_{xx} \\ \sigma_{yy} \\ \sigma_{zz} \\ \sigma_{xy} \\ \sigma_{yz} \\ \sigma_{zx} \end{pmatrix} = \begin{pmatrix} c_{11} & c_{12} & c_{12} & 0 & 0 & 0 \\ c_{12} & c_{11} & c_{12} & 0 & 0 & 0 \\ c_{12} & c_{12} & c_{11} & 0 & 0 & 0 \\ 0 & 0 & 0 & c_{44} & 0 & 0 \\ 0 & 0 & 0 & 0 & c_{44} & 0 \\ 0 & 0 & 0 & 0 & 0 & c_{44} \end{pmatrix} \begin{pmatrix} \epsilon_{xx} \\ \epsilon_{yy} \\ \epsilon_{zz} \\ \epsilon_{xy} \\ \epsilon_{yz} \\ \epsilon_{zx} \end{pmatrix} \quad (4-2)$$

In the current system only biaxial stresses are present (no torsion) and the equation can be simplified and inverted into the form

$$\begin{pmatrix} \epsilon_x \\ \epsilon_y \\ \epsilon_z \end{pmatrix} = \frac{1}{E} \begin{pmatrix} 1 & -\nu & -\nu \\ -\nu & 1 & -\nu \\ -\nu & -\nu & 1 \end{pmatrix} \begin{pmatrix} \sigma_x \\ \sigma_y \\ \sigma_z \end{pmatrix} \quad (4-3)$$

where  $E$  is Yong's modulus and  $\nu$  is the Poisson ratio. In the epitaxial conditions here,  $\sigma_x = \sigma_y$  and  $\sigma_z = 0$ , reducing the system of equations to one:

$$\epsilon_z = \frac{-2\nu}{1 - \nu} \epsilon_x \quad (4-4)$$

In this formalism, strain is defined as  $\epsilon \equiv \frac{d_{strained} - d_{unstrained}}{d_{unstrained}}$  and the two strains in Equation (4-4)

are  $\epsilon_z = \frac{d_{out-of-plane} - a_{film}}{a_{film}}$  and  $\epsilon_x = \frac{d_{in-plane} - a_{film}}{a_{film}}$ . In the case of a coherently strained film,  $d_{in-plane} = a_{Ge}$  and Equation (4-4) can be solved for the unknown film lattice constant to produce:

$$a_{film} = \frac{(1 - \nu)d_{out-of-plane} + 2\nu a_{Ge}}{1 + \nu} \quad (4-5)$$

Since the film is still largely Ge, the Ge Poisson ratio of 0.27 can be used in the calculation. The bulk strain is then:

$$\epsilon = \frac{a_{film} - a_{Ge}}{a_{Ge}} = \frac{1 - \nu}{1 + \nu} \left( \frac{d_{out-of-plane}}{a_{Ge}} - 1 \right) \quad (4-6)$$

All of the data discussed in this work is corrected for this elastic deformation and displayed as bulk strain unless noted otherwise.

#### 4.3b: Ternary Phase Diagram for Strain

Using the method described above, the strain state of the ternary epitaxial film was examined, including the binary regions of  $Mn_xGe_{1-x}$  and  $Co_xGe_{1-x}$  and are displayed as a function of

composition in Figure 4-11a. The CTR intensity profiles of films in regions I and II can be best described as those from 2D epitaxial films and look qualitatively similar at similar total doping concentrations as seen in the top two traces in Figure 4-11b. These regions are devoid of any of the detectable disorders described in Section 4.2. The film strains  $\epsilon$  can be characterized by two planes: one Co rich (I) and another Mn rich (II). Each plane can be fit to Vegard's law given by  $\epsilon = \epsilon_{Co} x + \epsilon_{Mn} y$ , where the variables  $x$  and  $y$  are the respective doping concentrations of Co and Mn with the corresponding strain coefficients  $\epsilon_{Co}$  and  $\epsilon_{Mn}$ , as they are listed in Table 4-1. Nearly the entire region I (Figure 4-11a) can be fit to a single plane, and in contrast, only the counterpart at low Mn concentrations fits to a plane to region II. However, upon close examination, even region I contains a second linear component at higher doping concentrations, as seen in the Co-binary region and shown in Figure 4-11c. The observed linear dependence of strains is a strong indication that the dopants are dispersed into the lattice. Notable, is the difference in the coherent region seen with x-ray and that seen using RHEED (Figure 4-3), which is due to RHEED's higher sensitivity to surface roughness.

Region of Composition	$\epsilon_{Co}$ (%)	$\epsilon_{Mn}$ (%)
Region I	$-0.9 \pm 0.1$	$2.8 \pm 0.1$
$Co_xGe_{1-x}$ for $x < 5\text{at.}\%$	$-1.4 \pm 0.1$	NA
$Co_xGe_{1-x}$ for $x > 5\text{at.}\%$	$-0.8 \pm 0.1$	NA
Region II for $y < 8\text{at.}\%$	$1.4 \pm 0.1$	$-0.5 \pm 0.1$
Region II for $y > 8\text{at.}\%$	$1.4 \pm 0.1$	$-1.2 \pm 0.1$

**Table 4-1: Vegard's law coefficients for the coherent regions (I and II in Figure 4-11a) of  $Co_xMn_yGe_{1-x-y}$  obtained from fitting the strains to  $\epsilon(x,y) = \epsilon_{Co}x + \epsilon_{Mn}y$ . Here the variations in the strain coefficients  $\epsilon_{Co}$  and  $\epsilon_{Mn}$  correspond to respective doping concentrations Co ( $x$ ) and Mn ( $y$ ) in at.%. The uncertainties correspond to variations in the fits made from selecting different compositional ranges.**

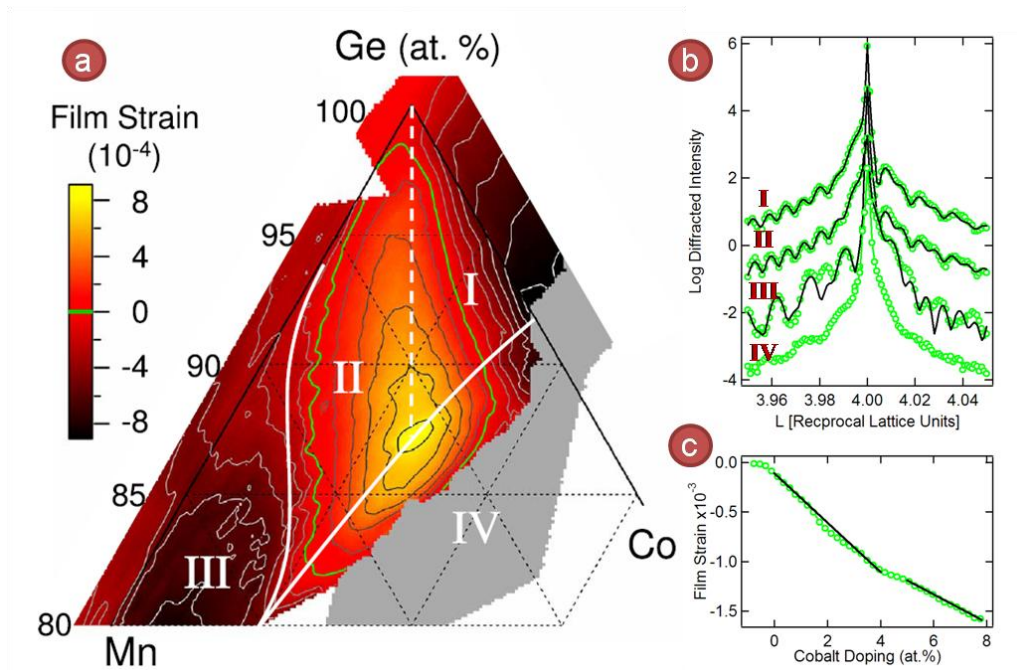


**Figure 4-11: (a)** Film strain as a function of composition for  $\text{Co}_x\text{Mn}_y\text{Ge}_{1-x-y}$  (001) and regions with different structural characteristics (separated by white lines). The interval between the strain contours is 0.015%. Regions I and II are free of detectable disorders. The film contains Mn surface precipitates in region III and stacking faults in region IV with gray area indicating rough films. **(b)** CTR profiles (circles) and fits (lines) for data in each region are offset in vertically for clarity. **(c)** Film strain (circles) for binary  $\text{Co}_x\text{Ge}_{1-x}$  with linear fits (lines).

The coefficients in Vegard's law are often directly interpreted as the difference in average atomic size between the dopant and the host matrix. However, the presence of two planes and their symmetry suggest that there are at least three species of dopants. The differences in strain state with annealing helped to uncover some characteristics of these different dopant species. Figure 4-12a shows a profile of the strain at 5.5 at.% doping concentration extracted from the ternary diagram and compared with CTR analysis from a separate unannealed binary sample, whose data and fits were shown in Figure 4-10. Both contain the two linear regions of strain with relative concentration, but the annealed film exhibits a constant expansive shift in strain compared with the as-grown counterpart, suggesting that annealing causes an increase in the population of dopant species larger than the substrate. Above Mn relative concentration of 80%, however, this relationship diverges. In this region, the strain in the annealed sample is more linear and continues

through zero to  $\epsilon = -2.5 \times 10^{-4}$  whereas the strain in the as-grown sample becomes non-linear and relaxes to near zero at the Mn binary composition.

Indications of the cause can be seen in the lower plot of Figure 4-12a where the film disorder is compared with that of the substrate in the unannealed sample. As expected, the substrate is more ordered with significantly lower RMS variance in the unit cell positions. However, in regions involving a single dopant (the far right and far left in the figure), this disorder increases and eventually matches that of the film. This suggests that in the absence of a codopant, either dopant is more able to diffuse throughout the matrix. Particularly, the increase of both the disorder in the substrate *and* the film above Mn 90% indicates the increased presence of highly mobile disorder states, and when compared with the strain dependence between annealed and unannealed samples, these disorders are clearly associated with an expansion of the lattice. A well known, highly mobile dopant state that expands the lattice in semiconductors is an interstitial and fits the evidence gathered here. Considering that the strain behavior of the annealed sample is more compressive in the Mn-binary region and surface aggregation of Mn precipitates was found here, it is likely that Mn interstitial are allowed to diffuse to the surface upon annealing. Other experimental annealing studies on Mn-doping using Auger spectroscopy<sup>17</sup> and Rutherford backscattering<sup>15</sup> reported this effect, as well as energy calculations of dopant diffusion in semiconductors.<sup>19</sup> Here, it is clear that the presence of Co is reducing the prevalence of Mn interstitials. In what follows, a likely atomistic mechanism is put forward for the stable dopant species, which is based on the evidence presented here and the energetics of the system.

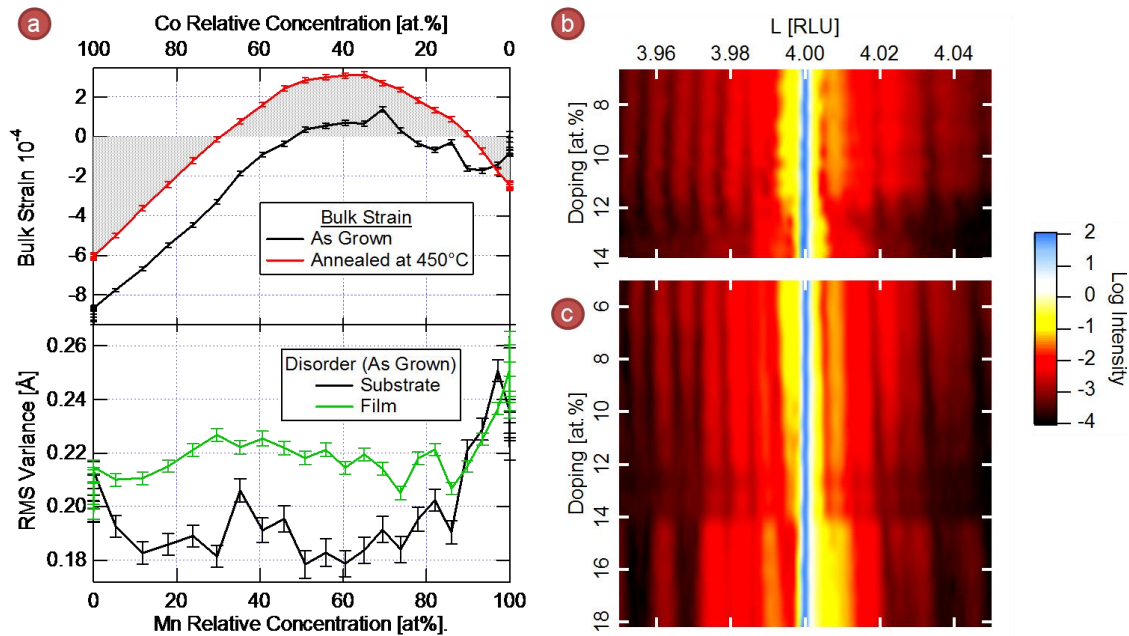


**Figure 4-12: (a) Strain and Debye-Waller disorder versus relative doping concentration at a fixed 5.5 at% total doping. For the strain, the red curve is extracted data from the ternary sample, while the black curve is data from a separate unannealed binary sample. Raw CTR log intensity profiles showing (b) the region I to IV transition with increasing doping concentration with a fixed relative concentration of Co:Mn=3:1 (c) the region II to III transition along Co:Mn=1:5. Reduction in intensities in the region between 12 and 14 at.% doping concentration is not intrinsic and is caused by a line of contamination during growth.**

Recent calculations<sup>24</sup> show that certain types of dimers are energetically more favorable than isolated substitutional monomers. Specifically, dimers with Co at a substitutional site and Mn at an adjacent interstitial site are by far the most stable, reducing energy by more than 1 eV/atom over those of the monomers. Although substitutional sites are calculated to be at a lower energy than interstitial sites for both isolated Mn and Co, Co is much more stable, having double the energy gain ( $\sim 2\text{eV}$ ) over Mn ( $\sim 1\text{eV}$ ).<sup>25</sup> Therefore, initial deposition of isolated dopants naturally has a larger Mn interstitial population. Additionally, it is well documented that these dopants diffuse much more rapidly in interstitial sites over substitutional.<sup>22</sup> The stable substitutional Co evidently plays the role of attracting mobile interstitial Mn to form the stable dimer, which in turn blocks a diffusion channel. This reduces the diffusion of other dopants and limits the population of larger clusters at finite temperatures, which agrees with the observed substantial effect that Co has on Mn even at

trace amounts (Figure 4-9b). Therefore, by forming Co-Mn dimers, Co acts as a trap for the otherwise rapidly diffusing Mn interstitials and alters the diffusion process, as discussed above (Figure 4-9).

This mechanism would result in three main populations of species that contribute to the epitaxial strain at low concentrations, Co-Mn dimers of the type described above, substitutional Co in the Co-rich region (I), and substitutional Mn in the Mn-rich region (II). A modified Vegard's law that includes all three species is necessary in order to describe the measured strains. For region I, strain depends on the concentration of Co-Mn dimers and on that of the excess Co, i.e.,  $\epsilon = \epsilon_{\text{Co}}(x-y) + \epsilon_{\text{Co-Mn}}y$ , and correspondingly for region II,  $\epsilon = \epsilon_{\text{Co-Mn}}x + \epsilon_{\text{Mn}}(y-x)$ , where the coefficient  $\epsilon_{\text{Co-Mn}}$  is associated with the size of the Co-Mn dimer. The symmetry of the boundary between the two regions (along Co to Mn atomic ratio of 1:1) is also consistent with this interpretation. Consequently, the values of atomic radii can be obtained by using the above definition of strain, and they are 0.121 nm for substitutional Co, 0.126 nm for interstitial Mn associated with the dimer, and 0.122 nm for substitutional Mn by using the Ge value of 0.122 nm. These values are in excellent agreement with the first principles calculations.<sup>25</sup> At higher doping concentrations, other populations of species may become energetically viable, including interstitial Co (Figure 4-11c). In Section 4.4, local probes shed more light on this atomistic interpretation allowing for continued refinement of an understanding of the dopant states.

In contrast to the regions of smooth 2D growth, CTR intensity profiles in region III of the ternary phase diagram clearly exhibit a much more complex pattern (Figure 4-11b), which is not fit well by the model (for example the oscillations at 3.985 and 4.015). In this region, where phase separation and surface aggregation was detected, there are likely other Fourier components from small disordered domains or layers within the film. As the profile of an in-plane rod was not



measured in this region, it is unknown whether the film is coherent, but due to the massive amounts of disorders, film coherence is unlikely. From the data, however, it is clear that the strain does in fact exhibit a negative trend with higher doping concentration, which is opposite of the typical effect from interstitial or precipitating dopants. Again, due to the massive amounts of surface segregation of dopants found in this region, it is likely that only a small percentage of dopants remain in the matrix and that their overall effect is to reduce the lattice size as will be discussed below. The transition from the 2D ordered region into this one is very gradual (Figure 4-12c) and supports the theory that the thin layer of surface Mn precipitates seen at lower doping grows in thickness with increasing Mn deposition, causing the additional Fourier components/complexities in the CTR profiles.

Finally, region IV is where 3D rough growth associated with stacking faults was observed. Interestingly, this does not destroy the interference pattern immediately but only after a significant intensity from twinned reflections is seen. This suggests a patchy or localized in-plane onset to 3D rough growth rather than a depth-dependent disorder, since it is impossible for (111) facets to be buried by smooth 2D (001) layers, especially after a stacking fault has occurred. Notably, the onset of stacking faults is also associated with a decrease in strain to zero just before the loss of fringe coherence as the film relaxes in-plane. In contrast to the Mn-rich transition, the one in this Co-rich region is more abrupt and can be seen in Figure 4-12b.

#### **4.4 Local Atomic Ordering and Dopant States**

The local atomic environment of a material is often what determines many of its macroscopic properties, so understanding where the dopants incorporate at the atomic level is very important to identifying the mechanisms behind the electronic and magnetic properties of the DMS material. Though strain measurements provide an indication of dopant states, it is, at best, an

indirect measurement of the structural environment of the dopant in the crystal lattice, especially in the presence of the complex composition dependence found in the system currently of interest. As with most XRD techniques, this is a global average of the effects from all dopant populations within the film. Using extended x-ray absorption fine structure (EXAFS), therefore, provided a complementary strategy of probing the local atomic structure to help distinguish dopant states and their effect on the lattice. Because this technique is spectroscopic, it also has the unique ability to probe each element individually. In this section, the information of the average atomic environment of each dopant element coupled with the information obtained from the strain measurements helped to uncover the various ways they incorporate into the lattice. How these dopant states combined to result in the electronic and magnetic properties of the material as a whole is also discussed.

#### 4.4a: Qualitative Elemental Environments

EXAFS on a binary sample of  $(\text{Co}_x\text{Mn}_{1-x})_{0.055}\text{Ge}_{0.945}$ , were taken at five compositions symmetrical about the Co to Mn relative concentration of 50%, including one spectra at each end where only one dopant species was deposited. The data was taken with a 50eV pre-edge through to 700eV after the edge or the equivalent photo-electron momentum of approximately  $14\text{\AA}^{-1}$ ;  $\Delta k$  was kept below  $0.9\text{\AA}^{-1}$ . In the program ATHENA, a background absorption edge spline, removed Fourier components up to  $R=1.3$  for Co and  $R=1$  for Mn. Figure 4-13 (a) and (b) shows an example of this for Co EXAFS. The Fourier transform into R-space used a Hanning window with a k-range of 2-13 for Co (Figure 4-13b) and due to its lower signal-to-noise, 3-11 for Mn. The Co amplitude reduction factor  $S_0^2$ , measured from fitting EXAFS of a Co foil was  $0.785\pm0.026$ , and for Mn,  $0.84\pm0.07$  was used from a Mn ferrite film. Each peak was fit with four parameters in the program ARTEMIS in R-space: A (amplitude),  $\sigma^2$  (disorder),  $\Delta R$  (position), and  $E_0$  (edge energy). Fitting multiple k-weights (0-3)

reduced correlations between  $A\text{-}\sigma^2$  and  $\Delta R\text{-}E_0$  parameters, with the final fit occurring with a k-weight of one.

Figure 4-13c shows a fit to EXAFS data at the Co Edge where two local environments have been modeled. Peak A is a model of Co incorporating into the matrix substitutionally (at the 8a site) with four Ge nearest neighbors (NN) at approximately 2.45Å. The second NN for this site at 4.00Å with coordination 12 are not seen. Peak B is modeled with the Co at the interstitial 32e site having one nearest neighbor at approximately 2.0Å. This site has only a simple constraint of being located somewhere along the (111) direction. (Symmetry and Bravais translations populate the rest of the cell.) These two sites can be seen graphically in Figure 4-14a. The symmetrical interstitial site (8b) was also modeled with the primary site at the (1/2, 1/2, 1/2) position in the unit cell; however, the nearest neighbor is identical to that of a substitutional dopant at  $R=2.45\text{\AA}$ . One difference, however, is a second nearest neighbor very near to the first at  $R=2.83\text{\AA}$  with a coordination of 6. Although a weak peak does appear in the data near this distance, the amplitude is not significantly above the noise level and an accurate reading is impossible. Attempts at fitting it produced non-physical results. Based on the relative peak heights, the noise level, and the relative coordinations of the two sites, at most 8% Co could occupy this site with the actual value probably much lower. The four Co EXAFS datasets taken are shown in Figure 4-13d. All datasets exhibit both A and B peaks, with no significant difference between codoping (Co relative concentration 20-80%) and Co-only doping (100% relative concentration) besides differing peak amplitudes. The peak that possibly could correspond to Co occupying the 8b interstitial site fluctuates widely in amplitude, width and even in position, suggesting it is part of the noise rather than a real signal.

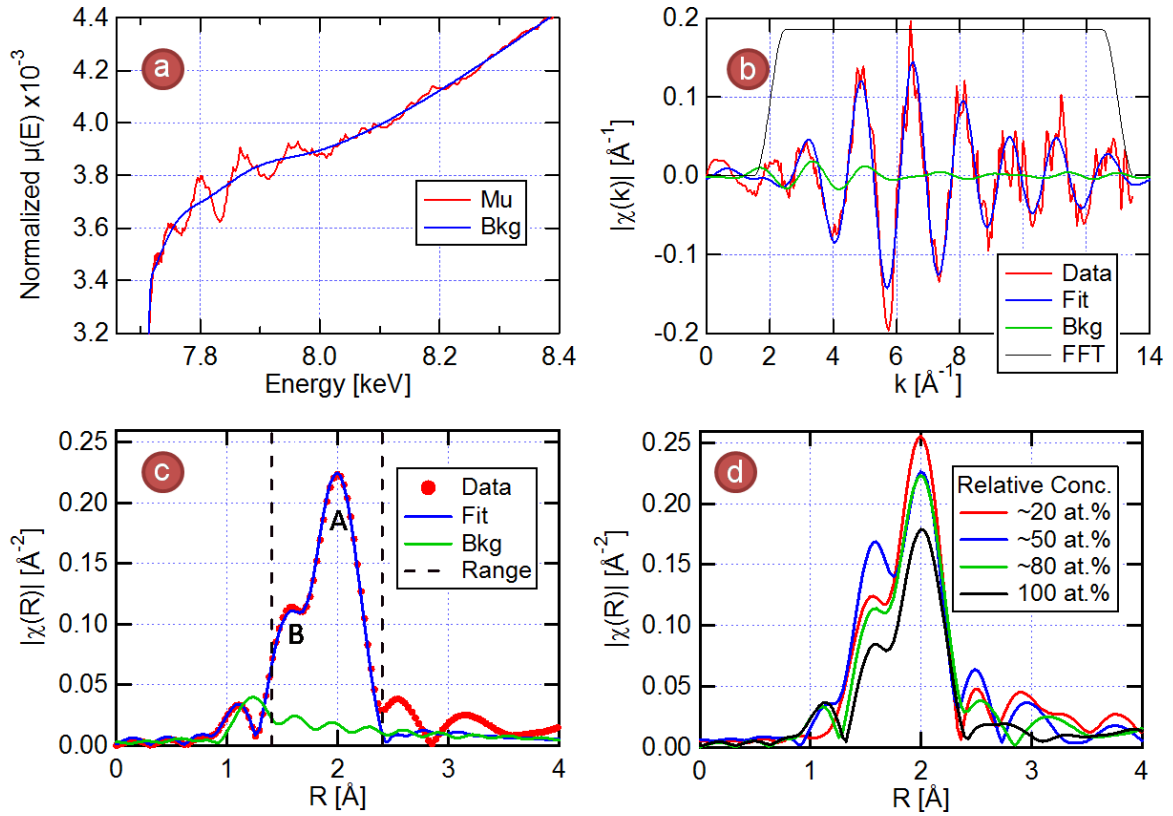


**Figure 4-13:** EXAFS data at the Co edge on a sample with a total doping concentration of ~5.5 at.%. (a)-(c) represent data and fit at the relative concentration Co 80%, Mn 20% or  $\text{Co}_{0.045}\text{Mn}_{0.012}\text{Ge}_{0.943}$ . (a) Absorption with bare-atom background fitted using ATHENA (b) Background subtracted data (k-weight of one) with fit and model from ARTEMIS. Hanning window for FFT is the black curve. (c) Fourier transformed from (b) showing the fit range. Peak positions are not phase shifted, and are therefore, not physical distances. Two peaks in the fit are modeled as an environment where the Co dopant is substitutional (A) and one where it is interstitial (B). (d) Composition evolution of the data.

Figure 4-14 displays atomic models consistent with these fitting results. One scenario is that the two peaks represent two independent or non-interacting environments as shown in (a), with some dopants incorporating substitutionally (red) and others interstitially (blue). At 5.5 at. % total doping, a homogeneous distribution would see one dopant every two or three unit cells, so this interpretation is a possibility. Unfortunately, with only the first coordination shell modeled for each environment, the model is not unique. In fact, because the atomic form factor (i.e.  $Z$ ) for each element is so close, it is uncertain which element is represented by this peak. Figure 4-14 (b) and (c) show configurations that could also occur under the current model. Indeed, others not shown here such as interstitial dimers, small clusters partially bonded with the Ge lattice, and even phase

separations could also explain the B peak without complementary studies to eliminate them. These specific possibilities are discussed below based on other findings.

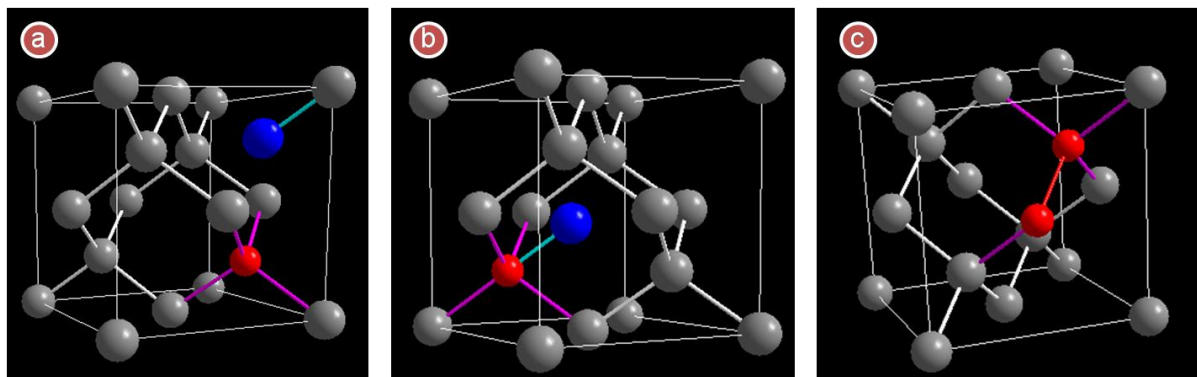


**Figure 4-14: Atomic models used in the fitting process. (a) The actual substitutional site (red) and interstitial site (blue) modeled in the fits. (b) Substitutional-interstitial dimer and (c) Substitution-substitutional dimer. Both (b) and (c) cannot be distinguished from the interstitial situation in (a).**

Fits of Mn EXAFS are shown in Figure 4-15 with (a) a fit for codoping and (b) for Mn-only doping. In the codoping case, three peaks fit well. The strongest peak is modeled as substitutional doping, and the weaker peaks B and C as interstitials (the same as peak B in Co) each containing a different R-value. The Mn-C peak is rather low in R and is slightly suspect as few bond distances are so short. However, repeated attempts to use a higher background removal wiped out both peaks, which seemed unphysical. Indeed in the example shown, peak C is of higher signal than peak B. Additionally, the gray traces in Figure 4-15b show that both peak B and C exist in each dataset where codoping occurred. Still this does not rule out the possibility that the data have systematical trouble with the low-R background removal and could be an artifact.

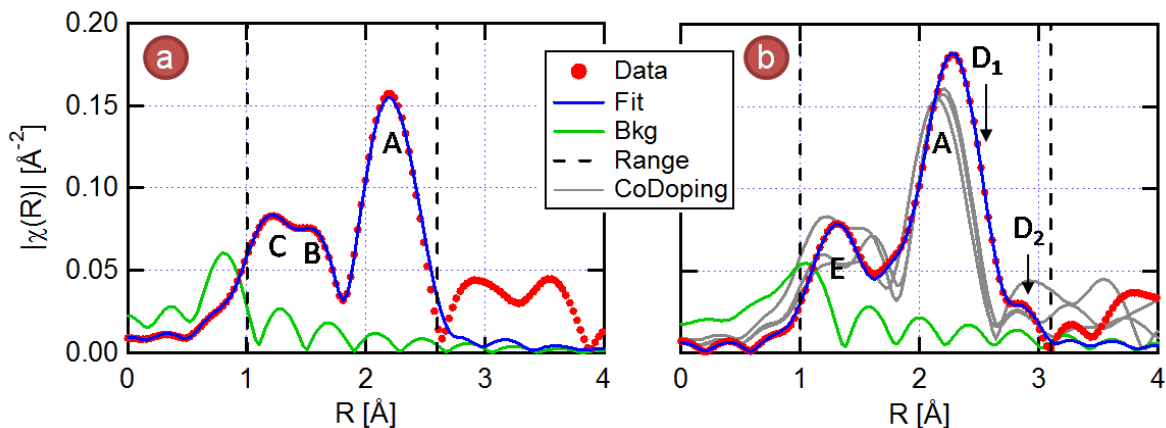


**Figure 4-15: Fourier transformed EXAFS at the Mn edge on the same sample as in Figure 4-13. (a) An example fit at the same concentration in Figure 4-13a, showing three peaks modeled by an environment where the Mn dopant is substitutional (A) and two where it is interstitial (B) & (C). (b) Fit of data where Mn is the only dopant, modeled by a substitutional peak (A), two unique neighbors of  $\text{Ge}_3\text{Mn}_5$  precipitates ( $D_1$  &  $D_2$ ), and NN for MnO (E). EXAFS data from other compositions shown in grey for comparison.**

With such a large contrast from the other datasets, data from the Mn-only doping region of the sample was fit to a much different model – the typical scenario of substitutional and interstitial environments failing to reproduce the data. Because it has been detected in both the binary region of the annealed sample as well as numerous other studies<sup>12-16</sup> of  $\text{Mn}_x\text{Ge}_{1-x}$ ,  $\text{Ge}_3\text{Mn}_5$  was modeled and fit to the data. This structure has a rather complex set of NN since there are two unique Mn sites and one Ge site in the unit cell, but the multiple neighboring distances are easily reduced to three, representing two tetrahedra in the structure. This same simplification was made in a recent study and a diagram of the structure and tetrahedra are described there.<sup>16</sup> A large gap of approximately  $1\text{\AA}$  separates these from the next neighbors, providing a good cut-off for the model. The first NN in this structure are at identical distances as with Mn substitutional sites, but the two other coordination shells with anti-phase relationships to the first allowed for a stable fit and sensitivity to the different environments. To reduce parameters, only one  $E_0$  and one  $\sigma^2$  parameters were used for the  $\text{Ge}_3\text{Mn}_5$  model. When fit, however, the amplitudes for peak A and  $D_1$  were highly correlated and equal to the values for the precipitate, suggesting that a large majority of the Mn was participating in this phase rather than incorporating into the lattice. The dynamic SIMS and XRF

analysis in Section 4.2b corroborate this result. The final peak E was successfully fit to the NN Mn-O bond in MnO, further supporting the presence of surface Mn aggregation even without annealing.

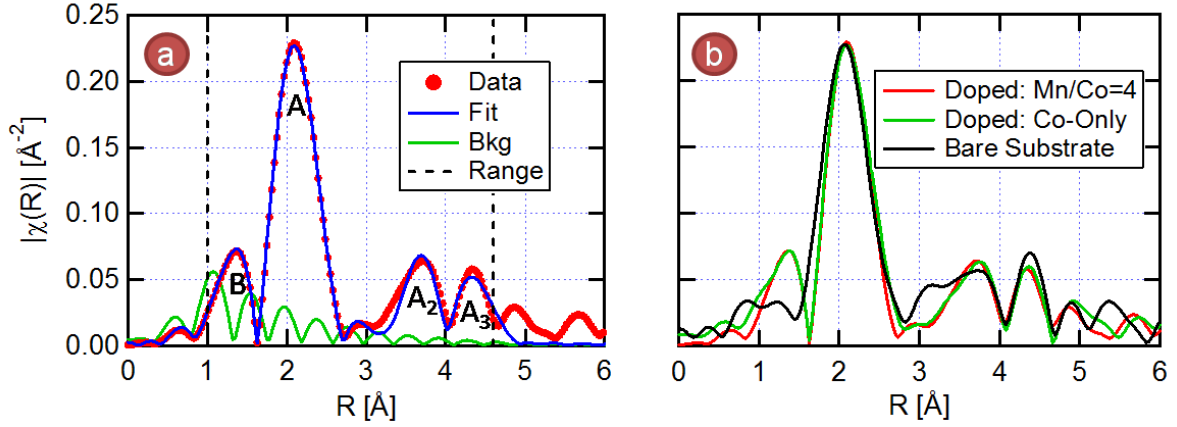


**Figure 4-16: Fourier transformed EXAFS at the Ge edge. (a) Fit to data using three NN for the Ge lattice (A, A<sub>2</sub>, and A<sub>3</sub>), and the same interstitial site (B) as in the Co and Mn datasets. (b) Two datasets from the doped film in Figure 4-13 (red and green) compared with a dataset from a bare substrate (black) whose main difference is the presence of the “B” peak in the doped film.**

To complete the study, a few sets of Ge EXAFS data were also taken. This was particularly challenging, since the film studied was on a Ge substrate. Taking EXAFS data in the traditional geometry would cause the EXAFS signal from the film to be washed out by that of the substrate. Additionally, such a bulk sample would have large self-absorption effects, which wash out the EXAFS signal entirely. To avoid these obstacles, the sample was oriented in grazing incidence geometry below the critical angle of the sample, which was measured to be approximately 0.18° at 12keV. The data was taken at 0.10°, which only probed the film due to the evanescent penetration of the incident beam to a skin depth of a few hundred Angstroms. However, at such a small angle, the footprint of the beam could easily wander off the sample from very small vibrations or beam motion during the scan. Because the data was taken on a binary sample, composition resolution was not compromised, but the success rate of repeatable data was very low. Numerous data sets were, therefore, taken during periods of low traffic in the experiment hall, and only clean, repeatable datasets were used.

The resulting three datasets and one fit are shown in Figure 4-16. Two sets of data were taken from the film and one of a bare substrate for comparison. The fit is of the data taken in the codoping region and clearly shows the first three coordination shells for the Ge lattice with one multi-scattering path also included.<sup>27</sup> These can be seen in all three datasets in Figure 4-16b. As is usual for Ge EXAFS, the amplitudes for  $A_2$  and  $A_3$  are much smaller than for peak A. Because more distant neighbors are well resolved here, their absence in Co and Mn EXAFS demonstrates the higher level of disorder that the substitutional dopants contribute to the lattice. More interesting, however, is the presence of the peak B and the fact that it is only observed in the data taken from a doped film. This peak, modeled with the same environment as peak B in the Co and Mn EXAFS strongly suggests a correlation of the low-R bonding dopant state with the lattice rather than phase separation.

#### 4.4b: Dopant Populations

From the fit parameters of each dataset, physical characteristics can be resolved, better defining the dopant state populations and their effect on the lattice. Figure 4-17a shows the occupancy ( $C$ ) of the dopants into substitutional sites. This was obtained from the amplitude parameter in the fits through the equation  $C=A/S_0^2$ , since the coordination for substitutional sites is known and included in the fit. The data show that codoping generally produces a higher rate of substitution than doping with one species only, which is in agreement with recent first principles calculations for this system.<sup>25</sup> Also in agreement with previous studies<sup>8</sup> is the strain effect from each dopant as inferred from the bond distance in Figure 4-17b. Co, with its shorter bond distance, contracts the lattice. Mn, on the other hand, clearly expands the lattice and the interpretations made in the previous section must be modified to account for this. For example, the Co-Mn dimer proposed above to explain the two linear regions of strain in the CTR analysis are unlikely as



substitutional Mn now explains the positive strain measurements. However, the negative strain in the Mn-rich region must be the result of the secondary Mn dopant species measured in the EXAFS.

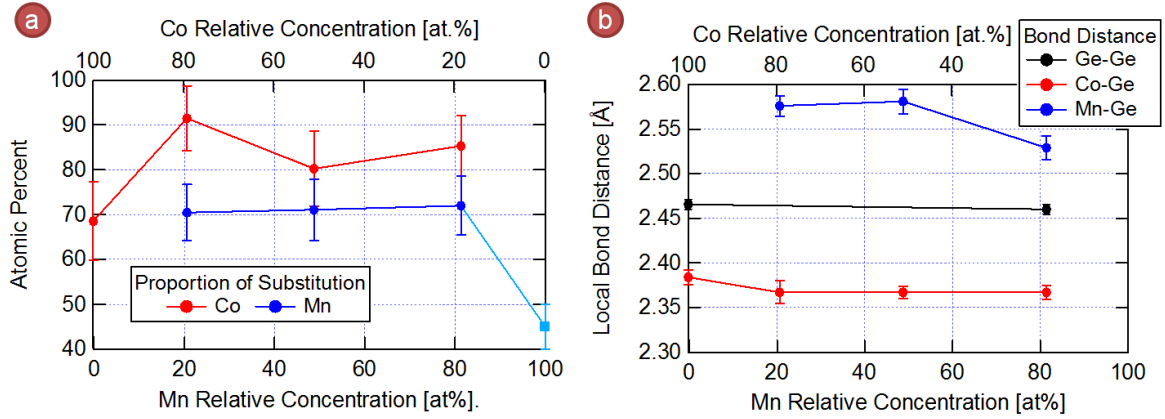


**Figure 4-17: Physical characteristics of the substitutional dopant states calculated from the fit parameters. (a) Occupancy of the substitutional state for each dopant. The value for Mn-only doping is taken from the literature.<sup>13</sup> (b) Bond distance compared to the ideal Ge-Ge distance of the lattice, measured from the Ge EXAFS.**

With the substitutional population and bond distance obtained from EXAFS as well as the doping concentration measured using XRF, the strain effects of the substitutional dopant species can easily be calculated using the following formula.

$$\epsilon = \frac{R_{Co} - R_{Ge}}{R_{Ge}} C_{Co} x + \frac{R_{Mn} - R_{Ge}}{R_{Ge}} C_{Mn} y \quad (4-7)$$

where  $R$  is the bond distance,  $C$  is the substitutional occupancy, and  $x$  and  $y$  are the doping levels for Co and Mn, respectively. Figure 4-18 shows this calculation compared with the strain measurements on the same sample through CTR analysis. In general, the calculated strain dependence is linear, agreeing fairly well with the measured strain in the Co-rich region but increasingly deviating from the measurement with excess Mn.

On the Co-rich side, the agreement of the two suggests that indeed the major dopant state is substitutional. The slight larger compressive strain seen in the calculation compared with the measurement in this region is likely due to other dopant species expanding the lattice. This could

come from peak B in the EXAFS if interpreted as isolated interstitial dopants, interstitial-substitutional dimers [Figure 4-14 (a) or (b)] or even interstitial clusters. Each of these states would cause an expansion of the average lattice constant measured by CTR analysis. At the Mn-rich side, however, there clearly is a population of dopant states counteracting the effect of substitutional doping to contract the lattice. As this effect has an onset at the Mn to Co ratio of 1 and increases with excess Mn, this difference in strain likely arises from a Mn dopant state.

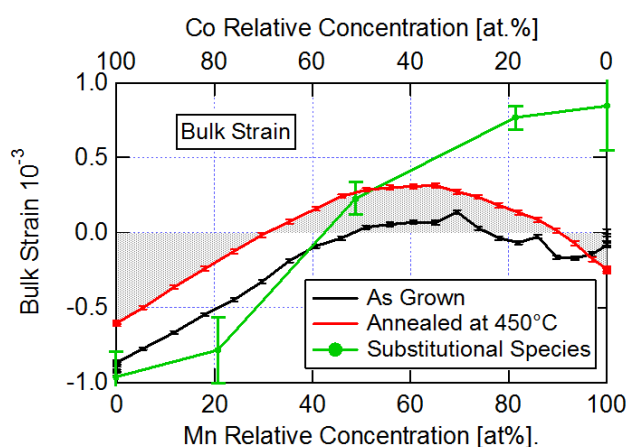


**Figure 4-18: Strain comparison between global XRD measurements and local EXAFS fit results for the as grown sample.**

Unfortunately, little can be resolved conclusively from the fit parameters of the secondary peaks B and C (modeled to be interstitials). One way to establish if the secondary peak seen in the EXAFS data are isolated interstitials or clusters of dopants is to calculate the coordination ( $N$ ) using the formula  $N = A \cdot C / S_0^2$ . This calculation is shown in Figure 4-19a, but the uncertainties from both the amplitude and occupation are so large that the coordination overlaps a range from one to six. Due to the presence of two secondary peaks in the Mn EXAFS, the occupation of each is unknown, and therefore, coordination cannot be determined for this species. Figure 4-19b shows the bond distance represented by the peaks. The bond distances for peak B in Co and Mn EXAFS are close and their uncertainties overlap. However, this does not determine whether they are correlated or they

are the cause of the negative strain at high Mn relative concentrations as the state of these dopants in the lattice (interstitial, substitutional, clusters, etc.) governs their effect on the lattice.

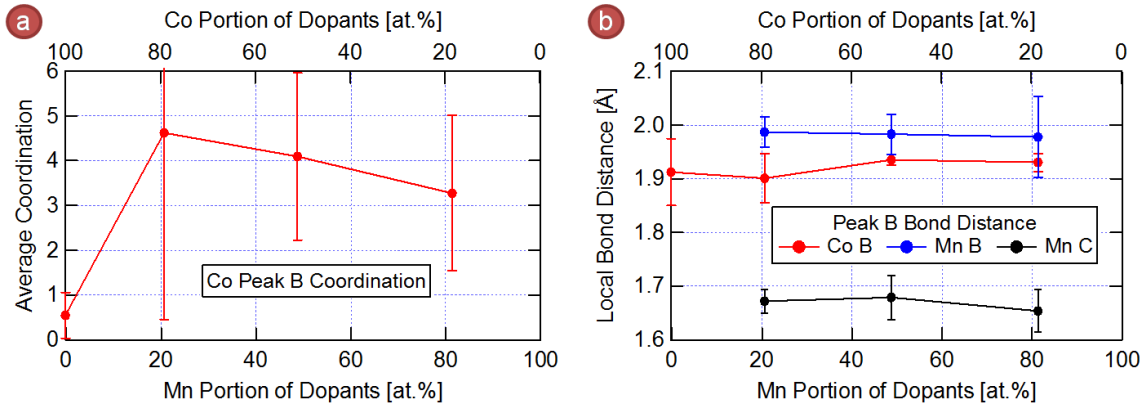


**Figure 4-19: Physical characteristics of the secondary dopant states calculated from the fit parameters. (a) Average coordination of neighbors at peak B in Co EXAFS. (b) Local bond distance measured from B and C peak position in the Mn and Co EXAFS fits.**

Uncertainties notwithstanding, the data do allow for some interpretations. The Co coordination could indicate the presence of small mixed clusters of a few dopants in interstitial locations with at least one bond to a Ge atom of the lattice due to their correlation in Ge EXAFS. This would provide a slight expansion of the lattice over the substitutional dopant effect in the Co-rich side, moving it more in line with the measured strain. The effect could also increase with annealing as seen in Figure 4-18. Additional energy calculations support this possibility with increasing energy savings for dopant dimers and trimers over monomers.<sup>24,28</sup> Atom probe tomography measurements taken on these systems definitively cap the upper end of the cluster size at 3-4 dopants. Able to quantitatively measure the concentration of dopants within a volume resolution of a few unit cells, this technique measures a maximum dopant concentration isosurface at 25 at.%.<sup>29</sup> Finally, the source of the negative strain in Mn-rich regions must be from a Mn-related dopant species that contracts the lattice. Recently, Ottaviano *et. al.* completed Mn EXAFS studies on  $\text{Mn}_x\text{Ge}_{1-x}$  in ion implanted samples and reported the same peak at  $2.0\text{\AA}$ , which they interpreted as a  $\text{Mn}_2$  substitutional dimer<sup>13</sup> based on favorable energy calculations.<sup>24</sup> The formation energy of these

dimers is calculated to be low relative to isolated dopants but to have no net magnetic moment as they interact antiferromagnetically. However, the same energy calculations showed other small clusters of 2, 3, and 4 atoms were also energetically favorable and could also explain both the low-R bond distance and lattice contraction. It is possible that Co clusters in the Co-rich region increasingly populate with Mn with increasing relative Mn concentration, gradually altering their structure to cause a contraction of the lattice when clusters are fully populated by Mn. Further study is necessary to fully probe these possibilities.

#### 4.4c: Electronic and Magnetic Properties

The question of whether codoping with Co is magnetically complementary to Mn doping in Ge and how electronic properties evolve with codoping has been examined using samples with a constant Ge concentration of 96 at. %. To accomplish this, six-terminal measurements were taken at various temperatures and applied fields providing both normal and Hall resistivities, in addition to the usual magnetic information provided by SQUID magnetometry.<sup>70</sup> Due to the magnetic ordering in the system below  $T_c$ , the Hall resistivity exhibits non-linear field dependence known as the anomalous Hall effect and is described using the formula  $\rho_{Hall} = \frac{\rho_0 B}{d} + \frac{\rho_s M}{d}$ , where  $\rho_0$  is the resistivity associated with the ordinary Hall effect,  $\rho_s$  is the coefficient associated with magnetization, and  $d$  is the film thickness.<sup>31</sup> Past magnetic saturation, the carrier concentration and carrier type was extracted from the slope of the Hall resistivity.

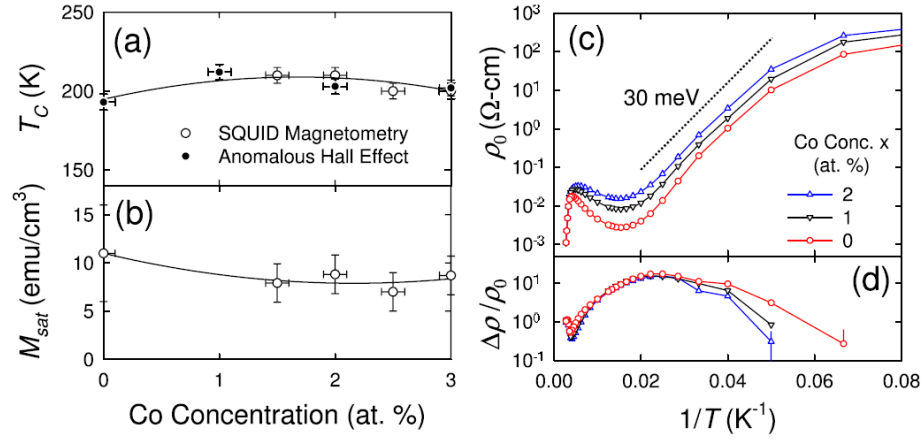


**Figure 4-20: Magnetic and magnetotransport properties of  $\text{Co}_x\text{Mn}_{0.04-x}\text{Ge}_{0.96}$  (001) epitaxial films versus Co concentration  $x$ . (a) Curie temperature and (b) saturation magnetization at 5 K versus  $x$ . (c) Resistivity in zero field and (d) magnetoresistance at 5 T [ $\equiv \rho(H=5\text{ T})/\rho_0 - 1$ ] versus inverse temperature for various  $x$ . The behaviors for  $x \geq 2$  at. % are nearly identical. Lines are guides for the eyes. (Excerpt from Ref. 20)**

The magnetic and magnetotransport measurements show that these samples are  $p$ -type ferromagnetic semiconductors with a very large positive magnetoresistance ratios ( $>10$  at 5 T) and very large anomalous Hall coefficients, consistent with an earlier report for the system.<sup>26</sup> As shown in Figure 4-20, substituting Mn with Co does not significantly affect magnetic and magnetotransport parameters. Although Curie temperature (Figure 4-20a) is slightly enhanced, the saturation magnetization  $M_{\text{sat}}$  (Figure 4-20b) is reduced, which corresponds to a change in the average moment per dopant ion from  $\sim 0.5\mu_B$  at  $x=0$  to  $\sim 0.3\mu_B$ . This is 10x less than calculations for the Mn substitutional dopant state of  $3\mu_B$ .<sup>25,32</sup> The resistivity in the  $p$ -type extrinsic regime also exhibits an increase as Co concentration increases (Figure 4-20c), which is accompanied by a corresponding decrease in the hole concentration from  $1 \times 10^{17}\text{ cm}^{-3}$  at  $x=0$  to  $6 \times 10^{16}\text{ cm}^{-3}$  at  $x=1$  at. % and to  $4 \times 10^{16}\text{ cm}^{-3}$  for  $x \geq 2$  at. %. This indicates that Mn as a dopant is more effective than Co in contributing to the hole concentration and to the magnetization in Ge, which is consistent with the theoretical work.<sup>25</sup>

These results suggest that, although Co increases the population of substitutional Mn species, compensating effects of other dopant states remain. Because Co does not seem to affect

the Mn dopant state that contracts the lattice, it is logical to conclude that this is the compensating state. The possible interpretation of Mn substitutional dimers is in line with these results as calculations show they have both low formation energy and interact antiferromagnetically. Still, the impurity states associated with the two dopants appear to be comparable to each other, as indicated by the nearly identical temperature dependence and activation energies for the transport parameters at low temperature (the dotted line in Figure 4-20c). These findings indicate that as codopants in Ge, Co and Mn are complementary both magnetically and electronically. The low activation energy compared with known values in the low doping regime ( $<1$  at.%)<sup>33</sup> suggests an energy landscape that is significantly different and relatively unexplored. Further spectroscopic studies are needed to better identify the full electronic structure in the band gap of these materials, and both tunneling heterostructures and scanning probe techniques are in development to pursue this information.

#### 4.5 The $(\text{FeCo})_x\text{Ge}_{1-x}$ System

As growth studies of the Fe-Co system also seemed promising, it was studied albeit in the more limited composition of a binary sample  $(\text{Fe}_{0.46}\text{Co}_{0.54})_x\text{Ge}_{1-x}$ . To fully appreciate the possible materials properties of the system, full ternary samples will be of interest in the future. However, growing a binary sample allowed for a study of strain effects from a second substrate GaAs, which has a mismatch of 0.07% with respect to Ge and is on the order of largest strains seen in the stable doping of Co and Mn (Figure 4-11a). To remove systematic errors of growth conditions between the two samples, each substrate was placed in the MBE chamber and grown simultaneously on the same holder. The usual buffer growth (250°C) and anneal (600°C) cycles were used to deposit a Ge buffer on both substrates as these are conditions comparable to those used in depositing Ge/GaAs superlattices.<sup>34,35</sup> Yet, subsequent SIMS analysis indicated the presence of trace Ga in Ge ( $<0.01\%$ ). Growth of the film involved Ge-Co-Ge-Fe multilayers at 250°C with  $x$  varying up to a doping

concentration of 17.1 at.% as determined by XRF. Deposition was terminated at 1000Å, where RHEED analysis determined the thickness dependence to be fully saturated. In this section, the structural disorders, strain states, dopant states, and magnetotransport properties on this sample are presented.

#### 4.5a: Disorders

The evolution of the stacking faults and the possible presence of powder intensities have been examined by XRD using an area detector and using high resolution 2D reciprocal space mapping with a point detector, as shown in Figure 4-21. As described above, we use the area detector to detect the secondary phase and to quantify the intensities of stacking faults and the reciprocal space mapping for quantifying the positions of the diffraction peaks. Shown in Figure 4-21 (a) and (b), intensities within the 2D regime are nearly featureless, while 3D counterparts show stacking fault peaks. There are no detectable intensities from secondary phases. The maximum volume fraction of even a textured secondary phase is estimated to be about 0.3% based on the discussion in Section 3-3d. By contrast, previous work on Fe-only doping into Ge at 5 at.% reported Fe-rich phase separations, which initially missed in standard XRD,<sup>36</sup> later showed levels on the order of 2% volume fraction under SPEM<sup>35</sup> – well within the detection limit of this method.

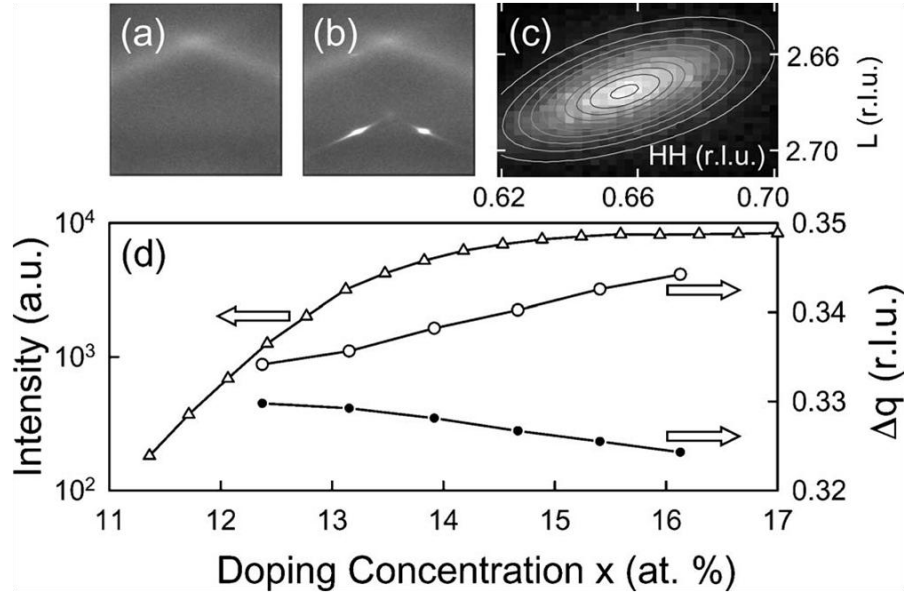


**Figure 4-21: Evolution of the intensity and position of the stacking fault peak for the sample grown on Ge (identical to that grown on GaAs). (a) and (b) XRD intensities detected by wide angle methods for  $x=8$  and 15 at.%, respectively. (c) A high resolution reciprocal map around the  $(2/3, 2/3, 8/3)$  stacking fault peak using a point detector. The elliptical lines are from a 2D Gaussian fit. (d) The integrated intensity (triangle) of the stacking fault peak (b) as a function of the doping concentration. The in-plane (HH) and out-of-plane (L) peak positions in reciprocal space of the stacking fault in (c) shown as differences ( $\Delta q$ ) to the nearest Bragg reflection:  $\Delta q=3-L$  (closed circles) and  $\Delta q=1-HH$  (open circles). (Excerpt from Ref. 38)**

The integrated intensity of the stacking fault peak exhibits an exponential decrease as the doping concentration decreases from 17 at. % towards the roughening transition of  $\sim 11$  at.%, as shown in the triangles in Figure 4-21d. This confirms the RHEED analysis discussed in Section 4.1b, such that the appearance of stacking faults coincides with the onset of the 3D rough growth. The stacking fault peaks as measured by the high resolution reciprocal space mapping (Figure 4-21c) have been fit using a 2D Gaussian function (elliptical contours in the figure). From the fit, the in-plane (HH) and out-of-plane (L) peak positions in reciprocal space of the stacking fault have been determined. The results are shown in Figure 4-21d, as they are expressed in the position of the stacking fault peak from that of the (113) reflection of the substrate. The lattice associated with the stacking faults appears to exhibit a very large tetragonal distortion along the growth direction, and the distortion increases monotonically with doping concentration.



Such a large effect does not appear to be consistent with effects associated with the strain relaxation process and differential thermal expansions. One possibility studied is the FeCoGe hexagonal phase whose in-plane lattice constant is equal to that of the Ge (111) at 4.00Å.<sup>39,40</sup> With lattice matching, this phase could grow epitaxially on (111) facets exposed during rough growth and could be the cause of the twinned reflections appearing in the surface sensitive RHEED studies. Upon indexing these reflections in the hexagonal coordinate system, however, the in-plane lattice constant moves away from FeCoGe in-plane lattice constant. Additionally, the c-axis hexagonal lattice constant of the twinned reflection changes lethargically from 4.90-4.92Å throughout the composition spread, never reaching the value of the FeCoGe phase at 5.03Å.<sup>39,40</sup> With this evidence and such a high metal concentration required, it is unlikely that the stacking faults are the result of this competing phase. Therefore, the large tetragonal distortion remains unexplained, requiring further study.

#### 4.5b: Strain States

The coherent 2D growth and presence of the roughening transition at 11 at.% is further confirmed by CTR analysis and high resolution reciprocal space maps. Data and fits from 2D and 3D regions of the film on both substrates are shown in Figure 4-22a with coherent interference fringes in the intensity profiles for atomically smooth 2D growth disappearing when the surface becomes rough at higher doping concentrations. Immediately from the data there are notable differences between the 2D growth of the film on Ge and GaAs substrates. The first is that the zeroth order fringe for the film grown on Ge (circles) is shifted to a higher value in reciprocal space (the shoulder on the right), indicating that the out of plane lattice constant of the film is smaller than that of the Ge substrate. In contrast the counterpart grown on GaAs (squares) is shifted to a lower value (the shoulder on the left), indicating a larger lattice constant than that of the GaAs substrate. The former corresponds to an out-of-plane compression, while the latter corresponds to a tensile strain out of

plane. A second important difference is the order to which the fringes remain above the noise. Although both samples exhibit fringes, those in data taken from the sample grown on GaAs die out much earlier than the counterpart on Ge. This indicates a higher surface roughness and internal disorder in the film on GaAs, which could be from random defects associated with Ga diffusion into the film.

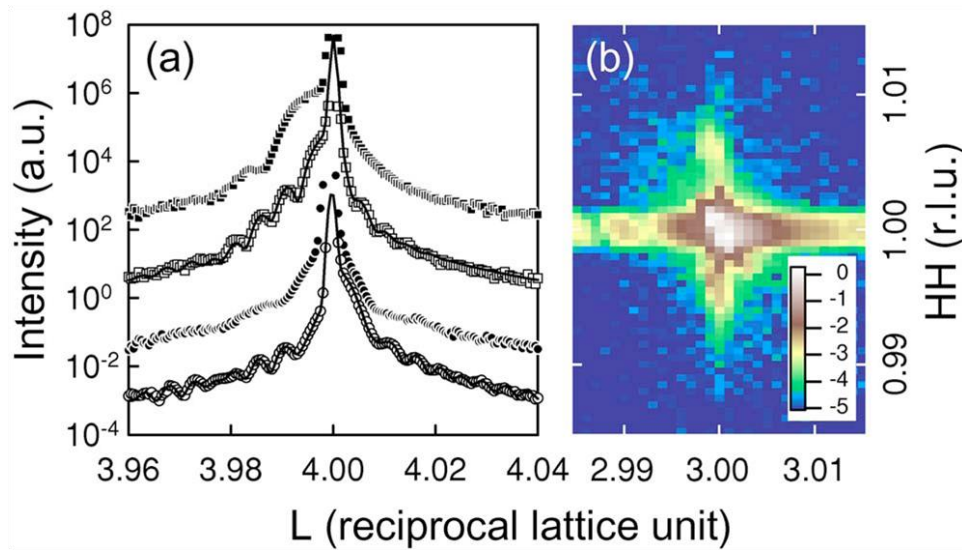


**Figure 4-22: (a)** X-ray diffraction intensities along [00L] rod through the Ge (004) reflection for samples at different doping concentrations and on different substrates. 2D coherent films exhibit XRD fringes (open symbols), which are absent in 3D rough films (solid symbols). The circle and square symbols correspond to films grown on Ge (001) and GaAs (001) substrates, respectively. The lines are fits discussed in Section 4.3. For clarity the curves are shifted vertically from each other by two decades. **(b)** High resolution reciprocal map around the (113) reflection at  $x \sim 8$  at.%. The numbers in the legend for the intensity corresponds to the exponent of the base 10 logarithmic scale. The coherent truncation rod with intensity oscillations (for  $L < 3$ ) along the [11L] direction is clearly shown. The rod width at  $L=3.01$  corresponds to instrument resolution. (Excerpt from Ref. 38)

A typical high resolution XRD reciprocal space map around the (113) Bragg reflection within the 2D growth regime is also shown in Figure 4-22b. The sharp truncation rod with coherent fringes along the out-of-plane (00L) direction shows that the film is coherent with respect to the substrate. In-plane relaxation of a 2D film would cause a separate truncation rod to form in reciprocal space offset in-plane (HH) from the substrate rod due to the different in-plane lattice constant. The width (along the in-plane HH direction, vertical in the figure) of the truncation rod away from the (113)

reflection of the substrate is that of the instrument resolution, resolving in-plane coherence to less than 0.1%. These reciprocal space maps were taken on each sample and showed the same characteristics of coherent 2D growth.

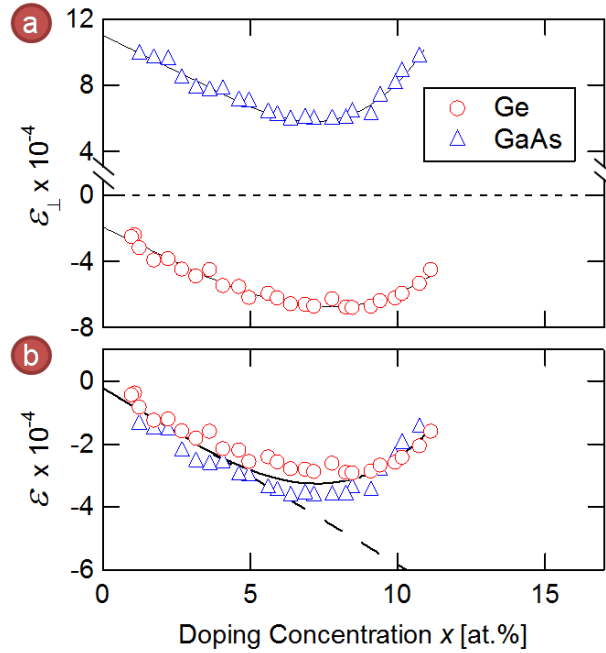


**Figure 4-23: Strain as a function of total doping for films grown on Ge (red circles) and GaAs (blue triangles). (a) Strain perpendicular to the respective substrates showing one with tensile strain and the other with compressive strain. (b) Bulk strain corrected for elastic distortion and compared with the Ge lattice constant.**

Using the fitting methods on the CTR intensity profiles described in Section 3.2c, the strain state of each film in the 2D growth regime was measured. Figure 4-23a shows the out-of-plane strain before correcting for elastic distortion due to in-plane coherence. Although the two films exhibit very different absolute strain on each substrate, the trends are identical with a roughening transition at 11at.% in agreement with RHEED analysis. After elastic correction, the bulk strain with respect to an undoped Ge lattice is shown in Figure 4-23b as defined by Equation (4-6). Here, the strain evolution of the film on the two substrates collapses onto each other, showing conclusively that the effects are an intrinsic composition-driven phenomenon. Up to 6 at.% doping concentration, the strain exhibits a linear composition dependence obeying Vegard's law. With

increasing doping, the strain reverses direction but remains 2D and coherent. The gradual reversal suggests a saturation of one dopant state and the nucleation of a new state.

#### 4.5c: Dopant and Magnetic States

The interpretation of a change in dopant states is supported by EXAFS data taken at both the Co and Fe  $K_{\alpha}$  absorption edges. Here the data were taken beyond  $k=15 \text{ \AA}^{-1}$  and background removals up to  $1.1 \text{ \AA}$  and  $1.2 \text{ \AA}$  were completed in ATHENA for Co and Fe data, respectively. Reversal in the linear strain dependence is correlated with very different near edge behavior as seen in the data below the Hanning window in Figure 4-24a. In this low- $k$  region, a large oscillation appears in the data taken at low doping (2.7 at.%), which is suppressed in the data taken above the reversal (7.0 & 13.1 at.%). In the high- $k$  region, the data at low doping appears to have more structure than at high doping, suggesting more ordering. Additionally, a shift in the B peak position is apparent in the Fourier transformed data (Figure 4-24b), from low to higher doping regions. Notably, the probable substitutional peak (A) does not change in any way other than being slightly wider at higher doping. Comparing the substitutional peak position with that in Figure 4-16 shows that the presence of substitutional Fe contracts the lattice as the Fe-Ge bond is clearly smaller than that of Ge-Ge.

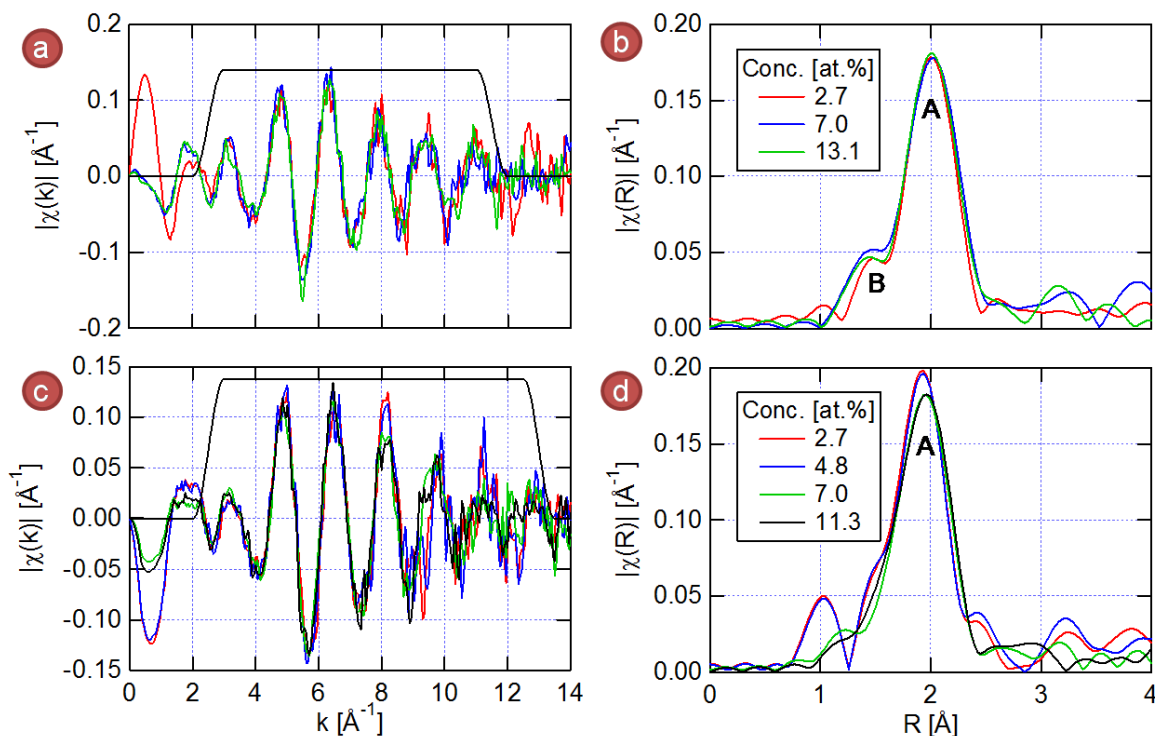


**Figure 4-24:** EXAFS on the  $(\text{Fe}_{0.46}\text{Co}_{0.54})_x\text{Ge}_{1-x}/\text{Ge}$  (001) sample for selected concentrations  $x$ . (a) & (b) represent Fe  $\chi(k)$  and  $\chi(R)$  data, respectively before the strain reversal (red curves), after the reversal (blue), and after the roughening transition (green). (c) and (d) are the same data for Co with two datasets (red & blue) before the reversal, and two (green & black) after. The Hanning window used for the Fourier transform is shown in black in (a) and (c).

More dramatic differences arise in the Co EXAFS. Again, the near-edge structure (low- $k$ ) below the strain reversal is different than that from data at higher doping (Figure 4-24c). Within the Hanning window, differences can be seen in the oscillations that result in a dramatically different  $\chi(R)$  in Figure 4-24d. At low doping (2.7 & 4.8 at.%), the A peak suggests a shorter bonding distance than with Co EXAFs taken earlier (Figure 4-13) and exhibits several surrounding peaks of lower amplitude. In contrast, data taken from after the strain reversal shows a peak A position consistent with earlier EXAFS and no satellite peaks. As this data has not been fit to models, specific dopant states cannot be determined, but the qualitative change in the local structure correlating with a strain reversal globally in the matrix points to a shift in dopant states above a critical doping concentration.

Further supporting this interpretation are results from x-ray magnetic circular dichroism taken on this sample. In this technique, circularly polarized x-rays incident on the sample are absorbed as their energy is scanned across an absorption edge that corresponds to an electron d-state transition. If the dopants are magnetically active in the matrix (i.e. their d-state electrons are spin-polarized), they will preferentially absorb one polarization over the other (right circular polarization versus left). Using this mechanism, the magnetic moment of the dopant in the matrix can be measured quantitatively. Measuring hysteresis curves can reveal the magnetic interaction that moment has in the matrix (ferromagnetic, paramagnetic, etc.). The results on both Fe and Co dramatically show a correlation between structure and magnetic moment. At doping concentrations below the strain reversal, the magnetic moment of both Fe and Co are linear with concentration. While hysteresis loops reveal Co to be paramagnetic in the matrix, the Fe are ferromagnetic with magnetic moment per ion similar to the species in bulk. Above the concentration of the strain reversal, the total magnetic moment of both Fe and Co dopants plateaus with additional dopants paramagnetic. This behavior suggests that Fe initially dopes into a ferromagnetic state up to a critical composition. Upon saturation of this state, Fe must dope elsewhere in the lattice where its magnetic properties are nullified. Furthermore, the similar behavior of the Co moment with  $x$  suggests a correlation between Fe and Co states in the lattice. The relatively low doping concentration at the strain reversal (much less than one dopant per unit cell) and the low values of strain at this point suggests that the growth conditions are not yet optimized for this material. Other growth conditions and dopant ratios could push this ferromagnetic doping state to higher concentrations.

#### 4.5d: Bulk Electronic and Magnetic Properties

Finally, electronic and magnetic studies of the material's bulk properties reveal key insights to important parameters behind ferromagnetic ordering. Properties of both films were investigated

using the Hall effect and SQUID magnetometry. At low doping concentrations, the film on a Ge substrate has semiconducting electrical properties with resistivities diverging as temperature approaches zero. Activation energies for extrinsic conduction occur at 70meV for doping concentrations up to the strain reversal as seen in Figure 4-25a. The film also exhibits large magnetoresistance ratios of 100 at 5T. As  $x$  increases further, the activation energy gradually decreases to 4meV resulting in metallic behavior associated with the onset of 3D rough growth at  $x > 11$  at.%. By contrast, the film on GaAs exhibits no activation energy, being fully metallic at all doping concentrations (Figure 4-25a black circles). This can be explained by the presence of Ga in the matrix with its shallow acceptor level in Ge.

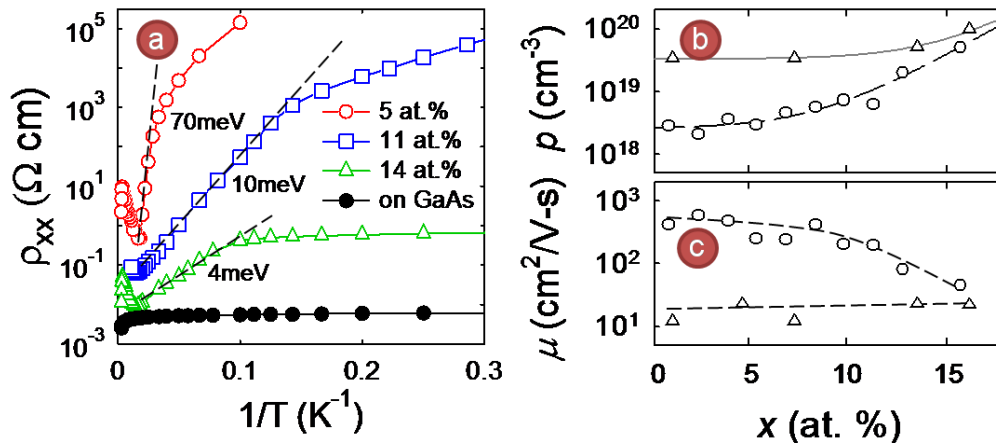


**Figure 4-25: Transport properties of  $(\text{Fe}_{0.46}\text{Co}_{0.54})_x\text{Ge}_{1-x}$ . (a) Resistivity versus inverse temperature at various doping concentrations  $x$ . (b) Carrier concentration and (c) carrier mobility measured via the Hall Effect for films grown on Ge (circles) and GaAs (triangles). Lines are guides for the eyes.**

The results for carrier concentration, shown in Figure 4-25b, also show the effect of Ga in the matrix with higher levels compared with the counterpart on Ge. Doping is still effecting both samples as carrier concentration in both increases with  $x$ , the two nearly merging at 16 at.%. The higher disorder associated with Ga diffusion into the lattice as measured in the CTR analysis also affects the electrical properties, as the carrier mobility (Figure 4-25c) is much lower in the film on the GaAs substrate than Ge. This provides a key difference for the magnetic ordering as the film on

Ge shows large magnetoresistance and Anomalous Hall effect near room temperature (signs of ferromagnetic ordering), while the film on GaAs shows neither. With higher carrier concentration and the same doping levels, the Zener model predicts ferromagnetic ordering for the film grown on GaAs given the it is measured in the film on Ge. From these results, it can be inferred that an important factor not considered in this simplified model is the carrier mobility.

#### 4.6 Summary

Compositional and epitaxial effects on the structural ordering of the full ternary compositional phase space of  $\text{Co}_x\text{Mn}_y\text{Ge}_{1-x-y}$  and the system of  $(\text{Fe}_{0.46}\text{Co}_{0.54})_x\text{Ge}_{1-x}$  have been studied using complementary techniques based primarily on x-ray scattering. In the Co-Mn system, codoping is shown to stabilize dopant incorporation into the lattice to much higher concentrations above the solubility levels of the individual dopants. Specifically, energetics and kinetics of growth are controlled to relieve strain and suppress the formation of crystal defects and dopant precipitates. Especially in the case of Mn doping, trace amounts of Co reduces dopant diffusion and prevents the formation of Mn phase separations and surface aggregation. Comparison of local atomic dopant environments and bulk strain show dopant effect on the lattice and reveal an increase of substitutional doping in the codoping region over using a single dopant. Although higher doping concentration can be achieved, codoping does not suppress compensating effects of a third dopant state (potentially Mn substitutional dimers or small clusters) that reduce the overall carrier concentration and magnetic moment.

Relatively high doping concentrations are also achieved in the Fe-Co system where coherent epitaxial growth is free from detectable crystal defects or phase separation and correlates with ferromagnetic signals in these materials. However, at lower doping concentrations, the ferromagnetic dopant state saturates, causing the excess dopants to incorporate into a



paramagnetic state. Finally, the presence of Ga in the matrix is seen to destroy ferromagnetic ordering, revealing carrier mobility as an important factor in magnetic properties in these materials.

## Bibliography

1. Ohldag, H. et al. Magnetic moment of Mn in the ferromagnetic semiconductor (Ga<sub>0.98</sub>Mn<sub>0.02</sub>)As. *Appl. Phys. Lett.* **76**, 2928-2930 (2000).
2. Yu, K.M. et al. Effect of the location of Mn sites in ferromagnetic Ga<sub>1-x</sub>Mn<sub>x</sub>As on its Curie temperature. *Phys. Rev. B* **65**, 201303 (2002).
3. Blinowski, J. & Kacman, P. Spin interactions of interstitial Mn ions in ferromagnetic GaMnAs. *Phys. Rev. B* **67**, 121204 (2003).
4. Máca, F. & Mašek, J. Electronic states in Ga<sub>1-x</sub>Mn<sub>x</sub>As: Substitutional versus interstitial position of Mn. *Phys. Rev. B* **65**, 235209 (2002).
5. Kroemer, H. & Kittel, C. *Thermal physics*. (W. H. Freeman: San Francisco,).
6. Matthews, J. *Epitaxial growth*. (Academic Press: New York, 1975).
7. People, R. & Bean, J.C. Calculation of critical layer thickness versus lattice mismatch for Ge<sub>x</sub>Si<sub>1-x</sub>/Si strained-layer heterostructures. *Appl. Phys. Lett.* **47**, 322-324 (1985).
8. Tsui, F., He, L., Tkachuk, A., Vogt, S. & Chu, Y.S. Evidence for strain compensation in stabilizing epitaxial growth of highly doped germanium. *Phys. Rev. B* **69**, 081304 (2004).
9. Ueno, K., Kawayama, M., Dai, Z., Koma, A. & Ohuchi, F. Growth and characterization of Ga<sub>2</sub>Se<sub>3</sub>/GaAs(100) epitaxial thin films. *JOURNAL OF CRYSTAL GROWTH* **207**, 69-76 (1999).
10. Oishi, K., Kobayashi, S. & Kaneko, F. Growth and characterization of CuGaS<sub>2</sub> thin films on (100) Si by vacuum deposition with three sources. *JOURNAL OF CRYSTAL GROWTH* **153**, 158-163 (1995).
11. Karpenko, O.P., Yalisove, S.M. & Eaglesham, D.J. Surface roughening during low temperature Si(100) epitaxy. *J. Appl. Phys.* **82**, 1157-1165 (1997).
12. Ottaviano, L. et al. Phase separation and dilution in implanted Mn<sub>x</sub>Ge<sub>1-x</sub> alloys. *Appl. Phys. Lett.* **88**, 061907-3 (2006).
13. Ottaviano, L. et al. Direct structural evidences of Mn dilution in Ge. *J. Appl. Phys.* **100**, 063528-4 (2006).
14. Bihler, C. et al. Structural and magnetic properties of Mn<sub>5</sub>Ge<sub>3</sub> clusters in a dilute magnetic germanium matrix. *Appl. Phys. Lett.* **88**, 112506-3 (2006).
15. Li, A.P. et al. Dopant segregation and giant magnetoresistance in manganese-doped germanium. *Phys. Rev. B* **75**, 201201-4 (2007).
16. Rovezzi, M. et al. Atomic structure of Mn-rich nanocolumns probed by x-ray absorption spectroscopy. *Appl. Phys. Lett.* **92**, 242510-3 (2008).
17. Edmonds, K.W. et al. Mn Interstitial Diffusion in (Ga,Mn)As. *Phys. Rev. Lett.* **92**, 037201 (2004).

18. Gambardella, P. et al. Surface characterization of  $\text{Mn}_{1-x}\text{Ge}_x$  and  $\text{Cr}_y\text{Mn}_{1-y}\text{Ge}$  dilute magnetic semiconductors. *Phys. Rev. B* **75**, 125211-7 (2007).
19. Zhu, W., Weitering, H.H., Wang, E.G., Kaxiras, E. & Zhang, Z. Contrasting Growth Modes of Mn on Ge(100) and Ge(111) Surfaces: Subsurface Segregation versus Intermixing. *Phys. Rev. Lett.* **93**, 126102 (2004).
20. Collins, B.A., Chu, Y.S., He, L., Zhong, Y. & Tsui, F. Dopant stability and strain states in Co and Mn-doped Ge (001) epitaxial films. *Phys. Rev. B* **77**, 193301-4 (2008).
21. Tsui, F. et al. Combinatorial synthesis and characterization of a ternary epitaxial film of Co and Mn doped Ge (0 0 1). *Applied Surface Science* **254**, 709-713 (2007).
22. Wei, L.Y. Diffusion of silver, cobalt and iron in germanium. *Journal of Physics and Chemistry of Solids* **18**, 162-174 (1961).
23. Robinson, I. *Surface Crystallography, Handbook on Synchrotron Radiation*. **III**, (North-Holland: 1991).
24. Continenza, A., Profeta, G. & Picozzi, S. Transition metal doping and clustering in Ge. *Appl. Phys. Lett.* **89**, 202510-3 (2006).
25. Continenza, A., Profeta, G. & Picozzi, S. Transition metal impurities in Ge: Chemical trends and codoping studied by electronic structure calculations. *Phys. Rev. B* **73**, 035212-10 (2006).
26. Tsui, F. et al. Novel Germanium-Based Magnetic Semiconductors. *Phys. Rev. Lett.* **91**, 177203 (2003).
27. Araujo, L.L., Foran, G.J. & Ridgway, M.C. Multiple scattering effects on the EXAFS of Ge nanocrystals. *Journal of Physics: Condensed Matter* **20**, 165210 (2008).
28. Continenza, A., Profeta, G. & Picozzi, S. Transition metal doping in Ge. *Journal of Magnetism and Magnetic Materials* **310**, 2147-2149 (2007).
29. Tsui, F. & Collins, B. Private Communication. (2009).
30. He, L. *Novel properties of magnetic epitaxial films of Co, Mn and Ge ternary system*. (2005).
31. Hurd, C. *The Hall effect in metals and alloys*. (Plenum Press: New York,, 1972).
32. Weng, H. & Dong, J. First-principles investigation of transition-metal-doped group-IV semiconductors:  $\text{R}_x\text{Y}_{1-x}$  (R=Cr,Mn,Fe; Y=Si,Ge). *Phys. Rev. B* **71**, 035201 (2005).
33. Woodbury, H.H. & Tyler, W.W. Properties of Germanium Doped with Manganese. *Phys. Rev.* **100**, 659 (1955).
34. Chang, C., Segmuller, A., Chang, L.L. & Esaki, L. Ge-GaAs superlattices by molecular beam epitaxy. *Appl. Phys. Lett.* **38**, 912-914 (1981).
35. Chang, C. & Kuan, T. Structural studies of Ge--GaAs interfaces. *J. Vac. Sci. Technol. B* **1**, 315-319 (1983).

36. Choi, S. et al. Ferromagnetic properties in Cr, Fe-doped Ge single crystals. *J. Appl. Phys.* **93**, 7670-7672 (2003).
37. Kang, J. et al. Spatial Chemical Inhomogeneity and Local Electronic Structure of Mn-Doped Ge Ferromagnetic Semiconductors. *Phys. Rev. Lett.* **94**, 147202 (2005).
38. He, L. et al. Epitaxial growth of  $(\text{FeCo})_{\text{x}}\text{Ge}_{1-\text{x}}$ (001). *J. Vac. Sci. Technol. B* **25**, 1217-1220 (2007).
39. Kanomata, T. & Goto, T. Note on the crystal-structure of FeCoGe and FeNiGe. *Physica Status Solidi A-Applied research* **111**, K1-K6 (1989).
40. Szytuła, A., Pezdziwiatr, A., Tomkiewicz, Z. & Bazela, W. Crystal and magnetic structure of CoMnGe, CoFeGe, FeMnGe and NiFeGe. *Journal of Magnetism and Magnetic Materials* **25**, 176-186 (1981).

# Chapter 5 Crystallographic and Chemical Ordering in Heusler Alloys

---

Heusler alloys are FCC ferromagnetic ternary compounds that contain two transition metal elements and a third element from either group III, IV, or V, and they chemically order in the  $L2_1$  structure, as detailed in Chapter 1. Some of them were the first predicted half metals, including  $\text{Co}_2\text{MnGe}$  and  $\text{Co}_2\text{MnSi}$ <sup>1</sup> the subject of this thesis, but despite extensive studies,<sup>2-4</sup> the highest spin polarization measured to date has been less than 60% in  $\text{Co}_2\text{MnSi}$ .<sup>5</sup> First principals calculations have revealed that states in the minority band gap can form near the Fermi level in the presence of various structural and chemical disorders.<sup>6-8</sup> Specifically, antisites and site swapping between Co and Mn were shown by Picozzi *et. al.* to have low formation energy and cause minority states to form.<sup>8</sup> Later, calculations by Galanakis and coworkers showed that the half metallic gap forms from strongly hybridized states between atoms in the Co sublattice that bond with neighboring Mn atoms, and therefore, disruption of this chemical ordering would destroy the half metallic state.<sup>9</sup> Neutron diffraction studies on bulk samples have indeed shown evidence of these disorders.<sup>10,11</sup> Epitaxial growth methods are of particular interest, therefore, to study the effects of nonequilibrium conditions on these disorders. Yet, studies completed thus far have not yielded definitive results due to their off-stoichiometry and small size precluding neutron studies.<sup>11,12</sup> In these studies, it is suspected that off-stoichiometry are causes of the disorders found. Combinatorial MBE is particularly well suited to study these effects, but a technique sensitive to the specific chemical disorders discussed above is required.

In this chapter, structural and chemical ordering in epitaxial films of  $\text{Co}_x\text{Mn}_y\text{Ge}_z$  and  $\text{Co}_x\text{Mn}_y\text{Si}_z$  using a variety of x-ray techniques is presented. The films were grown on Ge (111) substrates – this choice being the result of theoretical work<sup>13</sup> that suggests a more robust half-metallic state on this surface. Specific elemental and structural disorders, predicted to destroy the half-metallic state in these alloys, are identified and quantified using anomalous diffraction techniques. The dependence on composition has been examined. Through full spectrum modeling and fitting of these data, this method is found to be particularly sensitive to elemental site specific occupancies in the compound and, therefore, overcome the low atomic number (z) contrast of typical x-ray scattering techniques.

### 5.1 Epitaxial Phase Diagram of $\text{Co}_x\text{Mn}_y\text{Ge}_z$

In studying the extent to which the Heusler structure can be stabilized in compositional phase space, multiple samples were grown on Ge substrates and analyzed via RHEED analysis. These studies, similar to those on DMS materials, resulted in growth conditions aimed at maximizing the structural quality of the films deposited. Earlier work determined that the optimum parameters are at 250°C growth temperatures accompanied by a 20min annealing cycle at 450°C, producing smooth 2D epitaxial growth near the Heusler stoichiometry.<sup>14,15</sup> For a complete study of crystallographic ordering using x-ray techniques, one ternary sample was examined, comprising of the entire compositional phase space. The film thickness at the Ge apex was  $630 \pm 10 \text{ \AA}$  as determined by CTR analysis, corresponding to approximately  $350 \text{ \AA}$  in compositional regions near the Heusler stoichiometry. Using x-ray crystallography techniques, the structural phase and quality were studied as a function of composition to create an epitaxial phase diagram of this materials system.

### 5.1a: Crystallographic Phases

Preliminary studies show that  $\text{Co}_x\text{Mn}_y\text{Ge}_z$  films grow epitaxially and exhibit either hexagonal or cubic phases depending on the composition. It is important to note that in order to create a phase diagram from a ternary sample with any resolution, if a full crystallographic study were to be undertaken at every composition, a prohibitive amount of time would be required. A more practical approach would be to take a short reciprocal space scan sensitive to the phase boundaries at every composition and to carry out full crystallographic study at only several compositions. This would require a clear understanding of the symmetry and size of the reciprocal lattice for the various phases as shown in the schematic diagram in Figure 5-1. In order to conveniently express the epitaxial relationship between the alloy phases and the substrate and appropriately account for their strain, a hexagonal surface coordinate system<sup>16</sup> was employed, whose a- and b-axes are parallel to, and c-axis is perpendicular to the substrate surface. In this hexagonal coordinate system, the extended unit cell for the Ge substrate has a hexagonal structure with the lattice parameters,  $a = \frac{a_0}{\sqrt{2}}$  and  $c = \sqrt{3}a_0$ , where  $a_0$  is the cubic lattice constant of Ge. Consequently, the reciprocal space of the Ge substrate can be indexed using hexagonal indices,  $(HKL)_h$ , which are related to the conventional cubic indices,  $(hkl)_c$ , through the following coordinate transformation matrices.

$$\begin{pmatrix} H \\ K \\ L \end{pmatrix} = \begin{pmatrix} -1/2 & 1/2 & 0 \\ 0 & -1/2 & 1/2 \\ 1 & 1 & 1 \end{pmatrix} \begin{pmatrix} h \\ k \\ l \end{pmatrix} \quad \text{and} \quad \begin{pmatrix} h \\ k \\ l \end{pmatrix} = \begin{pmatrix} -4/3 & 2/3 & 1/3 \\ 2/3 & 2/3 & 1/3 \\ 2/3 & 4/3 & 1/3 \end{pmatrix} \begin{pmatrix} H \\ K \\ L \end{pmatrix} \quad (5-1)$$

Several examples of the conversion are shown in Figure 5-1.  $|\mathbf{q}_{\text{perp}}| = (2\pi/a)L$  and  $|\mathbf{q}_{\text{parallel}}| = (2\pi/a)\sqrt{4(H^2 + HK + K^2)}/3$ . Subscripts will be used to avoid confusion between the two systems.

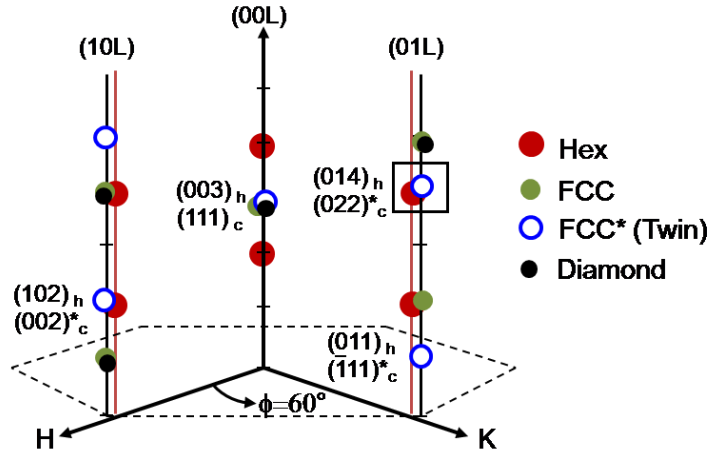


**Figure 5-1: Schematic diffraction patterns of  $\text{Co}_x\text{Mn}_y\text{Ge}_z$  grown on Ge (111) represented in the hexagonal coordinate system registered with the substrate. Circles represent diffraction spots for various phases. Key reflections are labeled by their hexagonal and cubic coordinates.**

In the schematic, the diamond pattern is shown as black circles and was used as a reference for scaling of reciprocal space, as these strong patterns occurred over the entire sample from the substrate. Since the diamond structure is two FCC sublattices separated by a basis, its pattern in reciprocal space is similar to that of FCC (green circles) with the noted absence of the  $(002)_c$  reflection. The lattice constant of the film can be obtained from the position of the film reflection in reciprocal space as this position measures the ratio between substrate and film spacings (i.e.  $H$  or  $K = a_{\text{Ge}}/a_{\text{film}}$  and  $L = c_{\text{Ge}}/c_{\text{film}}$  depending on the reflection). The diamond and FCC structures both have 3-fold symmetry about the  $(111)_c$  axis and must obey an ABC stacking sequence. However, with a stacking fault, a  $60^\circ$  twin domain can arise as shown by the blue open circles in Figure 5-1. At particular compositions, the film lattice constant can be very similar to that of the substrate, and therefore by monitoring the twinned reflections, the overwhelmingly bright reflections of the substrate can be avoided. By contrast, the hexagonal structure arises from AB stacking sequences leading to reflections (red circles in Figure 5-1) at even increments along the  $L$ -axis. Using this difference in symmetry of the diffraction patterns, the crystallographic phase in the film can be unequivocally determined



Based on the above discussion, the following procedure was employed to map the phase diagram. First, a short, out-of-plane ( $L$ ) scan of the  $(014)_h$  reflection was completed as this reflection is common to both the FCC\* and hexagonal structures (boxed in Figure 5-1). Upon a phase transition from one to the other structure, a discontinuity appeared in the position of the peak in reciprocal space representing a change in lattice constant upon reorganization of the unit cell and revealing the phase boundaries in the ternary sample. Once these phase boundaries were located, several points within the demarcated regions were selected for a full crystallographic analysis to identify the structural phase. This method minimizes motor movements required at each location on the sample, eliminates nearby substrate background reflections, and has a reduced beam footprint on the surface (Section 3.5). The scan was taken in a trapezoidal mesh of locations on the ternary sample between compositions of Ge 10 and 60 at.%, and the  $L$ -position of the reflection is displayed as a color plot on the ternary phase diagram in Figure 5-2.

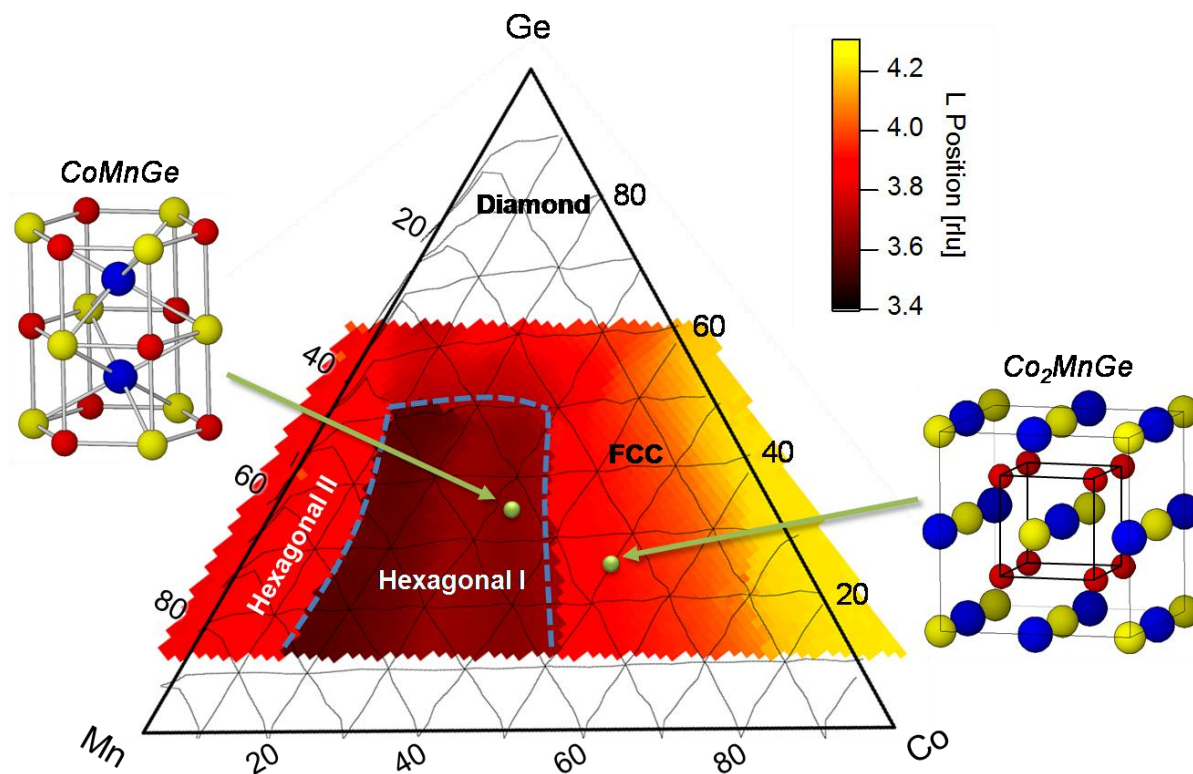


Figure 5-2: Ternary epitaxial phase diagram of the  $\text{Co}_x\text{Mn}_y\text{Ge}_z$  system with black composition contours. L-position of the  $(014)_h$  reflection is plotted in color with the purple dotted line representing phase boundaries separating two hexagonal and one FCC structures. FCC transforms into the diamond structure with increasing Ge concentration. Color outside of the triangle is from positions on the sample where the binary alloys ( $\text{Mn}_x\text{Ge}_{1-x}$  and  $\text{Co}_x\text{Ge}_{1-x}$ ) were deposited. Diagrams of two known stable phases are shown and located on the diagram where their structure has been identified and stabilized over a large compositional region.

Figure 5-2 also shows where known alloys were identified in the epitaxial phase diagram and the compositional regions where their structures were epitaxially stabilized. Near the Ge apex, the  $(014)_h = (022)^*_c$  reflection is absent as only the diamond structure of the dilute magnetic semiconductor discussed in Chapter 4 is present. The composition contours on the Mn-rich edge of the ternary region are skewed due to the loss of surface Mn from numerous cleanings – also discussed in Chapter 4. With decreasing Ge composition, the reflection studied here emerges from a gradual transition to an FCC structure. Below Ge 50 at.%, several hexagonal phases split off from the FCC in Mn-rich compositions and continue to the end of the ternary region. Adding in-plane measurements to those in Figure 5-2, the structure labeled Hexagonal I was identified as the stable

CoMnGe phase. The linear change in lattice parameter with composition suggests that this structure is stabilized over the region defined by the phase boundaries, where one element gradually replaces another in the structure as composition is varied. The lattice constants measured in the Hexagonal II region closely match those of the  $\text{Mn}_2\text{Ge}$  binary high temperature phase, which may be stabilized at lower temperatures under epitaxial growth. Finally, much of the large FCC region below Ge 50 at.% is identified as the Heulser  $\text{L2}_1$  structure, which is discussed below.

### 5.1b: Ordering and Phase Transitions

To examine the nature of phase transitions and the relative crystal quality of each phase, data along the Ge 25 at.% composition contour from the large scan in Figure 5-2 is shown in Figure 5-3. The reflection studied is fundamental for each of the identified phases [(022) for FCC and (102) for Hexagonal in their native index], which means all atoms in the unit cell interfere constructively to produce the diffracted intensity. Therefore, the intensity from this reflection is a good measure of the crystallographic ordering. The difference in atomic form factors at 10.5keV (energy at which the data was taken) only change this intensity by 13% between  $\text{Mn}_{0.75}\text{Ge}_{0.25}$  and  $\text{Co}_{0.75}\text{Ge}_{0.25}$ , which is insignificant next to the range of intensities observed here. In Figure 5-3, the three phases and their transitions can easily be distinguished by the appearance and disappearance of their distinct peaks of intensity along  $L$ . Their integrated intensity from Voigt fits are displayed in the panel directly below. The Hexagonal II phase, starting in the Mn-binary has the weakest intensity but notably has a constant lattice parameter until it disappears at around 20 at.% Co while the Hexagonal I phase begins to compete even below 10 at.% Co. Near the composition of  $\text{CoMn}_2\text{Ge}$ , the Hexagonal I phase has its strongest ordering. With increasing Co concentration, the phase weakens and gives way to the competing FCC phase. By far, the highest intensity occurs in this phase as a sharp peak

in composition at the Heusler stoichiometry. A small shoulder exists at  $\text{Co}_{0.60}\text{Mn}_{0.15}\text{Ge}_{0.25}$  where lattice matching occurs with the substrate before declining to the Co binary.

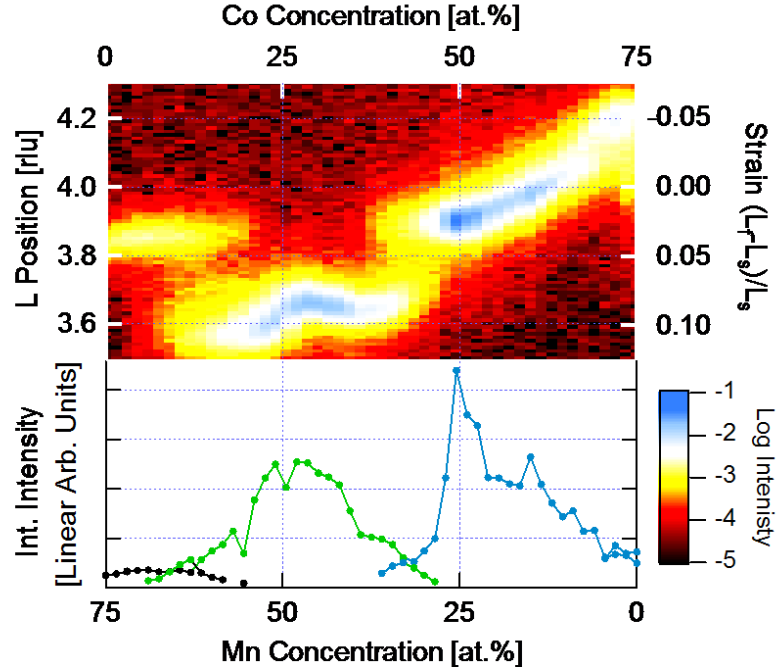


**Figure 5-3:** Log intensity of  $(01L)_h$  and strain (upper panel) and integrated reflection intensity from Voigt fits (lower panel) to Hex II (Black), Hex I (Green) and FCC (Blue) phases. Data is taken along the Ge 25 at.% composition contour or  $(\text{Co}_x\text{Mn}_{1-x})_{0.75}\text{Ge}_{0.25}$ .

The long phase transition between the Hexagonal I and II phase and the near constant lattice parameter of the Mn-binary phase suggests an interplay of composition between the two phases, allowing their simultaneous stabilization. With Co preferentially accumulating in the ternary Hexagonal I phase, the compositional variation in each is reduced. The jump in intensity and change of strain in the ternary phase upon the disappearance of the binary phase demonstrates how this interplay affects structural ordering.

The best ordering occurs in the Co-rich region with the FCC structure. Here the strain follows a linear trend where the small peak in integrated intensity associated with lattice matching shows that strain is affecting crystallographic ordering to a degree. However, the Heusler stoichiometry at  $\text{Co}_2\text{MnGe}$  clearly contains the best ordering by this measure, having nearly twice

the intensity of any other composition, even though its strain is > 2%. Possibly most profound is the extreme sensitivity of the ordering to the Co:Mn ratio as the intensity is drastically reduced just a few at. percent away from this stoichiometry. Groups reporting disorder in their samples consistently have compositions that are off in this manner, giving credence to their suspicions of off-stoichiometry being the cause.<sup>11,12,17</sup>

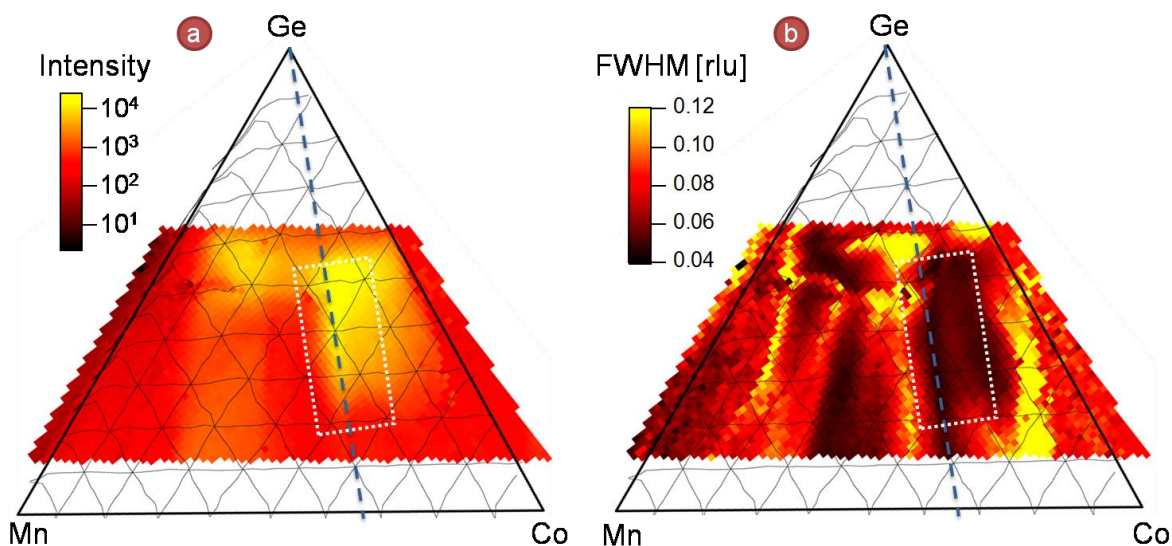


**Figure 5-4: Compositional evolution of (a) Integrated intensity and (b) peak FWHM of the dominant phase. Dashed line is along the Co:Mn 2:1 compositions, and the region of interest (ROI) inside the white dotted box are investigated further in later sections.**

A far more global view of crystallographic ordering with composition is presented in Figure 5-4. Adding to the integrated intensity, the peak full width half maximum (FWHM) is a measure of crystal coherence or domain size, as an increasingly narrow width demonstrates increasingly distant unit cells in the lattice diffracting coherently. Notable is the large peak width at phase boundaries, where competing phases reduce coherence. A particularly large region of high width near the  $\text{Co}_x\text{Ge}_{1-x}$  binary is from an unknown competing phase which starts as a shoulder and becomes a double peak in the binary region. No known binary phase matches these lattice parameters.

Using both parameters, the best crystallographic ordering in the phase diagram occurs along the Co/Mn=2 composition line (the dashed line in the figure) revealing a narrow ridge of high ordering between 20 and 50 at.% Ge. That the Heusler  $L2_1$  structure was found to exist along this ridge suggests that its structural ordering is very robust to a varying Ge composition. At slightly higher Co composition, along the Co/Mn=4 composition line the diffraction also has increased intensity and coherence due to perfect lattice matching with the substrate as noted above.

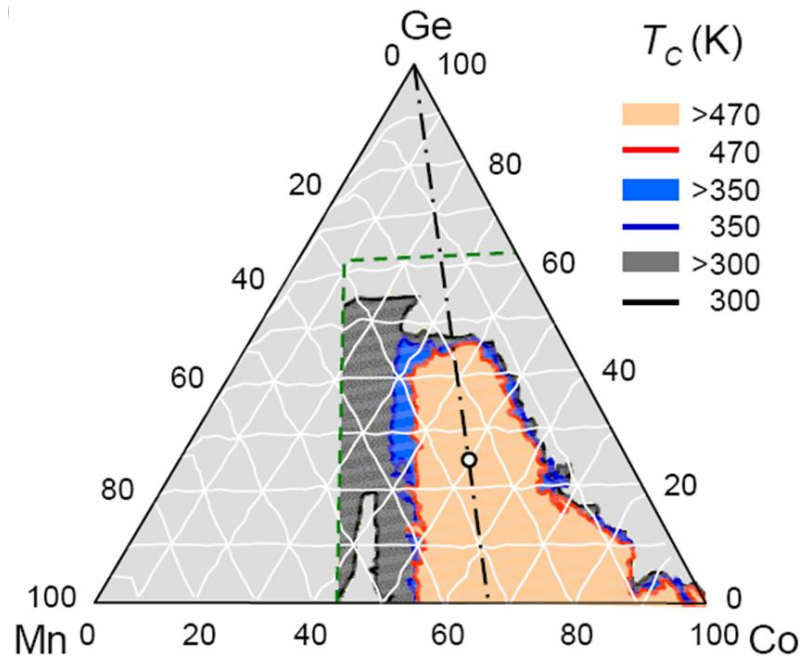


**Figure 5-5: Ferromagnetic regions and Currie temperature ( $T_c$ ) contours as a function of composition up to the maximum measured temperature of 470K using MOKE. The green dashed line displays the extent of the scan. The dash-dotted line represents the Co to Mn atomic ratio of 2 with the circle at the Heusler stoichiometry ( $\text{Co}_2\text{MnGe}$ ). The ferromagnetic region at 400K (not shown) is identical to that of 470K within experimental uncertainty. (Data courtesy of Pranaba Muduli)**

Magnetic properties of the compositional region exhibiting the Heusler structure also agree with those found in the bulk alloy with the entire region being ferromagnetic. As the ferromagnetic boundary does not change within uncertainty from above 350K to 470K, it is clear that the actual  $T_c$  of the region is significantly higher than the temperatures studied, making possible the bulk  $T_c$  of 905K at the Heusler stoichiometry or due to the symmetry of the region, all along the ridge of high crystallographic ordering. At the edge of the scanned region is the Hexagonal CoMnGe phase. It too

is a ferromagnetic phase with a reported  $T_c$  of 390K. The  $T_c$  between 300K and 350K measured here is close to this value and could be reduced by epitaxial constraints or growth conditions that are not optimized for this phase.

## 5.2 Ordering of the Ge Heusler

To create the Heusler structure, which involves an FCC lattice with a basis, specific structural and chemical ordering must occur. To study this structure requires a full understanding of the chemical sublattice organization and its effect on the structure factor of each Bragg reflection. Since there is a 1.5% mismatch between the substrate and the Ge Heusler lattice constant, strain could play a role in the ordering process. As the crystal under investigation was grown along the [111] direction, there is added potential for numerous structural and chemical stacking sequences that could disrupt the ordering of the crystal, making its growth unstable in this orientation. In the following section, the known structure factors of each Bragg reflection and their energy dependence was used to probe for full ordering of the Heusler structure.

### 5.2a: Structure Factor Considerations, Atomic Site Ordering and Strain States

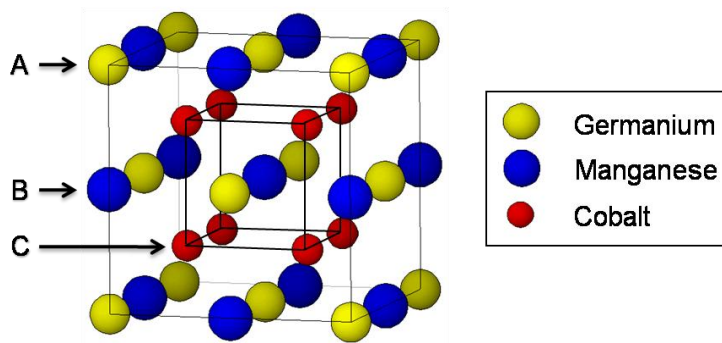


**Figure 5-6: Schematic of the Heusler structure, which has 3 unique sites each filled with one element: A-site with 4 Ge atoms, B-site with 4 Mn atoms, and C-site with 8 Co atoms.**

Full Heusler alloys crystallize in the  $L2_1$  structure, which consists of four interpenetrating FCC sublattices. For  $\text{Co}_2\text{MnGe}$ , Ge atoms are located at the 4 A-sites, Mn on the corresponding 4 B-sites, and Co on the 8 C-sites that occupy two of the FCC sublattices as shown in Figure 5-6. The  $L2_1$  crystal

structure produces three unique families of Bragg reflections: one “fundamental” (F) and two “superstructure” (S1 and S2) reflections. These reflections and their attributes are listed in Table 5-1. The fundamental reflection is insensitive to chemical disorder, as its structure factor is the sum of the atomic form factors for all sites in the unit cell as discussed above, whereas the superstructure reflections involve differences of sublattice form factors. The differences within the structure factors make the resulting diffraction intensities highly dependent on the chemical ordering of the lattice. For example, if the elements in the Heusler alloy were to randomly occupy the sites in this structure, the structure factors in the S1 and S2 reflections would add to zero and no diffracted intensity would be measured.

Studied Reflection			Structure Factor	Bragg Condition
Abbr.	Cubic	Hexagonal		
F	(022)*	(104)* = (014)	$f_A + f_B + 2f_C$	If $H+K+L = 2 \times \text{even}$
S1	(002)*	(012)* = (102)	$f_A + f_B - 2f_C$	If $H+K+L = 2 \times \text{odd}$
S2	(-111)*	(101)* = (011)	$f_A - f_B$	If $H+K+L = \text{odd}$

**Table 5-1: Three unique Bragg reflections of the Heusler structure are shown in both the traditional cubic notation and the convenient hexagonal notation along with their abbreviations used in the text. The stars indicate that the reflection studied was the 60°-rotated twin about the [111] direction. Also shown are the structure factors corresponding to each reflection and the selection rules for the three families of reflections.**

The integrated intensities of the three unique Bragg reflections were measured as a function of composition within the aforementioned ROI as shown in Figure 5-7. Although the composition changes across these graphs, the average atomic scattering factor changes by only up to 7%, which is insignificant compared with changes due to ordering. The fundamental (Figure 5-7a) was discussed previously, but the linear color scale displayed here accentuates the narrow ridge of high intensities at the Co to Mn atomic ratio of two. The intensity of the fundamental along the ridge indicates that more unit cells – and therefore more of the deposited material – participates in the FCC lattice with the maximum located near the composition of 50 at.% Ge. Of these participating



atoms, the extent to which they are organized by element into outer (A and B) sites and inner (C) sites of the unit cell (Figure 5-6) determines how bright the Superstructure I (S1) reflection is. Shown in Figure 5-7b, the composition dependence of this reflection is fairly similar to that of the fundamental, but dies off more quickly upon approaching the Heusler stoichiometry. Of note is that this bright ridge gradually moves away from the Co/Mn atomic ratio of two at their brightest point near 50 at.% Ge. The  $(111)_c$ -type or S2 depends on the chemical ordering between A and B sites and has a very different intensity evolution than the others as seen in Figure 5-7c. The composition of highest ordering, however, is still along the ideal Co/Mn atomic ratio but is split between 30 and 40 at.% Ge. The higher intensity of each reflection along the narrow region of Co/Mn atomic ratio of two demonstrates the extreme sensitivity of ordering to the relative composition of the two transition metal elements.

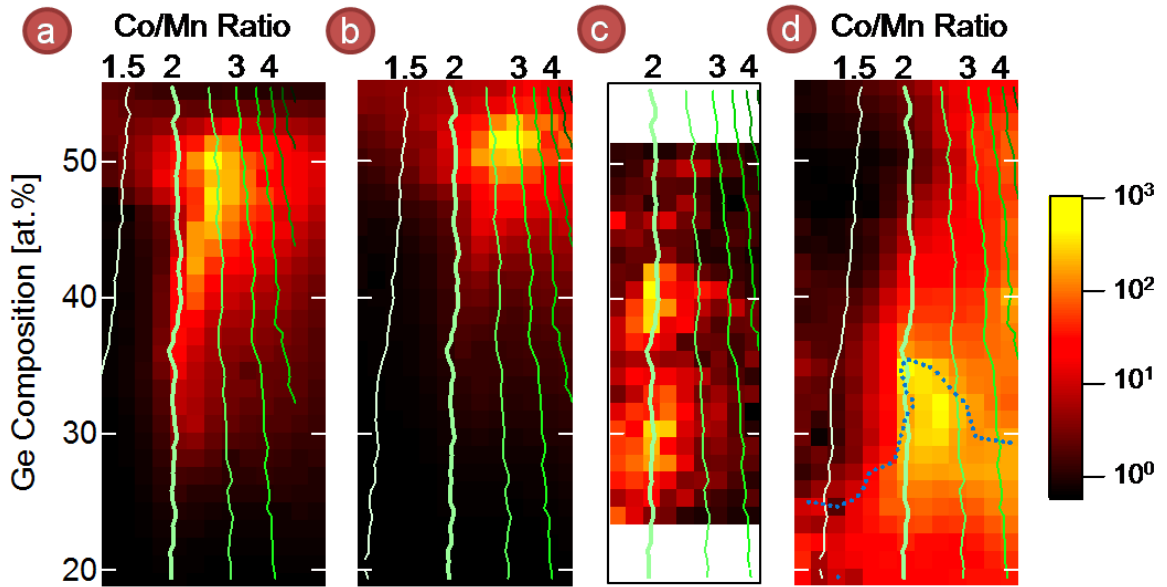


Figure 5-7: Composition evolution of the (a) F  $(014)_h$ , (b) S1  $(102)_h$ , and (c) S2  $(011)_h$  integrated intensities with Ge composition varied along the y-axis and Co/Mn atomic ratio along the x-axis, as measured via XRF spectroscopy (green contours). (d) Integrated Intensity ratio of the S1 reflection  $(102)_h$  with its twin  $(012)_h$ . The dotted line indicates where the  $(012)_h$  reflection could no longer be detected above the background. The ratio at lower Ge concentrations is calculated by dividing by the background level and, therefore, may be higher than is reported here. The color bar represents intensities in (d) only, with the others in an arbitrary linear scale.

The final dataset, shown in Figure 5-7d, is the intensity ratio between the S1 reflection  $(102)_h$  and its  $60^\circ$  twin  $(012)_h$ . This reflection is forbidden in the diamond lattice, so both of these reflections could be measured without interference from those of the substrate. As discussed above, a stacking fault in the crystal in the  $[111]$  direction causes this twinned reflection to appear. With numerous stacking faults, formation of the twinned domain is just as likely as the untwinned domain, and the intensity of the two reflections will be equal. This can be distinguished from the hexagonal structure as twinning does not affect the  $(00L)$  rod in reciprocal space. The figure shows a definite trend in stacking faults with Ge composition. The lattice is fully relaxed to 6-fold symmetry at 50 at.% Ge. With decreasing Ge, 3-fold symmetry is gradually established with the best ordering occurring at the Co/Mn atomic ratio of two. Below approximately 30 at.% Ge, full 3-fold symmetry is measured across the compositional region of interest within the detection limit.

Particularly important is the observation that the preferred orientation of the film is actually the  $60^\circ$  rotated domain. For example, due to the large strain of the film at the Heusler composition, careful measurements of the untwinned reflections can be made, whose position is far enough away from that of the substrate's. Here, no evidence of a twinned domain exists for any reflection. This observation may be due to the chemistry at the substrate-film interface upon initial deposition, causing a rotation as the Heusler structure is established. Experimentally, this effect is most advantageous as the structure can be studied in full without interference from any substrate reflections.

With the exception of the twinning measurement, each of the results displayed in Figure 5-7 suggests that the best ordering occurs at compositions other than that of the Heusler stoichiometry. Specifically, regions of higher ordering occur at compositions with excess Ge. To investigate the possible effects of strain on the ordering, the out-of-plane and in-plane positions of the reflections

relative to the substrate were used to calculate the strain state of the film in this compositional region of interest. Figure 5-8a shows that along the high-ordering ridge of the fundamental reflection, the strain in the out-of-plane direction is nearly constant at a value  $>2\%$  but is reduced at higher Ge composition as the ridge moves to higher Co/Mn ratio. The in-plane strain, shown in Figure 5-8b, exhibits a much more dramatic variation along the ridge. Here the zero strain contour clearly shows that the film is coherent with the substrate at 50 at.% Ge, but gradually the film relaxes as the Heusler stoichiometry is approached. In-plane dislocations at the substrate-film interface can be a catalyst for disorders in the film and reduce crystal quality as was seen in the DMS materials. This evidence suggests that the general crystallographic ordering of the Heusler structure along the ridge is primarily affected by the strain and degree of lattice relaxation.

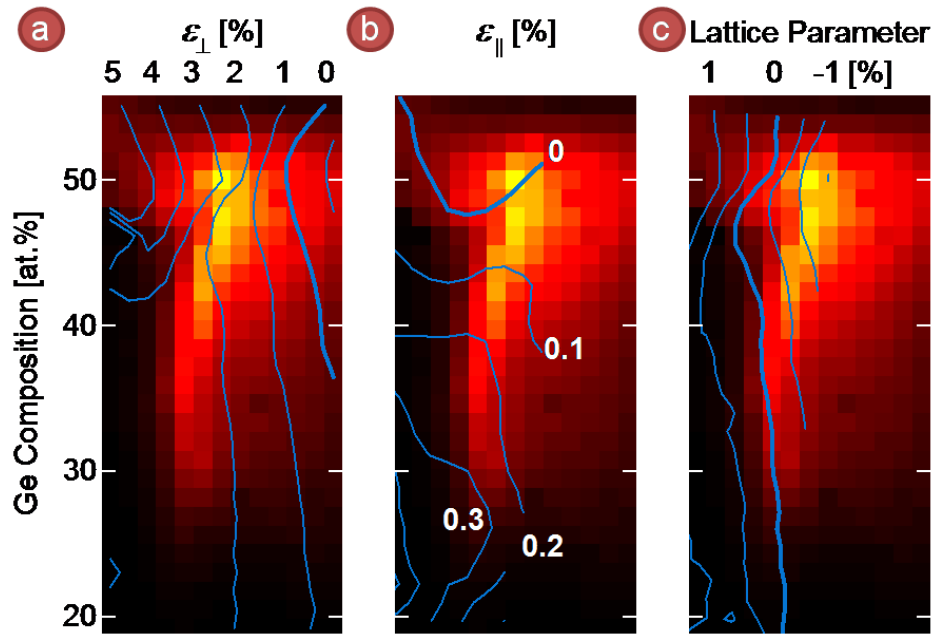


**Figure 5-8: Compositional evolution of film (a) Out-of-Plane strain (b) in-plane strain and (c) Lattice parameter in percent mismatch from the reported bulk value of 5.743Å. Each are compared with the integrated intensity of the fundamental reflection, showing the compositional ridge of high ordering. Compositional range of the image plots are identical to Figure 5-7a.**

As discussed in Section 4.3a, the elastic distortion from epitaxy can be corrected from knowledge of the in-plane and out-of-plane strain, resulting in a calculation of the bulk film lattice

parameter. To apply it in this (111)-oriented system requires a rotation of the elasticity tensor in its full form. Because the full form is actually a fourth-rank tensor  $c_{ijkl}$ , it obeys the following transformation relation.

$$c'_{ijkl} = \frac{\partial x'_i}{\partial x_m} \frac{\partial x'_j}{\partial x_n} \frac{\partial x'_k}{\partial x_o} \frac{\partial x'_l}{\partial x_p} c_{mnop} \quad (5-2)$$

where the differentials are the direction cosines between the sets of axes. Due to symmetries of the cubic lattice studied here, the result can still be reduced to a second rank tensor of the form in Equation 4-3, where the new constants are simple functions for those of a cubic lattice ( $c_{11}$ ,  $c_{12}$ ,  $c_{44}$ ) and the elastic tensor takes the following form.

$$c'_{ij} = \begin{pmatrix} c'_{11} & c'_{12} & c'_{13} & c'_{14} & 0 & 0 \\ c'_{12} & c'_{11} & c'_{13} & -c'_{14} & 0 & 0 \\ c'_{13} & c'_{13} & c'_{33} & 0 & 0 & 0 \\ c'_{14} & -c'_{14} & 0 & c'_{44} & 0 & 0 \\ 0 & 0 & 0 & 0 & c'_{44} & c'_{14} \\ 0 & 0 & 0 & 0 & c'_{14} & c'_{66} \end{pmatrix} \quad (5-3)$$

Again, applying the epitaxial conditions of biaxial strain, only the third row is required to solve for the film lattice parameter, and therefore only the needed coefficients are shown here:

$$c'_{13} = \frac{c_{11} + 2c_{12} - 2c_{44}}{3} \quad c'_{33} = \frac{c_{11} + 2c_{12} + 4c_{44}}{3} \quad (5-4)$$

With the epitaxial constraints, the third row equation becomes

$$\epsilon_3 = \frac{-2c'_{13}}{c'_{33}} \epsilon_3 \Rightarrow \epsilon_z = \frac{-2(c_{11} + 2c_{12} - 2c_{44})}{c_{11} + 2c_{12} + 4c_{44}} \epsilon_x = -A\epsilon_x \quad (5-5)$$

Using the definitions for strain defined in section 4.3a, the film lattice parameter is then

$$a_{film} = \frac{d_{out\ of\ plane} + A \cdot d_{in\ plane}}{A + 1} \quad (5-6)$$

In order to correctly convert the strain into the lattice parameter, the three elastic constants from this material are needed. Since this has never been measured, those of a similar metal Fe were used giving  $A=0.552$ . Numerous others were also used ranging from brittle Ge ( $A=0.369$ ) to Cu ( $A=0.7324$ )

to extremely malleable Au ( $A=1.2455$ ). With the exception of Au, the calculated film lattice constant did not vary significantly, and the lattice parameter shown in Figure 5-8c reveals the bulk Heusler lattice constant indeed forms along this ridge of high crystallographic ordering.

### 5.2b: Structural and Chemical Stacking Sequences

Diffraction obtained around an elemental resonance can provide an increased amount of information regarding the chemical ordering in a crystal. Specifically, anomalous diffraction intensities taken around the Co absorption edge provides a direct measurement of the structural and chemical stacking sequence of the Heusler structure. Deposited in the (111) orientation, the elements in the structure must order in a complicated structural and chemical pattern as displayed in Figure 5-9. Here, the unit cell is fully 12 layers, each containing an individual element in a pattern of three times Ge-Co-Mn-Co, while stacking in a structural sequence of four times A-B-C. An off-stoichiometric composition could easily cause the preferred sequence to change, altering the chemical structure and therefore the materials' properties.

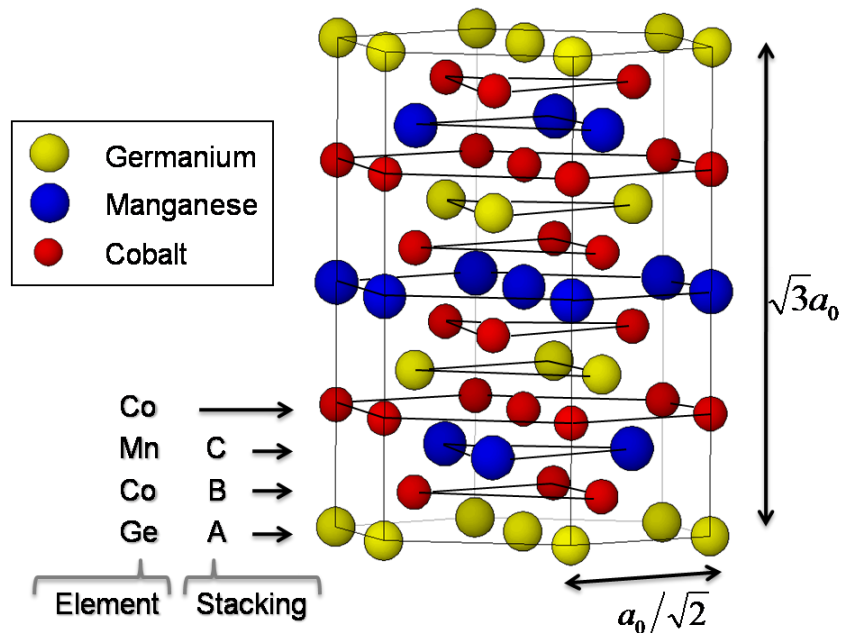
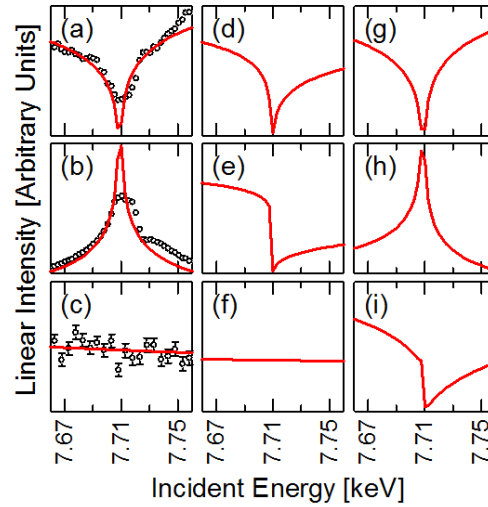


Figure 5-9: The structural and chemical stacking sequence of the Heusler alloy in the (111) orientation involving 12 atomic layers, each of which must be occupied by a single element in a particular order.

The three unique Bragg reflection intensities were modeled for various chemical and structural stacking sequences and compared with the measurements obtained at different compositions. A weighted elemental scattering factor has been used to model the elemental occupancy at each atomic position within the unit cell as given by

$$I(\mathbf{q}, E) = I_0 \left| \sum_n x_n f_{Co}(\mathbf{q}, E) + y_n f_{Mn}(\mathbf{q}, E) + z_n f_{Ge}(\mathbf{q}, E) e^{i\mathbf{q} \cdot \mathbf{r}_n} \right|^2 A(\mathbf{q}, E) \quad (5-7)$$

where the summation is over the three structural sites and the occupation coefficients ( $x$ ,  $y$ , and  $z$ ) scale the atomic form factors  $f(\mathbf{q}, E)$  for each element with anomalous corrections (Equation 3-4) tabulated originally by Cromer and Liberman<sup>18</sup> and ported subsequently to an IGOR library.<sup>19</sup> The self-absorption attenuation  $A(\mathbf{q}, E)$  was modeled as discussed in Chapter 3 but was found to be insignificant for the current analysis. The overall scaling factor  $I_0$  was used to scale the model with the data.



**Figure 5-10: Examples of models for different stacking sequences of the unit cell. Each plot is linear intensity vs. energy near the Co edge (7.709keV). The rows of plots show behaviors for the three reflections: Fundamental (top), S1 (middle), S2 (bottom). Columns of plots show the corresponding behaviors for various stacking sequences: [(a)–(c)] the Heusler stacking (ABC ABC ABC ABC), [(d)–(f)] (ABC ACB ABC ACB), and [(g)–(i)] (ACB ACB ABC ABC). Lines correspond to models, and circles in (a)–(c) are data taken near the Heusler stoichiometry. (Excerpt from Ref. 20)**

To test for a variation in preferred structural and chemical stacking sequences that could easily arise in this cubic system grown in the (111) orientation, hundreds of possible sequences have been modeled and compared with the diffraction data. Figure 5-10 illustrates three examples of the models for the anomalous diffraction intensities near the Co edge with unit cells containing correct chemical ordering but with different structural stacking sequences. The behavior for the Heusler structure with FCC stacking is shown in Figure 5-10 (a)-(c) for all three Bragg reflections. The features in the model can be easily understood by referencing the corresponding structure factor in Table 5-1. Figure 5-10 (d)-(i) show two other possible stacking sequences, each exhibiting qualitative features easily distinguishable from those of the correct Heusler stacking sequence. Among all the sequences modeled, the Heusler structure exhibits a unique set of features in the anomalous diffraction intensities.

A set of scans taken near the Heusler stoichiometry on the ternary sample is shown with the model in Figure 5-10 (a)-(c). They exhibit a remarkable resemblance to the Heusler structure and thus can be distinguished from all other models studied. The solid-state effects giving rise to the fine structures in the data above the absorption edge are not modeled in this study, but they would not affect the qualitative features in the models presented here.

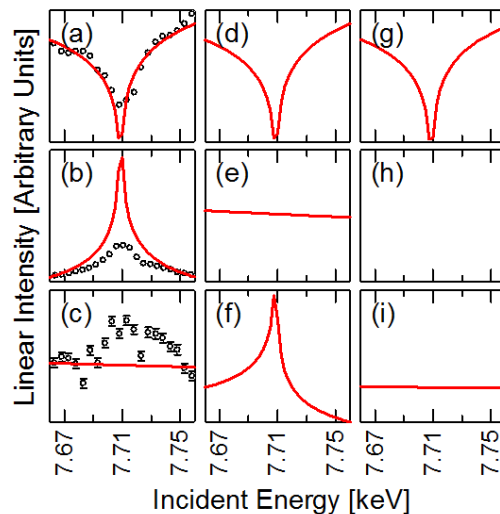


**Figure 5-11: Examples of models for different chemical sequences of the unit cell. The axes of each plot and the arrangement of rows of panels are the same as in Figure 5-10. Columns of plots show the behaviors for various chemical stacking sequences: [(a)–(c)] Heusler stacking with chemical sequence three times of GeCoMnCo, [(d)–(f)] three times of GeMnCoCo, and [(g)–(i)] twice of GeCoGeMnCoGe. The absence of a plot in (h) is a result of the forbidden Bragg reflection for the chemical sequence. The same as in Figure 5-10, lines correspond to models, and circles in [(a)–(c)] are data taken near the composition of  $\text{Co}_2\text{MnGe}_3$ , at the composition of highest structural ordering. (Excerpt from Ref. 20)**

Figure 5-11 shows several models with different chemical stacking sequences in the same energy range as those shown in Figure 5-10. Again, Figure 5-11(a)–(c) show the behaviors of three unique Bragg reflections for the Heusler structure with sequence three times of Ge–Co–Mn–Co. In contrast, Figure 5-11 (d)–(f) show the behavior of a unit cell containing the same stoichiometry but with an alternative sequence of three times Ge–Mn–Co–Co. A different stoichiometry is modeled in Figure 5-11 (g)–(i), illustrating what the behavior might look like at the composition near  $\text{Co}_2\text{MnGe}_3$ . Here, the data from composition approximately  $\text{Co}_2\text{MnGe}_3$  are shown with the model in Figure 5-11 (a)–(c). Although the fits are not nearly as good as those shown in Figure 5-10, the data can still be distinguished from the other models. In all, approximately 100 models were explored by changing the chemical sequence as well as the stacking sequence, layer number, and even the layer configuration (e.g., that for the diamond lattice). All of these suggest that anomalous diffraction can be used to distinguish the Heusler structure from others. The fact that the Heusler chemical and structural ordering is seen in compositions far from the correct stoichiometry and indeed the entire



compositional region of interest studied here reinforces the established notion that this structure is very stable.

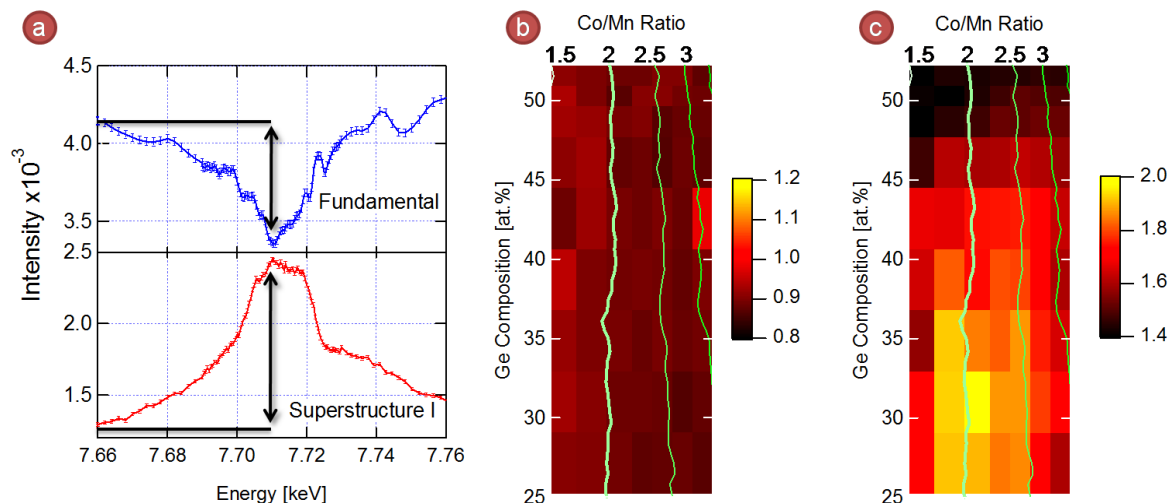


**Figure 5-12: Ratio of diffracted intensities taken at the Co edge (7.71keV) to those taken below the edge (7.66keV) as indicated by the arrows in (a) showing anomalous diffraction intensity for (b) the F and (c) the S1 reflections. Contours are again the Co to Mn atomic ratio measured using XRF spectroscopy.**

As a final qualitative measure of the chemical ordering, the Co edge strength of the anomalous features, shown in Figure 5-12, gives a powerful indication of the composition where the Heusler structure has the best elemental organization. As noted above, the structure factor of the fundamental reflection causes it to be insensitive to elemental organization in the lattice, and the results in Figure 5-12b clearly show no compositional dependence of this parameter, as expected. In contrast, that of the S1 reflection, clearly exhibits the strongest edge strength at 30 at.% Ge and at the Co to Mn atomic ratio of 2. This result is particularly important as any elemental swapping or vacancies with the exception of A-B site swapping, will degrade this feature due to its structure factor. Again, it is of note that the highest degree of elemental ordering does not occur at precisely the Heusler stoichiometry but at a composition of excess Ge.

### 5.3 Quantitative Study of Site-Specific Elemental Disorders in the Ge Heusler

Density functional theoretical calculations show that atomic defects in the Ge Heusler alloy create minority states in the half-metallic band gap.<sup>8</sup> Specifically, Co-Co hybridized bonding states occur in the C-site sublattice, which in turn, hybridize with the Mn atoms.<sup>9</sup> Therefore, a disruption in the elemental organization of these sublattices can cause a breakdown in the bonding arrangements and a depolarization of the spin states. In particular, the half metallic state in this material is sensitive to Co antisites, where Co atoms occupy the non-native A or B sites in the structure. Energy calculations<sup>8</sup> show that the most damaging to the half metallic state and the most likely to occur is Co-Mn site swapping, evidence of which has been reported in bulk samples of the Si Heusler using neutron diffraction.<sup>11</sup> However, neutron intensities are far too low to resolve these disorders in a combinatorial thin film. Recently, an anomalous diffraction study at one elemental resonance and one reflection showed promise of quantitative sensitivity to this disorder in polycrystalline thin film samples grown on a (100)-oriented GaAs substrate via pulsed laser deposition.<sup>21</sup> Therefore, this technique was duplicated for the sample studied here. It is found, however, that anomalous diffraction can be sensitive to far more than one specific disorder in the crystal. Rather, careful study of full spectrum diffraction intensities around each resonance and reflection allows for the quantitative characterization of elemental occupation and relative vacancy of each site in the Heusler structure.

#### 5.3a: Individual Elemental Resonances and Reflections

The recent anomalous study<sup>21</sup> involved modeling and fitting of the S2 reflection around the Co resonance was accomplished on data from the sample studied here, using the theory and data acquisition procedures discussed in Chapter 3. As in the published study, the only data processing involved background subtraction of the x-ray fluorescence. The fit function used here was also similar and involved four parameters: The amount of Co occupying the Mn B-site, the film thickness

determining the level of self absorption, and a linear function representing extrinsic instrumental effects represented by  $I_0(E)$  in Equation 3-17. The result is shown in Figure 5-13, which yielded a value of  $3.5 \pm 0.3\%$  occupation and a film thickness of  $344 \pm 21 \text{ \AA}$ . The thickness agrees very well with the value measured with XRF spectroscopy as discussed above.

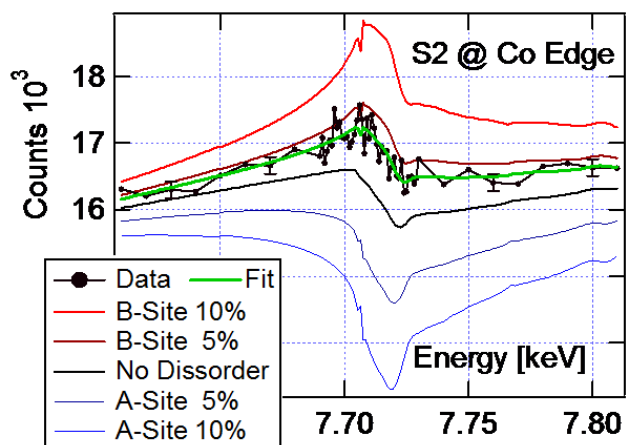


**Figure 5-13: Models of Co-antisites and a fit to intensities of the S2 reflection  $[(111)_c\text{-type}]$  around the Co absorption edge, with fit result of  $3.5 \pm 0.3\%$  Co in the B-site. Uncertainties are shown with a few data points in the data.**

A fifth parameter not considered in the published study, Co occupation of A-sites, was also seen to affect the anomalous diffraction. Models of both of these Co-antisites (Figure 5-13) show how drastically each affects the form of the data. When added to the fit, this parameter yielded a zero value but was highly correlated with B-antisites, resulting in uncertainties much larger than the parameters themselves. This shows that the analysis is only sensitive to the relative amounts of the two disorders. This can be easily understood by considering how the S2 structure factor (Table 5-1) is affected by equal amounts of Co in A and B sites, proving that this limited experiment cannot quantify absolute amounts of the disorder in question. Only in measurement of multiple edges and reflections is this correlation removed to reveal absolute occupations.

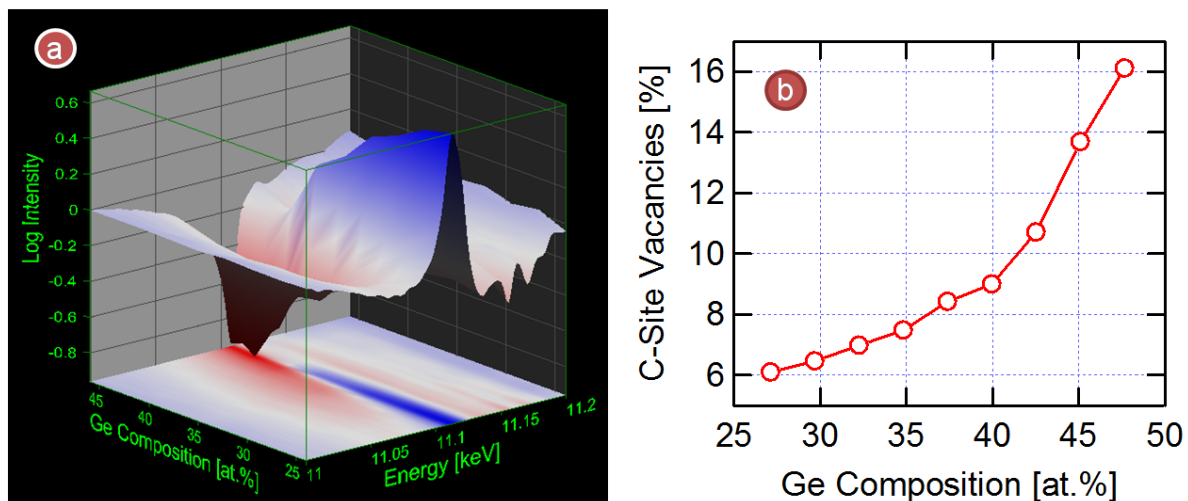


**Figure 5-14: (a) Anomalous diffraction intensities in log scale at the S1 reflection  $[(002)_c\text{-type}]$  around the Ge-edge as a function of Ge composition along the Co/Mn atomic ratio of 2 and normalized to the intensity at 11.0 keV. The surface is projected on to the bottom of the graph for redundant viewing. (b) Fit results to these data for C-site vacancies (uncertainties within the circles).**

With a complete set of data taken at multiple compositions, the sensitivity of this experiment to other types of disorders in the crystal becomes apparent. A reflection mentioned earlier for its high sensitivity to disorders is the S1 or  $(002)_c\text{-type}$ . Anomalous diffraction data from this reflection around the Ge absorption edge and varying compositions is shown in Figure 5-14a. A dramatic change in the energy dependence of this reflection is shown as an increasing amount of excess Ge is added to the Heusler stoichiometry, while preserving the Co/Mn atomic ratio. At the Heusler composition, a strong peak occurs at the Ge edge of 11.103keV with noticeable fine structure above the edge. With progressively more Ge, this peak diminishes with a growing valley centered just below the edge at 11.100keV. The solid state effects also change, flattening out and increasing in characteristic wavelength. A similar function to the one previously discussed involving the S2 reflection was used to fit for vacancies at the C-site producing a clear increasing trend as a function of Ge composition. While this limited data is also in danger of correlations with other disorders not included in the fit, the same trend is seen in the full spectrum analysis and can be

easily understood as a gradual transition to the eventual Ge diamond phase which has a C-site occupancy of 50%.

### 5.3b: Fitting Procedures for the Complete Model

The data from each edge and reflection were assembled and processed, resulting in two sets representing the intensity ratios of the S1 and S2 reflections normalized to the chemically insensitive fundamental reflection as described in Chapter 3. This had the consequence of eliminating several energy dependent extrinsic effects and normalizing the signal to the number of atoms participating in the structure as described above. Each intensity ratio was represented by models similar to the form of Equation (5-7) and fit simultaneously.

$$I_q(E) = \left| \sum_n C_n f_{Co}(q, E) + M_n f_{Mn}(q, E) + G_n f_{Ge}(q, E) e^{i\mathbf{q} \cdot \mathbf{r}_n} \right|^2 A(q, E) S(q, E) D(q) T(q) \quad (5-8)$$

Here  $A(q, E)$  is the self absorption,  $S(q, E)$  is the slit function correction and  $T(q)$  is the film thickness correction – each function set based on methods described in Chapter 3. The Debye-Waller Disorder term  $D(q)$  with the square variance parameter  $\sigma$  was also discussed in Chapter 3, and despite being measured, special procedures were used to set this parameter and are discussed below. These correction factors were used to eliminate the need for free scaling parameters as absolute values of the ratios were important for the fitting process. For this experiment, anomalous corrections to the form factors were obtained from the HEFAESTUS program in the FEFF8 software package,<sup>22</sup> which only contained small differences from the IGOR library used earlier.<sup>19</sup> The nine occupancy variables ( $C_n$ ,  $M_n$ , and  $G_n$ ) were parameterized into a set reflecting the specific defects of interest. The conversion can be found in Table 5-2. Here the three site-swapping parameters are those modeled in the literature, where two elements typically found in particular sublattices randomly switch positions. Vacancies are the usual antithesis of site occupancy, and Ge Anti-sites are excess Ge replacing elements in other sites as described above. Anti-site parameters are

different from site-swapping as they change the composition of the resulting fit. These were chosen due to the fact that the data were taken at compositions of stoichiometric Co to Mn atomic ratios but with increasingly excess Ge. Of note is that additional to populations of defects and disorders, the results of the fit also output an estimated composition of the material studied.

Type	Site	Elements	Conversion
Site-Swapping	A-B	Ge-Mn	$\min( M_A, G_B )$
	B-C	Mn-Co	$\min( C_B, 2 \cdot M_C )$
	C-A	Co-Ge	$\min( 2 \cdot G_C, C_A )$
Vacancies	A	Ge	$100 - C_A - M_A - G_A$
	B	Mn	$100 - C_B - M_B - G_B$
	C	Co	$100 - C_C - M_C - G_C$
Ge Anti-sites	B	Mn	$G_B - M_A$
	C	Co	$G_C - C_A/2$

**Table 5-2: Parameters used in the fit function and their relation to occupancy parameters in Equation (5-8). Values are in site percentage, and therefore a factor of 2 enters calculations related to degenerate C-sites.**

Several special procedures were followed to obtain the best fit. First, all fits were completed in log base 10 scale to emphasize resonance features over high intensities. Due to correlations between the three vacancy parameters, the one with the lowest value in the fit was set to zero and only seven parameters were allowed to vary. With excess Ge in the compositions studied, it was surprising that the A-site vacancy parameter did not have the lowest value. Rather, the B-site parameter was consistently the lowest for all datasets, although A-site vacancies were consistently below 1%. As initial fits yielded Ge compositions lower than the measured values, constraints were used to assure correct Ge output compositions, in addition to those on all parameters keeping values between 0 and 100%. Finally, a large variety of starting parameters were used in multiple fits of each dataset to ensure fit uniqueness.

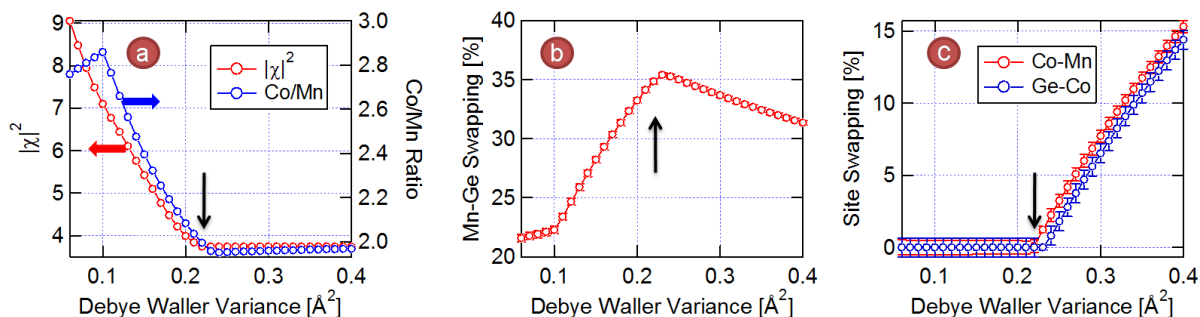


**Figure 5-15: Evolution of key fit parameters with the Debye-Waller square variance for data taken at 35 at.% Ge and Co to Mn atomic ratio of 2. (a) Output parameters used to determine the proper value of  $\sigma$  (Normed chi squared and the Co to Mn atomic ratio). (b) Mn-Ge site swapping and (c) Co-Mn and Ge-Co site swapping. Black arrows indicate the chosen value for the final fit.**

As indicated above, special procedures were used to set the Debye-Waller term. The function employed in the fit is a simplification, as this parameter can vary with crystallographic direction. Although a value was measured for a few pairs of reflections, this only sets the approximate magnitude. If free in the fit, this term can act as a scale parameter for the ratios and so is highly correlated with the other parameters. Therefore, to set this parameter,  $\sigma$  was systematically varied in a region of values experimentally measured (0.1-0.25) and was selected based on a minimum chi square value and the correct output Co to Mn atomic ratio. Figure 5-15a shows the trends of these two parameters for fits to the dataset with 35 at.% Ge. Here both parameters are far from ideal at low values of the square variance but rapidly approach the best value where they plateau with increasing  $\sigma$ . The lowest value of the square variance that provided the best chi square and Co to Mn atomic ratio was chosen for the final fit. All datasets exhibited the same behavior and were chosen under the same criteria, with the worst Co/Mn ratio of 2.4 output for data taken at a composition of 45 at.% Ge. The fact that all other fit parameters show a sudden change in behavior at this point as well [Figure 5-15 (b) and (c)], suggests the parameterization used in the fit function allows for a continuous adjustment once the correct composition has been achieved, indicating that the square variance at this point is the best value. This relative ambiguity

in the Debye-Waller factor, however, remains the primary weakness of the experiment, and more thorough measurement could eliminate this step.

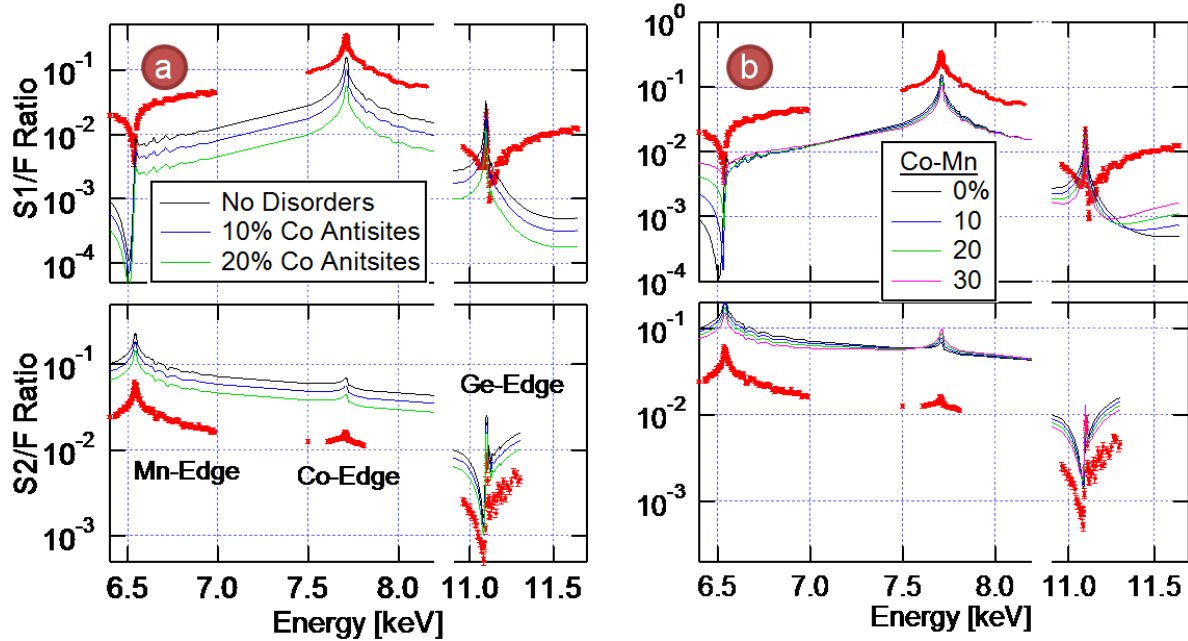


**Figure 5-16: Models of disorders discussed in the literature compared with data from a composition of 30 at.% Ge. (a) Equal amounts of Co into A and B sites, which cannot be distinguished through analysis of one reflection. (b) Varying amounts of Co-Mn swapping.**

The model was further tested for uniqueness and sensitivity to various combinations of disorders. One example, shown in Figure 5-16a, is the combination of disorders indistinguishable in the single reflection fitting completed in the previous section, where equal amounts of Co in A and B sites produce the same functional result. Here, there is a clear trend with varying amounts of these Co antisites. The clear sensitivity of this experiment can also be seen in the extreme qualitative difference in the data compared with the model when no disorders are added. Additionally, the disorder considered to be the most likely in the literature is clearly not able to reproduce the data in Figure 5-16b. No amount of Co-Mn site swapping alone will make the model amenable to the data.



### 5.3c: Full Spectrum Fit Results

Using results from the x-ray studies previously discussed here, four compositions were chosen for the full spectrum fitting analysis. Each composition had stoichiometric Co to Mn atomic ratios with variation in the Ge concentrations yielding 30, 35, 40 and 45 at.%. The Heusler stoichiometry was not measured nor compositions off the high ordering ridge due to limited intensities. For this study, the data statistics and energy spacing were taken as to obtain the near edge fine structure along with EXAFS signal, which was simultaneously measured and used for solid state correction as described in Chapter 3. Without these strenuous requirements, far more full sets of data could be taken, including those in regions exhibiting low diffraction intensities as near-edge structure is not generally important to the fits.

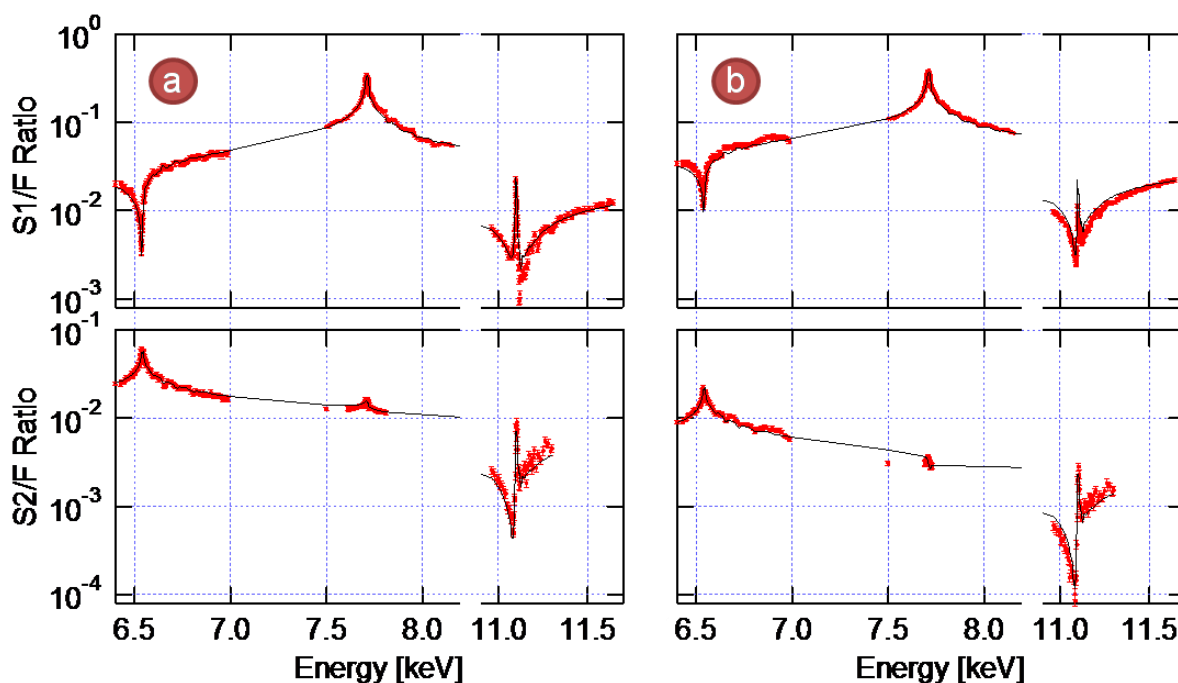


Figure 5-17: Full spectrum fits (black lines) for data (red dots) at (a) 30 at.% Ge and (b) 40 at.% Ge.

Figure 5-17 (a) and (b) show fits to two sets of data at 30 and 40 at.% Ge, respectively. Good agreement is achieved with the fit being within uncertainty of most of the data points. Particularly important to the fit are the level and shape of the intensity ratios with energy, although the fine

structure and near edge features also are well reproduced. The numerical results from each fit are also displayed in Table 5-3 along with uncertainties, which are clearly able to resolve below percent level populations of the seven defects fit in the analysis. In general, correlations between parameters were low. Only Ge antisite parameters had correlations larger than  $\pm 0.9$  with some of the swapping parameters, others being at  $\pm 0.8$  and below. Notably, Co-Mn site swapping returns zero for all compositions studied. This is not surprising as accurate stoichiometry was studied for these two elements, giving support to the suspicion in Ref 21 that an excess of Co and deficiency of Mn is related to their detection of  $\sim 13\%$  Co-Mn swapping. From the analysis the dominant form of disorder, even near the Heusler composition, is Mn-Ge swapping.

Disorder Type	30 at%. Ge	35 at%. Ge	40 at%. Ge	45 at%. Ge
$\sigma$	0.11	0.22	0.19	0.24
Mn-Ge Swapping	26.6(2)	34.5(2)	26.4(2)	26.1(2)
Co-Mn Swapping	0.0(5)	0.0(5)	0.0(4)	0.0(4)
Ge-Co Swapping	1.0(6)	0.0(4)	4.3(4)	0.0(6)
A-Site Vacancies	0.34(4)	0.29(2)	0.33(2)	0.5(2)
C-Site Vacancies	7.17(4)	6.93(3)	8.37(3)	9.31(7)
Ge Replacing Mn	10.5(8)	16.2(7)	26.9(7)	38.5(8)
Ge Replacing Co	2.7(8)	9.5(6)	13.3(7)	16.7(6)

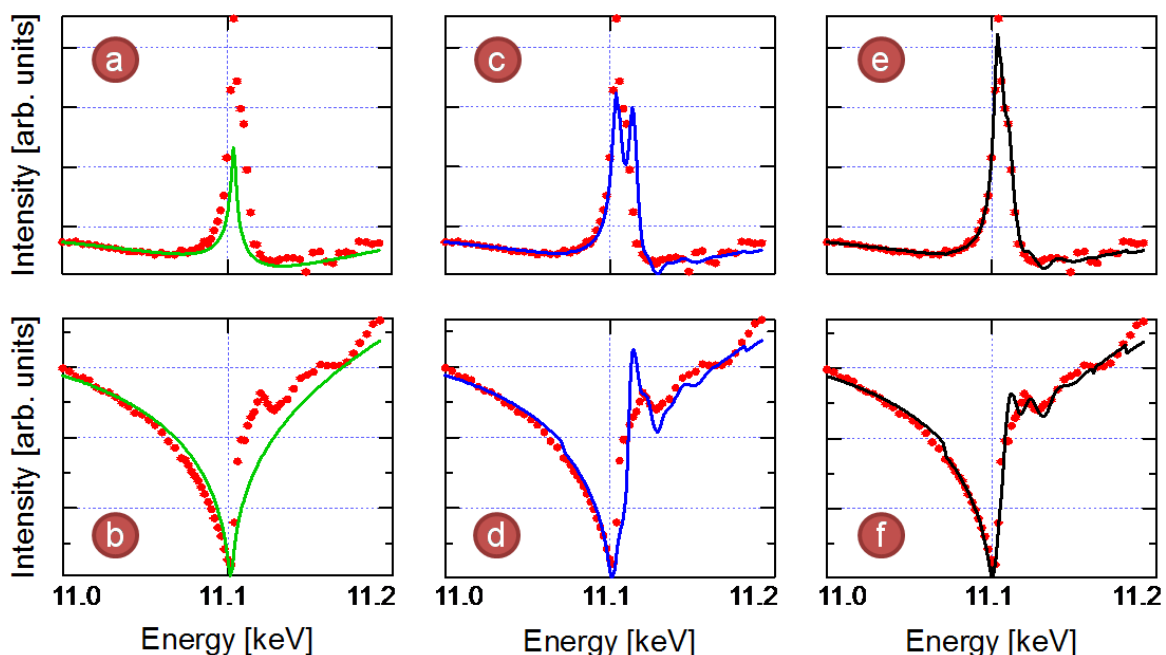
**Table 5-3: Fit results for the four data sets. Values are in percents for each site with uncertainty of the last decimal in parenthesis.**

The near edge fine structure in the data is not typically important for the fits, and adding them to the Co and Mn anomalous form factors did not change the fit results, barring a smaller chi squared value. However, the analysis was more sensitive to the Ge edge as the features here were more intricate (Figure 5-17). Due to the fact that the film studied was deposited on a Ge substrate, EXAFS could not be taken to obtain solid state scattering factors. Instead, *ab initio* calculations, completed under the FEFF8 software package,<sup>23</sup> were used to model the photoelectron interaction from a Ge absorber and calculate the Ge atomic form factor near the absorption edge.

Photoelectrons below approximately 20 eV have no inelastic excitations available in the free electron gas, being below the plasmon energy. Therefore, their mean free path becomes very long

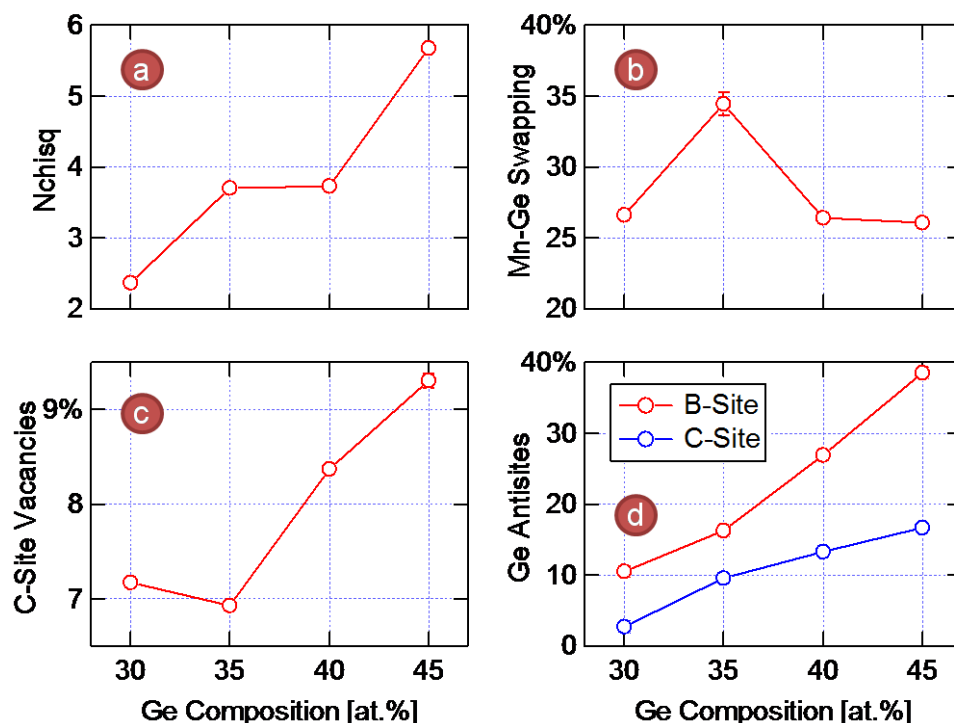
in the crystal and can scatter coherently from distant neighboring atoms and thus become sensitive to the types of disorder under investigation.

Figure 5-18 shows examples of this calculation on two datasets at different compositions of the S1 reflection near the Ge-edge. Without the solid state corrections [Figure 5-18 (a) and (b)], the near edge structure in the data is clearly not reproduced well by the model, although the pre-edge and extended post-edge trends overlap the data. With the addition of the calculated solid state corrections in Figure 5-18 (c) and (d), there is some improvement in the near edge structure, but a large peak 10eV above the edge exhibited in the calculations does not exist in the data. Finally, Figure 5-18 (e) and (f) show calculated solid state corrections for the Heusler structure modeled with random 30% site swapping between A and B sites (Mn and Ge swapping). Here the calculations reproduce the data extremely well for both compositions and were used in all full spectrum fits shown in Figure 5-17 and Table 5-3. Data and fits shown here are actually those for the study discussed in Section 5.3a and displayed in Figure 5-14. This result delivers powerful supporting evidence to the large Mn-Ge swapping obtained from the full spectrum anomalous diffraction fits.



**Figure 5-18: Two datasets and fits of the S1 reflection at the Ge edge with different solid state effects. Top row is data from 25 at.% Ge and bottom row from 45 at.% Ge. (a) & (b) are fits with only Cromer Liberman anomalous corrections (no solid state corrections). (c) & (d) are fits with calculated solid state corrections for the Heusler alloy. (e) & (f) are fits with calculated solid state corrections for the Heusler alloy with 30% Mn-Ge site swapping.**

Figure 5-19 shows trends of the most prevalent disorders found in the Ge Heusler measured from the full spectrum fitting analysis. Normed chi squared values shown in Figure 5-19a reflect the fact that only statistics from the data were used to generate uncertainties in the fit. Uncertainties associated with the measured correction factors, for example, were not included. Already discussed is the large value of Mn-Ge site swapping shown in Figure 5-19b, where other than results from the data at 35 at.% Ge, the level of this disorder is constant at ~26%. The other three types of disorders dominant from the analysis all generally have increasing levels with Ge composition. C-site vacancies are seen to increase in a similar fashion seen in the fits completed at the S1 reflection around the Ge-edge in Section 5.3a. The population of Ge antisites also increases with Ge concentration with a two-fold preference of the B-site over the C-site.



**Figure 5-19: Compositional trends of the most significant disorder populations found from the full spectrum anomalous diffraction analysis along the ridge of high crystallographic ordering. (a) Normed chi squared for each fit, (b) Mn-Ge site swapping, (c) C-site vacancies, (d) Ge antisites as a percentage of site population. Uncertainties are shown with each data point.**

The constant value of Mn-Ge swapping in the fit results suggests that composition and lattice relaxation do not significantly affect this disorder. Some amount of Mn-Ge swapping is not surprising as it has been noted in the Ge Heusler in an early neutron study<sup>10</sup>, even though later calculations suggest it is not energetically feasible.<sup>8</sup> It is possible for the current study that strain may be a cause of high levels of this disorder as out-of-plane strain is roughly constant for compositions where the data were taken. Band structure calculations, show that this type of disorder does not significantly affect the half-metallic energy gap as the Ge hybridized levels are well below the Fermi level.<sup>9,8</sup> However, such a large level of these disorders was not considered in the calculations.

The other three types of disorders dominant from the analysis are clearly composition related. As noted above, C-site vacancies are required for the diamond structure that eventually dominates

at Ge concentrations above 50 at.%. The significantly lower level of Ge in C-sites compared with B-sites suggests that excess Ge prefers to occupy B-sites, especially near the Heusler stoichiometry where Ge occupation of C-sites is nearly zero. However, due to the fact that there are twice as many C-sites as B-sites, the total number of Ge atoms in each site is fairly similar. The lack of B-site vacancies from the fit is surprising as this sublattice becomes fully vacant at 100% Ge. Clearly, with the reduction of Mn concentration, Ge are occupying the site vacancies. It is possible that the large Ge Heusler lattice parameter remaining through to 50 at.% Ge and the more metallic bonding exhibited in such a material could allow enough room for these defects in the unit cell rather than catalyzing the onset of vacancies. To fully understand this behavior, however, the local structure must be examined further. Analysis of the diffraction anomalous fine structure (DAFS) is similar to EXAFS with the added advantage that it is also site specific, owing to structure factor considerations of diffraction. This type of analysis was initially attempted on the data, but due to ambiguity in site occupancies resulting from the low contrast between elements in this technique, little could be determined. By adding information of the elementally resolved site occupancies measured from the study completed here, DAFS could be used to reveal local structure at Ge antisites to better understand possible bonding arrangements in these defects and draw a clearer picture of the physics behind their existence.

#### **5.4 Structural and Chemical Ordering of the Si Heusler**

The Si Heusler alloy is very similar to its Ge counterpart and is often theoretically studied in parallel, where first principles calculations typically show similar band structures<sup>1,13</sup> and defect energies.<sup>8</sup> One important difference is the lattice constant of the material. With Si, the bulk lattice constant has been measured to be 5.654Å, which has only a 0.07% mismatch with Ge. This is on the order of the strain seen in coherently grown Ge doped magnetic semiconductors discussed earlier, and when compared with the strain measured in the Ge Heusler, all but eliminates the strain in the

system. Additionally, the bulk material has been measured to have a higher Currie temperature at 985K and calculated to have a larger half metallic band gap at 0.81eV versus 0.54eV.<sup>17</sup> As the defect energies are similar for this system, an investigation into the structural and chemical ordering of the Si Heusler was undertaken using the techniques described above.

#### 5.4a: Thickness and Temperature Dependence

To explore the growth mode and crystal quality as a function of thickness, a  $(\text{Co}_x\text{Mn}_{1-x})_{0.77}\text{Si}_{0.23}$  binary sample was grown on a Ge (111) substrate at 300°C and analyzed by RHEED analysis. The resulting patterns show a quasi-2D growth for  $x$  between 50 and 100 at.% up to a critical thickness where a roughening transition occurs. Figure 5-20a shows the integrated intensity of the specular reflected beam which is highest at approximately  $x=75$  at.% up to 150Å. With increasing thickness, the highest intensities shift to  $x\sim 90$  at.% before the specular beam is extinguished at  $\sim 300$ Å. This trend follows the behavior of the roughening transition where 3D RHEED patterns appear just above 100Å at  $x=50$  at.% and gradually occurs over the entire composition range with increasing thickness (blue curve in Figure 5-20). The zeroth-order 3D diffraction peak has also been analyzed, whose transverse and longitudinal widths remain relatively constant with composition. In Figure 5-20b, the transverse integrated intensity of this peak is shown and exhibits a maximum intensity at  $x=66.7$  at.% (the Co to Mn atomic ratio of 2). This suggests that although the growth mode is 3D, surface crystal quality is superior at the Heusler stoichiometry. The fact that other compositions show stronger 2D growth at low coverages, however, suggests competing forces exist on the ordering of this structure. Binary samples were also grown at lower temperatures of 150°C and 225°C and showed similar thickness dependence, but compositions varied to greatly to quantitatively compare critical thickness or other growth characteristics.

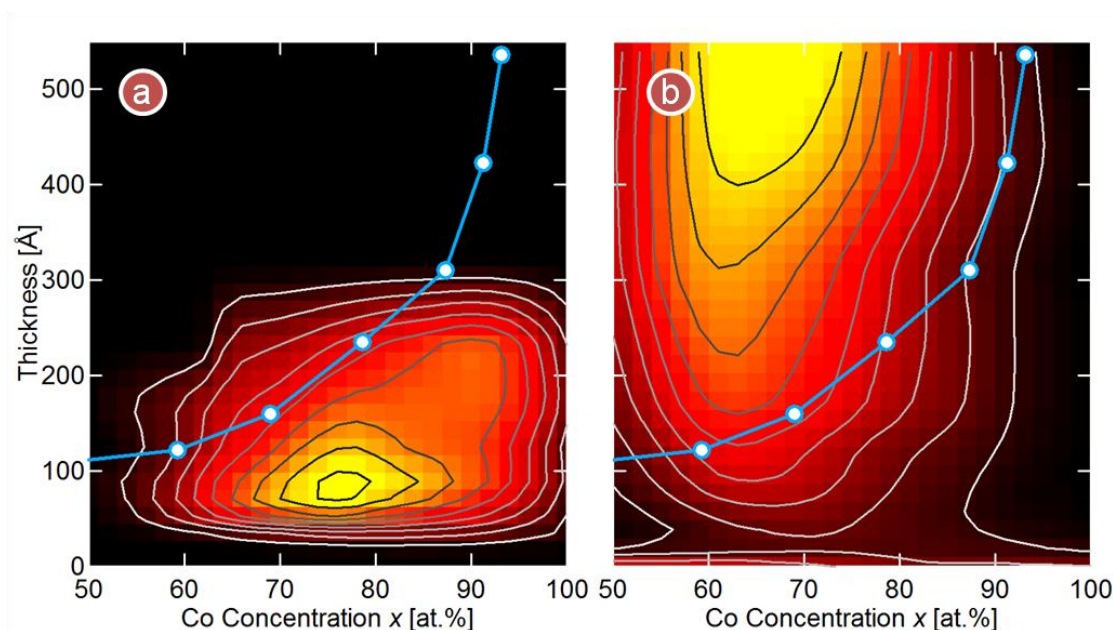


**Figure 5-20: Thickness dependent RHEED intensities of a  $(\text{Co}_x\text{Mn}_{1-x})_{0.77}\text{Si}_{0.23}$  binary sample grown at 300°C. Readings at varying thicknesses have been interpolated to fill a regular grid. (a) 2D specular intensity is fit and integrated longitudinally along the rod to remove rod background. (b) 3D diffracted intensity is fit and integrated perpendicular to the rod to reduce inseparable rod intensity contributions. The blue curve is the roughening transition. Intensities are on an arbitrary linear scale. (Data Courtesy of Liang He)**

Solid circles in Figure 5-21 show XRD analysis on the sample grown at 300°C. The composition dependence of the fundamental intensity contains peaks at both the Heusler stoichiometry and at  $x \sim 85$  at.%, suggesting high ordering at both compositions. These peaks correlate well with the compositions of maximum 3D diffracted intensity and maximum critical thickness, respectively, in the RHEED analysis described above. As XRD is a bulk probe, this sensitivity to higher ordering potentially occurring at different depths in the film is reasonable. Continuing this bulk/surface relationship, the superstructure XRD reflections both exhibit high intensities between these two compositions at  $x \sim 78$  at.% where RHEED 2D specular reflected intensities were the brightest at low coverages. As discussed in Section 5.2a, the XRD results show a superior chemical ordering within the unit cell at these compositions. In concert with the high structural and chemical ordering, the FWHM of the fundamental, shown in Figure 5-21b, is also narrow in this compositional region of the sample. As width corresponds to crystal coherence, the



wider width in the out-of-plane direction compared with in-plane suggests a coherent domain limited only by film thickness. This is also corroborated by the presence of truncation rod interference fringes (not shown) in this region of composition. The out-of-plane strain (Figure 5-21c) exhibits a linear Vegard's law composition dependence, suggesting each element is incorporating into the lattice. Finally, the in-plane strain shows that the film is epitaxially coherent across the compositional region of high ordering as expected from the similar lattice constants of Ge and the bulk Si Heusler.

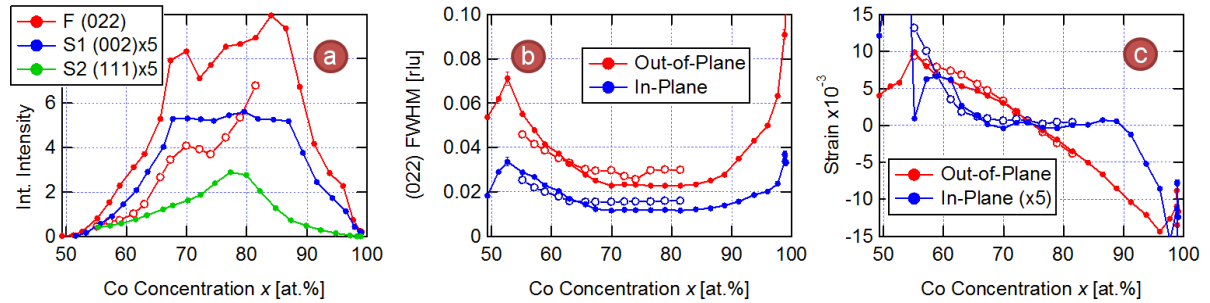


**Figure 5-21: XRD analysis of  $(\text{Co}_x\text{Mn}_{1-x})_{0.77}\text{Si}_{0.23}$  samples grown at 225°C and 360Å thick (open circles) and 300°C and 540Å thick (closed circles). (a) Integrated Intensity along the out-of-plane direction of the F, S1, and S2 reflections. S1 and S2 intensities are multiplied by 5 and the fundamental intensity from the sample grown at 225°C is reduced by a factor of 3. (b) FWHM of the fundamental reflection both in-plane and out-of-plane. (c) Strain with respect to the substrate in both the in-plane and out-of-plane directions. In-plane strain is enhanced by a factor of 5.**

For XRD, two ternary samples were also grown to assess the effects of growth temperature at identical compositions: 225°C and 300°C. In comparing samples at identical compositions and growth temperatures, the XRD integrated intensities were found to be proportional to film thickness with widths inversely proportional, further supporting the notion of film thickness limiting crystal coherence length. Data from the ternary sample grown at lower temperature (225°C) are extracted and shown as open circles in Figure 5-21 for temperature comparison. Integrated intensities of the fundamental (Figure 5-21a) show a similar pattern with a peak at the Heusler stoichiometry and increasing toward higher Co concentrations. Despite being a thinner film, the integrated intensities of the sample grown at 225°C are significantly higher than that of the film grown at 300°C, especially

at higher Co concentrations. (The data for the low temperature growth are reduced by a factor of 3.) This suggests higher ordering with the film grown at lower temperatures. Comparing widths of the two samples in the high-ordering region, in Figure 5-21b, the relative difference is simply that of the thicknesses as film thickness seems to be the dominant effect on crystal coherence rather than temperature. One noticeable difference is where the widths begin to increase. Here, the thinner film is able to retain better coherence (i.e. narrower width) at a larger composition range due to stronger epitaxial effects from the substrate. This is not surprising given the thickness evolution results from RHEED. Finally, Figure 5-21c shows similar values of strain both in-plane and out-of-plane with possibly more linear dependence at  $x=60$  at.% in the thinner film.

#### 5.4b: Ternary Phase Diagram

Figure 5-22a shows intensity profiles along the (01L) truncation rod which reveal the differences in structural ordering of the three distinct compositional regions of the  $\text{Co}_x\text{Mn}_y\text{Si}_z$  ternary system shown in Figure 5-22b. The reflection at  $L=5$  seen in all three profiles is the diamond (113)<sub>c</sub> reflection from the substrate. As described in Figure 5-1, the FCC (red curve) has reflections at  $L=1$  and  $L=4$  and have at least an order of magnitude higher intensity than any other phase in the ternary diagram. The reflection at  $L=2$  has been identified as stacking faults within the Ge substrate due to its position and width. A compositional region exhibiting a second phase with the FCC is seen in Figure 5-22b. Intensity profiles here show a degraded FCC phase with a peak at  $L=3.96$  with an unknown phase which has a reflection at  $L=3.73$ . Although there is a reflection from the film just below  $L=2$  there is no intensity between  $L=5.5$  and 6, ruling out a hexagonal phase. Finally, Mn and Si-rich regions of compositional phase space show only polycrystalline signals in RHEED and no significant reflections in XRD (green data in Figure 5-22a). This is likely due to a large variety of Mn silicides, which do not grow epitaxially on Ge.

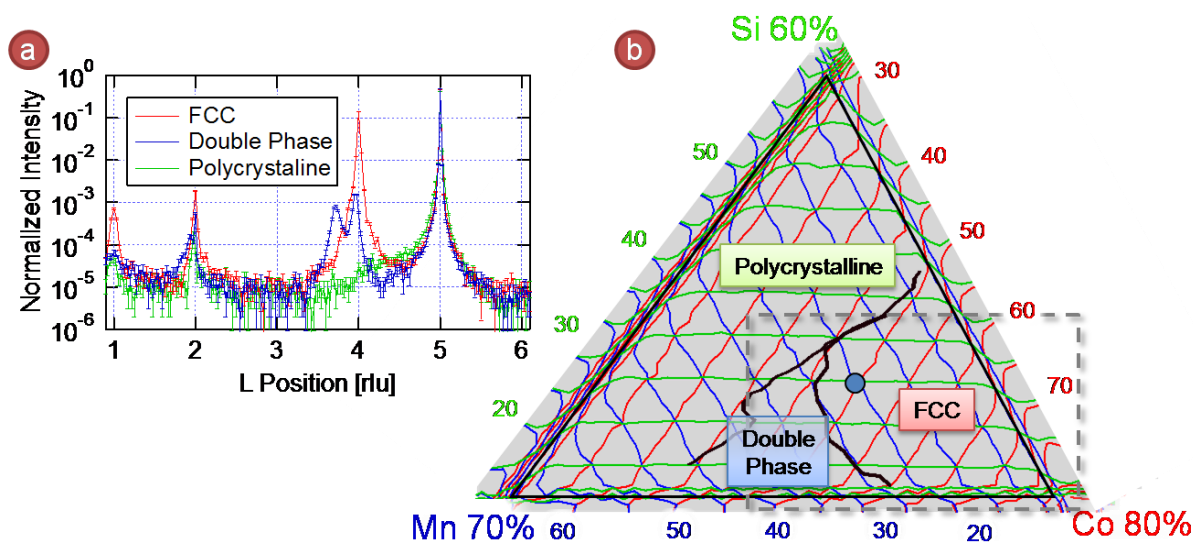


**Figure 5-22: Ternary epitaxial phase diagram of  $\text{Co}_x\text{Mn}_y\text{Si}_z$  showing three distinct phase regions. (a) Truncation rod intensity profiles along (01L) from each of the regions. FCC, Double Phase, and Polycrystalline data taken at compositions of  $\text{Co}_{0.54}\text{Mn}_{0.20}\text{Si}_{0.26}$ ,  $\text{Co}_{0.44}\text{Mn}_{0.38}\text{Si}_{0.18}$ , and  $\text{Co}_{0.38}\text{Mn}_{0.28}\text{Si}_{0.34}$ , respectively. (b) Evolution of crystallographic phase with composition where black curves delineate the phase boundaries. The blue circle is the Si Heusler composition, and the grey box indicates the ROI where further studies of crystallographic ordering were conducted.**

The phase boundaries and regions of coherence in the ternary samples did not significantly vary with growth temperature, and therefore, only the sample grown at the temperature promoting the best ordering (225°C) is discussed further. To focus on the Si Heusler, only a partial ternary sample was grown with compositions at the three apexes of only 60, 70, and 80 at.% of Si, Mn, and Co, respectively as seen in Figure 5-22b. But due to the large region of polycrystalline growth, this region of interest is further reduced (gray box in Figure 5-22b) to that containing the Heusler composition (indicated by the blue circle) and where FCC structural ordering was measured. Here, crystal quality and coherence are determined from the fundamental reflection intensity and width and are displayed in Figure 5-23. As noted above, high intensities are measured across the entire region of FCC structural ordering diminishing in the double phase region. However, the composition of highest integrated intensity is not the Heusler stoichiometry, but rather at  $\text{Co}_{0.64}\text{Mn}_{0.13}\text{Si}_{0.23}$ , which is within the compositional region studied above in the binary sample. Crystal coherence (Figure 5-23b) is also highest at this composition with a mosaicity spreading less than  $0.2^\circ$  in the azimuth,

although the entire FCC region – including the Heusler composition – is also highly coherent with a FWHM below  $0.5^\circ$ . Indeed, brighter diffraction intensities and narrower widths at Co-rich compositional regions were seen in all samples studied.

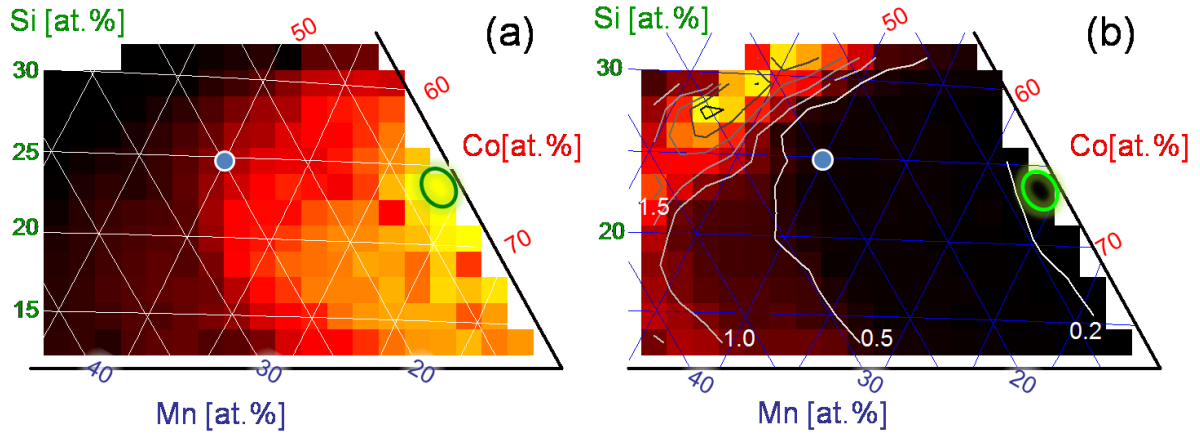


**Figure 5-23: Crystallographic ordering in the  $\text{Co}_x\text{Mn}_y\text{Si}_z$  ternary system as measured peak fits to the fundamental reflection. (a) linear integrated intensity along the out-of-plane ( $L$ ) direction and (b) FWHM of the reflection along the azimuth with contours labeled in degrees. Blue circles indicate the Heusler stoichiometry and green ellipses are the composition of highest intensity.**

Crystallographic strain perpendicular to the sample surface is displayed in Figure 5-24a and shows a linear compositional dependence. In plane, a wide compositional region is coherent with the substrate and includes both points of interest. Notably, the boundary of this coherent region coincides with that of the region of high intensity as well as the onset of the second phase, suggesting that epitaxial relaxation plays a role in phase separation in this ternary system. Within the FCC region, strain does not seem to play major a role in ordering, as the composition of highest ordering exhibits more than twice the strain of the Heusler stoichiometry.

The in-plane and out-of-plane strains are combined through elastic theory described in Section 5.2a to calculate the lattice parameter of the film, which is compared with that of bulk Si Heusler in Figure 5-24c. Neither the Heusler composition nor the composition exhibiting the highest ordering exhibits the bulk lattice constant. Rather, they show equal but opposite mismatch with this parameter. The film lattice parameter exhibits Vegard's law behavior in a large region of

composition that includes the double phase region as shown by the green curve in Figure 5-24.

Although the region looks fairly linear, a slightly quadratic surface provided a better fit to the data than a plane, with quadratic coefficients one to two orders of magnitude smaller than linear ones. It is unclear if quadratic terms are necessary for reasons intrinsic to the film or simply result from instrumental effects. From this surface, the metallic atomic radii were extracted to be 1.19Å for Si, 1.22Å for Co, and 1.25Å for Mn with uncertainties of 0.01Å. These are in excellent agreement with the Goldschmidt radii for Co (1.22Å) and Mn (1.28Å) but have been noted to vary depending on the magnetic state they take in an alloy.<sup>24</sup> For example, these deviate somewhat from those reported in Reference 25.

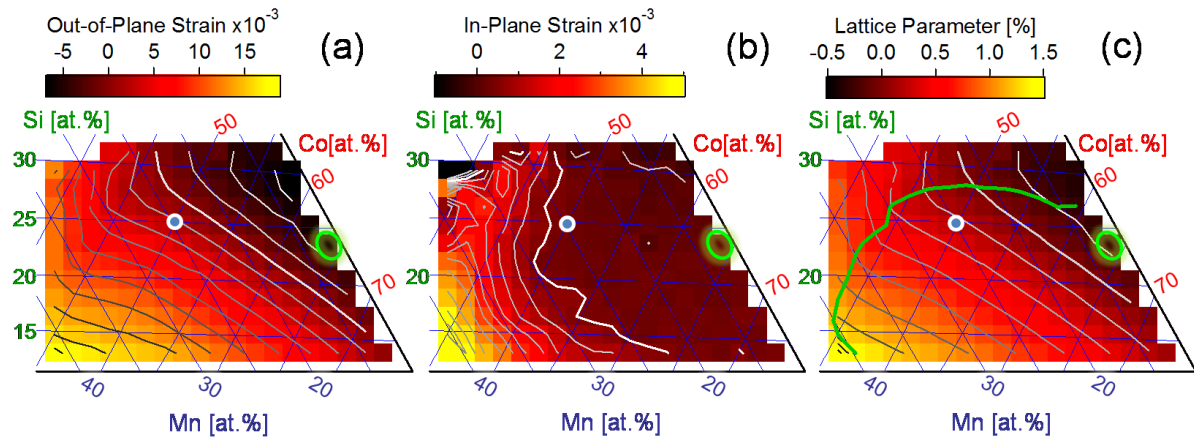


**Figure 5-24: Compositional evolution of film (a) out-of-plane strain ( $(L_{\text{film}} - L_{\text{Ge}})/L_{\text{Ge}}$ ), (b) in-plane strain, and (c) elastically corrected lattice parameter relative to that measured for the Si Heusler alloy. Circles and ellipses mark the same points of interest in Figure 5-23. The green contour in (c) is where the data deviates from a quadratic fit to the lattice parameter, indicating a region obeying Vegard's law. Bold contours indicate out-of-plane lattice matching, in-plane crystal relaxation threshold, and bulk lattice parameter of the Si Heusler, respectively.**

The results described here give rise to several interesting questions that awaits further investigations: Why does the best ordering and lattice parameter occur at compositions other than that of the Heusler stoichiometry, even at larger strains? Why can 2D growth of the Ge Heusler alloy be stabilized under large strains and lattice relaxation, while the Si Heusler alloy exhibits rough 3D growth in the absence of strain? In fact, high-quality crystal formation and fully epitaxial

heterostructures of this alloy are shown to be stable under a variety of synthesis techniques including the Czochralski method<sup>12</sup> and magnetron sputtering.<sup>26</sup> And finally, what are the spin polarizations of these compositions?

## 5.5 Summary

Ternary epitaxial phase diagrams for  $\text{Co}_x\text{Mn}_y\text{Ge}_z$  and  $\text{Co}_x\text{Mn}_y\text{Si}_z$  on Ge(111) substrates have been presented. In Ge alloys, epitaxial phases were observed in the entire compositional phase space including the Ge Heusler structure, which is stabilized over a large compositional region. By contrast, deposition of Si alloys result in mostly polycrystalline films over much of the composition studied except for the Co-rich quadrant of the phase diagram where the Si Heusler structure was observed.

The effects of composition, epitaxial strain, and temperature on structural and chemical ordering have been studied in group IV based Heusler alloys using primarily synchrotron x-ray techniques. Both structural and chemical ordering of the Ge Heusler is shown to be extremely sensitive to the Co to Mn atomic ratio resulting in a narrow ridge of high ordering along this ratio at Ge compositions between 20 and 50 at.%. XRD measurements suggest structural and chemical ordering along this ridge decrease with increasing in-plane lattice relaxation, but anomalous measurements show that the chemical and stacking sequences of the structure are robust to variations in composition and strain. Full spectrum anomalous diffraction analysis is shown to quantitatively measure specific elemental disorders within the unit cell impossible to study in combinatorial samples using other techniques. This experiment reveals that the dominant elemental defect in these materials is Mn-Ge site swapping – a result that is corroborated by *ab initio* modeling of the fine structure near the Ge edge. Other forms of disorder such as C-site

vacancies and Ge antisites occur due to off-stoichiometry, whereas an anticipated defect of Co-Mn site swapping is not present.

In contrast to the Ge Heusler, the Co to Mn atomic ratio is not critical to ordering of the Si Heusler alloy, as it exhibits strong coherent epitaxial ordering over a large region of relative concentration of the metallic elements. The structure is also robust to a variation of Si concentration with high diffraction intensities and the lattice parameter obeying Vegard's law from 10 to 30 at.% Si. However, with the loss of in-plane epitaxial coherence the structural ordering breaks down more severely than the Ge Heusler becoming multi-phased or polycrystalline. Additionally, thickness dependent RHEED analysis shows a roughening transition within a few hundred Angstroms of deposition although the Ge alloy exhibits none and composition of highest intensities depending on film thickness. Combined with XRD, these studies suggest multiple chemical forces at work, causing superior structural and chemical ordering to occur at films containing excess Co even under negligible strain from the substrate.

## Bibliography

1. Ishida, S., Masaki, T., Fujii, S. & Asano, S. Theoretical search for half-metallic films of  $\text{Co}_2\text{MnZ}$  ( $Z = \text{Si, Ge}$ ). *Physica B: Condensed Matter* **245**, 1-8 (1998).
2. de Groot, R.A., Mueller, F.M., Engen, P.G.V. & Buschow, K.H.J. New Class of Materials: Half-Metallic Ferromagnets. *Phys. Rev. Lett.* **50**, 2024 (1983).
3. Hirohata, A. et al. Heusler alloy/semiconductor hybrid structures. *Current Opinion in Solid State and Materials Science* **10**, 93-107 (2006).
4. Katsnelson, M.I., Irkhin, V.Y., Chioncel, L., Lichtenstein, A.I. & de Groot, R.A. Half-metallic ferromagnets: From band structure to many-body effects. *Rev. Mod. Phys.* **80**, 315-64 (2008).
5. Ritchie, L. et al. Magnetic, structural, and transport properties of the Heusler alloys  $\text{Co}_2\text{MnSi}$  and  $\text{NiMnSb}$ . *Phys. Rev. B* **68**, 104430 (2003).
6. Orgassa, D., Fujiwara, H., Schulthess, T.C. & Butler, W.H. First-principles calculation of the effect of atomic disorder on the electronic structure of the half-metallic ferromagnet  $\text{NiMnSb}$ . *Phys. Rev. B* **60**, 13237 (1999).
7. Orgassa, D., Fujiwara, H., Schulthess, T.C. & Butler, W.H. Disorder dependence of the magnetic moment of the half-metallic ferromagnet  $\text{NiMnSb}$  from first principles. *J. Appl. Phys.* **87**, 5870-5871 (2000).
8. Picozzi, S., Continenza, A. & Freeman, A.J. Role of structural defects on the half-metallic character of  $\text{Co}_2\text{MnGe}$  and  $\text{Co}_2\text{MnSi}$  Heusler alloys. *Phys. Rev. B* **69**, 094423 (2004).
9. Galanakis, I., Mavropoulos, P. & Dederichs, P.H. Electronic structure and Slater–Pauling behaviour in half-metallic Heusler alloys calculated from first principles. *Journal of Physics D: Applied Physics* **39**, 765-775 (2006).
10. Brown, P.J., Neumann, K.U., Webster, P.J. & Ziebeck, K.R.A. The magnetization distributions in some Heusler alloys proposed as half-metallic ferromagnets. *Journal of Physics: Condensed Matter* **12**, 1827-1835 (2000).
11. Ravel, B., Raphael, M.P., Harris, V.G. & Huang, Q. EXAFS and neutron diffraction study of the Heusler alloy  $\text{Co}_2\text{MnSi}$ . *Phys. Rev. B* **65**, 184431 (2002).
12. Raphael, M.P. et al. Presence of antisite disorder and its characterization in the predicted half-metal  $\text{Co}_2\text{MnSi}$ . *Phys. Rev. B* **66**, 104429 (2002).
13. Ishida, S., Fujii, S., Nagayoshi, H. & Asano, S. Novel half-metallic films of  $\text{Co}_2\text{MnZ}$  ( $Z=\text{Si, Ge}$ ) coated with Mn layers. *Physica B: Condensed Matter* **254**, 157-165 (1998).
14. Chu, Y.S. et al. Structural investigation of  $\text{CoMnGe}$  combinatorial epitaxial thin films using microfocused synchrotron X-ray. *Applied Surface Science* **223**, 175-182 (2004).
15. Tsui, F. et al. Structure and magnetism of  $\text{Co}_{1-x}\text{Mn}_x\text{Ge}$  epitaxial films. *Applied Surface Science* **252**, 2512-2517 (2006).



16. Chu, Y.S., Robinson, I.K. & Gewirth, A.A. Properties of an electrochemically deposited Pb monolayer on Cu(111). *Phys. Rev. B* **55**, 7945 (1997).
17. Picozzi, S., Continenza, A. & Freeman, A.J. Co<sub>2</sub>MnX (X=Si, Ge, Sn) Heusler compounds: An ab initio study of their structural, electronic, and magnetic properties at zero and elevated pressure. *Phys. Rev. B* **66**, 094421 (2002).
18. Cromer, D.T. & Liberman, D. Relativistic Calculation of Anomalous Scattering Factors for X Rays. *J. Chem. Phys.* **53**, 1891-1898 (1970).
19. Ilavsky, J. Atomic scattering factors and attenuation using the Chromer-Liberaman code for IGOR PRO ver. 4.0. (2006).at <<http://www.uni.aps.anl.gov/~ilavsky/AtomicFormFactors.html>>
20. Collins, B.A., Zhong, Y., Chu, Y.S., He, L. & Tsui, F. Anomalous x-ray diffraction study of disorders in epitaxial films of the Heusler alloy Co<sub>2</sub>MnGe. *J. Vac. Sci. Technol. B* **25**, 999-1003 (2007).
21. Ravel, B. et al. Atomic disorder in Heusler Co<sub>2</sub>MnGe measured by anomalous x-ray diffraction. *Appl. Phys. Lett.* **81**, 2812-2814 (2002).
22. Ravel, B. & Newville, M. ATHENA, ARTEMIS, HEPHAESTUS: data analysis for X-ray absorption spectroscopy using IFEFFIT. *Journal of Synchrotron Radiation* **12**, 537-541 (2005).
23. Rehr, J., Deleon, J., Zabinsky, S. & Albers, R. Theoretical X-ray Absorption Fine Structure Standards. *Journal of the American Chemical Society* **113**, 5135-5140 (1991).
24. Fu, C.L., Liu, C.T., Wang, X., Krcmar, M. & Fernandez-Baca, J.A. Magnetism-induced solid solution softening in NiAl with Co, Fe, Mn, and Cr solute atoms: theory and experiment. *Intermetallics* **12**, 911-919
25. Greenwood, N.N. & Earnshaw, A. *Chemistry of the Elements*. (Butterworth-Heinemann: Oxford, 1997).
26. Sakuraba, Y. et al. Giant tunneling magnetoresistance in Co<sub>2</sub>MnSi/Al--O/Co<sub>2</sub>MnSi magnetic tunnel junctions. *Appl. Phys. Lett.* **88**, 192508-3 (2006).

# Chapter 6 Conclusions

---

In this thesis, structural and chemical ordering in ternary magnetic epitaxial films that contain two transition metal elements and a group IV element have been examined as a function of composition and epitaxial constraints using synchrotron x-ray techniques. Combinatorial x-ray methods were developed to systematically investigate these complex materials. Complementary techniques involving diffraction and spectroscopy have been integrated to study dopant states and chemical ordering on the atomic scale. A new analytical method, full-spectrum anomalous diffraction analysis, has been developed to quantify atomic site-specific elemental disorders and occupancies in an epitaxial thin film.

In the study of epitaxial films of doped magnetic semiconductor materials, this work has shown that codoping with two transition metal dopants in Ge can promote higher solubility and a higher population of substitutional doping in the semiconducting matrix than with a single dopant. In Ge (001) films codoped with Co and Mn, doping with even trace amounts of Co was found to reduce and suppress the formation of Mn precipitates and surface segregation. Analysis of diffraction and EXAFS measurements reveals the presence of a third dopant state at Mn-rich compositions, in addition to populations of substitutional Co and Mn. The nature of this dopant state is inconsistent with the presence of interstitials but suggests the presence of small clusters, perhaps Mn-Mn substitutional dimers, which have been calculated to have low formation energies and to interact antiferromagnetically. Magnetic and magnetotransport measurements indicate low

carrier concentration and weak ferromagnetic interactions in these materials, which may be attributed to the characteristics of these dimers.

In films codoped with Fe and Co, doping concentrations up to 7 at.%, strain states obey Vegard's law and Fe ions are ferromagnetic whereas Co are paramagnetic. At higher doping levels, a change in strain state and dopant local environments takes place, associated with a saturation of magnetic moment in both Fe and Co. This finding suggests that the population of magnetically active dopant states reaches a saturation with the remaining dopants becoming inactive. Film grown on GaAs substrates have also been studied. Their structural properties are identical to those of films on Ge, except for a higher level of disorder associated with trace amounts of Ga from the substrate, which has been attributed to the strikingly different electrical and magnetic properties. This observation suggests that electron mobility also plays an important role in magnetic ordering in DMS materials, perhaps over and above the parameters, including carrier concentration and concentration of magnetic ions, at the focal point of popular models. These findings for both DMS systems show that a full understanding and control of dopant states is critical to tailoring a material's electronic and magnetic properties.

In studying the ternary Heusler alloys that contain Co, Mn and Ge (or Si) grown on Ge (111) substrates, full epitaxial phase diagrams have been investigated for the first time. The study has shown that epitaxial films can be grown over a large region of chemical composition, stabilizing a small number of crystalline phases. In the case of the Ge Heusler, two hexagonal phases in the Mn-rich region of the composition have been observed, in addition to the Heusler FCC  $L2_1$  structure in the Co-rich region and the diamond structure in the Ge-rich region. The structural and chemical ordering of the Ge Heusler is determined to be extremely sensitive to the Co to Mn atomic ratio, but less so with respect to the Ge concentration. The highest structural ordering occurs within a narrow

region of composition with Co:Mn = 2, where the film lattice constant is determined to be approximately that of the bulk. Within this region, however, the degree of structural ordering decreases with Ge concentration, accompanied by an increase of in-plane lattice relaxation, while no detectable change in structural and chemical stacking sequences has been observed. Using the newly developed full-spectrum anomalous diffraction analysis, the primary type of disorders in this material is determined to be Mn-Ge swapping, followed by Ge antisites and Co vacancies, while the expected defect of Co-Mn site swapping is absent. Although Mn-Ge swapping is not calculated to destroy the predicted half metallic state in this material, levels of 30% are surprisingly large and could disrupt the bonding symmetry needed to preserve the half metallic band gap. The populations of the secondary defects increase with increasing Ge concentration. For the Si Heusler, single-phase epitaxial films can also be grown on Ge (111) substrates over a large compositional region, but in this system, in-plane lattice relaxation results in a much larger deterioration of ordering, with the film incurring secondary phases or becoming polycrystalline. Yet even in regions of relatively small lattice mismatch and coherent epitaxy, a transition from smooth growth at low coverages to rough growth at higher coverages occurs with a critical thickness for the transition increasing with Co concentration. The highest structural and chemical ordering is observed at compositions with Co to Mn atomic ratios that are much higher than 2 (the stoichiometric value), where the epitaxial strain is much larger than that at the Heusler stoichiometry. These results indicate that the critical roles are played by the chemistry and interfacial effects rather than epitaxial strain and highlight the need for a better understanding of these phenomena.

In this work, the ability to resolve structural and chemical ordering on the atomic scale has proven critical in understanding important issues related to dopant states and elemental defects in these spintronics materials candidates. The work also demonstrates the power of combinatorial epitaxial synthesis to control and stabilize the formation of specific structures in a large

compositional space. These, in turn, will provide viable means for atomic scale exploration of new materials and properties.

# Curriculum Vitae

---

Brian Akira Collins was born in Cedar Rapids, Iowa on October 7<sup>th</sup>, 1980 and graduated with a B.A. in physics and music minor magna cum laude from Gustavus Adolphus College in St. Peter, MN in 2003. He attended the physics and astronomy program at the University of North Carolina at Chapel Hill where he was conferred the degrees of Masters of Science in December 2005 and, with the culmination of this work, Doctor of Philosophy in August 2009 both in the area of physics. Under the mentorship of Professor Frank Tsui, he completed structural studies on combinatorial ternary epitaxial films. Part of the work was completed at the Advanced Photon Source at Argonne National Laboratory under the mentorship of Dr. Yong S. Chu, who is now a group leader at the National Synchrotron Light Source II at Brookhaven National Laboratory. While at Argonne, he was able to attend the National School for Neutron and X-ray Scattering and present his findings at seminars and user conferences. Brian also developed scanning probe microscopy studies in the Tsui laboratory at UNC. He gave presentations at numerous conferences and was awarded the Outstanding Student Paper Award at the 24<sup>th</sup> North American Conference on Molecular Beam Epitaxy in 2006. Throughout his years as a graduate student, he was awarded the UNC Board of Governors Fellowship in 2003 and the UNC Graduate School Dissertation Completion Fellowship in 2008. Brian was also involved in many service groups and positions: sitting on the UNC Administrative Board of the Library (2007-2009), acting as the Graduate Student Association Grievance Officer (2007-2009), participating in the K-12 Physics Outreach Team (2007-2009), and leading in program recruitment as the Graduate Student Recruitment Liaison (2003-2005). He also

taught several introductory physics courses and tutored high school AP and college students in physics during his time at UNC. He is an avid participant in choral singing and playing the piano.

## Publications

1. P.K. Muduli, W.C. Rice, L. He, B.A. Collins, Y.S. Chu, F. Tsui, "Study of magnetic anisotropy and magnetization reversal using the quadratic magnetooptical effect in epitaxial  $\text{Co}_x\text{Mn}_y\text{Ge}_z(111)$  films." *Journal of Physics: Condensed Matter*, **21**, 296005 (2009).
2. B.A. Collins, Y.S. Chu, L. He, Y. Zhong, and F. Tsui, "Dopant stability and strain states in Co and Mn doped Ge (001) epitaxial films." *Phys. Rev. B*, **77**, 193301 (2008).
3. F. Tsui, B.A. Collins, L. He, A. Mellnik, Y. Zhong, S. Vogt, Y.S. Chu, "Combinatorial synthesis and characterization of a ternary epitaxial film of Co and Mn doped Ge(001)." *Appl. Surf. Sci.* **254**, 709 (2007).
4. Yuncheng Zhong, Yong S. Chu, Brian A. Collins, Frank Tsui., "High-resolution X-ray diffraction studies of combinatorial epitaxial Ge(001) thin-films on Ge(001) substrates." *Appl. Surf. Sci.* **254**, 714 (2007)
5. Brian A. Collins, Yuncheng Zhong, Yong Chu, Liang He, Frank Tsui. "Anomalous x-ray diffraction study of the Heusler Alloy  $\text{Co}_2\text{MnGe}$ ." *J. Vac. Sci. Technol. B* **25**, 999 (2007).
6. Liang He, Brian Collins, Frank Tsui. "Epitaxial Growth of  $(\text{FeCo})_x\text{Ge}_{1-x}(001)$ ." *J. Vac. Sci. Technol. B* **25**, 1217 (2007).
7. E. V. Barrera, L. P. F. Chibante, B. Collins, F. Rodriguez-Marcias, M. Shofner, J. D. Kim, and F. D. S. Marquis. "Recycling Nanotubes from Polymer Nanocomposites." *Powder Materials Current Research and Industrial Practices*, F. D. S. Marquis, E. V. Barrera, and N. Thadani, eds., TMS Pub. (2001): 267-282.